Sorbonne Université

École doctorale n°564 Physique en Île-de-France

Institut Curie, Laboratoire Physique des Cellules et Cancer (UMR168)
Équipe Macromolécules et Microsystèmes en Biologie et en Médecine

MAGNETIC ENGINEERING OF ANISOTROPIC MUSCLE TISSUE

Thèse de Doctorat de Physique

Présentée par

Noam DEMRI

Dirigée par **Claire WILHELM** et **Stéphanie DESCROIX**

Présentée et soutenue publiquement le **2 septembre 2025**
Devant un jury composé de :

Nicolas MINC DR, CNRS, Institut Jacques Monod	*Président du jury*
Delphine DUPREZ DR, CNRS, Sorbonne Université	*Examinatrice*
Catherine LE VISAGE DR, INSERM, Nantes Université	*Rapportrice*
Neil TELLING Professeur, Keele University	*Rapporteur*
Claire WILHELM, DR, CNRS, Institut Curie	*Directrice de thèse*
Stéphanie DESCROIX DR, CNRS, Institut Curie	*Co-directrice de thèse*

Remerciements

Comme me le répètent souvent mes collègues et amis : « faire du muscle c'est pas facile, surtout quand on est en thèse. » Cependant, les tissus musculaires conçus au cours de ces quatre dernières années, et mes travaux de doctorat dans leur ensemble, n'auraient pu voir le jour sans l'aide, le soutien et les contributions de toutes les personnes qui m'ont entouré. C'est pourquoi j'ai le grand plaisir de pouvoir commencer ce manuscrit, comme le veut la tradition, en remerciant toutes les personnes qui ont contribué de près ou de loin à sa réalisation.

Je tiens tout d'abord à remercier les membres de mon jury pour avoir accepté d'évaluer mon travail: Catherine Le Visage et Neil Telling, en tant que rapporteurs, Delphine Duprez, en tant qu'examinatrice, et Nicolas Minc, en tant que président du jury.

Ma gratitude va également à Françoise Brochard et Léa Trichet, membres de mon comité de suivi de thèse, pour leur accompagnement constant et pour la richesse des conseils et discussions que nous avons partagés.

Au cours de ma thèse j'ai eu le privilège de collaborer avec Cécile Martinat, Lise Morizur et Morgan Gazzola de l'ISTEM, que je remercie sincèrement pour avoir partagé leur expertise musculaire toujours précieuse, et que je qualifierais même de « plus que musclée. »

J'ai eu la chance de réaliser ma thèse dans un cadre véritablement unique, en plein cœur du quartier latin à Paris, au sein de l'UMR 168, à l'Institut Curie et à l'Institut Pierre-Gilles de Gennes, et je suis profondément reconnaissant pour tous les moyens dont j'ai pu bénéficier.

En particulier, j'ai profité de l'expertise cellulaire des ingénieurs de la plateforme BMBC de l'Institut Curie, notamment Fanny Tabarin-Cayrac et Carine Vias. J'ai également eu beaucoup de chance d'avoir eu accès, à peine un étage au-dessus de mon bureau, à la plateforme de l'Institut Pierre-Gilles de Gennes, dont les ingénieurs m'ont accompagné tout au long de ma thèse, notamment Bertrand Cinquin, Audric Jan et Taha Messelmani.

Je ne remercierai jamais assez mes directrices de thèse, Claire Wilhelm et Stéphanie Descroix, sans qui mes travaux de doctorat n'auraient jamais vu le jour.

Plus que son rôle de directrice de thèse, Claire a été, et restera toujours à mes yeux, un modèle de scientifique vers lequel aspirer. Travailler avec elle, c'est se laisser emporter par un tourbillon d'idées toujours nouvelles et stimulantes qui tracent un itinéraire vers la science de demain. Des nanoparticules aux cellules magnétiques, en passant par les vésicules, on peut suivre ce chemin au rythme de ses éclats de rire qui résonnent au 4e étage de l'Institut Pierre-Gilles de Gennes. Mais au-delà de ses qualités scientifiques, j'ai été particulièrement touché par la bienveillance et la gentillesse dont elle a fait preuve à mon égard.

Stéphanie, quant à elle, met des paillettes dans la science, y compris ma thèse, aussi bien au sens propre qu'au sens figuré. De chacun de nos échanges au cours de ces quatre années, je suis ressorti grandi, nourri de perspectives plus critiques, plus rigoureuses, et plus scientifiques. Je serai toujours reconnaissant d'avoir pu bénéficier de son expérience, de son aide et de son soutien tout au long de ma thèse.

Je me souviens encore de notre première rencontre, où, au-delà de la passion scientifique pour mon futur projet de thèse qui les animait, j'ai été marqué par leur sourire qui laissait à peine présager le mentorat, et aujourd'hui l'amitié, qui en découleraient.

Bien évidemment, le soutien quotidien que j'ai reçu au cours de ma thèse ne se limite pas à mes directrices de thèse. J'ai eu l'immense honneur de partager ces quatre années avec les membres exceptionnels de l'équipe MMBM.

A mon arrivée, j'ai bénéficié de l'aide d'Efrain Perez et Manh-Louis Nguyen, qui m'ont formé aux techniques de l'équipe. Je suis particulièrement reconnaissant à Giacomo Gropplero, qui, au cours de ces quatre années a eu réponse à (presque) tous les problèmes que j'ai pu avoir. J'ai aussi eu la chance de travailler avec Simon Dumas, qui a eu la gentillesse et la patience de me transmettre nombre de ces techniques. A mon tour, j'ai eu le plaisir de former deux stagiaires, Corentin Moreau et Polina Petrova Tsvetkova, et je les remercie pour l'aide qu'ils m'ont apportée. Je suis aussi reconnaissant envers Aurore Van de Walle, Sylvie Coscoy et Jean-Louis Viovy pour l'aide et les conseils qu'ils ont pu m'apporter.

Sans craindre le cliché, je dois dire que l'équipe MMBM est véritablement devenue une seconde famille. Merci à tous ces collègues, aujourd'hui devenus des amis : Paul Valois, pour son soutien aussi bien au sein du labo au début de ma thèse qu'en dehors après son départ ; Anastasiia Dubrova, pour tous ces moments de complicité, en particulier nos discussions sans fin le long du Boulevard Saint-Michel ; Maxime Simon, pour avoir partagé sa curiosité scientifique et ses talents de maestro ; Caroline Parent, pour toutes les discussions enrichissantes que nous avons eues ; Guilhem Curé, pour sa gentillesse et ses talents de pâtissier; Elliot Lopez, pour son enthousiasme ; Brice Lapin, pour son aide constante ; Moencopi Bernheim-Dennery, pour sa joie de vivre communicative ; Charlotte Bouquerel, pour sa bienveillance. Une attention toute particulière va à mes compagnons de bureau qui m'ont vu au plus près au cours de ces années : Emile Gasser, qui m'a toujours aidé et guidé dans les moments difficiles, Juliette Jin qui m'a montré qu'on peut faire preuve de rigueur scientifique tout en restant « fun », et Niccolò Schintu pour ses encouragements au cours de ma dernière année de thèse.

Je remercie également Elliot Thouvenot, Fahima Di Federico, Jessica Vandensteen, Lucas Chassate, Solène Lenoir, Vivian Aubert, Lucile Alexandre, Monica Araya, Lauriane Gérémie, ainsi que toutes celles et ceux qui, à un moment ou un autre, m'ont apporté leur aide.

Au cours de ma thèse, j'ai aussi eu la chance d'être entouré de mes amis, dont le soutien a été précieux. Merci à Camille, Lorraine, Flore, Marie, Maïalen, Théana, Léa, Aubin, Julie, Aline, Maëlle, Luc, et bien d'autres encore !

Enfin, je ne pourrai jamais remercier suffisamment ceux qui m'ont aidé autant qu'ils le pouvaient à chaque étape, chaque moment, chaque épreuve de ma thèse : mes parents. Faire du muscle n'aurait pas été possible sans eux !

Merci !

Summary

Tissue engineering aims to recreate physiologically relevant, functional biological tissues for biomedical applications. Among the most challenging targets are anisotropic tissues, such as skeletal muscle, where oriented architectures are essential to both structure and function. By leveraging the properties of magnetic nanoparticles internalized by cells, remote magnetic forces can be applied to guide anisotropic tissue morphogenesis.

After reviewing the biology of anisotropic tissues and the current engineering strategies, this PhD thesis introduces three original magnetic anisotropic tissue engineering approaches, specifically applied to skeletal muscle. These studies were made possible thanks to an initial optimization of magnetic nanoparticle internalization by myoblasts. The first magnetic platform was designed for generating small spheroids from these magnetically labeled cells at high throughput, aligning them in a collagen matrix, and ultimately revealing a transition from a linear arrangement of spheroids to a continuous fiber. To further enhance control over tissue shape and function, a novel magnetic bioprinting technique was established. This system enabled the engineering of wrench-shaped tissues that can be clipped onto two magnetic attractors, to preserve their initial shape and allow up to 100% stretching. Magnetic trapping and mechanical stimulation accelerated the differentiation of functional muscle tissues in just a few days, particularly when they were engineered with myoblasts derived from human induced pluripotent stem cells. The versatility of magnetic bioprinting was then explored by creating tissues of arbitrary shapes - triangles, droplets, squares, and crosses. The cross-shaped tissues, in particular, allowed for a clear demonstration of the relationship between tissue geometry, mechanical constraints, and differentiation. Additionally, this work investigated the resistance to rupture of magnetically printed tissues while also establishing the feasibility of co-culturing fibroblasts, using magnetism to precisely control the spatial segregation of different cell types.

Overall, this PhD thesis highlights the potential of magnetic forces for engineering structured, functional tissues, particularly skeletal muscle, and paves the way for biomedical applications in disease modeling, mechanobiology, and remotely guided tissue grafting.

Keywords: Tissue engineering – Magnetic nanoparticles – Magnetic bioprinting – Skeletal muscle – Biomechanics – Microfabrication

Résumé

L'ingénierie tissulaire a pour but de reconstituer aussi fidèlement que possible des tissus biologiques, à des fins biomédicales. Parmi les structures les plus difficiles à reproduire figurent les tissus anisotropes, tels que le muscle squelettique, dont l'alignement cellulaire est essentiel à son architecture et sa fonction. L'internalisation de nanoparticules magnétiques par les cellules est une stratégie prometteuse permettant de leur appliquer des forces magnétiques à distance afin de guider une morphogénèse anisotrope.

Après avoir passé en revue les principes biologiques des tissus anisotropes et des méthodes actuelles pour les concevoir en laboratoire, cette thèse introduit trois approches originales pour l'ingénierie tissulaire magnétique de tissus anisotropes, spécifiquement appliquées au muscle squelettique. Ces trois études ont été rendues possibles par une optimisation préalable de l'internalisation de nanoparticules magnétiques par des myoblastes. La première plateforme magnétique repose sur la production à grande échelle de petits sphéroïdes à partir de ces cellules marquées magnétiquement, dans le but de les aligner au sein d'une matrice de collagène, afin de permettre la fusion des chaines de sphéroïdes en fibres cellulaires. Afin d'améliorer notre contrôle sur la morphogénèse et la fonctionnalisation musculaire, nous avons ensuite développé une technique innovante de bioimpression magnétique. Cette plateforme a permis la conception de tissus musculaires en forme de clé à molette, capables d'être piégés entre deux attracteurs magnétiques, et d'être étirés jusqu'à 100%, favorisant une différenciation musculaire rapide, en particulier à partir de myoblastes dérivés de cellules souches pluripotentes induites humaines. Les possibilités de la bioimpression magnétique ont ensuite été explorées plus en profondeur, par la création de tissus de formes variées – étoile, goutte, triangle, croix. Les tissus en forme de croix ont servi à mettre en évidence la relation entre géométrie, contraintes mécaniques et différentiation. Par ailleurs, la résistance mécanique de ces tissus ainsi que la possibilité de co-cultiver des fibroblastes ont été analysées, en utilisant le magnétisme pour ségréger les différents types cellulaires dans un même tissu.

Dans son ensemble, cette thèse de doctorat démontre le potentiel des forces magnétiques pour concevoir des tissus complexes et fonctionnels, particulièrement le muscle squelettique, et ouvre la voie vers des perspectives pour la modélisation de pathologies, l'étude de la mécano-biologie et le développement de greffes contrôlées à distance.

Mots-clés: Ingénierie tissulaire – Nanoparticules magnétiques – Bioimpression magnétique – Muscle squelettique – Biomécanique – Microfabrication

TABLE OF CONTENTS

Remerciements ***1***

Summary ***3***

Résumé ***4***

Table of contents ***5***

Chapter 1. Introduction ***9***

Chapter 2. Anisotropic tissues in vivo and how to engineer them in vitro ***17***

I. Introduction 18

II. Anisotropic tissues in the human body: structure, mechanics, and function 19

1. Main classes of anisotropy 19

a. Fibrous 19

b. Tubular/hollow 22

c. Honeycomb/porous 24

d. Layered 24

e. Gradient 26

2. Skeletal muscle tissue: a prime *in vivo* example of structural anisotropy 27

a. Myogenesis: the origins of muscle cells alignment 27

b. Skeletal muscle architecture: anisotropy across all structural scales 30

c. Uniaxial muscle contraction: a not-so-straightforward mechanism 31

III. Replicating native anisotropy in tissue engineering 33

1. Main tissue engineering techniques 33

a. Starting with 2D anisotropic substrates 33

b. Modular assembly approaches 35

c. Molding and microfluidic systems for organ-on-chip development 39

d. Spinning techniques and melt electro-writing 41

e. Bioprinting 43
f. Force-induced anisotropic microfeatures 45
2. Impact of cells' self-reorganization in anisotropic tissue engineering 47
a. Spontaneous self-alignment 48
b. Matrix remodeling 48
c. Surface tension sorting 51
IV. Engineering anisotropic tissues with magnetic forces 52
1. Magnetic nanoparticles in bioengineering 52
2. Alignment along the magnetic field lines 53
3. Shaping tissues through magnetic patterning: a bioprinting-like approach 57
4. Assembling cellular building blocks with magnetic forces 59
5. Stimulating and moving tissues with magnetic actuation 62
V. Conclusion 65
Chapter 3. Remote magnetic microengineering and alignment of spheroids into 3D cellular fibers 67
I. Introduction 71
II. Results and Discussion 73
1. Internalization of magnetic nanoparticles (NPs) in cells 73
2. Magnetic field configuration for magnetic cell alignment in 3D microenvironment 75
3. Magnetic cell alignment varies with cell labeling and concentration 77
4. Magnetic cell alignment fades over culture time 80
5. High-throughput production of magnetic spheroids using micropatterned NiFe attractors 80
6. Alignment of magnetic spheroids 83
7. Spheroid chain fusion and muscle tissue differentiation 85
8. Versatility of the method 89
III. Conclusion 91
IV. Experimental procedures 92

Chapter 4. Magnetic printing and actuation of stretchable muscle tissue..... 99

I. Introduction 103

II. Results 105

1. Magnetic bioprinting of wrench-shaped 'clip-on' muscle tissues 105

2. Trapping the magnetic-printed muscle tissue between two magnetic needles 107

3. Preserving tissue anisotropy for myogenesis 109

4. Stretching improves muscle differentiation 111

5. Transposing to myoblasts derived from human induced pluripotent stem cells 115

6. Stretching improves functionality and specialization 119

III. Discussion 122

IV. Experimental procedures 127

Chapter 5. Controlling and probing the geometrical and mechanical properties of magnetically bioprinted tissues..... 135

I. Introduction 139

II. Results 141

1. Versatile magnetic bioprinting for custom tissue architecture 141

2. Tissue maturation drives contraction towards spherical geometry 142

3. Magnetic trapping stabilizes tissue architecture 146

4. Magnetic trapping and stretching enable mechanical characterization of printed tissues 149

5. Magnetic cell segregation enables spatial organization in co-culture tissues 151

III. Discussion 154

IV. Experimental procedures 157

Chapter 6. Conclusion and Perspectives..... 163

I. Achievements 164

1. Technological advances 164

2. Engineering mature, functional muscle tissue 165

3. Investigating tissue biomechanics 165

II. Limitations 167
1. Potential impact of magnetic nanoparticles 167
2. Scaffolds in tissue engineering 168
3. Force measurement 169
III. Perspectives 170
1. Enhancing the complexity of the muscle constructs 170
2. Improving the technology 172
3. Future applications 174
Appendix A. Supplementary information of Chapter 4 177
Appendix B. Supplementary information of Chapter 5 211
References 221

Chapter 1

Introduction

Repairing human bodies requires access to functional, living tissues. The global demand for organ and tissue transplants continues to rise, yet less than 10% of these needs are met every year[1]. As the population ages, the prevalence of degenerative diseases further increases the need for new sources of healthy tissues[2]. In addition to therapeutic procedures, such tissues have recently become even more sought after as models for drug screening purposes, in an effort to address the high failure rate - over 90% - when transitioning from animal models to human clinical trials[3,4], and to reduce animal experimentation for ethical reasons. And yet, biomedicine still struggles to fully replace, regenerate or even model physiologically relevant human tissues. Tissue engineering emerged in the late 1980's as a promising solution to this challenge, combining engineering techniques with biomedical science to recapitulate *in vitro* the full complexity and functionality of living tissues as they exist in the human body[5–7].

Historically, the field of tissue engineering was preceded by widespread use of two-dimensional (2D) cell culture on flat substrates, which existed since the beginning of the 20th century[8]. This revolutionary idea that cells could be cultured outside of the body has been at the forefront of research in cellular biology since then. However, it became increasingly evident that cellular behavior is profoundly influenced by the physical and biochemical properties of the surrounding environment[9–12]. As a result, traditional 2D cell culture was found to incompletely mimic the complexity of native tissues[13,14]. This resulted in the development of three-dimensional (3D) cell constructs, starting with the spherical multicellular aggregates called spheroids[15], and eventually leading to the rise of tissue engineering. With this approach, cells were no longer merely cultured on their own on 2D substrates but were instead seeded into 3D scaffolds. Using biomaterials such as collagen type I[16] or Matrigel[17], these scaffolds were meant to replicate the extracellular matrix and the cellular microenvironment within native tissues. Skin and cartilage were amongst the first tissues to be engineered, and even in some cases implanted *in vivo* [7].

While the use of 3D matrices did reduce the gap between *in vitro* and *in vivo* architectures, native tissues are not merely uniform networks of cell laden hydrogels. Organs and tissues in the human body are complex, heterogeneous and anisotropic[18]. And so should be their *in vitro* counterparts, to be perfectly physiologically relevant. Indeed, these characteristic features play a key role in tissue functionality. Many tissues, including skin and bone[19], have anisotropic structures that provide improved mechanical properties in specific directions. On the other hand, tubular organs such as the ones in the vascular[20] or digestive [21,22] systems enable the proper transport of various cargos within the body. Almost every single system in the human body has anisotropic features and uses them for functional purposes.

This relationship between structure, mechanics, and function is best exemplified in skeletal muscle tissue, whose anisotropy is both essential for its contraction and its formation. Indeed, skeletal muscle, which represents more than 30% of the body mass[23], is characterized by a hierarchical fibrous anisotropy. When myoblasts, muscle precursor cells, align they can fuse together to form giant muscle fibers[24], mature muscle cells that are often several

centimeters long and can contain more than a thousand nuclei. Bundled into fascicles, muscle fibers are all aligned in the same direction as the whole muscle, spanning from tendon to tendon [25,26]. Within muscle cells, contractile filaments also have this identical orientation, enabling the coordinated contraction of all muscle cells in the same direction and therefore optimizing force generation at the scale of the entire muscle. As any other tissue, skeletal muscle function and development can be impacted by various disorders ranging from genetic muscular dystrophies[27] to degenerative conditions such as sarcopenia[28,29], as well as volumetric muscle loss following trauma[30]. In order to engineer skeletal muscle tissue, either to research or even maybe one day cure these conditions, recapitulating the aligned architecture of skeletal muscle is essential.

Whether it is for skeletal muscle or any other type of anisotropic tissue, many tissue engineering approaches now aim to recapitulate key structural features[31,32]. First developed on 2D substrates, moulding and microfabrication techniques have become more and more integrated to 3D systems. Recapitulating native geometries within microfluidic devices notably led to the rise of organ-on-chip technologies[33–40], which are usually aimed towards biophysical investigation and disease modeling. Other approaches focus a lot more on the development of scaffolds with high control over their anisotropic features, such as electrospinning techniques [41]. More recently, bioprinting has emerged as a versatile method to extrude[42,43] or photopolymerize[44] cell-loaded scaffolds in any desired 3D shapes, even enabling precise placement of multiple cell types within the same tissue [45]. Nonetheless, such precision remains limited, and issues surrounding bioink physiological relevance and stresses on cells during bioprinting processes leave the door open for new technologies to emerge.

Still in its early stages, magnetic tissue engineering is beginning to demonstrate significant potential for tissue engineering. This approach is based on the use of biocompatible magnetic nanoparticles[46,47], which can be manipulated using external magnetic fields. They can be loaded into a scaffold, on which magnetic forces can then be applied, or internalized by cells through endocytosis, effectively endowing cells with magnetic properties. Originally developed as contrast agents for magnetic resonance imaging (MRI), magnetic nanoparticles have since found to have many bioengineering applications. Alternating magnetic fields, for instance, can induce localized hyperthermia for cancer treatment[48,49], while magnetophoretic forces have been used to guide magnetic drug delivery vectors[50,51]. Beyond theranostics, early work with magnetically aggregated cell sheets[52] opened the door to bioengineering applications, showing that magnetic fields could be harnessed to manipulate cellular organization. Since then, a range of techniques has demonstrated that magnetic forces can be used to align or patterns cells, assemble spheroids or even stimulate tissues [46,53–60]. Despite this growing body of work, magnetically engineered tissues have not yet reached the same structural and functional complexity achieved with other approaches, such as bioprinting. However, the intrinsic ability of magnetic actuation to remotely guide and organize cellular assemblies makes it particularly appealing for the engineering of anisotropic tissues, such as skeletal muscle.

Within this context, this PhD work aims to take magnetic anisotropic tissue engineering a step further and showcase its potential for future bioengineering applications. These objectives, which we aim to answer in this manuscript, can be summarized as follows:

I) To advance current magnetically driven strategies for engineering structurally complex and anisotropic tissues.

II) To demonstrate the value of these methods through two key applications:

1) **The engineering of mature, aligned and functional skeletal muscle tissue.**
2) **The investigation of how geometrical, mechanical and functional cues interact in shaping muscle tissue architecture and behavior.**

To tackle these challenges, understanding the specific native anatomy of anisotropic tissues, notably skeletal muscle, as well as the current methods to engineer them *in vitro* is an essential first step. **Chapter 2** of this manuscript is therefore dedicated to laying this foundational knowledge, reviewing key biological and engineering principles that pose the scientific groundwork on which the rest of this work is based on (Fig. 1). This chapter begins with a description of the diversity and functionality of anisotropic tissues in the human body, and classifies them between fibrous, tubular, porous, layered and gradient geometries. Skeletal muscle tissue, which belongs to the first category, is described in more details, since this fibrous tissue is the most prominent example of anisotropy in the human body, and is also at the core of the three original studies of this manuscript. After detailing the source of muscle tissue's anisotropy during myogenesis, its hierarchically aligned architecture is presented in adult muscles, particularly the molecular structures enabling contraction. Having introduced native skeletal muscle and other anisotropic tissues, how to engineer them remains to be explained. Starting with 2D anisotropic substrates, we then move on to 3D approaches such as modular assembly, moulding and microfabrication techniques, like electrospinning, which will naturally lead us to bioprinting. We will also discuss the use of external mechanical forces in anisotropic tissue engineering, as well as remote forces that can be electric, acoustic or temperature based. While these current methods for anisotropic tissue engineering aim to precisely control the tissue microenvironment, cells also have self-reorganization abilities that need to be considered, notably self-alignment, matrix remodeling and surface tension sorting. Among the emerging technologies discussed, magnetic tissue engineering stands out for its versatility and potential. Although still underexplored compared to more established approaches, magnetic methods enable dynamic and non-invasive control over cell alignment, patterning, assembly, and stimulation. Overall, this review motivates not only our interest towards engineering anisotropic tissues such as skeletal muscle, but also our choice to use magnetic tissue engineering to do so in the following studies.

Chapter 3 presents a first approach based on a collagen scaffold, following in the footsteps of most current tissue engineering techniques, which improves on magnetic alignment and assembly by combining these established methods, in order to align muscle spheroids into cellular fibers. A first essential part of this work, and of this whole manuscript, is to optimize the magnetization of the cells during their incubation with magnetic nanoparticles. We show

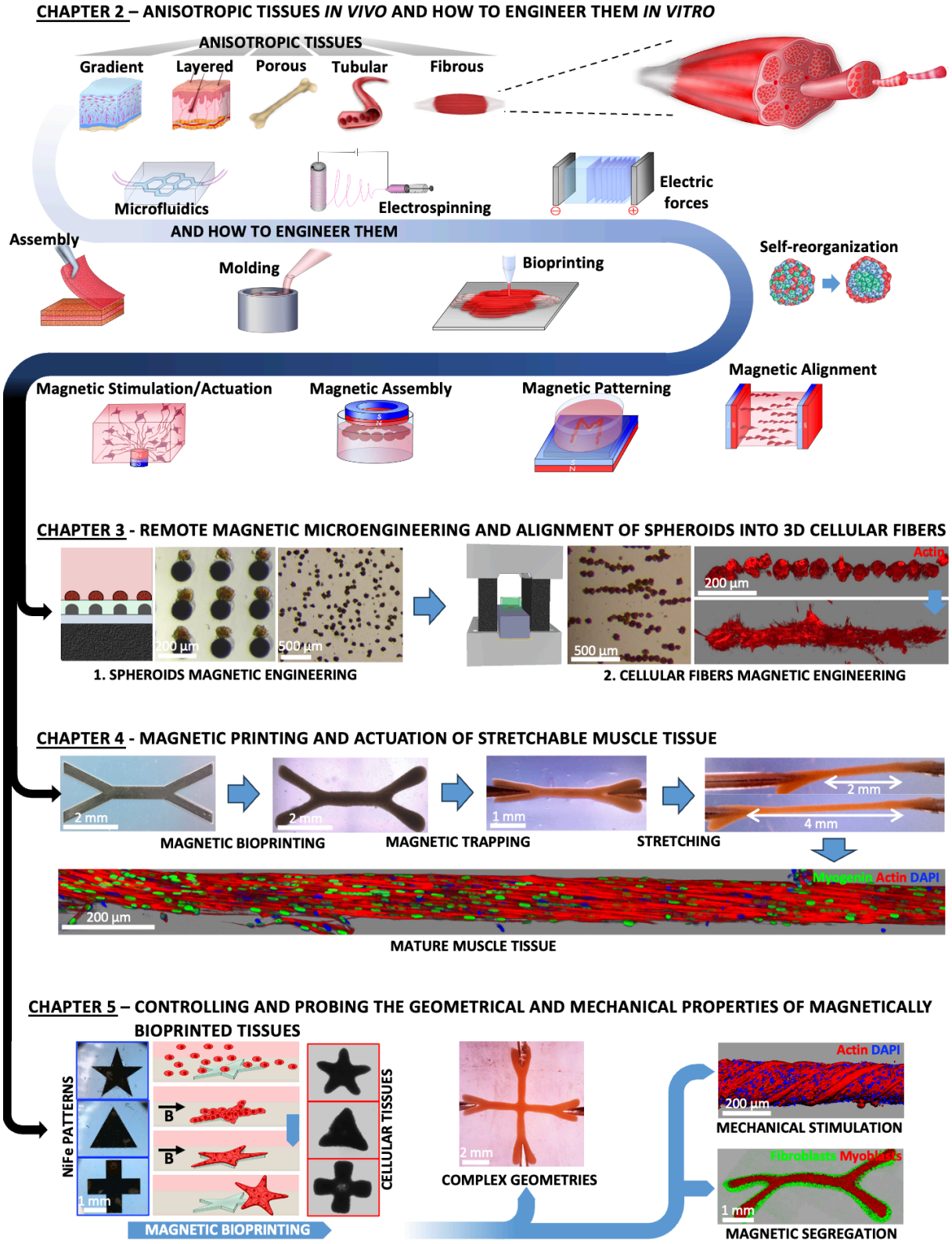

Figure 1. *Visual walkthrough of the work presented in this manuscript composed with the visual tables of contents of the review of Chapter 2 "Anisotropic tissues in vivo and how to engineer them in vitro," and the three original studies of Chapter 3 "Remote magnetic microengineering and alignment of spheroids into 3D cellular fibers," Chapter 4 "Magnetic printing and actuation of stretchable muscle tissue" and Chapter 5 "Controlling and probing the geometrical and mechanical properties of magnetically bioprinted tissues."*

that instead of increasing the concentration or duration of the incubation, doing sequential incubations makes it possible to have C2C12 myoblasts internalize 20 pg of iron per cell. These cells can then be mixed into a collagen prepolymer solution, still liquid at 4 °C, which is poured into a PDMS chip, and then placed between two strong magnets within an incubator. This drives cells to align and form chains along the magnetic field lines, while the collagen polymerizes, fixing this anisotropic configuration. Unfortunately, myoblasts start colonizing the matrix and lose their anisotropy in a matter of days. In order to preserve the alignment, instead of aligning individual cells, we decide to align larger, preformed spheroids. Since cells are magnetic, we use that to our advantage to aggregate cells into spheroids using arrays of NiFe magnetic patterns in the shape of 100 µm dots. Not only does this method enable precise control over spheroid size based on cell density during patterning, but no matter the size these spheroids can be magnetically aligned the same way individual cells can. More importantly, these chains of spheroids fuse together, and form aligned cellular fibers in a matter of days, preserving the overall anisotropy of the tissue. To further explore the versatility of our approach we show that we can easily include a non-magnetic cell type within the collagen matrix, such as fibroblasts, which would be randomly dispersed around the magnetic cells or spheroids alignment. Moreover, tissues can also be stretched in order to improve the anisotropy of the tissues over time, and we demonstrate that our approach is not limited to skeletal muscle, as we align spheroids of various sizes made from fibroblasts and mesenchymal stem cells (MSCs).

Nonetheless when it comes to muscle differentiation there are limitations with this first platform. In addition to a desire for improved control over the tissue's architecture, this led us to move towards a new scaffold-free approach, exploring further what can be done with the magnetic patterning technique used to engineer magnetic spheroids. Indeed, the study of **Chapter 4** introduces a next-generation magnetic tissue engineering toolbox to (1) magnetically bioprint anisotropic scaffold-free skeletal muscle tissues with a functionalized shape, and (2) clip them onto magnetic attractors for controlled morphogenesis and stretching. We demonstrate that NiFe patterns can actually be engineered in any desired shape and then used for magnetic bioprinting of wrench-shaped tissues out of myoblasts. This technique made it possible to generate within a couple of hours 3D skeletal muscle constructs specifically tailored for magnetic remote actuation and physical stimulation. Indeed, the central fiber of these tissues reproduces skeletal muscle tissue geometry while the clamps make it possible to clip them onto magnetic needles. Leveraging magnetic forces to preserve this precise geometry, for both initial bioprinting and subsequent tissue maintenance and stretching, promoted muscle maturation. Results indicate significant improvements in muscle differentiation, evidenced by enhanced cell fusion and myogenin expression, and functionality, showcased by increased calcium activity and contractility. Mechanical stimulation is investigated much further than in the previous study, and stretched tissues display both superior maturation and functionality, as well as increased levels of satellite-like cells, which are essential for muscle regeneration. The positive impact of mechanical cues on myogenesis, which has so far mostly been studied on murine cell lines, is notably demonstrated here for myoblasts derived from human induced

pluripotent stem cells (iPS), opening many future possibilities for clinical applications thanks to their physiological relevance.

However, our magnetic bioprinting platform is not limited to wrench shaped tissues and can engineer high resolution centimeter scale tissues of any desired shape, potentially rivaling current bioprinting approaches, without the need for any scaffold. The last study of this manuscript, presented in **Chapter 5**, delves deeper into the potential of this new technique, by producing a wide variety of cellular structures, both at the macroscopic and microscopic scale, while at the same time investigating the biomechanical properties of the printed tissues. In particular, bioprinted tissues would naturally mature towards a spherical shape, due to cell contractility and surface tension forces. Using cross shaped tissue, we try various strategies to prevent the loss of the original geometry, including casting the tissues within a collagen matrix. However, the only successful method consists in functionalizing the cross-shaped tissues the same way wrench shaped tissues were, by adding clamps to their edges and trapping them to four magnetic needles. This make it possible to culture muscle tissue in a cross geometry over a week, resulting in improved differentiation in the anisotropic branches compared to the disorganized center of the tissue, which demonstrate how important geometry is in tissue maturation. In order to further study the mechanical cohesion of the printed tissues, we then shift our focus to wrench shaped tissues that could more easily be stretched until rupture. When it comes to maximum deformation before rupture, the speed of stretching is the main parameter at play in linear stretching, whereas the stretching amplitude and the geometry of the tissue are also involved in cyclical stretching. Moreover, we display the possibility of magnetic segregation to engineer co-cultured tissues, which were then used to show how various internal organizations of two different cell types can impact resistance to deformation.

As we will conclude in **Chapter 6**, these three original studies fulfil the challenges we aimed to address at the beginning of this manuscript. These studies further advance magnetic tissue engineering approaches by combining and developing the techniques introduced in the review chapter. Moreover, they prove the high potential of magnetic based approaches to engineer anisotropic tissues, especially mature skeletal muscle, and to study the link between shape, function and biomechanics in living muscle tissue. However, these approaches do have limitations that we will also tackle in this last chapter, notably the potential impact of magnetic nanoparticles, the drawbacks of scaffold free approaches, and the needs for improved force measurement within our constructs. These will eventually lead us towards potential improvements and perspectives of this work, starting with increasing the complexity and therefore also physiological relevance of the constructs, notably by adding other cell types like motor neurons. Finally, while this work focused on muscle tissue, the magnetic engineering toolbox developed in this PhD work will also be shown to be applicable to other tissue types. The manuscript will end by discussing its potential for future biomedical applications - including disease modeling, drug screening, and magnetically actuated grafts - highlighting the broader translational value of this technology.

Chapter 2

Anisotropic tissues *in vivo* and how to engineer them *in vitro*

I. Introduction

Since tissue engineering was first introduced by Drs. Joseph Vacanti and Robert Langer in the late 1980's[5–7], it has become more and more evident that 2D cell culture is not sufficient to fully recapitulate the complexity of native tissues. Not only has 3D cell culture advanced our understanding of *in vivo* biological processes[61], but it also offers significant potential for crucial biomedical applications , notably new models for drug screening and potential grafts[3]. Although 3D culture can already achieve far more elaborate structures than 2D culture ever could, it has yet to recapitulate the full complexity of *in vivo* tissues [13,14]. Unlike isotropic homogenous cell seeded scaffolds, *in vivo* organs have intricate geometries and many present key anisotropic features. Indeed, many tissues in the human body have structural and functional properties, such as stiffness, that vary depending on the direction of measurement[18]. Skeletal muscle tissue is a prime example of anisotropy in native tissues, as it presents a strong direction of alignment at every scale, from the whole organ to myofibrils, all oriented in the same direction[62]. This marked fibrous anisotropy links geometry to function, as this alignment optimizes the coordinated and uniform contraction of all functional units of the tissue for force generation. Indeed, anisotropy is not merely a structural feature, as it is crucial for the functions of all anisotropic tissues and organs. Replicating such complex architectures *in vitro* has therefore emerged as the next logical step in tissue engineering to fully recapitulate native anatomy[11,31,32,63]. Starting with the use of anisotropic 2D substrates[64], anisotropic tissue engineering has progressively evolved towards 3D approaches such as modular assembly or moulding, eventually leading to the emergence of organ-on-chips technologies [33–40]. The development of electrospinning [41] and bioprinting [42,43] have enabled the creation of even more complex anisotropic geometries. All these techniques rely heavily on the use of scaffolds, which can make it difficult to access or actuate their contents deep within. As a result, new approaches have begun to use strategies for remote control, such as acoustic or magnetic forces, as tools for tissue engineering and stimulation. Based on the use of magnetic nanoparticles, originally used for imaging purposes[65], magnetic tissue engineering started with the generation of cellular sheets[52]. This technique gradually increased in complexity and demonstrated an ability to create intricate anisotropic architectures[46,55,59,60], while at the same time enabling remote stimulation[54,66]. Magnetic bioprinting, possibly combined with other current techniques, is emerging as a powerful tool with the potential to significantly advance anisotropic tissue engineering.

In this first chapter, we will introduce and review the main concepts and themes related to this PhD work. After providing an overview of the various anisotropic tissues in the human body, we will take a closer look at skeletal muscle tissue, as a key example of anisotropic architecture. We will then discuss the different strategies aiming to replicate anisotropy *in vitro*, including approaches harnessing the cells innate self-organizing properties. Finally, magnetic based techniques will be introduced as a promising avenue for anisotropic tissue engineering.

II. Anisotropic tissues in the human body: structure, mechanics, and function

1. Main classes of anisotropy

The hallmark of an anisotropic material is a variation of its properties depending on the direction in which they are measured. This means that the material is heterogeneous and often implies that it is oriented along a specific axis. For instance, wood, with an elastic modulus about 10 times higher in the longitudinal direction than in the radial one, is a common example of anisotropic material. Such materials contrast with isotropic materials, whose properties are uniform, independently of the direction, such as glass or plastic.

Anisotropic tissues *in vivo* are usually characterized by specific orientations of cells and matrix microfeatures, or variations in matrix composition, along a designated axis. For example, skeletal muscle tissue is clearly anisotropic with its organization of aligned fibers. However, it is far from the only anisotropic tissue, or even type of anisotropy in the human body. Indeed, anisotropic tissues can be classified under multiple categories and skeletal muscle falls under what we will call **fibrous** anisotropy. Some tissues or organs, with a more duct like geometry, fit in the **tubular or hollow** geometry whereas others display a **layered** structure. These three categories, first introduced in a previous review[18], can also be complemented with **gradient** and **honeycomb or porous** anisotropic architectures (Fig. 2.1). As will be discussed, several tissues possess attributes from more than one of these categories, thereby combining their respective advantages, and optimizing their material properties with regards to their anisotropic functionality.

a. *Fibrous*

Fibrous anisotropic tissues encompass all tissues composed of an assembly of fiber-like structures, organized so that they all share a similar orientation. This alignment gives the tissue preferential properties along that direction.

Fibrous materials are present throughout the body, as connective tissues and extracellular matrices, as well as basement membranes. They are composed of an entangled network of crosslinked filamentous proteins, classified as either collagen, reticular or elastic fibers[67]. It is admitted that collagen fibers are the most abundant proteins in the human body and represent up to 30% of its dry mass[68,69]. Organized in 1 to 100 µm-thick bundles of fibrils, each between 20 and 500 nm in diameter and spanning up to several tens of millimeters[70], collagen fibers are mostly present in connective tissues such as tendons, ligaments, bone or cartilage[71]. Reticular and elastic fibers are smaller, with diameters below 2 µm and fibrils no more than 40 nm wide[72]. Reticular fibers are mostly found in more cellular tissues, like the spleen or the liver, while elastic fibers are usually found in tissues undergoing mechanical deformation such as blood vessels or lungs. Although these different fibers are often organized in an isotropic mesh, they

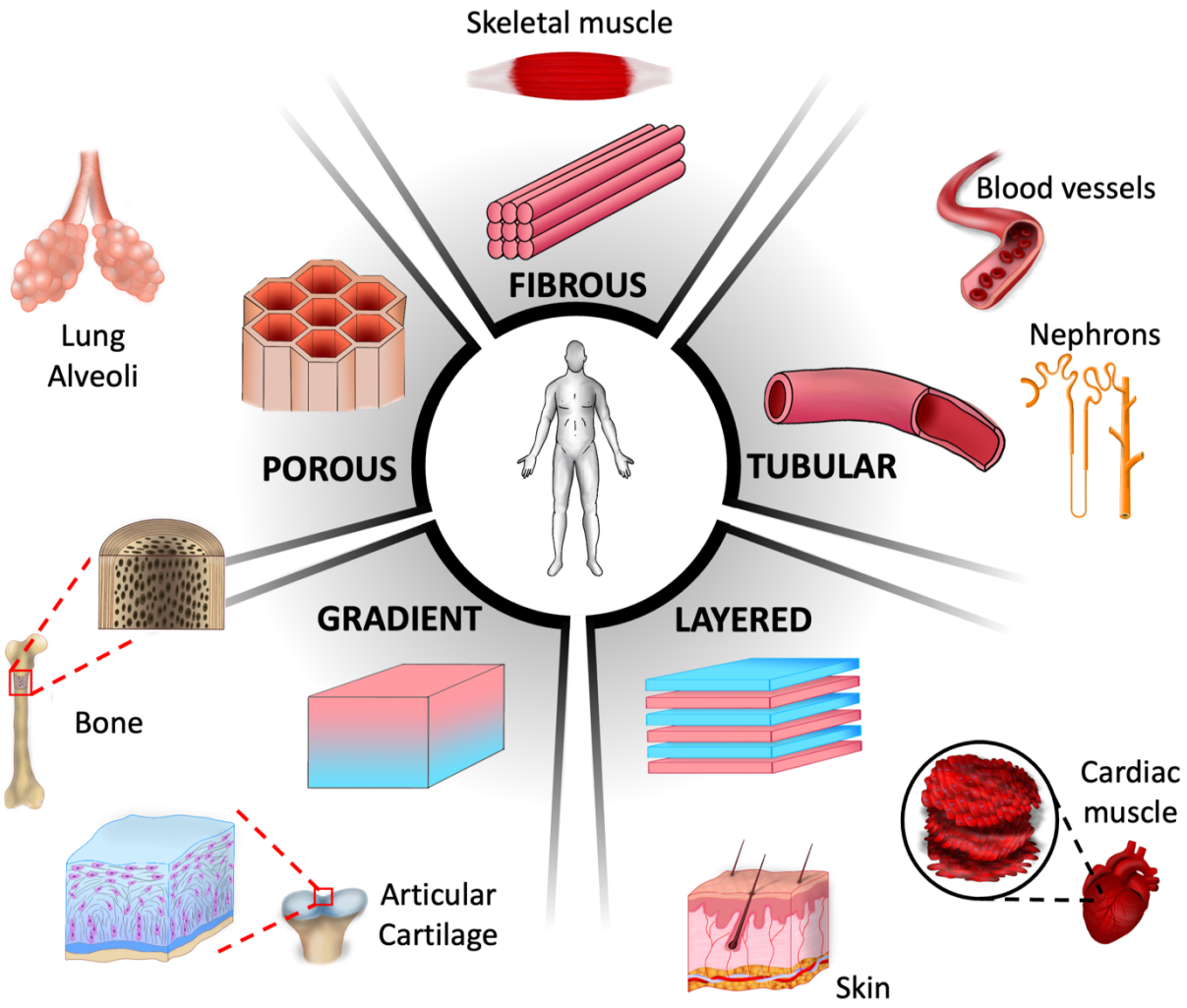

Figure 2.1. Main classes of anisotropic tissues in vivo.

are individually anisotropic, both because of their elongated geometry and their mechanical properties. Indeed, collagen type I fibrils and fibers in PBS exhibit a Young's modulus - which refers to a materials' resistance to deformation - of the order of 100 MPa in the longitudinal direction (Fig. 2.2A), whereas their shear modulus - the resistance to sliding between layers in a material - is a hundred times smaller in the perpendicular direction[73,74]. This gives collagen fibers much higher resistance under tensile stress - the pulling force per unit area - although they may buckle when compressed[74].

When all these fibers align within an extracellular matrix, it leads to the formation of fibrous anisotropic tissues with much higher resistance to stress in the alignment direction. This can be observed in skin, where a dense network of collagen fibers aligns along Langer's lines. Consequently, the Young's modulus of the skin is ten times higher when measured parallel to these lines than perpendicular to them[19]. The impact of fiber orientation is also very visible in articular cartilage, where collagen fibers transition from aligned to isotropic, leading to a decrease in the Young's modulus parallel to the initial alignment. On the other hand, the Young's

Modulus in the perpendicular direction can be 10 to 50 times smaller than in the parallel direction in the aligned parts of the tissue[75,76]. Therefore, such fibrous alignment is particularly interesting for tissues meant to withstand uniaxial loads. This applies to tendons, linking muscles to bones, and ligaments, stabilizing joints or bones together. They share a similar structure[77] and are mostly composed of parallel collagen fibers. Similarly to these fibers, they present a Young's modulus two orders of magnitude higher in the parallel direction than the transverse one[78,79]. Their high tensile strength - the maximum pulling stress before failure - of about 100 MPa enables proper force transmission without failure[80], while their lower resistance to transverse deformations allows for greater flexibility and range of motion in the musculoskeletal system.

Alignment not only optimizes force transmission but also enhances force generation in skeletal muscle tissue. Unlike tendons and ligaments which exhibit a low cell density, this anisotropic fibrous tissue draws most of its anisotropy not from collagen fibers, but from the densely packed muscle cells: the muscle fibers or myofibers (Fig. 2.2B). These giant multinucleated cells are all aligned in the direction of contraction of the muscle (Fig. 2.2A). They have a very high aspect ratio as they often span the whole length of the muscle, which can go up to half a meter for the sartorius muscle[81], while their diameter is approximately 100 µm[82]. As we will discuss in more depth in a following section, each muscle fiber contains a succession of sarcomeres, the contractile units of the cell, which contract along the fiber axis[82]. This anisotropic organization enables the coordinated contraction of all the sarcomeres, which individually can apply between 10 and 100 $nN.\mu m^{-2}$ [83,84], resulting in whole-muscle forces on the order of 1 kN for large muscles like the quadriceps[85,86].

While skeletal muscle represents the most prominent type of anisotropic fibrous tissue, cardiac and smooth muscles also display some fibrous like characteristics. Their cells are much smaller, as cardiomyocytes are usually 100 µm-long and smooth muscle cells range between 20 to 500 µm, with a diameter of about 10 µm in both cases[87]. They still showcase a preferred alignment and elongation in the direction of contractions, as well as a main orientation of contractile filaments. In smooth muscle cells, this arrangement forms an oriented crisscross pattern within the cells. In both cases they form layers of cells with a specific fibrous anisotropy, and the combination of different layer orientation leads to a layered anisotropy, as well as tubular anisotropy for smooth muscle cells.

In addition to muscle cells, neurons can exhibit an aligned fibrous geometry, with 0.1 to 10 µm-thick[88] axons often extending across several centimeters, and even 1m in the spinal cord[89]. These axons can share the same path, forming anisotropic fibrous tissues. This is particularly visible in peripheral nerves, where thousands to a hundred thousand axons, bundle into a few tens of fascicles, all aligned in the same direction[90,91], in a similar fashion to skeletal muscle fibers. High degrees of alignment can also be observed in some regions of the central nervous system, such as the brain stem (Fig. 2.2C). While this naturally enhances mechanical performance in the fiber direction[92], the main function of this alignment is here to optimize and coordinate the transport of information.

b. *Tubular/hollow*

After the fibrous geometry, the next most prominent anisotropic architecture is the tubular one, as many vessels and conduits of all shapes and sizes run through the body.

The most typical tubular tissues are most likely the blood vessels (Fig. 2.2D). From the aorta with a diameter of 3 cm and a wall thickness of 2 mm, to capillaries with a lumen less than 10 µm-wide[93], the vascular system exhibits a lot of diversity in tubular geometries to deliver blood throughout the body. With a blood flow that can reach up to a few meters per second during exercise[20], these tissues have to withstand shear stresses - the parallel force from fluid flow over a surface - from 10 to 100 dyne/cm^2 for smaller capillaries or arterioles (Fig. 2.2E). The endothelial cells lining the lumen of blood vessels are meant to withstand such stresses without leakage, sometimes even increasing the diameter of the vessels to get back to an average 15 dyne/cm^2 shear stress[94]. In addition to aligning endothelial cells, flow and shear stress in the longitudinal axis also contribute to the cells' apical-basal polarity in the radial direction of the tube, which further complexifies the tubular anisotropy of blood vessels. This polarization enables the selective exchange of materials between the blood and the surrounding tissues[95].

Like the vascular system, the lymphatic system includes similar tubular vessels. Lymph is carried in vessels ranging from 10 µm capillaries to several millimeters-wide thoracic ducts[96]. While their dimensions are similar to blood vessels, they operate at speeds of only a couple of millimeters per second, leading to shear stresses 10 times lower than in the vascular system[97].

Epithelial tissues constitute another large family of diverse anisotropic tubular tissues, usually connecting the body to the outside world. For instance, milk is transported in the breasts through 2 mm wide lactiferous ducts[98], while nephrons filter and evacuate urine from the kidney in 60 µm channels[99]. In the digestive tract, food is progressively moved and transformed through 9 m of various hollow organs, that are a few centimeters wide[21,22]. In addition to this motion and the apical-basal polarity of epithelial cells lining the gastrointestinal system, another anisotropic feature of the gut is the radial orientation of crypt and villi structures, which increases the surface for nutrient exchange while regulating it.

Crypt and villi are actually formed by the buckling of the epithelial cell layer radially compressed by the surrounding smooth muscle cells[100]. After morphogenesis, the digestive tract remains encased in this tubular structure of smooth muscle tissues. They apply a pressure between 70 and 200 mN/mm^2, in peristaltic waves - traveling muscle contractions - that drive the intestinal bolus[101] (Fig. 2.2E). Smooth muscles also regulate directed movement in other hollow organs, such as the respiratory tract or the uterus. They are also present throughout vasculature where smooth muscle cells can apply 350 mN/mm^2 pressure to regulate blood vessels diameter and flow[102].

Mechanical forces are also responsible for bending and buckling of the neural groove into the neural tube, the hollow tubular structure from which the central nervous system arises during embryogenesis[103,104]. This tube persists in the shape of the spinal cord, spanning from

the brainstem to the lower back. There, neurons run parallel around the central canal meant for nutrient and waste exchanges[105].

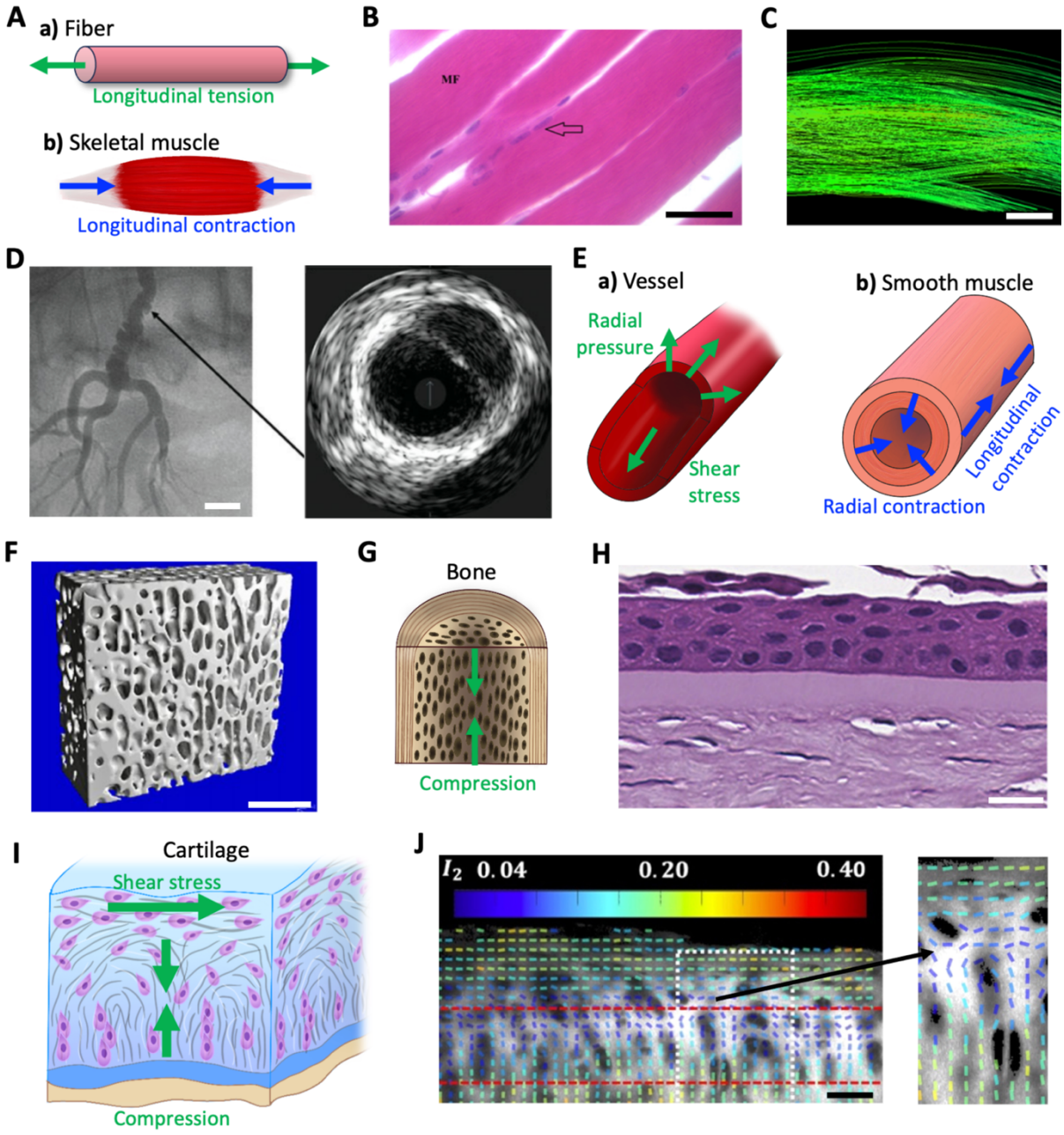

Figure 2.2. Native anisotropic tissues. *(A) Schematics of the main stresses at play in fibrous tissues, either (a) exerted on a fiber or (b) produced by skeletal muscle tissue. Green arrows represent the stresses applied from the surrounding environment on the tissues and blue arrows represent the stresses due to muscle contractions. (B) Longitudinal histological sections of gastrocnemius muscle fibers (MF) with multiple nuclei (arrow)[29] (Scale bar = 50 µm). (C) Diffusion tensor imaging of bovine brain stem and axons[92] (Scale bar = 2 cm). (D) Angiogram and intravascular ultrasound imaging of a renal artery[106] (Scale bar = 1 cm) (E) Schematics of the main stresses at play in tubular tissues, either (a) exerted on a vessel or (b) produced by*

smooth muscle tissue. (F) Microtomography imaging of trabecular bone[107] (Scale bar = 2 mm). (G) Schematic of the compression stresses at play in bone tissue. (H) Histological section of the first layers of a human cornea[108] (Scale bar = 20 µm). (I) Schematic of the main stresses at play in cartilage. (J) Map of the orientation and alignment (I_2) of collagen fibrils in a cartilage-bone explant[109] (Scale bar = 50 µm).

c. *Honeycomb/porous*

While tubular tissues are characterized by a single large, oriented lumen, other materials in the body are characterized by a network of anisotropic pores, giving them a honeycomb-like structure, as well as unique mechanical properties.

The trabecular (also called cancellous) part the bone is filled with such pores, ranging from 10 µm to 1 mm[110] and oriented in the direction of the bone main load with high aspect ratios[111] (Fig. 2.2F-G). This makes it possible to drastically reduce the weight of bones, with a porosity above 75%[110,112], while preserving their inner structural integrity thanks to an increased elasticity and stiffness[113], as well as resistance to cyclical fatigue[114] - material damage from repeated stress cycles - in the load bearing direction. While most of the bone's stiffness comes from the outer compact cortical bone, shock absorption is actually trabecular bone's main mechanical function due to its spongy structure. This energy dissipation mechanism is also affected by the pores' anisotropy. Indeed, femur head were shown to absorb more energy in the medial-lateral axis, than in other directions[115]. Permeability was also shown to be higher in the pores' main direction[116], which promotes anisotropic nutrient diffusion and likely facilitates vascularization, and overall cell migration in this direction[117].

Next to bone tissue, one of the most well-known porous tissues in the body is the lung, due to its hollow alveoli and branches structure. Although alveoli are often assumed to be isotropic, more and more evidence points out to their anisotropic morphology and behavior. Indeed, the average distance between airspaces in mouse lungs was shown to consistently be the highest when measured in the longitudinal axis of the lungs[118], and even more so when expanded. This also proved to be the preferential direction of gas diffusion in the alveoli, as it was shown with MRI that ^{3}He would diffuse two to three time better in the longitudinal direction rather than the transverse direction of the lungs, in both healthy and pathological cases[119]. Combined with alveoli anisotropic expansion [120], these elements highlight how the porous anisotropy of the lungs aims to favor the back-and-forth air movements through the respiratory tract.

d. *Layered*

Some materials in the human body are composed of distinct layers, either alternating or sometimes markedly different in composition, stacked together. This organization introduces

directional differences between the stacking axis and each individual layer, resulting in layered anisotropy.

Cornea is a typical example of lamellar materials. From the outer epithelium layer to the inner endothelium layer, it displays six sharply defined successive layers with completely different compositions[121] (Fig. 2.2H), each with specific functions in addition to their common purpose of regulating light passage and refraction. The epithelium is 50 µm-thick[122] and displays the lowest adhesion, to fulfil its barrier function, whereas the endothelium is a cell monolayer on the opposite end of the adhesion spectrum. The 500 µm stroma is the thickest and stiffest layer, likely to ensure structural integrity of the cornea[123,124]. This stacking results in an overall mechanical anisotropy with a compressive stiffness - resistance to deformation under a compressive load - four times higher than in plane stiffness[125].

In addition to fibrous anisotropy, the skin is also constituted of three main layers with similar functions to the ones in the cornea. The epidermis is filled with cells, mostly keratinocytes, and acts as a barrier with a thickness ranging from 30 to 600 µm[126,127]. The intermediate layer, the dermis, is a connective tissue a few millimeters deep[128], mostly composed of a collagen fibers network with a low cell density, whereas the deepest layer, the hypodermis, is mainly characterized by adipocytes, as well as the presence of the vascular, nervous and lymphatic systems.

Similarly, the cerebral cortex is composed of six layers that each serves a specific purpose. From the outer molecular layer, mostly composed of horizontal axons and dendrites, to the inner multiform layer, with a wide range of cell types and shapes, each region of the cortex has its own composition and function. For instance, layer IV receives sensory input while layer V sends motor output. Overall, this lamellar architecture of the cerebral cortex optimizes information processing[129].

Not all layered anisotropic tissues display such a strong difference of compositions between layers, and some can simply be constituted of a repeating motif. Unlike the previously discussed trabecular part of the bone, cortical bone is composed of a succession of compact concentric layers forming an outer protecting sheath, with an elastic modulus of about 20GPa, much higher than for the softer tissues inside the bone[130]. Thanks to this stacked structure, elasticity is also twice higher in the longitudinal axis than the transverse plane[131]. Moreover, to protect the bone from torsion, the orientation of the mineralized collagen fiber shifts from one lamella to the other[132].

Such a layered orientation shift can be observed in the outer region of the intervertebral disc, called the annulus fibrosus. It is composed of 15 to 25 concentric lamellae, each made of a dense network of parallel collagen fibers resulting in anisotropic mechanical properties[133]. However, from one layer to another, there is an abrupt change of the direction of the fibers by 60°, improving the resistance to multiaxial stresses to better protect the nucleus pulposus, the softer inner region of the disk.

Instead of preventing complex stresses, smooth and cardiac muscles use orientation changes between cell layers to induce them. Indeed, smooth muscles will form two orthogonal consecutive layers around a tubular structure: the cells in the inner layer follow the circumferential direction whereas the cells in the outer layer are aligned along the axis of the tube, to produce peristaltic waves[134]. In the case of cardiac tissue, the orientation of cardiomyocytes slightly shifts from one layer to another, leading to an overall change of orientation from +60° at the endocardium to -60° near the epicardium[135]. This twisting architecture ensures a uniform stress distribution that can efficiently eject 60 to 70% of the blood within the heart despite cardiomyocytes only contracting by about 15%[136]. Due to the gradual rotation of layers, cardiac tissue exemplifies a transitional case between layered and gradient anisotropy, which we will now explore.

e. *Gradient*

Although gradient anisotropy shares similarities with layered architectures, instead of tissues with a succession of distinct or repeating layers, it characterizes structures where a specific parameter, such as cellular orientation or a geometrical property of matrix microfeatures, changes in a continuous fashion along one direction. In some cases, gradient anisotropy can be at play in conjunction with another type of anisotropy, as we have just mentioned with the heart.

This also applies to skin, where in addition to having different layers, a gradient of the orientation of collagen fibers can be observed, especially in the dermis, which accounts for more than 80% of the skin thickness[128]. Indeed, collagen fibers are parallel close to the surface of the skin, but they become progressively less and less aligned the deeper they are in the skin[137]. As alignment favors mechanical properties, this is likely due to superficial layers being more exposed to external stresses.

Gradual changes in collagen orientation can also be observed in articular cartilage (Fig. 2.2I-J). Indeed, fibers start by running parallel to the surface, and they progressively rotate until they become perpendicular to the surface in the deeper zone of the cartilage[109]. This gradient of orientation also results in a gradient of elastic properties. The Young's modulus normal to the surface progressively increases 10 to 50 times from the superficial to the deeper zone of the cartilage, whereas the one measured parallel to the surface the Young's modulus follows the inverse trend [75,76].

Other features can lead to a gradient of mechanical properties, such as pore size and density in cancellous bone. Indeed, not only is cancellous much softer and more porous than cortical bone, but this difference increases the further away cancellous bone is from cortical bone, with a progressive increase in pore size and number[138,139].

Gradients can also be observed in tissues undergoing dynamic changes and remodeling, such as stiffness gradients in the matrix of scars and other fibrotic tissues[140]. In addition to stiffness variations, tumor environments also display a wide variety of gradients, such as oxygen

or vascularization gradients[141,142], driving tumor invasion. Aside from pathological cases, the coupling of mechanical and chemical gradients is crucial during embryogenesis, as they guide spatially specific morphogenic cues[143].

Overall, there is a broad spectrum of anisotropic tissues in the human body. Distinct anisotropic characteristics often coexist within the same tissues. For example, bones are filled with anisotropic pores exhibiting a size gradient, while smooth muscles consist of two superimposed tubular layers. Anisotropic features arise either from cellular organization, as seen in cardiac muscle, or matrix properties, as in the skin. Moreover, they exist across multiple scales, from collagen fibrils to entire skeletal muscles, with microscopic features contributing to macroscopic anisotropic properties of the whole tissue, such as the bone. The anisotropic structures of these tissues are critical to their material and mechanical properties, which are closely tied to their functions. Indeed, these features often optimize load bearing or force generation capabilities in the main functional axis of tissues, highlighting the essential role of material properties in the human body.

2. Skeletal muscle tissue: a prime *in vivo* example of structural anisotropy

Among all these different types of anisotropic geometries and tissues, skeletal muscle stands out, by the distinctiveness of its anisotropic fibrous structure, as well as its contractile function, which we can observe on an everyday basis. Indeed, not only are skeletal muscles responsible for voluntary motion, but they account for more than 30% of the body mass[23], making them the largest source of anisotropic tissue in the human body. The striking structure and crucial role of skeletal muscle tissue led us to choose it as an ideal model tissue for developing the innovative magnetic tissue engineering techniques that are introduced in the following chapters. In addition to introducing one of the main themes of this manuscript, we will now present more in depth skeletal muscle tissue to showcase how anisotropy can be central to a tissue's development, structure and function.

a. *Myogenesis: the origins of muscle cells alignment*

Myogenesis is a process that begins in the first few weeks of embryogenesis, leading to the formation of more than 650 muscles by the time of birth, and that continues throughout life, adapting to the various stages of human growth (Fig. 2.3A).

The first steps in the formation of skeletal muscle can be traced back as early as three weeks into gestation, when the paraxial mesoderm starts to form cubic structures along the embryo called somites[144]. Parts of these somites specialize into the dermomyotome, within which the myotome layer will eventually give rise to skeletal muscle tissue. The expression of the

transcription factor Pax3 regulates these first steps prior to myogenesis[145]. Mutations in Pax3 can lead to abnormal myotome development[146], and even prevent muscle formation down the line altogether[147]. Once cells in the somites start to downregulate Pax3, the joint expression of the transcription factors Myf5 and MyoD is considered as the trigger that turns them from progenitor cells to the myogenic lineage, properly initiating myogenesis. This determination process in the myotome will eventually lead to the formation of the trunk muscles[148]. Limb muscles on the other hand, are derived from progenitor cells which have delaminated from the dermomyotome and migrated towards the limb buds, where they will start expressing Pax7, another transcription factor characteristic of skeletal muscle precursor cells, before they start a determination process similar to that occurring in the somite myotome[149].

Despite being committed to the muscle lineage, these muscle precursor cells at this stage are still myoblasts, mononucleated cells that can still proliferate. Terminal differentiation begins with the expression of the myogenin transcription factor, combined with an increase in MyoD expression, turning myoblasts into myocytes which can no longer differentiate[150]. From then on, these myocytes start to produce proteins essential for skeletal muscle tissue, such as myosin heavy chains, alpha-actinins and desmin[151,152]. Myocytes also start to elongate and align along the antero-posterior axis of the somites[153] or the proximal-distal axis of the limbs, displaying the first mechanism at the origin of the fibrous anisotropy of skeletal muscles[154]. The alignment process is essential as it enables the fusion of mononucleated myocytes into multinucleated myotubes. Indeed, this alignment favors recognition and adhesion between consecutive cells, leading to the remodeling of their adjacent membranes by fusogens called Myomaker and Myomerger[155]. In the somites, fusion occurs between already elongated myocytes, usually with border cells, and does not increase fiber length, whereas it is much faster in limbs where fusion increases fiber length and therefore participates in the elongation of the cells[156]. This is the primary myogenesis process, resulting in multinucleated, but still immature, myotubes that express slow and embryonic myosin heavy chains (Myh7 and Myh3)[157].

These aligned primary myotubes will act as a base for the secondary phase of myogenesis. Indeed, after primary myogenesis, $Pax3^+$ muscle progenitors will start to express Pax7 instead of Pax3, leading them to start fusing with each other and with the primary myotubes, giving rise to fetal myotubes[158,159]. These myotubes become larger and will start expressing new types of myosin heavy chains, starting with perinatal ones (Myh8), and progressively fast myosin heavy chains (Myh 1, 2 and 4) characteristic of mature adult myofibers[160].

While limbs and muscles are formed by the time of birth, full maturation of the myofibers does not end there. Indeed, in addition to further increasing the expression of fast myosin heavy chains, myofibers continue to grow in size, but not in number[161]. This growth is mainly associated to Pax 7^+ cells, originally derived from the dermomyotome, which end up forming a consequent pool of muscle progenitor cells throughout postnatal muscle tissue[162]. These cells can fuse with existing myofibers, increasing their sizes and numbers of nuclei[163].

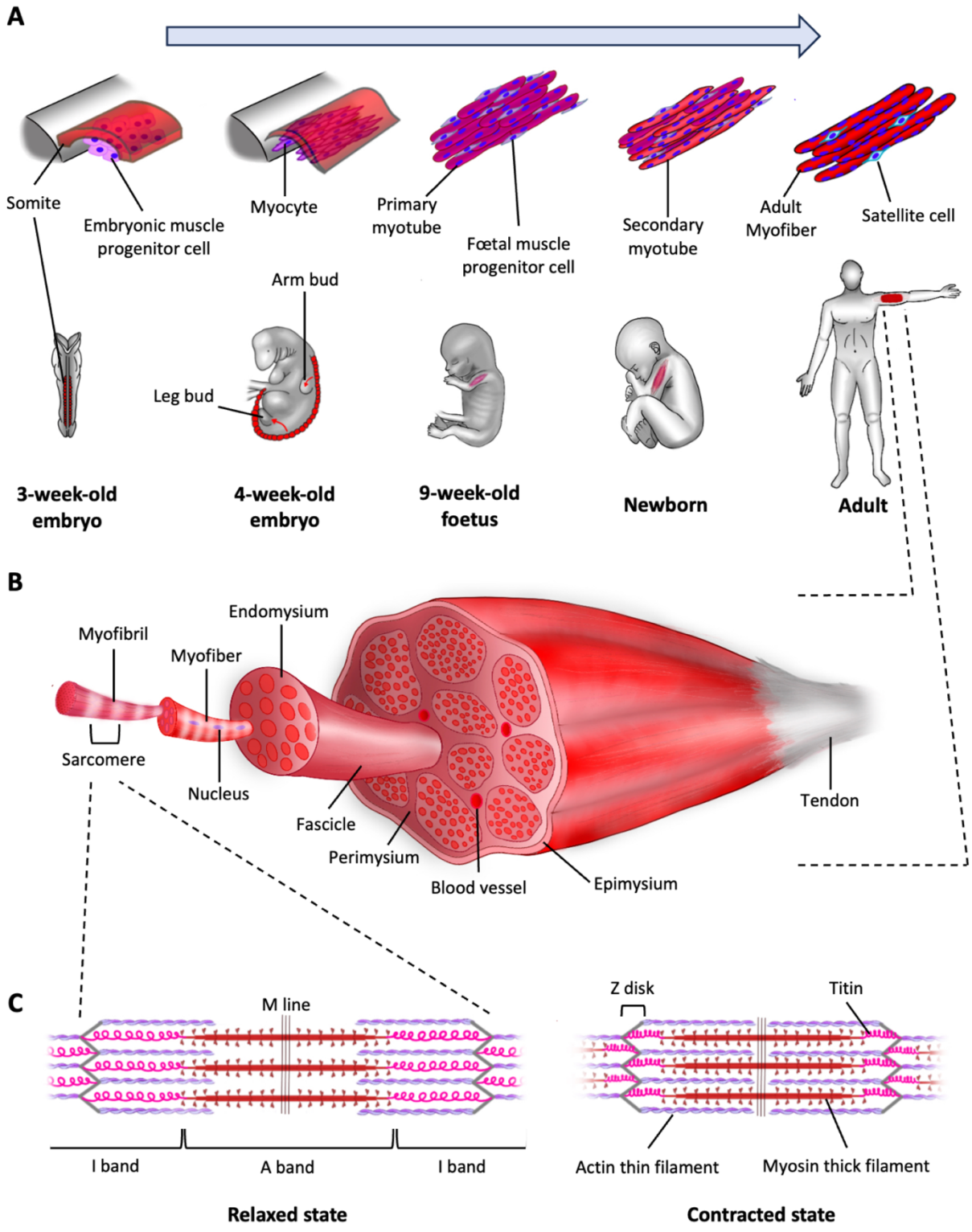

Figure 2.3. Skeletal muscle anisotropy. *Diagrams of (A) myogenesis at every stage of human development, leading to the formation of (B) the hierarchical aligned structure of adult skeletal muscle, which enables (C) the coordinated contractions of the sarcomeres by filament sliding.*

After post-natal development, $Pax7^{+}$ muscle progenitor cells enter a quiescent state and become a much smaller population of satellite cells that can be activated throughout life[164,165].

Following mechanical stimulation, particularly after an injury, these satellite cells can once again become proliferative[166]. They will then successively express MyoD, Myf5 and myogenin, before fusing together or with existing myofibers, in a similar fashion to secondary myogenesis[167]. Myogenesis can therefore occur throughout life, acting as a regenerative mechanism until the depletion of satellite cells due to sarcopenia and aging[28].

b. ***Skeletal muscle architecture: anisotropy across all structural scales***

As previously mentioned, skeletal muscle tissue is constituted at every level of fiber-like structures, all highly aligned in the same direction (Fig. 2.3B).

Already at the organ level, skeletal muscles have an elongated structure, usually with a high aspect ratio, which can reach 10 to 20 for the sartorius muscle[168]. Each skeletal muscle is connected on either end to tendons, transmitting the forces generated by muscles to bones in most cases, or sometimes allowing the movement of specific parts of the body, such as the eyeball or facial skin. The entire muscle is sheathed within a layer of extracellular matrix, the epimysium[169]. Within the muscle, up to several hundred thousand muscle fibers are all oriented in the same direction and bundled into fascicles[170]. Each fascicle is surrounded by another layer of matrix, the perimysium, and can contain hundreds of muscle fibers[171]. This matrix is mostly composed of collagen I, with collagen III, IV and V present as well[172,173]. While it represents less than 10% of the muscle tissue [174], it accounts for half its load-bearing capacity[175]. The most commonly known muscle architectures are fusiform or with muscle fibers parallel to the axis of the muscle, like the biceps brachii. However, in some muscles, such as the ones in the quadriceps, fibers can have an oblique orientation, resulting in a pennation angle relative to the muscle axis[176]. Some muscles are even divided into distinct regions, each with their own pennation angle along which all myofibers are aligned.

With a length of at least a few centimeters long, and usually several tens of centimeters[177], and a width between 40 and 100 µm[178], skeletal muscle cells not only have one of the highest aspect ratios but are also the largest cells in the human body. They can span from 10 to 90% of the total muscle length[177] and hold the record of the highest number of nuclei in a single cell. Indeed, through mononucleated myocytes fusion, a single mature muscle cell usually has at least a few hundred nuclei within the same cytoplasm[179], and in optimal cases about 100 nuclei per mm[180], which would mean more than 40000 nuclei for muscle fibers in the sartorius muscle[181]. These nuclei are evenly spaced and align at the periphery of the cell membrane[182], while the center of the cell is packed with thousands of myofibrils [183]. They span the entire muscle fiber, aligned in the same direction and surrounded by the sarcoplasmic reticulum, a form of endoplasmic reticulum filled with Ca^{2+} ions[184]. The myofibers and myofibrils are characterized by a pattern of striations which represent the series of successive sarcomeres, the contractile units of the cells, each 2 to 3 µm long[177] and oriented to shorten in the direction of the myofibril and the cells[185–188].

In addition to myofibers, skeletal muscle tissue hosts several cell types, starting with satellite cells. With the potential to become active myocytes for muscle regeneration purposes, these stem cells represent between 2 and 7% of the nuclei in muscle tissue[189], with usually a progressive decrease with aging[190]. They are found between the basal laminae and plasma membranes of myofibers[191], close to capillaries[192]. About two capillaries run along each myofiber, resulting in a dense network of endothelial cells that ensure a constant supply of oxygen and nutrients[193]. Fibroblasts are also present in order to maintain and repair the surrounding extracellular matrix[194]. As skeletal muscle function is voluntary movement, it is also highly innervated. Motor neurons, whose main cell bodies are usually in the spinal cord, project their axons to the muscles, where they form neuro-muscular junctions with myofibers. When a signal arrives from the central nervous system, motor neurons release a neurotransmitter called acetylcholine, which binds to myofibers' receptors specifically located at the synapses[195]. This triggers a cascade of mechanisms, eventually leading to muscle contraction, which we will now examine in the following section.

c. *Uniaxial muscle contraction: a not-so-straightforward mechanism*

While myogenesis is essential to understand skeletal muscles, the first question that shaped most early studies on skeletal muscle was the source of their contractile ability, which we will explain in this section by retracing some of skeletal muscle scientific history.

The link between brain and muscles was already sensed as early as the Antiquity, by figures such as Hippocrates or Galen, who believed that a flow of animal spirit activated muscle contraction[196]. The understanding of muscle function would not progress until the Renaissance, thanks to new studies on human anatomy like *Humani Corporis Fabrica*, the 1543 work of Andreas Vesalius[197]. The activation of muscle contraction through nerves would later be established by Jan Swammerdam[198] and William Croone[199] in the middle of the 17th century and further highlighted by the famous experiments of frog leg contraction upon electric stimulation by Luigi Galvani in 1791, which were used to make the first galvanoscope out of a contracting frog leg[200,201].

Regarding contraction at the cellular level, the first insights can be traced back to observations of striations within muscle fibers thanks to Antony van Leeuwenhoek's light microscope at the end of the 17th century[202]. These striations alternate A bands, named after their anisotropic birefringence, and isotropic I bands. In 1875, Leon Fredericq showed that when insect muscles contract, only I bands shorten whereas A bands stay the same length[188]. This was the first study hinting at what would later be the sliding filament theory, but it was disregarded at the time because it did not fit the dominant theories[203] viewing muscle contraction as the result of folding or coiling of continuous myosin fibers, earlier discovered in the 19th century by Wilhelm Kühne[204]. The "myosin" extracted at the time was later revealed to be a heterogeneous mixture of what we currently call myosin and an activator of myosin: actin. Albert Szent-Gyorgy showed in 1942 that when a large filament of this mixture was exposed to ATP it would drastically contract, displaying the root of muscle contraction at the protein

level[205]. But he still believed that this further supported the folding of a continuous network of actin and myosin.

This dogma in muscle biology was once again refuted by two key papers in muscle biology, published in the same issue of *Nature* in 1954. Thanks to electron interference microscopy, Andrew Huxley and Rolf Niedergerke[187] showed that when live muscles shorten, only the I bands shrink, and at the same time Hugh Huxley (unrelated to Andrew Huxley) and Jean Hanson[186] demonstrated the same thing on extracted individual myofibrils. They also showed that A bands were made of myosin and I bands of actin, eventually leading up to the sliding filament theory: myofibers are made of alternating and overlapping filaments of myosin and actin sliding with one another[185] (Fig. 2.3C). Despite this evidence, Hugh Huxley would still have to wait for electron microscopy to further progress so he could obtain much more detailed images of thin actin and thick myosin filaments in the I and A bands respectively to fully assert the sliding filament theory[206].

Following studies focused on the mechanisms used by actin and myosin for sliding and generating forces, notably the 1969 swinging crossbridge hypothesis of Hugh Huxley[207]. After proving that actin filaments could spontaneously start moving on a myosin bed when exposed to ATP[208], the team of James Spudich showed thanks to a dual laser beam trap that myosin head would bind to actin with a force of about 2 pN[209]. Combined with a better understanding of actin and myosin molecules in the 1990's, this further confirmed the idea that myosin had a lever arm that could crawl onto actin[210]. In resting muscles, myosin binding sites are blocked by tropomyosin, preventing movement. When motor neurons stimulate muscle cells, they release from their sarcoplasmic reticulum Ca^{2+} ions, binding to troponin. This causes tropomyosin to move, myosin can bind and therefore stroke actin, sarcomeres shorten, and the whole muscle contracts[211].

Overall, the history of research on muscle contraction not only shows how intricate the anisotropic structure of skeletal muscle must be in order to contract but also illustrates how only scientific and technological innovation has made it possible to fully understand these mechanisms.

III. Replicating native anisotropy in tissue engineering

Understanding the *in vivo* architecture of tissues is a first step. With this knowledge comes the possibility to reverse engineer what has been observed in native tissues and reproduce them in a lab. Indeed, in the past few decades, technological innovations have displayed incredible progress in the field of tissue engineering, especially when it comes to reproducing complex anisotropic structures. In this section we will discuss the various approaches that have now become common for anisotropic tissue engineering.

1. Main tissue engineering techniques

a. *Starting with 2D anisotropic substrates*

Just as 2D cell culture preceded 3D cell culture, the first approaches for anisotropic tissue engineering started on 2D substrates, both as a historical and a logical starting point. Indeed, they established some of the fundamental concepts and methods for cell alignment, which are essential to later understand 3D tissue engineering strategies. The impact of a substrate topography was first observed by Ross Harrison in 1912 on chick embryo cells which displayed significant movement and alignment along the threads of the spider web on which the cells were cultured[212]. This phenomenon was named contact guidance in 1945 by Paul Weiss, who observed a similar axon alignment on grooved mica[12] and later theorized that cells are able to sense and consequently react to the topography of the substrate[213].

Advancements in microfabrication, notably photolithography and soft lithography in the 1990's, made it possible to further study this mechanism, starting by creating substrates with microgrooves (Fig. 2.4A). Early studies notably showed that while parallel microgrooves can promote cell alignment, this is conditioned by the geometry of the grooves [214]. Indeed, fibroblasts were shown to align only if ridges width was smaller than 4 µm, independently of other geometrical parameters[215]. Further technological advances also enabled the engineering of nanogrooves no wider than 50nm[216]. However, when the grooves were smaller than 80nm, fibroblasts were no longer guided, showing that contact guidance works in a specific window. The response to microgrooves is also cell dependent[217], since unlike fibroblasts, Schwann cells alignment doubled when increasing microgrooves width from 10 to 20 µm or depth from 0.5 to 1.5 µm[218]. More complex geometries can even direct specific mechanisms, such as substrates with droplet shaped grooves which induced unidirectional migration of endothelial cells and favored vascularization when implanted in rats[219]. Microgrooves can even control the differentiation of C2C12 cells, mouse skeletal muscle cells, as improved alignment thanks to microgrooves has been shown to increase multiple myogenic markers[220,221] (Fig. 2.4B).

Substrates' anisotropy can also be induced by patterning adhesion molecules, such as contact microprinting techniques. In this case, a PDMS stamp with an anisotropic pattern is covered with matrix proteins, like fibronectin, and then pressed onto the substrate. Simply

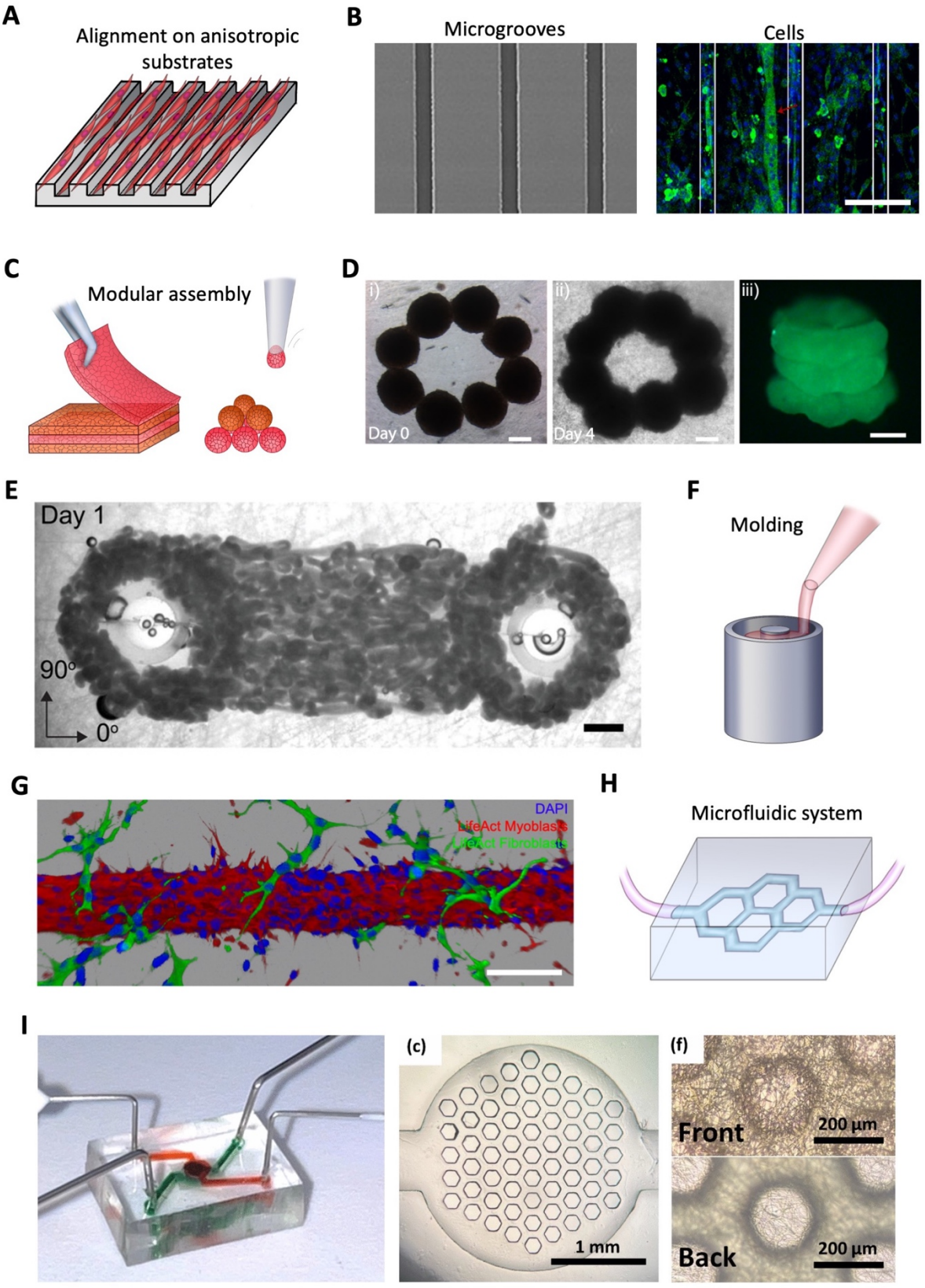

Figure 2.4. From anisotropic 2D substrates to organs-on-chips. *(A) Illustration of cells aligning on an anisotropic substrate and (B) microgrooved substrates, imaged by SEM (scanning electron microscopy), on which myotubes, imaged by confocal microscopy, can align*[220]*. (C) Illustration of cell sheets and spheroids assembly and (D) MSCs spheroids pipette-*

positioned to form a tubular microtissue[222]. (Scale bar = 200 µm) (E) Dumbbell shaped tissue bioprinted with a bioink loaded with smaller dumbbell-shaped cardiac microtissues[223] (Scale bar = 1 mm). (F) Illustration of scaffold casting in a hollow cylindrical mould. (G) Muscle fascicle-like tissue, made with myoblasts seeded in a collagen channel moulded with a needle, with surrounding friboblasts[224]. (Scale bar = 100 µm) (H) Illustration of a microfluidic system. (I) Lung-on-chip with deformable honey-combed shaped membrane with cells on both sides[225].

changing the surface chemistry to create an anisotropic pattern on the substrate, without impacting the microscopic geometry, still had a similar effect, and could induce alignment of human aortic vascular smooth muscle cells[226]. This technique can even be used with multiple coatings, each with its own specificity. For instance, this made it possible to create an aligned network of neurons where the soma was mainly on poly-lysine coating, whereas axons stayed on laminin patterns[227]. Moreover, the opposite effect of cell repulsion can also be achieved using anisotropic patterns of molecules with low protein binding like PEG (polyethylene glycol). Photolithography can also generate similar chemical patterning parallel lines in favor or against cell adhesion and could be used to create cell sheets with more than 90% myotubes within a ± 10° orientation, which also displayed increased lengths and diameters [228].

Along other original approaches, like using oriented meshes[229] or decellularized grass[230] to name a couple, these platforms for creating 2D aligned cell sheets have laid the groundwork by advancing both biomechanical understanding and technological developments, paving the way for 3D anisotropic tissue engineering.

b. ***Modular assembly approaches***

2D approaches have established the foundations for advancing 3D anisotropic tissue engineering, opening the door to more complex methods such as modular assembly, which allows for the creation of more intricate and functional 3D tissue constructs by assembling biological building blocks (Fig. 2.4C, Table 2.1), such as cell sheets.

This is particularly efficient to create systems with layers of different cell types, organization or composition. To replicate the layered anisotropy of the cornea, stacking can be achieved using transwell wells, making it possible to have stromal cells at the bottom of the well while the epithelial cells are at the air-liquid interface[231]. A more direct stacking approach consists of engineering cell sheets with the desired cell type on a robust, but detachable substrate, like polyethylene [232] or collagen[233] thin films, stacking them and then binding them together, with collagen for instance. Although more technically challenging, manipulating cell sheets has been facilitated by thermoresponsive surface treatments, like poly(N-isopropylacrylamide) brushes which can enable cell sheets detachment when exposed to 20 °C for 30 min[228,234]. These surface treatments, in conjunction with microgrooves, can also be used to align cells, making it possible to stack layers with different orientation. This can be used to reproduce the plywood orthogonal organization of lamellae in cornea, as well as in the annulus

fibrosus[235,236]. Indeed, after implanting multilayered anulus fibrosus constructs in rat tails, the expression of collagen and aggrecan was twice as high in patterned tissues. Rotating the orientation of cell layers is also crucial for cardiac tissue engineering[234,237]. While aligning cardiomyocytes on individual sheets drastically increases contraction speed, these contractions are only uniaxial. Stacking multiple cell sheets with a progressively changing angle makes it possible to create multiaxial contractions, characteristic of native tissues[238]. In the case of smooth muscle, orthogonal stacking of cell sheets also favored contractile functionalization, showcased by increases in Myh1 expression and calcium activity[239].

To reproduce peristaltic contractions in smooth muscle, layers not only have to be orthogonally stacked[240], but they also must be rolled into a tubular shape. This can be achieved by transferring the cell sheets in a mould and fixing their position with additional hydrogel[241]. If the cell sheet is soft enough, such as silk nanofibers scaffolds, a system similar to a rolling pin is enough to create the tubular shape. The direction of the rolling motion can change in between layers, and other cells can even be seeded in between layers, to innervate the junction between layers for instance[239]. Many approaches meant to recreate nervous tissue specifically are also based on rolling cell sheets in order to create a tubular nerve guidance conduit, a structure reminiscent of the embryonic neural tube or the spinal cord. In addition to mechanical rolling[242,243], these approaches often rely on self-crimping scaffolds[244–248]. Because of the mechanical memory of materials like electrospun nanofibers, after being seeded, flat scaffold sheets can curl up and form a tubular shape when exposed to the right temperature or after a certain time. Layered and tubular anisotropy can also be combined by inserting inside the tube a layered scaffold[249], or by placing multiple smaller tubes on a larger scaffold about to self-roll, resulting in a hierarchical structure similar to the one observed in a nerve with multiple fascicles[244]. These various nerve guidance conduit constructs, which are usually a few millimeters wide, not only displayed neural maturation *in vitro*, but when implanted in mice *in vivo* showed similar results to autografts, in terms of tissue colonization and functionality[242,244,247]. Nonetheless, these approaches depend on cell sheets that must be sufficiently robust to allow precise individual manipulation without breakage. As a result, scaffold materials are often selected primarily for their mechanical properties rather than physiological relevance, and there is a limit to the thinness of each layer, as well as the cell density within the scaffold.

Cell sheets are not the only building blocks for anisotropic tissue engineering, and other pre-formed cellular constructs can be assembled together, like spheroids. Spheroids can be made in many different ways, such as hanging droplet techniques, agarose wells or magnetic patterning[46,222,248,250–255]. Individually, these spherical cell aggregates rarely display any kind of anisotropy, but several methods have been developed to use them to create larger, anisotropic tissues. Complex geometries can be created by aspirating spheroids and then placing them with an automated micromanipulator in a support hydrogel (Fig. 2.4D). With this approach, lines, rings, cylinders, pyramids, or even words can be made in 3D out of spheroids formed from any type of cells[222,256] (endothelial cells, cardiomyocytes, stem cells...). Moreover, spheroids from

	Modular Assembly	Moulding	Microfluidics	Spinning	Melt Electro-writing	Extrusion Bioprinting	Light-based Bioprinting	Stretching	Acoustic Forces	Electric Forces	Temperature Gradient
Skeletal Muscle	46,228,257	224,257–273	224,258,259,262	274		42,43,45,275–278	279	46,261,265–267,279,280	281		275
Cardiac Muscle	222,223,237,238,282,283	223,241,283–286	283,284	237,238		223,237,287–290	291				284
Smooth Muscle	239–241,292,293	241,292,294	295	240,294,296		297					292
Vascular	283,293,298	259,283,284,299–302	259,283,284,299,301–305	303,306,307		276,288,305,308	291	309,310	311	312	284
Nervous	58,242–244,246,247,249,282,313,314	249,313,315,316	262	242–244,247,317,318	245,246					249	
Bone	296,319	320,321	322,323	296,319,321		45,324,325	326	327		312,320	323,328
Lung	329	225,330,331	225,332	225				225,332			330
Cartilage	53,333,334	335–337	335,336	338	339	45,325,338–341	342				
Skin	234,343	344	304,344			343,345,346				347	
Cornea	232,233,348	231–233,349				350–354	355				
Cancer	58,314	302,356,357	302,358,359								360
Kidney	361,362	363–365	362–364								
Tendon	319			319,366–368		366,369	369		369		
Annulus Fibrous	235,236	235,370		371		372		235,236			370
Non-specific*	46,256,373–376	374,377	256,377,378					46,378	379		378

*Refers to studies applied to multiple cell types, or using non-specific cells or tissues, such as stem cells or NiH3T3 fibroblasts.

Table 2.1. *Table referencing various studies leveraging some of the most common techniques for 3D anisotropic tissues engineering, classified by the techniques employed and the tissue engineered.*

different cell types can be assembled into the same structure, making it possible to see how they would fuse together, or in the case of HUVECs (Human umbilical vein endothelial cells) spheroids how they could vascularize the rest of the structure. The anisotropy of cardiac fibrosis could also be modeled by creating a ring of spheroids in which one or two were previously scarred[222]. This would create tissues with specific regions with reduced calcium activity and contractility, which could also be treated with microRNAs to regain a more homogenous tissue. While this approach offers high precision, it is quite time consuming and requires a complex automated system to place each spheroid individually. Although less precise, other techniques have attempted to improve spheroid assembly by providing a more coordinated assembly, for example through magnetic assembly[46,53,333], which will be presented in the last section.

Similar to spheroids, microtissues can also be used as elementary biological bricks for tissue engineering. Some are spherical, by making them on degradable gelatin microbeads[343], while others are already preformed into a functional shape[223]. They can then be mixed into a bioink to be bioprinted into the desired macroscopic geometry. One study[223] even bioprinted 2cm dumbbell-shaped tissues out of 2 mm dumbbell-shaped microtissues made of cardiomyocytes (Fig. 2.4E). This original approach makes it possible to first optimize the maturation of the microtissues and then to create a specific internal hierarchical anisotropic structure. However, the complexity and the number of steps of such process, in addition to the added difficulty and lowered resolution that comes with extruding microtissues instead of cells, must be factored in when considering this type of approach.

Textile-like weaving techniques also have the ability to achieve such hierarchical anisotropy. Polymer nanofiber yarns are knitted or woven to create a network with a repeating pattern. When seeded prior to assembly, cells can align along the nanofibers and will therefore locally follow the direction of the yarn string[296]. Moreover, it makes it possible to weave together yarns with different cell types to form a layered anisotropy. Even when seeding is done after weaving, heterogeneity can be achieved by pre-loading the yarns with different components. For instance, by weaving a tapestry-like network of yarns with a gradient of 0 to 15% hyaluronic acid, bone marrow stem cells could exhibit a gradual differentiation from tendon-like to bone-like tissue[319]. Similarly to sheet-based assembly, weaving techniques depend on selecting an appropriate yarn composition and often involve complex weaving systems. Cellularization of these scaffolds is also limited, making them less suitable to replicate tissues with a high cellular content *in vivo*. However, they are particularly effective to engineer tissues with a low cell density, like tendons or ligaments, even more so considering the fibrous nature of the yarn.

c. ***Moulding and microfluidic systems for organ-on-chip development***

Moulding techniques are not limited to simply patterning scaffolds with microgrooves to align cells[231–233,241,263,292,313,320,349], which were introduced in the previous section on 2D patterning, but also extend to more complex geometries and macroscopic structures (Table 2.1). First, other patterns can be imprinted such as honeycombs to recreate lung alveoli[225,321] or crypts and villi to mimic intestinal tissues[380]. To do so, a mould with the desired patterns, acting as a stamp, is needed. Such mould can be made using photolithography to create any type of thick 2D patterns with a micrometric precision on the mould and therefore the scaffold[225,283,321], but it is a complex process, and the depth of the imprint is usually below 200 µm. Although designs may be less precise, one way to create deeper structures is to use micro milled[380], or even 3D printed[46,224] moulds. These moulds can also be used for microscale 3D film thermoforming shapes with very thin membranes, for instance to recreate 3D spherical alveoli[330].

While these techniques create anisotropic geometries (since there is a difference of behavior in the plane of the patterns and perpendicularly), they mostly focus on interfaces. Aside from microfabrication, gels can also be moulded at the macroscopic scale to create fully 3D anisotropic tissues, such as a cube, a cylinder, a tri-leaflet or even more complex shapes [249,296,337,344,370] (Fig. 2.4F). For instance, in most skeletal muscle tissue engineering approaches, cell-loaded gels are cast into centimeter scale moulds with a specific 3D anisotropic design, such as a dumbbell shape including holes for anchors [261,262,266,268,269,271,272]. A heart valve could also be shaped via a multi-step injection moulding process of two gels with different cell types[286].

The internal structure of the moulded tissue can be controlled by the mould filling process, which can notably generate gradients in a hydrogel [299,335,336]. To do so, two (or more) different pre-polymer solutions are prepared and fed into a mixing microfluidic system at varying speeds, so that the mould is first filled with one solution, which is then progressively replaced with the other. This was used to create a compression gradient within the same tissue, ranging from 2 to 60 kPa, by creating a PEG concentration gradient from 2 to 20%, leading chondrocytes to produce more collagen II on one end, but more collagen X on the other[335]. Multiple composition gradients can be generated in a gel, and during the filling process spheroids can even be added at different times to see how they would react at different positions, and therefore for different gel compositions[299].

The internal geometry of a tissue can also be controlled by moulding it from within. A simple method consists in inserting a needle or a pin in a gel prior to polymerization, resulting in the formation of a tubular channel within the matrix which is then connected to a microfluidic system to seed it, usually with muscle[224,258], endothelial[259,302] or epithelial cells[363,364] (Fig. 2.4G, Table 2.1). In addition to fibrous or tubular anisotropy, concentric layers of different cell types can be achieved through sequential seeding, making it possible to create a muscle fascicle-like structure with a central hollow blood vessel, which increases contractility of the construct compared to myoblasts-only constructs [259]. Needles are easy to remove from a gel, but they can only create straight channels. Sacrificial objects embedded in a gel can be used to engineer

more complex networks. For example, a vascular network within a cardiomyocyte loaded gel could be made with a 3D printed carbohydrate template which was inserted prior to polymerization and could later be dissolved to seed the channels with endothelial cells[284]. Although more technical, similar results can be achieved by multiphoton ablation which can carve any shape within collagen gels[301,365], making it easier to generate more physiological architectures with enhanced resolution.

In addition to cell seeding, microfluidic flows can also be used to directly shape hydrogels and tissues (Table 2.1). Co-axial microfluidic systems can be used to create cell loaded tubular gel filaments. For instance, an outer endothelial cell loaded GelMA (gelatin methacryloyl) pre-polymer solution can flow around an inner Ca^{2+} ion solution, forming a lumen to recreate blood vessels[305]. Droplet based techniques could even induce radial stiffness gradients in such tubes to create radial phenotype shifts in ductal carcinoma models[359]. When transitioning from a narrow channel to a larger chamber in the proper microfluidic network, shear stress can also align collagen fibers during injection. Collagen chambers can even be formed with a progressive rotation of fiber orientation, which can then induce a corresponding change in the orientation of cells, such as endothelial or cancer cells[305,358]. Microfluidic systems (Fig. 2.4H) can not only reproduce the anisotropic geometry but also the anisotropic stresses in native tissues, such as shear stress or intraluminal pressure, even after tissue formation. For instance, kidney cell channels moulded in collagen dilate when exposed to *in vivo* pressures, with even stronger effects in the case of pkd1 mutations[381]. Similar bioreactors can be used to reproduce blood flow in vascular systems or lung pressure on alveolar membranes[225,332] (Fig. 2.4I).

Overall, microfluidic systems are very versatile tools for 3D cell culture. They can accommodate different cell types and their structural needs in separate compartments, such as a skeletal muscle microtissue anisotropically trapped in one chamber while axons from a motor neuron spheroid extend towards it through a microfluidic channel[262]. Cells can also be separated by thin membranes, which are useful for recreating lung structure[332], and can be exposed to a wide variety of stresses replicating *in vivo* conditions [225,332,381]. Cell-loaded gels are often used to fill chambers, moulded in various shapes, to recreate the native 3D environment[46], but they can also be used to create chemical or physical gradients between compartments, such as those present in skin[304,323]. These microfluidic chips meant to replicate native organ or tissue architecture were coined as “organs-on-chips” by Donald Ingberg in 2010[37,38]. While they have been used to model far more than just anisotropic structures, even extending to multi-organ models known as “human-body-on-chip”, they can be particularly useful for anisotropic tissue engineering. While the low cell numbers limit regenerative medicine applications of organs-on-chips, they can be particularly useful for drug screening, disease modeling, and gaining biomechanical insight into a specific organ[37,382,383]. For example, a bone-on-chip with parallel and progressively smaller channels could reproduce the gradual changes in pore size between healthy and osteoporotic bone and demonstrate that smaller channels favor osteogenesis[322]. These models can also take advantage of other biofabrication techniques, such as electrospinning, which was used create aligned fiber networks within a vascular microfluidic

chip, demonstrating that the impact of mechanical anisotropy outweighed chemical gradients in endothelial cell migration[303].

d. *Spinning techniques and melt electro-writing*

Electrospinning is an ideal method to create anisotropic scaffolds, and particularly fibrous anisotropy. An electric field between a polymer filled syringe and a collector causes the solution to jet out of the syringe, elongating into very thin fibers that dry and accumulate on the collector[384] (Fig. 2.5A). Although this microfabrication technique first emerged in the early 20th century, it gained significant traction after the 1990's and started to be used for biological applications. Indeed, electrospinning can now generate nanometric fibers similar to those found in native tissues out of biocompatible polymers, whether they are natural, like collagen or fibrinogen[319,321], synthetic like PCL[237,238,240] (polycaprolactone) or PEO[338] (polyethylene oxide), or even semi-synthetic like methacrylated hyaluronic acid[303,307]. The geometry of the electrospun fibers can be controlled by parameters such as polymer properties, electrical field, or spinning distance. The most common way to align the fibers is to collect them on a rotating mandrel, with high speed inducing fiber alignment while low speed results in no alignment[240,306,307]. Fibers can also be aligned depending on the collector and electrode shapes[238], or the protrusions on the collector, that can be used to generate alternating areas with perpendicular fiber alignment, which can be very efficient to replicate the orientation changes in cardiac tissue[237]. After cell seeding, the contact guidance cues induced by these parallel fibers, usually with a diameter of about 1 µm[240,242,306], will result in a similar cell alignment, whether the cells are cardiomyocytes[238], smooth muscle cells[240], neurons[247] or any other cell type (Table 2.1).

In addition to cell aligning properties, these electrospun scaffolds possess remarkable attributes. Similar to *in vivo* tissues, these aligned scaffolds display improved mechanical properties in the direction of alignment, with a longitudinal elastic modulus that can be ten times higher than in the transverse direction and three times higher than unaligned scaffolds[238]. This is crucial to ensure structural stability, especially when culturing muscle tissue, as cell alignment also induces coordinated stresses in this direction. Moreover, polymers such as poly(lactide-co-trimethylene carbonate) can be used to create scaffolds with shape memory properties[244]. Gradients can also be induced within these fibrous scaffolds. For instance, solvent vapor annealing at only one end of the scaffold results in a gradient transition from anisotropy to isotropy. Such transition could be leveraged to guide endothelial cell migration and adhesion[306] (Fig. 2.5B). Both mechanical and chemical gradients can also be generated from the beginning of the spinning process by progressively switching between two polymer solutions. This was notably used to demonstrate that infiltration of cells from chick aortic arch explants seeded on electrospun scaffolds was significantly increased when exposed to a low to high gradient of adhesive molecules compared to the opposite [307]. Scaffold properties can also be modified by adjusting spinning techniques. Instead of using a collector as an electrode, two oppositely charged syringes can simultaneously expel polymer filaments towards a central rod

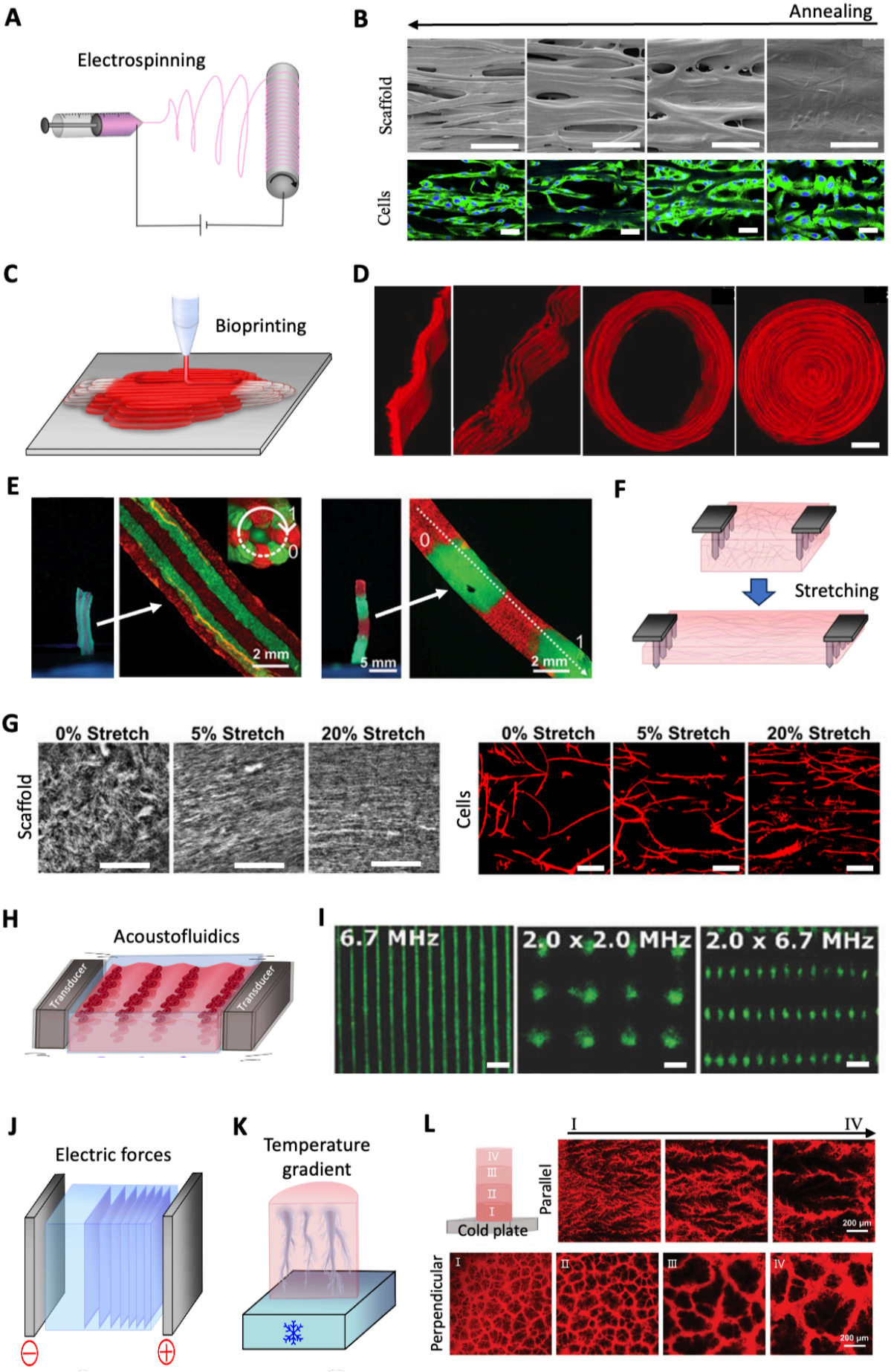
A
Electrospinning
B
Annealing
Scaffold
Cells
C
Bioprinting
D
E
2 mm
5 mm
2 mm
F
Stretching
G
0% Stretch
5% Stretch
20% Stretch
Scaffold
0% Stretch
5% Stretch
20% Stretch
Cells
H
Acoustofluidics
Transducer
Transducer
I
6.7 MHz
2.0 x 2.0 MHz
2.0 x 6.7 MHz
J
Electric forces
K
Temperature gradient
L
I
IV
Cold plate
Parallel
200 µm
Perpendicular
200 µm

***Figure 2.5. Electrospinning, bioprinting and force-induced microfeatures**. (A) Illustration of electrospinning. (B) Electrospun scaffold with gradient vapor annealing and cell anisotropy[306] (Scale bar = 50 µm). (C) Illustration of extrusion bioprinting. (D) Bioprinted constructs with shear alignment of microfibers[276] (Scale bar = 2 mm). (E) Two bioprinted filaments with alternating bioinks[275] (one labeled in green and the other in red). (F) Illustration of scaffold mechanical stretching. (G) Alignment of a collagen scaffold and endothelial cells at various levels of stretching[309] (Scale bar = 200 µm). (H) Illustration of cell alignment in an acoustofluidic system. (I) Cellular patterns generated with acoustic forces using one or two pairs of piezo-electric transducers at varying frequencies [281] (Scale bar = 200 µm). Illustrations of (J) nanofibers layers forming in a gel under an electrical field and (K) directed pores forming in a gel exposed to unidirectional freezing (L) Longitudinal and transverse sections of a scaffold with gradient porous anisotropy formed by unidirectional freezing[275].*

or funnel, enabling the twisting and braiding of multiple fibers into an anisotropic yarn filament that can later be used to create a woven scaffold[296,319].

Some spinning methods do not require electric forces. Filaments can be extruded, elongated and spun using centrifugal forces[317]. Microribbons could also be wet-spun by spinning a gelatin solution around a U-shaped collector in an ethanol bath, resulting in microporous gels that facilitate cell encapsulation, which can sometimes be challenging for electrospun scaffolds[294]. For example, this approach proved to be particularly efficient to promote smooth muscle cells adhesion and alignment.

Another variant of electrospinning, which combines elements of 3D printing, is melt electro-writing (MEW). Instead of creating very thin fibers, a heated and charged syringe jets a polymer solution onto a collector oppositely charged[245,246,339]. Although it is more time consuming and complex than electrospinning, this method can create very precise designs with fibers only 10 µm wide, and potentially toxic solvents are no longer needed. Although the fibers are larger, cells will still align along them[246], and they also exhibit similar shape memory properties[245]. They can also be used to create a frame, which will then be filled with another cell loaded gel[339]. This frame can be used to imbue the whole gel with anisotropic mechanical properties, according to the elongation of the voxels, or to create different layers or regions within the gel, by changing the geometry of the voxels, which can then guide cell behavior. Mimicking meniscus architecture with this method notably made it possible to favor mesenchymal stem cells maturation towards fibrocartilaginous tissue.

e. *Bioprinting*

Since the early 2000's bioprinting techniques have emerged as a powerful tool to create biological tissues with a wide range of possible geometries, including of course anisotropic ones (Table 2.1). First pioneered by inkjet techniques based on the piezoelectric or thermal

propulsion of polymer droplets[354,385,386], bioprinting has now shifted more towards extrusion platforms, and to some extent photopolymerization approaches.

Extrusion bioprinting is akin to regular extrusion 3D printing, but replaces the plastic filament with a bioink, usually a cell loaded hydrogel solution, which is progressively extruded by pneumatic pressure onto a collector (Fig. 2.5C). During the process, the trajectory of the nozzle is controlled by a preprogrammed design, making it possible to precisely control not only the overall 3D shape of the tissue but also but also the positioning of each extruded filament within. In addition to the speed of extrusion and nozzle displacement, the choice of bioink is essential. Not only do these pre-polymer solutions have to be biocompatible, but they also need to have the right viscosity to be extruded without losing their shape. Moreover, they need to easily polymerize, especially if they are pre-loaded with cells[325]. To achieve this smooth transition from viscous bioink to polymerized gel, bioinks are usually polymerized as they are printed, by UV curing for PEG-Fibrinogen[42] or GelMA[275,277] bioinks, temperature changes for collagen-based solutions[289,340], or by thrombin or Ca^{2+} exposure for fibrinogen[43,45] or alginate[305] gels respectively. If this exposure is not uniform, it leads to stiffness gradients within the printed tissue, which can be used to mimic gradients in tissues such as the skin and drive cell migration towards stiffer regions[345].

In the case of stereolithography and laser-based approaches, light curing is not only used to fix the shape of the tissue after it has been printed, but it is also leveraged to precisely expose a vat of bioink to polymerize it layer by layer in the shape of the desired tissue. In most cases, cells are seeded after printing as components of such bioinks for stereolithography, like photoiniators, can be toxic to cells[291,326]. Nonetheless, new stereolithography apparatuses and bioinks aim to encapsulate cells during the bioprinting process, notably using GelMA based bioinks, with which a cell-loaded cornea shaped scaffold could be photocrosslinked with less than 25% of cell death[355].

In the case of extrusion based bioprinting, although some approaches seed scaffolds after printing[324], most do so beforehand, as this allows for increased cell density, already limited in cell-loaded bioinks, and precise control of cell distribution especially when multiple scaffolds and bioinks are involved. In addition to biocompatibility issues of bioinks prior to polymerization, one of the main issues of loading cells prior to extrusion is the shear stress they are exposed to during extrusion due to the viscosity of the bioink. Not only can it limit cell density, but it requires fine tuning to reduce cell mortality. One study showed that H9C2 cardiomyocytes viability was impacted when shear stresses surpassed 80 Pa[289], while another focused on overall extrusion pressure, which had to be below 70 kPa to prevent the death of bone mesenchymal stem cells[325]. However, when properly controlled shear stress can also be advantageous for anisotropic tissue engineering, as it can align polymer fibers and encapsulated objects during extrusion[223,276,289,308,351] (Fig. 2.5D). Such shear induced alignment is of course dependent on the viscosity of the bioink but can also be enhanced by decreasing the nozzle diameter[351] or increasing its aspect ratio[289]. Indeed, when extruding bioink with approximately 20mg/mL of collagen, at a flow rate of 0.0024 $mm.s^{-1}$ collagen fibrils would begin to show a clear aligned distribution when nozzle diameter was less than 0.5 mm.

In addition to controlling the anisotropy of the general 3D shape of the printed scaffold, and the alignment of the polymer fibers, extrusion bioprinting can also induce an anisotropic internal organization of the scaffold at the intermediate scale. Since the extruded materials are filament like, the trajectory of these filaments, for instance parallel or perpendicular arrangement can lead to internal anisotropy[276,277,288]. However, much more complex anisotropic structures can be created with extrusion bioprinting by alternating between bioinks. Simply switching between a cellularized and a decellularized bioink makes it possible to create patterns of cell distribution, and notably to create parallel cellular rows within an acellular matrix, which can induce muscle cell alignment and consequently fusion[43]. Rotation of these rows between layers can also reproduce the crisscross organization observed in the cornea[350]. The complexity can be further increased by using multiple bioinks that incorporate different cell types. This approach enables the creation of distinct regions in the printed tissue, such as a bilayered osteochondral unit[325] or a tissue with an outer shell with annulus fibrosus cells surrounding a core with nucleus pulposus cells[372]. The juxtaposition of these bioinks can become significantly more intricate. In one study, scaffolds were made from alternating filaments made from four different bioinks, one with a sturdier PCL scaffold, two with different cell types and one designed to degrade and create micropores[45]. One way to reduce printing time with this more complex approach, is to use multi-nozzle printing heads, each nozzle dispensing at the same time a different cell loaded gel[275] (Fig. 2.5E).

Layer anisotropy can not only be achieved by switching bioinks between filaments, but even within each filament, which can result in a striped filament [275] (Fig. 2.5E). Radial layers within a single bioprinted filament are also possible using a co-axial nozzle to create a coculture core-shell structure within each filement[308] or even a tubular one to reproduce blood vessels[305].

While bioprinting platforms are very versatile and capable of recreating a broad spectrum of anisotropic architectures, they rely on significantly more complex systems than most other tissue engineering approaches. In addition to constraints related to bioink composition and the impact of shear stresses on cell viability and density, achieving large, structurally stable structures remains challenging. At the microscopic scale, current systems still struggle to reach resolutions below 100 µm. This limitation makes it especially difficult to bioprint tissues with specific anisotropic microfeatures, motivating the exploration of alternative tissue engineering strategies, presented in the next section.

f. *Force-induced anisotropic microfeatures*

To form anisotropic microfeatures throughout a scaffold without having to generate them one by one, various forces can be applied at the scale of a whole tissue. Excluding magnetic forces, which will be discussed in the final section of this chapter, this includes mechanical stretching as well as remote forces such as acoustofluidics, electric forces and temperature gradients.

Even when a scaffold is originally isotropic, mechanical forces, particularly stretching, can induce anisotropy (Table 2.1). Indeed, if a gel is solid enough to be deformed, stretching it will cause the polymer fibers to align (Fig. 2.5F). Even when released, this configuration will be preserved, especially if polymerization was not yet finalized when stretching the scaffold. This will then induce cell alignment, such as the formation of parallel blood vessel[309] (Fig. 2.5G). If a scaffold, still polymerizing, is stretched while inclined, it can even create a transition between aligned fibers at the top of the gel and disorganized ones at the bottom, which in the case of inclined stretched chitosan gels led to gradients in cell alignment and in stiffness from 22 MPa to 1 MPa[310]. Similarly, porous anisotropy can also be achieved by stretching a scaffold during pore formation. For instance, stretching a PCL scaffold during the extraction of its PEO phase led to the formation of aligned pores with an aspect ratio of 4, leading to a 350% increase in collagen I expression increase after *in vivo* implantation to repair rat cranial deffects[327].

Stretching can not only align scaffolds, but it also induces anisotropy by directly affecting cell behavior. Multiple studies have shown that stretching drives cells to align, notably for skeletal muscle where alignment promotes myoblasts fusion into aligned myotubes[46,261,265–267,280]. Although in static conditions cells tend to align with the matrix in the direction of stretching, under cyclical stretching other orientations, such as perpendicular or oblique ones can be observed depending on cell aspect ratio and density, but also on stretching conditions [387]. In fibroblast-loaded scaffolds, cyclical stretching can even provoke a gradual shift in cell orientation from perpendicular to the stretching on the tissue surface to parallel at the core [388,389].

With acoustofluidics, aligned cellular patterns can be created prior to polymerization. A cell loaded hydrogel solution is placed between piezo-electric transducers generating opposing ultrasound waves, driving cells towards the planes perpendicular to the pressure nodes[369] (Fig. 2.5H). Arranging cells in such parallel lines proved particularly beneficial for the anisotropic fusion of myoblasts into myotubes, with a tenfold increase in the expression of the myogenic factor MRF4 compared to unpatterned tissues[281]. Additional pairs of transducers can be added to trap cells into more varied patterns, such as wavy lines or a network of rectangles, whose properties can easily be controlled by the combinations of the different transducers' frequency (Fig. 2.5I). Although the range of achievable patterns with acoustofluidics is limited, moulds can be used to further guide the acoustic waves and therefore add another level of complexity to the possible structures, such as networks of adjacent vortexes[379] or 3D spirals[311].

Aside from electrospinning, electric forces are capable of creating a pattern of aligned layers of silk nanofibers within a scaffold[249,312,320,347]. A silk nanofibers solution is placed between two electrodes. Due to their charge, the electric field triggers the formation of consecutive layers perpendicular to the current direction that collect near the positive electrode (Fig. 2.5J). After formation of the layers, freeze drying is used to preserve this anisotropic configuration in microporous structures. The thickness of the layers is typically on the order of micrometers and increases with current exposure time. This, in turn, enhances the compressive modulus in both parallel and perpendicular directions, although the former always remains higher than the latter due to the anisotropic geometry[312]. This layered geometry can also be adjusted by modulating the placement and geometry of the electrodes. For instance, in one

study[320], a cylindrical positive electrode was used as a mould, combined with a central rod acting as the negative electrode to create concentric silk nanofiber layers. Moreover, as layers were evenly spaced near the positive edge, and progressively more and more spaced out in the center, this successfully replicated bone geometric transitioning from a cortical layered anisotropy to a trabecular gradient one. Although this approach is limited to charged silk nanofibers gels, which must be seeded after scaffold formation due to freeze-drying, thanks to their anisotropic features these structures enable fast cell migration and colonization in a matter of days[249].

When it comes to remote actuation, temperature control is relatively easy to engineer. This is partly why freeze-drying is a widely used method to create micro-porous scaffolds from a wide selection of materials, such as collagen[360], silk fibroin[328] or chitosan[284] hydrogels. While uniform freezing results in an isotropic pore distribution, if freezing is done from only one end of the gel, resulting in a temperature gradient along one axis in the gel, pores will elongate in the direction of the gradient (Fig. 2.5K). This can then favor cell migration in this direction, making it possible to study tumor invasion for example[360]. Bioprinting a gel onto a freezing plate enables the growth of lamellar ice crystals from the substrate, eventually resulting in honeycomb-like pores in the scaffold, even without lyophilization. This directional freezing not only orients the channels, but also results in a gradient of pore size, with pores getting larger the further they are from the freezing source[275] (Fig. 2.5L). This increases the elastic modulus in the pores' direction and can later favor alignment of myotubes or endothelial cells. Additionally, pore size and distribution can be controlled by adjusting the overall temperature field and the scaffold composition. Temperature gradients can also be used for thermophoresis to attract particles or polymer fibers that will naturally migrate from the hot side to the cold side of a prepolymer solution[323]. This results in crosslinking, and by extension stiffness gradients. This technique could induce osteoblast differentiation gradients, as they exhibited increased mineralization on the stiffer part of the gel.

2. Impact of cells' self-reorganization in anisotropic tissue engineering

The methods described previously impose initial conditions on tissue architecture, either by precisely positioning cells or by strongly guiding and constraining them in an anisotropic manner. These approaches actively rely on the cells' ability to sense and respond to topographical and mechanical cues, as seen in phenomena such as contact guidance and alignment under mechanical stimulation. However, this response reflects only one aspect of the broader morphogenic capabilities of cells. Indeed, cells also have an intrinsic ability to self-assemble and self-organize[9,11,390–392], independently of the initial structure of the scaffold. Gaining a deeper understanding of the morphogenic processes driving spontaneous cellular reorganization, even after the initial tissue structure has been established, is therefore essential for advancing anisotropic tissue engineering. In the following section, we will introduce three key spontaneous cellular reorganization mechanisms, which can contribute to the formation of anisotropic structures.

a. *Spontaneous self-alignment*

While we already discussed the ability of cells to align due to external cues, they can also spontaneously align on their own, both in 2D and 3D systems (Fig. 2.6A). It is particularly evident with skeletal muscle cells (Table 2.2), most likely because of their high contractility.

On 2D substrates already, differentiating myoblasts will tend to locally align to fuse into parallel myotubes. However, this self-alignment is only visible on areas of at most a few hundred micrometers, and at the macroscopic scale tissues appear isotropic. Nonetheless, this self-alignment can be increased or guided by the shape and size of the boundaries of the substrate, as cells formed an aligned pattern on 400 µm wide circles while they formed a spiral pattern on 1500 µm wide circles[393]. In this study, boundary constraints notably highlighted the tissue's correlation length, the maximum distance over which alignment propagates. Similarly, NiH3T3 fibroblasts also have the ability to form monolayers with aligned domains over a correlation length of about 500 µm. This organization was especially correlated to cell density, as aligned regions only appeared when cell density exceeded 50%[394]. Other factors, such as the cells' geometry and aspect ratio, can also impact cellular alignment[390,395].

In 3D, attaching a myoblast loaded scaffold of any shape to two pillars will automatically result in cells aligning between the two anchors[260,264,265,270,272], even if the gel is cast in an isotropic circular mould (Fig. 2.6B). Due to the cells' contractility, longitudinal stresses develop between the anchors, whereas the absence of radial constraints only leads to deformation and no other stresses. This stress alignment leads cells to self-align, in an attempt to minimize deformation energy, a mechanism involved in several morphogenic processes[11,391,396], and very often harnessed in skeletal muscle tissue engineering.

Such self-alignment in 3D scaffolds can also be observed with other cell types, such as other muscle cell types[397], fibroblasts [393], or cancer cells[398]. One of the common denominators in these observations of self-alignment is cell contractility. This was even evidenced in glioma cell-loaded gels suspended between two posts [398]. Tissues displayed growing contractility over time, and in parallel, a progressive alignment of cells in the direction between the two pillars. However, when blocking antibodies selective for integrin were used to inhibit cell contraction, cells no longer aligned and adopted an isotropic organization.

Overall, self-alignment refers to the ability of cells to align due to intrinsic properties, such as their contractility and geometry, in specific initial conditions, including boundary constraints and cell density.

b. *Matrix remodeling*

Changes in the matrix often occur due to cells' ability to remodel it, a process frequently involved in generating tissue anisotropy (Fig. 2.6C, Table 2.2). Even cells that are not naturally contractile, can remodel the scaffold's fibrils, causing the matrix to contract[399]. For instance, when a collagen scaffold, loaded with dental pulp stem cells and their neural derivatives, was

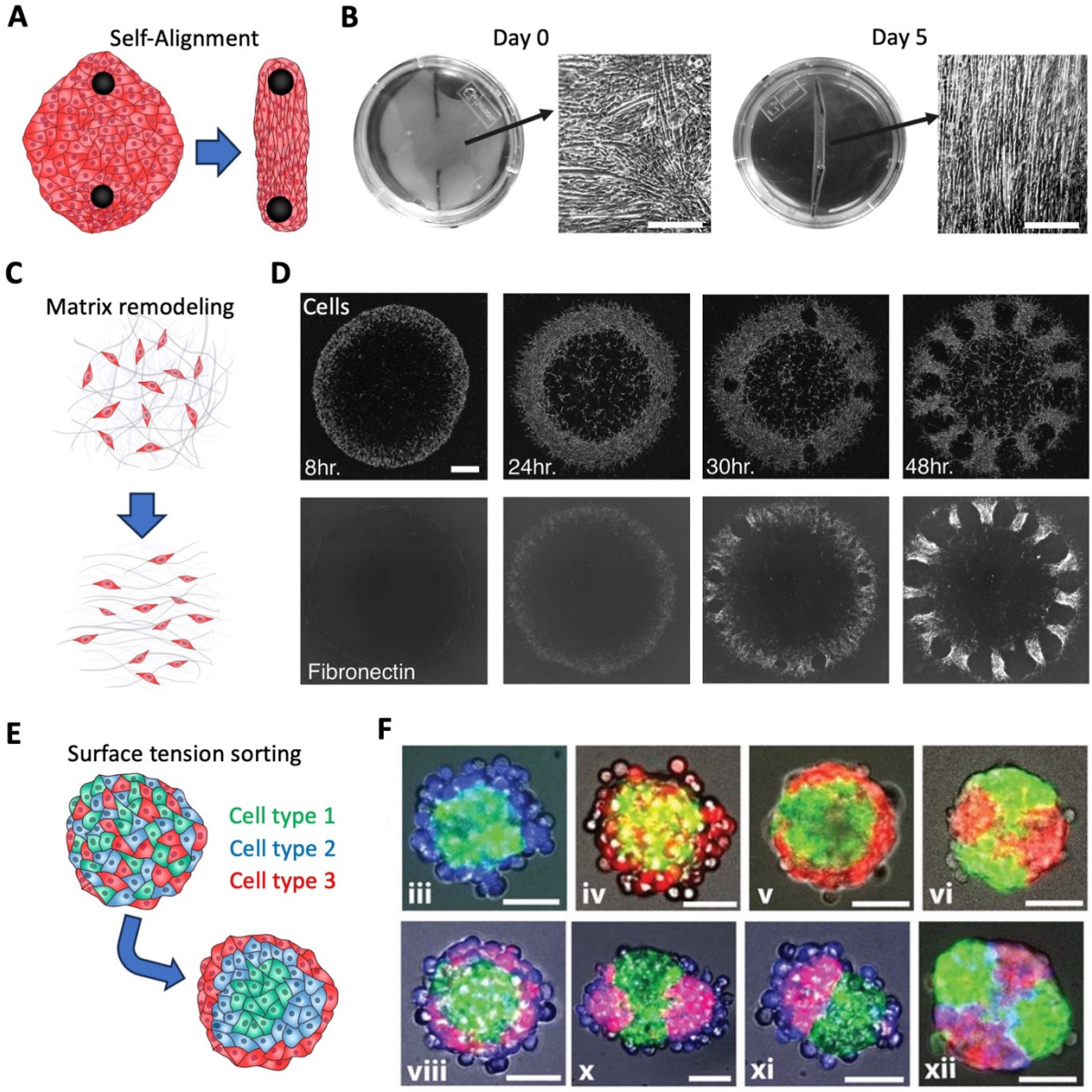

Figure 2.6. Anisotropic tissue engineering approaches leveraging cellular spontaneous reorganization. *(A) Illustration of cellular self-alignment and (B) spontaneous alignment of muscle tissue constrained by two pillars*[260]*. (Scale bar = 60 µm) (C) Illustration of matrix remodeling and (D) fibronectin scaffold remodeled by avian dermal fibroblasts into follicle patterns*[400]*. (Scale bar = 500 µm) (E) Illustration of surface tension cell sorting. (F) Various multicellular constructs made with two or three different cell types (labeled in blue, red or green), pre-programmed with the synNotch→adhesion toolkit to have different adhesion and tension surface properties to induce specific layering and cell sorting* [401]*. (Scale bar = 100 µm)*

constrained by two clamps, not only were the fibrils rearranged to align between the clamps, but collagen density also increased. Simulations have shown that such matrix remodeling processes are related to how cells interact with each other in a matrix. Fibrils density and alignment would particularly increase between two cells, in order to favor force transmission, cell migration and durotaxis[402]. This must be considered in tissue engineering, as it can also

lead to structural collapses. For instance, when avian skin cells were patterned either in a straight or circular line, they would remodel the 3D matrix so that fibrils would follow the direction of the pattern[400]. This would further align cells and increase their contractility, which in turn would enhance matrix remodeling, eventually resulting in evenly spaced collapsed cell and matrix aggregates in a straight or circular line, showcasing the process of formation of avian skin follicle patterns (Fig. 2.6D).

While matrix reorganization is actually highly controlled in morphogenic processes, it is completely erratic in cancer tissues[403], making it an essential element to reproduce the anisotropy of the tumor microenvironment. Indeed, tumors can first degrade the surrounding isotropic matrix with metalloproteinase enzymes. Then, contraction, extracellular matrix production and enzymatic crosslinking of the cancer cells induce strain-hardening of the surrounding matrix. This orients the fibers radially, and induces anisotropy in the matrix compliance, which becomes lower in the extension direction of the tumor[404]. Moreover, such anisotropic remodeling is closely associated with the invasiveness of the tumor. Indeed, expression of the Lox collagen-crosslinking enzyme is higher in the more aggressive MDA-MB-231 than the MCF7 cell line, resulting in a denser, more organized and anisotropic matrix architecture[356]. Anisotropic remodeling also promotes the migration of metastatic cells, which, through their contractile forces, further organize and align the matrix fibers, in the direction of migration of the cells[405].

	Self-Alignment	**Matrix remodeling**	**Tension sorting**
Skeletal Muscle	260,264,265,270,272		
Cardiac Muscle	223		
Vascular		283,288	
Nervous		399	316
Skin		400	
Cancer	398	356,404	406
Non-specific			401,407,408

Table 2.2. *Table referencing various studies leveraging the cells spontaneous reorganization properties for 3D tissue engineering, classified by the type of reorganization and the tissue engineered.*

Degradation of the matrix by metalloproteinases is also essential for angiogenesis[409], enabling endothelial cells to spontaneously sprout and gain a tubular organization. This tubular anisotropy can be guided *in vitro* by the matrix geometry. Indeed, a microfluidic channel filled

with an endothelial cell loaded gel will see cells remodel the matrix to create a lumen in the center and transform the fully filled channel into a hollow vessel[283]. A similar phenomenon can also be observed if such a gel is bioprinted. Within an extruded 3D lattice, endothelial cells tend to degrade the center of each filament branch, resulting in a network of hollow channels whose direction is controlled by the original path of the printer[288].

c. *Surface tension sorting*

In addition to self-alignment and matrix remodeling, anisotropic tissue engineering can benefit from spontaneous surface tension sorting of cells (Table 2.2). Indeed, surface tension, the cohesive force at the interface between a liquid and another medium, plays a role in tissue behavior, as cellular assemblies often exhibit fluid-like properties. Cell-cell adhesion and contractility regulate surface tension in tissues, driving them to self-organize to minimize deformation energy, notably at their surface[11]. Differences in structural properties, such as collagen content, also result in a large spectrum of surface tensions according to the cell type. Even endothelial cells and mesenchymal stem cells, although both derived from the mesoderm, have very different surface tensions, 14 and 66 mN/m respectively[256].

When engineering a tissue with a single cell type, surface tension will mainly regulate how easily a tissue will change its shape to minimize surface energy. But when multiple cell types are mixed into a tissue, surface tension will determine how they organize with each other within the tissue. In particular, surface tension differences between the cell types will result in their segregation into consecutive layers (Fig. 2.6E). In these layered anisotropic structures, cells are organized from the highest surface tension at the center to the lower surface tension at the periphery of the tissue. When mixing cells from the ectoderm and the mesoderm of zebrafish, ectoderm cells would migrate towards the center while mesoderm cells move to the edge of the spehroids[407]. However, when the mesoderm is replaced by endoderm tissue, having a higher surface tension than ectoderm, the situation is reversed, and ectoderm cells end up at the edge of the tissue[408]. Even with neurons and glial cells extracted from the same nervous tissue, neurons with a lower surface tension end up excluded to the edge of the spheroid[316].

Surface tension sorting can therefore be a very powerful tool to create a layered anisotropic architecture. At the very least, it needs to be taken into consideration as cells will spontaneously sort themselves, even if they were not intended to. There are also ways to control cell sorting by modifying cell adhesion or contractility properties. Indeed, sorting can be prevented by using a rock inhibitor, preventing cell contractility, or even inverted by inhibiting myosin expression in the cells with the highest surface tension[407]. Cell adhesion can also be regulated through the expression of E-cadherin molecules. Indeed, transfecting cells to reduce E-cadherin expression or adhesion, would decrease overall cell adhesion, leading to the exclusion of these cells from the center of the construct. Increasing E-cadherin expression or adhesion has the opposite effect[406]. More complex modifications of cell adhesion even made it possible to program cells to self-assemble into structures with three layers that are not necessarily concentric and can extend beyond spherical symmetry[401] (Fig. 2.6F).

IV. Engineering anisotropic tissues with magnetic forces

Despite the remarkable advancements of current tissue engineering methods, whether they rely on active control of cell positioning and behavior or on spontaneous self-organization mechanisms, fully replicating the complexity of native tissues remains challenging. One approach that has displayed a lot of potential for anisotropic tissue engineering is the use of magnetic forces. As we will describe in the following section, magnetic tissue engineering can not only recreate any type of anisotropic tissue *in vitro,* but can do so remotely, making magnetic based approaches both efficient and versatile.

1. Magnetic nanoparticles in bioengineering

In magnetic tissue engineering, forces are mediated through magnetic micro- or nanoparticles, in particular superparamagnetic iron oxide nanoparticles. First developed in the 1980's using the Massart method of co-precipitation of ferric and ferrous salts[410], these particles have a core made of iron oxide, usually hematite $\alpha - Fe_2O_3$, magnetite Fe_3O_4 or maghemite $\gamma - Fe_2O_3$, which can be as small as a few nanometers wide[411]. To ensure stability of the nanoparticles in aqueous conditions, the core is surrounded by a coating, the most commonly used being PEG, PVA (Poly(Vinyl Alcohol)), chitosan, PVP (Poly(Vinyl Pyrrolidine)), dextran or citrate[412–414]. While particles made with the Massart method are usually rock-shaped, other techniques, like thermal decomposition or the polyol process, can result in rod shaped objects or flower-like multicore nanoparticles[415]. These changes not only alter the shape of the nanoparticles but also their chemical and physical properties. The key feature of these nanoparticles is their superparamagnetism. Indeed, while bulk iron oxide is usually ferrimagnetic, at the scale of the nanoparticles (usually of the order of 10 nm) it becomes superparamagnetic. A magnet can apply a force on these particles but as soon as it is removed there is no lingering magnetism, allowing precise magnetization and manipulation of the nanoparticles.

For biomedical applications, nanoparticles can either interact with the matrix or directly with the cells. In the former case, nanoparticles can be directly mixed into the matrix solution before polymerization[278,297] or spinning[317,366]. To avoid nanoparticles from leaking from the scaffold, they can also be coated with various molecules to increase binding to the matrix. Magnetic nanoparticles can even be functionalized to adhere to cell membranes, for instance by coating nanoparticles with streptavidin, which can bind to biotinylated cells[416]. Nonetheless, the most common cell labeling technique is through nanoparticles internalization[417]. Indeed, when exposed to superparamagnetic nanoparticles, cells can viably internalize and confine them within endosomes[417,418]. This internalization grants cells superparamagnetic properties, making it possible to directly apply magnetic forces on them. Endocytosis depends on cell type [419], as well as nanoparticles size and surface chemistry[420]. Both the level of iron internalization and consequently the magnetic moment of the cells, are also impacted by the concentration and duration of the nanoparticles incubation[46,421], which can be measured through

magnetophoresis[422]. The biocompatibility of superparamagnetic nanoparticles is not only attested by their viable internalization, but also by their degradation by the cells[417,423]. More recently, studies have even shown that iron degraded from nanoparticles could regain magnetic properties after extended periods of time, which opens new possibilities for magnetic nanoparticles biosynthesis[424], and therefore magnetic tissue engineering.

Magnetic nanoparticles were first used as contrast agents, since their magnetic properties can modify the relaxation of surrounding protons, which is the basis for magnetic resonance imaging. In addition to their tendency to migrate towards inflammation and cancerous sites, they can be further functionalized to target specific tissues[425]. Moreover, cells or tissues labeled with magnetic nanoparticles *in vitro* can be monitored through MRI after implantation, for instance making it possible to track labeled stem cells implanted into the mouse brain after more than a month[65]. These particles have also been investigated for their therapeutic properties. Indeed, when exposed to an oscillating magnetic field, they can release heat to the surrounding cells and matrix, leading to the development of cancer treatments through hyperthermia[48,49,426]. In the scientific community of magnetic nanoparticles, applications working on tissue engineering are still emerging. Nonetheless, since they were first used to magnetically engineer cell sheets in the early 2000's[52], magnetic based techniques have shown considerable progress, which we will now discuss in the context of anisotropic 3D tissue engineering.

2. Alignment along the magnetic field lines

One of the first ways to use magnetic forces to engineer anisotropic structures is magnetic alignment (Table 2.3). Indeed, when superparamagnetic nanoparticles, or objects loaded with them, are exposed to a magnetic field, they gain a magnetic moment in the direction of the magnetic field lines and are subjected to a magnetic force proportional to their moment and the magnetic field gradient[46]. This results in their orientation and the migration along the magnetic field lines, already creating alignment[274,278,367,427,428].

This notably applies to magnetic micro-objects, such as nanoparticle loaded microgels or scaffold fibers. Indeed, it is particularly efficient to align electrospun fibers made with a prepolymer solution loaded with magnetic nanoparticles. They can be aligned as they are electrospun, by placing a magnet near or below the collector[274,318]. Varying the distance to the magnet can even induce a gradient of fiber alignment, and consequently of cell alignment, which is ideal to mimic the structural gradients of musculoskeletal interfacial tissues[367]. Multiple magnets can be used to create even more complex gradients. Aligned chains of nanoparticles can also be generated during bioprinting. Indeed, the combination of the extrusion shear stress with magnetic forces can result in nanoparticles forming aligned chains in the direction of extrusion[297]. This could be achieved by passing the printing head through a ring magnet[278]. The more ring magnets used, the more anisotropic the scaffold becomes, which would directly impact the differentiation of muscle cells encapsulated in this bioink. Indeed, going from 1 to 3 ring magnets doubled the myotube fusion index and increased their

maturation rate fivefold. These strategies leveraging magnetic alignment within usually non-magnetic approaches, such as electrospinning or bioprinting, showcase how magnetic forces can be used to complement them to further enhance the desired anisotropic features.

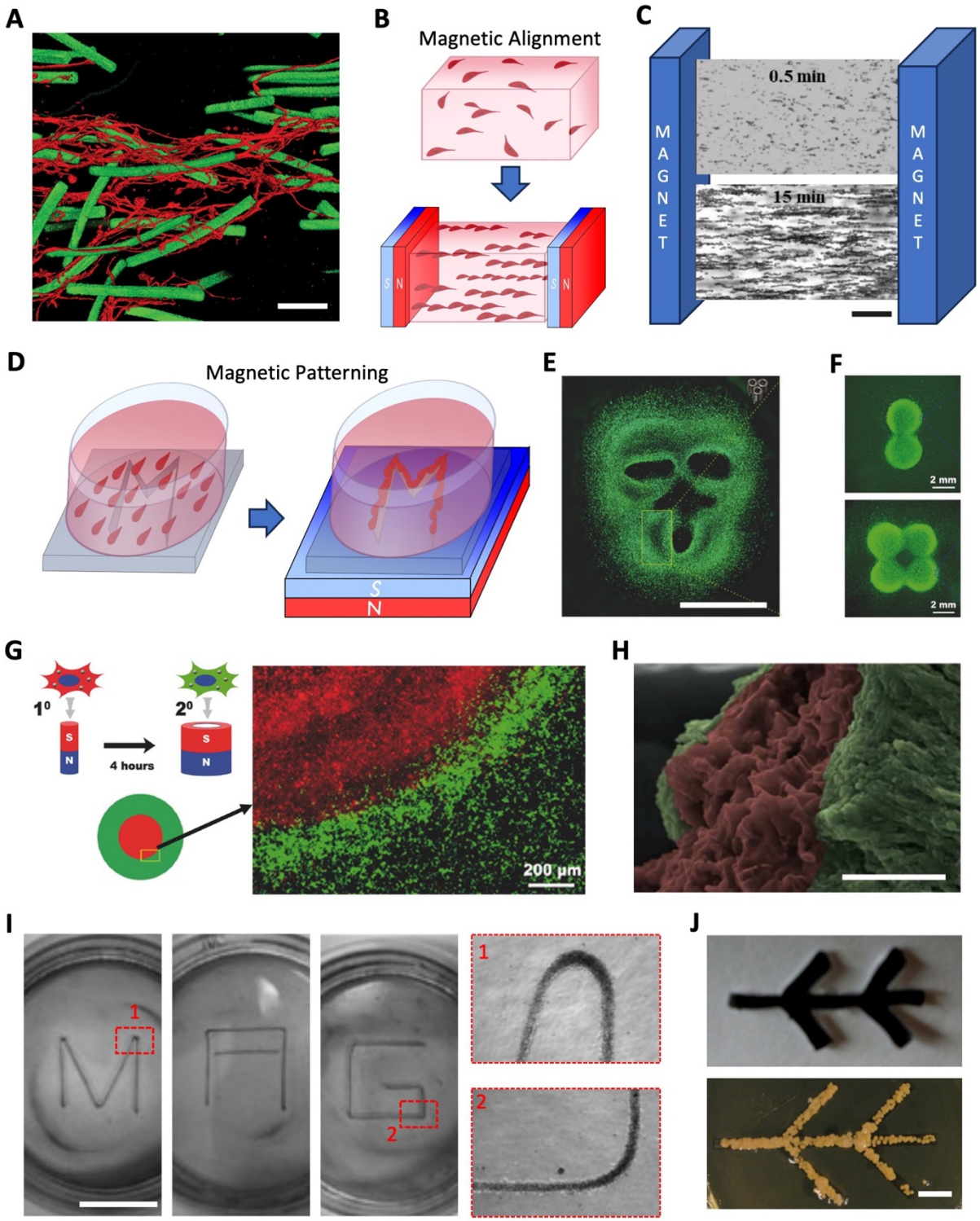

Figure 2.7. Magnetic alignment and patterning. *(A) Magnetically aligned iron-doped rod shaped microgels guiding nerve cell orientation*[429] *(Rods in green, cells in red, scale bar = 20*

µm). (B) Illustration of magnetic cell alignment and (C) cardiomyocytes, labeled with iron oxide nanoparticles, aligned under a magnetic field[412] (Scale bar = 100 µm). (D) Illustration of magnetic cell patterning. Magnetically labeled cells patterned into (E) a face-like shape with three hollow cylindrical magnets (Scaler bar = 5 mm) and (F) pixelized shapes with small cylindrical magnets [430]. (G) Sequential magnetic patterning of two different cell types (labeled in red or green) using a small plain cylindrical magnet and a larger hollow cylindrical magnet to form a core-shell organization [430]. (H) SEM imaging of HUVECs sandwiched between two layers of adipose-derived stromal cells by magnetic patterning[431] (HUVECs in red, stromal cells in green, scale bar = 30 µm). (I) Letters "M," "A," "G" magnetically patterned out of fibroblasts [432] (Scale bar = 1 cm). (J) Iron nanoparticle loaded spheroids, made of mouse yolk-sac endothelial cells, assembled with a magnetic pattern[255] (Scale bar = 2.5 mm).

However, when there is no flow nor other mechanical forces applied on the gel, encapsulated magnetic particles will naturally collect towards the magnets[46]. To avoid this, the gradient needs to be null. This is the case when the gel is placed in the region separating two poles of a magnet[318,433], or in the space between two opposite magnets, where the magnetic field is uniform, with parallel field lines spanning between the two magnets. There, the gradient is null, but the magnetic field itself is not. Therefore, the superparamagnetic objects conserve their magnetic moments, resulting in dipolar interactions. Each object generates a weak magnetic field oriented in the direction of the magnetic field lines. When the density of these objects is high enough, the magnetic fields produced by each of these magnetic dipoles can result in forces on the neighboring objects sufficiently strong for them to align and start forming chains[313,317,366,428]. As these objects migrate within the pre-polymer solution, the matrix also polymerizes, and these aligned objects are trapped in a uniform distribution throughout the scaffold. This approach can create magnetic nanoparticles chains[313,427] and can be applied to magnetically labeled microtome-cut electrospun PCL fibers, collagen bundles[434], or PEG microgels[428,429], all eventually leading to cell alignment in the gel due to 3D contact guidance cues (Fig. 2.7A).

If the parallel objects can be dissolved, this can also be used to create anisotropic pores in the scaffolds. Magnetic alginate microparticles could be aligned in a hydrogel and then degraded with EDTA, resulting in a porous anisotropic scaffold with axons colonization comparable to that of isografts' after *in vivo* implantation[315]. Anisotropic pores can also be made by aligning magnetic nanoparticles when freezing an alginate gel, so that pores form under the guidance of the magnetic nanoparticles' chains[435]. Although these methods do favor cell alignment, they both require seeding the gel from the outside after gelation.

Cell alignment can also be achieved by directly aligning them, instead of intermediary matrix components, with a magnetic field (Fig. 2.7B, Table 2.3). Once cells have been labeled with magnetic nanoparticles, as previously explained, they will behave like superparamagnetic dipoles when exposed to a magnetic field, and they can align in the same way as inanimate magnetic particles[46,436]. For instance, magnetically labeled cardiomyocytes can be mixed into a

	Magnetized scaffold				Magnetically labeled cells			
	Alignment	**Patterning**	**Assembly**	**Actuation***	**Alignment**	**Patterning**	**Assembly**	**Actuation***
Skeletal Muscle	278,429,434			279,437,438	46	46,273,439	46,257	
Cardiac Muscle				290,440	412	60,441		
Smooth Muscle	297	298,442	298,442			293,300	293	
Vascular		298,443	298	444		255,293,300, 431,432,439, 443,445–448	255,293	445,446
Nervous	313,315,317, 318,427		58,314			316		66,449
Bone	433			450–452		430,431		
Lung				331			329	
Cartilage		337	53	337,453–455	456	333	333,334	
Skin	428							
Cancer			58,314			357,416		
Kidney	362		362					
Tendon	366,367							
Non-specific	457,458	374	374–376	377,458	46,459	46,373,460,461	46,373,461	

*Refers to all methods meant to guide, stimulate or actuate a tissue after it has been formed.

Table 2.3. *Table referencing various studies leveraging magnetic-based techniques for 3D anisotropic tissues engineering, classified by the techniques employed, the type of tissue engineered and whether the scaffold or the cells were magnetic.*

thermoresponsive Pluronic or collagen hydrogel solution at 4 °C, which is then placed between two strong magnets in an incubator at 37 °C. While the gel polymerizes, the cells align and form chains, whose length is controlled by the magnetic labeling and the cell density[46,412] (Fig. 2.7C). Although the alignment did not significantly increase the beating rhythm of the cardiomyocytes, magnetically aligned cells displayed the same markers of maturation as non-labeled ones, showcasing the viable use of magnetic nanoparticles directly within cells. More complex cell alignments can be achieved by polymerizing the scaffold step by step, while changing the orientation of the magnetic field. It can also be achieved directly with the proper magnetic field, such as a three-magnet system, which can also result in bent parallel field lines. This gradient or layered cell anisotropy applied to magnetic chondrocytes is ideal for reproducing the cartilage arch-like orientations[456]. Further configurations of cells alignment are possible with Halbach systems, such as a cylindrical chain of rotating magnets, which can create much more complex magnetic fields and gradients guiding the cells[459]. It is also worth noting that when cells are magnetically aligned, so are the magnetic endosomes within them, opening new possibilities for intracellular magnetic actuation and measurements[462,463].

Overall, magnetic alignment techniques, whether they are applied to magnetically labeled cells or other microscopic objects, fall in the previously mentioned category of approaches relying on tissue-scale forces to induce the formation of anisotropic microfeatures, such as mechanical stretching [309] or acoustofluidics[281]. However, these platforms rely on direct physical contact with the tissue or polymer solution, affecting every element within them. Not only can magnetic forces generate microfeatures remotely, making it possible to align objects within systems or chambers otherwise difficult to reach, but they can also specifically target the magnetic elements without necessarily impacting the rest of the microenvironment[46]. The remote nature of these forces also enables their application over large objects, if there is a need to upscale the size of the tissue.

3. Shaping tissues through magnetic patterning: a bioprinting-like approach

While these dipolar interactions are ideal to create arrays of aligned microscopic structures, classical magnetophoretic forces can be used to pattern cells or microtissues into anisotropic structures (Fig. 2.7D, Table 2.3).

When seeding magnetically labeled cells onto a scaffold, this makes it possible to attract them to a specific region, creating an asymmetric or heterogeneous distribution of the cells[443,446]. If the magnet is placed below the scaffold, magnetically labeled cells in a suspension or in a pre-polymer solution will naturally migrate and aggregate in the shape of the magnet[460]. So, if the magnet is anisotropic, so will the cell aggregate[374]. One study even used star-shaped magnets to create a star-shaped cellular pattern[416], but in most cases geometries are usually limited since most natural magnets are parallelepipedal, cylindrical or ring shaped. Nonetheless, magnetic ring patterning is still particularly interesting to reproduce tissues with radial

anisotropy like smooth or cardiac muscles[60,442]. For example, ring-shaped tissues, magnetically patterned with cardiomyocytes, not only displayed cardiac functionality markers, such as sarcomeric striations and coordinated beating over several weeks, but they could even be implanted in rats' hearts while being monitored with magnetic image resonance. Despite the 2D nature of the magnets surface, the aggregates they create can also be 3D. Indeed, cells will aggregate on one another and the 3D shape of the magnets, as well as the number of cells, will impact the 3D aspect of the tissue[46,448].

One way to increase the complexity of the possible patterns is to use multiple magnets. For instance, three ring magnets were used to aggregate cells into a face-like pattern (Fig. 2.7E). Arranging multiple small cylindrical magnets into the desired shape is another way to create a specific geometry in a pixelized approach[430] (Fig. 2.7F). In the case of red blood cells, their diamagnetic properties make it possible when they are placed in a paramagnetic medium to constrain them with multiple magnets into forming macroscopic anisotropic structures such as lines or three pointed stars[447].

Instead of using multiple magnets at the same time, they can also be used sequentially. This makes it possible to change the shape of the magnets in between, as well as the cell type. A first cell type can be aggregated on top of a cylindrical magnet, and after a few hours, a second cell type can be aggregated around using a ring magnet [430] (Fig. 2.7G). Even without changing the magnet, sequential seeding can result in various layered anisotropies. Indeed, after magnetically labeled cells have aggregated around a magnet, consecutively flowing other cell types, one after the other, will create multiple layers. Asymmetrical core-shell structure can even be achieved by flowing cells towards the magnet in a specific direction[461]. When cells are consecutively seeded on top of the magnets, magnetic patterning can also create multilayered constructs. This made it possible to sandwich a layer of HUVECs between two layers of adipose derived stromal cells (Fig. 2.7H), which enhanced osteogenesis, as evidenced by increased ALP activity and mineralization[431]. A similar sequential seeding can be applied in a hollow cylindrical magnet, making it possible to engineer a multilayered anisotropic tubular tissue[300].

Magnetic forces can also be used in conjunction with other patterning or moulding techniques. These approaches provide geometrical guidance, while magnets can force cell aggregation[316]. For example, a magnetic cardiomyocyte- or myoblast-loaded gel can be cast into a well with a pillar at the center and a plain cylindrical magnet below the well. This will result in a hollow disk-shaped scaffold around the central pillar with a high cell density. As cells contract, the tissue will mature into a very thin ring around the pillar, which is even more densely cellularized[273,441]. However, magnetic moulding is not limited to the ring shape. Photolithography can generate magnetic PEGDA (polyethylene glycol diacrylate) polymer blocks with virtually any shape that can be used as moulds to guide cells while they are magnetically forced to aggregate into tissues with a specific shape, with a resolution of 150 µm. After removing the mould, a second cell-type can even be used to fill the space previously blocked by the mould[357]. Preferential cell adhesion can also be achieved using magnetic surface patterning instead of moulding. Indeed, PEG arms bound to magnetic particles can be magnetically patterned, repelling subsequent cell adhesion where the magnets were instead of

attracting them. Removing the PEG coating allows new cells to adhere where the first ones could not, enabling a co-culture system[464]. Although a broader range of architectures can be engineered with these combined approaches, they also raise significantly the level of technical complexity.

In order to only use magnetic forces to aggregate cells and still engineer intricate geometries, the structure of the magnetic gradient needs to be precisely controlled. One study used neodymium magnetic sheets cut-out in the desired shape[255], while others steered towards magnetizable patterns that showcase a higher resolution. For instance, placing a vertical thin steel plate between a magnet and a solution of magnetically labeled cells, drives cells to aggregate along the line of the edge[333]. These lines can be much more elongated than what would be achieved with a magnet, making it possible to engineer very thin vascular channels on top of homogeneously distributed non-magnetic muscles cells[439]. Although the steel plate is not magnetic on its own, when exposed to a magnetic field, it concentrates both the magnetic field and gradient, especially near edges, resulting in magnetic forces much higher than those near a magnet[46]. Creating magnetic patterns out of the edges of these steel plates can therefore enable many other types of magnetic anisotropic aggregations, such as the formations of letters out of cellular aggregates[432,439] (Fig. 2.7I). Magnetic templates can also be made with photolithography and NiFe electrodeposition, enabling the formation of high-resolution magnetic patterns for cell aggregation[46,465].

Compared to other patterning techniques, magnetic strategies dispense with the need to precisely controlling the geometry or surrounding environment of the cells or tissues, as is the case with 2D grooved[215] or chemically patterned[227] substrates, and 3D moulding techniques[224]. While the level of complexity of achieved structures is not yet on par with extrusion bioprinting[466], magnetic patterning holds the unique advantage to create complex structures solely out of cells, without the need for matrix. This could enable a better understanding of cell-cell interactions in 3D tissues, as well as highlight, through its absence, the role played by extracellular matrix. Moreover, matrix could always be added later, with the possibility to precisely control when and how to add it to the magnetically patterned tissues.

4. Assembling cellular building blocks with magnetic forces

Magnetic patterning is not limited to individual cells and can also assemble multiple magnetic microtissues or spheroids together (Fig. 2.7J, Table 2.3). Indeed, spheroids can first be made using conventional methods, like agarose wells[255], or magnetic aggregation[46,333]. Placing them on top of a magnetic pattern, whether it is a line, a ring or any other shape will result in the formation of a tissue with the desired shape[255,293,333,373,374]. After assembly, cellular remodeling usually leads to the fusion of these different building blocks into a cohesive tissue. The size of spheroids or microtissues is adjustable[46], and for the latter, even their shapes can be moulded[374,375]. In addition to more versatility of the internal microfeatures of the tissue, this enhances the 3D aspect of the tissue, often flatter when made with individual cells. Magnetic

labeling can also be performed during spheroid or microtissue formation[53,298]. Indeed, instead of labeling cells, magnetic nanoparticles can be mixed with matrix material, which becomes trapped between cells during their aggregation. However, since these objects are larger than cells, drag forces are higher, which can hinder the patterning process unless the system is regularly shaken[255]. Similar considerations are also at play when aligning biological modules along magnetic field lines within a hydrogel[46]. The shape and the distribution of magnetic nanoparticles is particularly important in magnetic alignment, as asymmetrical geometries will result in wave-like alignments of the microtissues[362].

Magnetic alignment and patterning aside, the assembly process can be achieved by magnetic manipulation. This can be done using a magnet to manually move the spheroids towards one another, sometimes aided with additional magnets to hold them in place together while they fuse[333] (Fig. 2.8A). This notably enabled the fusion of magnetic mesenchymal stem cell spheroids into cellular rods, which significantly increased cartilage functionalization. Indeed, expressions of collagen II and aggrecan, two of the main proteins in cartilage, were much higher in magnetically assembled constructs than in centrifuged pellets of the same size. In the case of magnetic sheets, a cylindrical magnet can also be used to easily roll the tissue into a tubular construct[257]. However, magnetic manipulation can be much more complex, allowing magnetic picking of individual spheroids that are then automatically placed at the desired positions[248,314], similar to spheroid pipetting techniques. One study used magnetic manipulation to engineer rings or pyramids out of alternating ventral or dorsal forebrain neural organoids, to replicate neural architecture. Tumor progression could even be modeled by assembling organoids from three different brain regions from the same patient, spanning from the origination site to metastasized tissue[314]. Multiple spheroids or microtissues can also be picked up at the same time. They will usually form a ball around the magnetic tip. Sequential picking without release results in anisotropic layered constructs[248,374].

Such layering and assembly can also be achieved through magnetic levitation (Fig. 2.8B). Indeed, just as individual cells can be magnetically levitated to form spheroids, so can spheroids be levitated to assemble larger tissues[53,58,293,329,375]. If different objects are successively levitated, it will result in multilayered tissues. Such magnetic levitation not only made it possible to assemble four layers of epithelial, smooth muscle, pulmonary fibroblasts and pulmonary endothelial cells, but it could also maintain the resulting tissue at the air-liquid interface[329]. These constructs notably displayed 3D regional differences specific to each cell type, such as collagen I mainly localized around the fibroblasts layer, and enhanced epithelial phenotypic markers compared to 2D and 3D monocultures. While similar to patterning, magnetic levitation is performed with magnets on top of the cell solution. Although this technique is much better to engineer 3D tissues, it requires higher forces to counteract gravity, making larger more magnetic microtissues or spheroids more appropriate building blocks. Moreover, without additional control, the most complex typically achievable structures are often ring shaped[58] (Fig. 2.8C). The density of the matrix of microtissues can be used to further control their levitation and therefore assembly[375]. Some studies have tried to use more intricate 3D systems of magnets to precisely control microtissues 3D assembly[334], even attempting it in

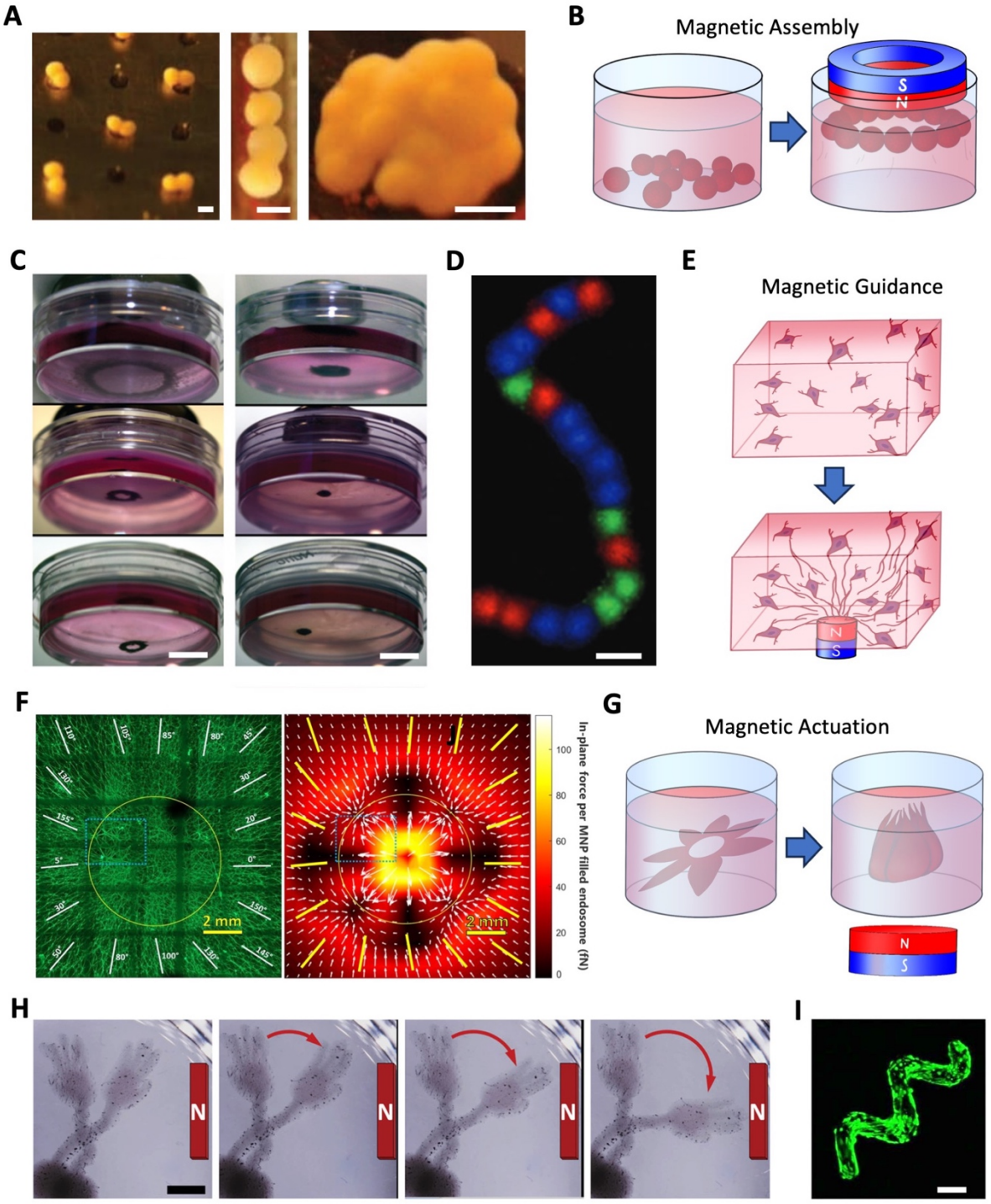

Figure 2.8. Magnetic assembly, guidance and actuation. *(A) Cellular constructs engineered by magnetically induced fusion of MSCs spheroids[333] (Scale bar = 1 mm). (B) Illustration of spheroid assembly by magnetic levitation. (C) Assembly of glioblastoma spheroids by magnetic levitation with a ring or a disk magnet[58] (Scale bar = 400 µm). (D) Assembly of a chain of spheroids made from three different cell types (labeled in red, green and blue) by magnetic levitation[376] (Scale bar = 100 µm). (E) Illustration of magnetic cell guidance. (F) Map of the neurite network orientation of magnetically labeled SH-SY5Y cells, compared to the map of the magnetic force field applied during culture[66]. (G) Illustration of a tissue folding by magnetic*

actuation. (H) Unpaired magnetic actuation of hand shaped magnetic hydrogels[458] (Scale bar = 1 cm). (I) Fibroblast loaded magnetic hydrogel micromotor [377] (Scale bar = 80 µm).

space to minimize the bias of gravity[53]. While the range of possible geometries remains limited, microtissues were still able to viably fuse together into anisotropic 3D cartilage tissues in these more advanced levitational systems. An approach to achieve other forms of magnetic levitation is to use a paramagnetic medium[375,376]. Increased control can also be obtained by restraining the environment of the levitating objects, making it possible to trap a queue of levitating spheroids made from different cells in a channel to induce their anisotropic fusion[376] (Fig. 2.8D). This strategy could notably be applied to study the structural and biomechanical properties of constructs made from human stem cells, brain cancer cells and breast cancer cells, which not only still proliferated after magnetic assembly, but also displayed typical phenotypic markers for each cell type. Although 3D magnetic levitation assembly remains challenging, it could lead to a truly 3D form of magnetic bioprinting where biological building blocks are levitated and positioned to form precisely defined geometries.

Setting aside the remote nature of the forces involved in magnetic assembly, this set of techniques could reduce the complexity of the manipulation usually necessary when assembling non-magnetic cellular building blocks. Magnetic forces can provide a more gentle and controlled handling of the modules that otherwise have to be aspirated[222], woven [296] or extruded [223], with the possibility to turn down or even off the magnetic field if necessary. Moreover, the idea of collectively assembling tissues in a single step with the right magnetic field, as illustrated by magnetic levitation approaches[53,58,293,329,375], could greatly diminish the complexity of the experimental process. Experiments in space[53] even showed that it was possible to automate this process to some extent in less favorable experimental conditions, by simply letting spheroids assemble in the desired magnetic field with minimal outside manipulation.

5. Stimulating and moving tissues with magnetic actuation

In the various approaches so far, magnetic cells and tissues have been presented primarily as objects manipulated by physical forces. However, even after a scaffold has polymerized and the cells positions are set within it, magnetic forces can influence cell migration and behavior (Fig. 2.8E, Table 2.3).

Within a polymerized matrix, neurons labeled with magnetic nanoparticles tend to extend neurites and migrate towards magnets, leading to the formation of anisotropic neural tissue[47,449] Schwann cells and astrocytes, that usually do not mix with one another, can even be made to intermingle under such magnetic cues[449]. Magnetic guidance was proven to be effective over areas larger than 1cm^2, even with forces as low as 10 fN per magnetic nanoparticle-loaded endosome. Using multiple magnets could even make it possible to further control the neural network, as neuroclusters would localize where magnetic forces would converge[66] (Fig. 2.8F). Similar increases in migration and proliferation towards magnets can also be observed with

stem cells or endothelial cells, promoting the radial vascularization of tubular constructs[445,446]. While magnetic forces are applied on cells, they do not directly displace cells firmly attached to a substrate or matrix. However, magnetic forces act on magnetic endosomes within the cells, which will trigger mechanotransduction pathways, therefore favoring cell motility in a specific direction[436].

Similar mechanotransduction cues can also be achieved through the actuation of magnetic matrices. Indeed, magnetic forces can pull on a magnetic scaffold and consequently stretch it, which can favor muscle cell alignment in the stretching direction, as well as promote their differentiation[279,438]. On the other hand, tissues meant to resist anisotropic compression, such as bones, show improved differentiation under magnetic compression, achieved by placing a magnet under a magnetic scaffold[450–452]. Magnetic stimulation of the matrix alters focal adhesion, which can activate integrin signaling pathways in osteoblasts, resulting in improved osteogenesis markers such as increased alkaline phosphatase activity and mineralization. Cyclic magnetic pressure can be applied to tissues that endure dynamic loads *in vivo*, such as cartilage scaffolds displaying better chondrogenesis under an oscillatory magnetic field than a static one[453,454]. Such cyclic magnetic actuation can also deform membranes. For instance, a suspended thin magnetic hydrogel layer seeded with cells can alternate between a flat and a curved configuration under magnetic forces to reproduce cartilage *in vivo* stresses[454,455]. Pre-conditioning can even result in membranes that fold into wave like patterns under magnetic forces, in order to reproduce the regular dilation of epithelial lung tissues[331].

Indeed, in addition to temporal variations of the stimulation, spatial heterogeneity further reinforces the anisotropy of the tissue. For instance, applying a magnetic field to a bioprinted scaffold with alternating magnetic and non-magnetic bioinks results in a layered anisotropy of the stress field[467]. Stiffness gradients can also be engineered in magnetorheological elastomers, which can stiffen under magnetic forces, simply due to the progressive decrease of the intensity of the magnetic field with the distance from the magnet. This makes it possible to model the dispersion of the fibrotic reaction of cardiac fibroblasts during an infarct, localized at the site of the magnet, and to observe the spatiotemporal entanglement of the fibrotic response[440]. Such magnetic stiffening is also impacted by the orientation of the magnetic objects within the matrix. Indeed, when exposing a matrix to a magnetic field, if the magnetic rods within are pre-aligned with the field lines, the matrix can become three times stiffer than with unaligned rods[457]. Aligned magnetic objects in a scaffold will also heat more if they are parallel to the alternating magnetic field, making it possible to create an anisotropic response to magnetothermal stimulation[468].

The impact of the alignment of magnetic microfeatures can also be used for directed movement of shape morphing hydrogels (Fig. 2.8G, Table 2.3). For instance, a cell loaded matrix shaped like a hand will bend towards a magnet if the magnetic nanoparticles were previously aligned, whereas it will not be affected if the particles are isotropic[458] (Fig. 2.8H). Such precise magnetic actuation of biological constructs opens up many possibilities for the creation of biological robots, cell loaded gels engineered to achieve specific movements. In addition to mechanical stimulation, these movements are meant to grant these living constructs

with a specific function. With the right geometry they can bend in order to stroke[469], morph into a more compact shape[437,470], or even assemble on demand[290]. These soft robots are usually designed to be remotely guided towards a specific location, with movement within the human body usually in mind. Once a hydrogel robot has reached its goal, the cells it contains can proliferate, mature and intermingle with native tissues for biomedical purposes, such as a magnetic helical micromotor loaded with cells, capable of moving through tubes for vascular repair[377] (Fig. 2.8I).

As we have already highlighted, the key feature of magnetic approaches is the possibility for remote actuation. Once 3D tissues are formed, stimulation is very limited and is usually mostly possible via mechanical stimulation[309] that impacts the whole tissue. Magnetic forces can remotely stimulate magnetically labeled cells or components, even at the core of the tissue, making it possible to guide their movements in complex fashions[66] and apply varied mechanical cues throughout culture time[440], even after implantation, which most other approaches cannot achieve. Moreover, with the emergence of 4D bioprinting, control over tissue movement and actuation over time is essential and has mostly been achieved so far only via magnetic-based strategies[437,470].

V. Conclusion

Anisotropy is a defining feature of many native tissues, from the aligned fibers of cardiac and skeletal muscle to the directional vascularization of engineered constructs. While anisotropy is not limited to skeletal muscles, they represent the most prominent anisotropic tissues in the human body. Their anisotropy, which stems from their alignment and fusion during myogenesis, enables the coordinated contraction of all their sarcomeres.

To engineer skeletal muscle or any other anisotropic tissue, understanding their specific architecture is essential. Replicating such complexity *in vitro* remains a major challenge in tissue engineering. In this review, we explored how various strategies, particularly those leveraging magnetism, can be used to induce and control anisotropy in engineered tissues. Starting from 2D substrates, tissue engineering approaches have progressively gained in complexity using microfabrication and assembly techniques, eventually leading to the more recent rise of bioprinting. We then focused on magnetic approaches, highlighting how magnetic nanoparticles, field-aligned assemblies, patterning techniques, and programmable actuation can guide cellular organization, shape morphogenesis, and tissue maturation. We discussed how these tools not only enable precise control over spatial architecture but also open new possibilities for dynamic stimulation, biohybrid robotics, and regenerative medicine.

The three studies that follow are grounded in this scientific context and build upon both the structural and magnetic tissue engineering strategies discussed in this chapter. They advance the complexity of magnetic alignment, assembly, bioprinting and actuation. These developments have facilitated the engineering of skeletal muscle tissue and enabled investigation into the intricate interplay between geometrical and mechanical cues in myogenesis, and more broadly in morphogenesis. By leveraging the potential of magnetic-based approaches, these studies further reveal their considerable capacity for anisotropic tissue engineering and advocate for a more prominent role for such methods in biomedical and biophysical research.

Chapter 3

Remote magnetic microengineering and alignment of spheroids into 3D cellular fibers

Context and motivations

Like most tissue engineering platforms previously discussed, the first research study presented in **Chapter 3** relies on a cell laden scaffold. The originality of this approach stems from the combination of magnetic alignment and assembly techniques. They enable remote actuation of cells and spheroids, thereby allowing the engineering of skeletal muscle tissue with a wide variety of anisotropic structures. Moreover, this first study introduces many techniques and results on which the following two studies build upon.

Indeed, since all three studies rely on magnetically labeled cells, maximizing the amount of internalized iron is an essential first step to optimize any form of magnetic manipulation. This requires quantifying iron uptake under various labeling conditions, which is possible thanks to magnetophoresis techniques previously developed within our lab[422,448,471]. While increasing the duration or the concentration of the magnetic labeling results in improved internalization, there are usually limits that are also cell type dependent[419]. Moreover, extreme nanoparticles incubations can impact the cells metabolic activity, viability and even function. Not only are the best parameters for magnetic labeling of myoblasts investigated at the very start of this study, but we also present an original sequential strategy that achieves significantly higher intracellular iron levels without affecting myoblasts metabolic activity nor their myogenic fusion. This lays the groundwork for all forms of magnetic labeling throughout this manuscript.

Once sufficiently magnetized, the muscle precursor cells can be aligned using magnetic fields. This was inspired by a previous study to align magnetically labeled cardiac cells within fibrin hydrogels[412]. That study showed that magnetically induced cell chains could be formed over variable lengths, depending on cell density and magnetization levels, while preserving contractile function and cardiac markers. Since alignment is essential for muscle precursor cell fusion, we adapted this method to skeletal muscle, anticipating that aligned myoblasts chains would fuse into mature fibers.

The effect of alignment on muscle maturation was notably evidenced in one our past studies, on which we also base our expertise on muscle tissue engineering. There, a microfluidic chip was designed to have a central reservoir filled with collagen in which channels were moulded with removable needles[224]. These channels were then filled with myoblasts using a pressure controller, and then the tubular geometric constraint would induce aligned fusion. However, it was a long and tedious process to seed each channel, whereas magnetic alignment simultaneously forms a multitude of aligned structures independently of the scale of the samples.

As we will see, magnetic alignment is not limited to individual cells and can also be applied to spheroids. Those were made through magnetic patterning, leveraging the magnetic properties of the cells to their full extent. Magnetic spheroid formation is often based on magnetic levitation[58], or using small magnets or magnetized tips below the cell culture medium [333]. However, the resulting spheroids are often quite large, at least a few hundred microns. Here

we use NiFe patterns, originally used to create magnetic tweezers within a microfluidic chip[465], to aggregate the cells into much smaller spheroids. These patterns are central to the magnetic bioprinting techniques presented in the next two chapters, which rely heavily on the high control we can have over the shape of these patterns. However, in this study their main advantage is the possibility to engineer them at high number and density within a very small surface. This is essential to create enough biological building blocks.

This magnetic assembly relies on magnetic alignment, previously applied mostly to individual cells[412,456,459] or cell loaded magnetic microgels[362], when it comes to cellular structures. Aligning magnetic spheroids not only represents a new variation of these magnetic tools but also enables control over the size of the aligned objects without needing to form microgels. Although previous approaches did assemble spheroids into lines, the scale was often limited as they required precise magnetic positioning of each spheroid[248,314,333]. Remote magnetic alignment aims to alleviate this process, while making it possible to engineer muscle tissues with a wide variety of possible anisotropic structures.

This specific context led to the study detailed in the remainder of this chapter, originally published in *Advanced Functional Materials* in August 2022[46]. **Chapter 3** has been adapted from that publication.

Abstract

Developing *in vitro* models that recapitulate the *in vivo* organization of living cells in a 3D microenvironment is one of the current challenges in the field of tissue engineering, in particular for anisotropic tissues where alignment of precursor cells is required for them to create functional structures. Herein, we propose a new method that allows alignment in the direction of a uniform magnetic field both individual cells (muscle, stromal and stem cells) or spheroids in a thermoresponsive collagen hydrogel. In an all-in-one approach, spheroids are generated at high throughput by magnetic engineering using microfabricated micromagnets and are used as building blocks to create 3D anisotropic tissue structures of different scales. The magnetic cells and spheroids alignment process is optimized in terms of magnetic cell labeling, concentration, and size. Anisotropic structures are induced to form fibers in the direction of the magnetic alignment, with the respective roles of the magnetic field, mechanical stretching of the hydrogel or co-culture of the aligned cells with non-magnetic stromal cells, being investigated. Over days, spheroids fuse into 3D tubular structures, oriented in the direction of the magnetic alignment. Moreover, in the case of the muscle cells model, multinucleated cells can be observed within the fibers.

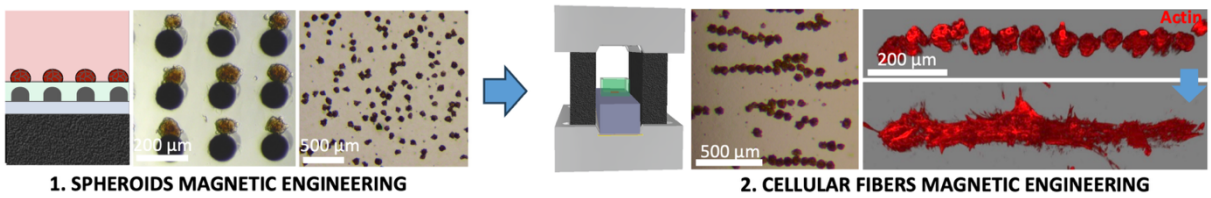

Visual table of contents of Chapter 3

I. Introduction

In various research fields including life sciences, translational research and clinics, the development of *in vitro* cell culture models that faithfully recapitulate *in vivo* complexity remains a cornerstone. It is now admitted that 2D cell culture approaches differ from physiological or pathophysiological conditions in particular regarding cell-cell and cell-matrix interactions. In this context, organ-on-chip technology has emerged as a solution to mimic *in vivo* complexity, and to offer control of the cellular microenvironment. More specifically, these micro-physiological systems offer the possibility to co-culture different cell types in 3D extracellular matrix to recapitulate organ features and functions as best as possible. Over the past decade, the field of organs-on-chips has markedly expanded, with various technological approaches being proposed to recapitulate many different organs in microfluidic devices[472]. These micro-devices offer an unprecedented level of control, provide a unique opportunity to better understand how function and structure are intimately linked, and can focus on a single organ or even mimic organisms with multi-organ platforms[37,383,473–475]. Yet, they rely mostly on 3D scaffold to self-organize cells within. There is now a need to better control cell positioning in on-chip 3D extracellular matrix to better mimic *in vivo* 3D tissue organization.

For instance, one hallmark of muscle tissue is the spatial alignment of the component cells. The parallel arrangement of cardiomyocytes or skeletal muscle myofibers is necessary for efficient electromechanical coupling, electrical anisotropy and directional contractile force generation[476–481]. Bioengineered muscle constructs must therefore contain muscle cells densely packed in a 3D structure, and amenable to alignment with one another in a preferential direction[25,258,482]. Most attempts to align muscle cells [228,229,483] have been achieved by taking advantage of the substrate anisotropy and/or topography[228,229,483], for example, using nanofibers[484–486] or micropatterning[487,488]. Cell alignment within a 3D engineered tissue construct remains a challenge. One solution consisted of orienting muscle cells by anchoring them between two posts that guide 3D cell alignment[263,270,489–493].

To orient cells within a 3D scaffold, one possibility is to manipulate them remotely to make them interact and self-organize. To achieve this, magnetic forces acting at a distance are appealing candidates, provided the cells are first rendered magnetic. The idea is then to take advantage of magnetic nanoparticles (NPs), already exploited for theranostics applications as contrast agents for magnetic resonance imaging or as heat mediators in photothermal or/and magnetic hyperthermia therapies[494–497]. The strategy of using cells loaded with magnetic nanoparticles for cell manipulation and tissue engineering is more recent[498,499]. It was initially pioneered with the concept of magnetic sheet engineering[52,500,501], allowing tissue formation via successive cell layering in the presence of a magnetic field gradient. Magnetic forces have next been further exploited for controlled tissue assembly[58], to create cell spheroids[250,251,502], towards 3D tissue engineered structures[53,60,333,503,504], with the possibility for in situ magneto-mechanical stimulation[56,505,506].

Among the existing methods for 3D cell culture, one of the most popular approaches remains spheroids. Spheroids offer multiple advantages as they allow high cell cohesion and

facilitate handling of the cell constructs with conventional equipment. Though often advantageous, spheroids do not offer the same level of complexity as *in vivo* tissue in terms of spatial organization, and do not allow the implementation of external forces or tissue deformation. In recent studies, spheroids have been used as building blocks to recreate complex *in vivo*-like structural organization[507–512]. Many of these methods rely on bioprinting, where the spheroids are mixed with a hydrogel scaffold to make a bioink, which is then extruded on a surface before polymerization[513–516]. Most current spheroids production methods, including the magnetic-based ones, still suffer from poor spatial control over spheroids, from large diameter over 100 µm , or/and from low number of spheroids produced.

In this context[18], we propose a multiscale magnetic approach for anisotropic tissue engineering, that is based on the high-throughput production of size-controlled magnetic spheroids with diameters in the 50-100 µm range.

Based on an optimized cell labeling protocol by iron-oxide NPs, we started by developing a magnetic method to form size-controlled spheroids using magnetic micro-patterns. We then exploited the magnetic dipolar forces created in between magnetic individual cells or spheroids by a uniform magnetic field to act as a “compass” and create preferential alignment of either single cells or spheroids. This magnetic alignment was achieved in a 3D scaffold made of a mixture of collagen I and Matrigel, that could additionally be mechanically stretched thanks to a specific microfluidic chip design or co-cultured with stromal cells. The method was initially developed using muscle cells, leading to the formation of cohesive muscle cell fibers, but was also demonstrated to work with stromal and mesenchymal stem cells, illustrating its versatility.

II. Results and Discussion

1. Internalization of magnetic nanoparticles (NPs) in cells

The cellular magnetic labeling was developed with muscle C2C12 cells, using citrate-coated iron oxide NPs (8 nm in diameter). These negatively charged nanoparticles are internalized in cells following the endocytotic pathway, and concentrate within endosomes, where they are slowly degraded over time, while the iron released is stored within ferritin[254,417,517]. Although the properties of these magnetic nanoparticles are not identical in solution and when stored within the cells, most of the properties essential for subsequent magnetic manipulation, notably their magnetization curve[518] or their hydrodynamic size[519], remain unchanged, over the duration of the labeling procedures. Moreover, the presence of citrate in RPMI labeling solution prevents protein aggregation and ensures nanoparticle stability. Herein, different magnetic labeling conditions were investigated with the goal to determine non-harmful conditions with high intracellular magnetic NPs content. This was done by varying iron concentration (ranging from 1 to 32 mM) and incubation time (from 15 min to 16 h). The amount of NPs internalized by cells was assessed by single cell magnetophoresis while the effect of NP internalization on cell viability was measured by resazurin-based metabolic test.

As expected, cells internalized more NPs when increasing incubation time or NP concentration in the labeling solution (Fig. 3.1). For a magnetic labeling performed at a constant iron concentration of 2 mM and by varying incubation time, we observed a saturation reached for incubations longer than 4 hours (Fig. 3.1A). Similarly, at a given incubation time of 30 min, the NPs internalization increases with the iron concentration and rapidly reaches a plateau above 8 mM (Fig. 3.1B). Interestingly, cell viability was reduced in a dose dependent manner (Fig. 3.1A-B), either for incubation times longer than 2h (at 2 mM of iron) or for iron concentrations above 8 mM (30 min duration). These results suggest that the maximum level of NPs internalized by cells without impacting cells metabolic activity is about 10 pg per cell. To further increase this level, we developed and evaluated the potential of a multistep sequential labeling (Fig. 3.1C): C2C12 cells were incubated for 30 min with 2 mM of iron on consecutive days, with one incubation a day, with up to 3 days of incubation (referred to as NP1, NP2 and NP3 according to the number of consecutive incubations). This sequential magnetic labeling allowed internalizing twice or three times as much NPs per cell as with single step labeling procedures, while perfectly preserving the cells metabolic activity. Altogether, these results evidenced that the use of sequential magnetic labeling provides the cells with high NPs internalization, in the range of 20 pg of iron per cell without impacting cells metabolic activity. This suggests that rather than the overall amount of iron internalized, it is the internalization rate that has more impact on the cells metabolic activity. In addition to the metabolic activity assays, the impact of the NP1, NP2 and NP3 labeling conditions on cell viability was tested using a LIVE/DEAD assay. The proportion of dead cells was 0.7 ± 0.5% for the non-labeled control cells, and was found at 0.9 ± 0.8%, 1 ± 0.6%, and 0.5 ± 0.3% (n=3) for NP1, NP2, and NP3 labeling conditions, respectively, showing no significant impact on cell viability. Next step was to investigate the NP3 high content magnetic labeling on the muscle cells differentiation.

To do so, magnetically labeled cells were grown in 2D cell culture in a medium promoting differentiation. Cell differentiation was evidenced by histological, confocal, and electron microscopy imaging, characterized by the fusion of several muscle precursor cells into myotubes[520]. Figures 3.1D-H show that after 8 days of culture magnetically labeled cells fuse to form large myofibers. In addition, both the histological (Perls) and electron microscopy imaging localize the NPs inside the cells, within endosomes, either right after labeling (day 0) or after the differentiation process (day 8 or day 12). All observations converge towards the presence of multinucleated cells, that are clearly detected by confocal (Fig. 3.1F) or electron microscopy imaging (Fig. 3.1H), confirming qualitatively that the magnetic labeling of muscle cells does not impede the first stages of their differentiation. Further investigations would require to evaluate quantitatively the impact of nanoparticles on muscle differentiation by real-time qPCR.

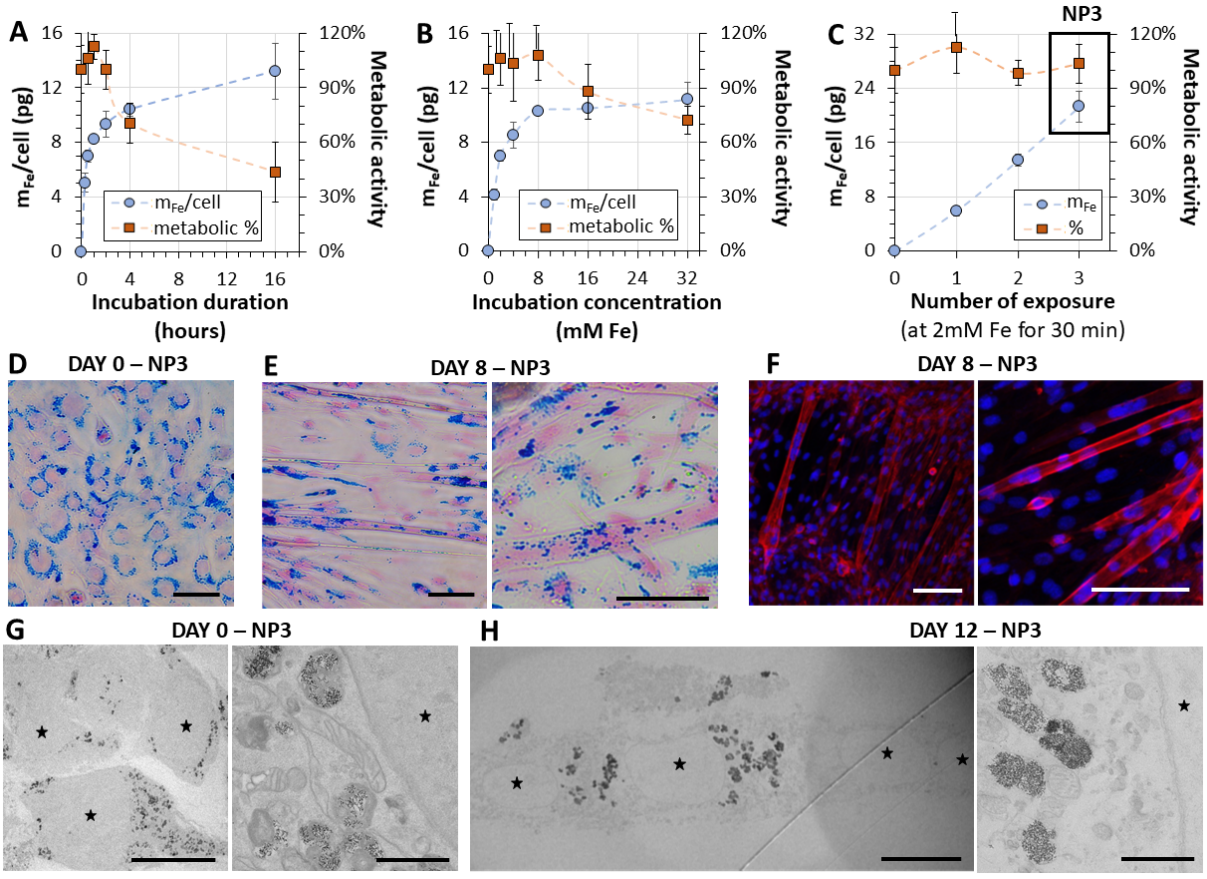

Figure 3.1. Optimizing magnetic nanoparticles internalization by myoblasts. *(A-C) Quantification of magnetic nanoparticles internalization in cells measured by magnetophoresis and cell metabolic activity after labeling measured with Alamar Blue reagent. (A) Incubation at [Fe] = 2 mM for durations ranging from 15mn to 16h, (B) Incubation for 30 min with concentration of iron ranging from 1 to 32 mM, (C) Incubation at 2 mM for 30 min, once a day, for 1 (NP1 labeling), 2 (NP2 labeling) or 3 (NP3 labeling) consecutive days. Magnetophoresis was performed on 200 cells per condition and data are shown as the mean ± standard deviation*

(SD). (D) Perls iron blue staining counterstained with Nuclear fast red, for cells labeled in NP3 condition, right after labeling (day 0). (E) Perls staining of cells after 8 days of differentiation (2D cell culture). (Scale bars = 100 µm) (F) Confocal imaging of cells after 8 days of differentiation, with the actin stained in red and nuclei in blue. (Scale bars = 100 µm) (G,H) Transmission electron microscopy of cells labeled with NP3, (G) after labeling on day 0 or (H) left differentiating on a 2D surface for 12 days, which shows endosomes filled with nanoparticles in both cases and cells with several nuclei (each nucleus is indicated with a star) upon differentiation. (Scale bars = 10 µm (left image) and 1 µm (right image))

2. Magnetic field configuration for magnetic cell alignment in 3D microenvironment

To further develop a muscle-on-chip model based on magnetic cell positioning, we investigated how magnetic forces can be exploited to align on chip magnetized cells in a 3D hydrogel scaffold serving as an extracellular matrix (ECM). The principle of magnetic alignment is illustrated in Figure 3.2. Collagen I being the most abundant protein of muscle ECM, a mixture of collagen I (2 $mg.mL^{-1}$) and Matrigel (10% v/v) was used to provide cells with a 3D scaffold. This scaffold solution was mixed with the magnetically labeled cells and poured into a glutaraldehyde treated PDMS chip. The glutaraldehyde treatment was necessary to covalently graft collagen to PDMS, preventing collagen detachment due to forces exerted by muscle cells. To study cell response to a magnetic field in a 3D hydrogel, the chips were placed in between two magnets for 30 min at 37 °C, to trigger cell alignment before hydrogel polymerization (Fig. 3.2A). Such an alignment is supposed to happen due to magnetic dipole interactions between magnetized cells, each one holding a magnetic moment in the presence and direction of an applied magnetic field.

Magnetic cell alignment yet necessitates an optimized magnetic configuration developing a perfectly uniform magnetic field. Indeed, the challenge here is to avoid any magnetic field gradient that would generate a magnetophoretic mobility of the cells within the chips. To achieve a strong yet uniform magnetic field, the simplest configuration is to face two magnets symmetrically (Fig. 3.2B). The two magnets inter-distance was adjusted using finite-element simulations to minimize the magnetic field gradient in the chamber and avoid magnetic attraction of the cells towards the magnets. As expected, the symmetrical magnets configuration generates a magnetic field with lines perpendicular to the direction of the magnets (Fig. 3.2B). The optimal distance between the magnets that minimizes the magnetic field gradient is achieved at 3.6 cm (Fig. 3.2C). This 3.6 cm inter-magnet distance and a 10 cm one were experimentally tested for magnetic cells alignment. Figure 3.2D shows that for a distance of 10 cm, even if remarkably aligned, the magnetic cells are not homogeneously distributed along the y-axis of the chamber, most of them migrating towards one of the magnets, which confirms the presence of a magnetic field gradient. In contrast, when using the optimal inter-distance of 3.6 cm, magnetic cells are both aligned along the magnetic field lines and homogeneously distributed along the y-axis (Fig. 3.2E). In this configuration and considering that nanoparticle

saturation above 150 mT[518] is reached between the two magnets, the average dipole/dipole force that attracts cells together and make them align is around 25 pN between two cells in contact labeled with NP3. For both conditions, the chips were left for 30 min at 37 °C within the magnets, allowing the hydrogel to fully polymerize. After polymerization, the cells can no longer move freely in the gel and are trapped in this aligned configuration, even when removed from the magnets, and then the chip is filled with medium promoting differentiation.

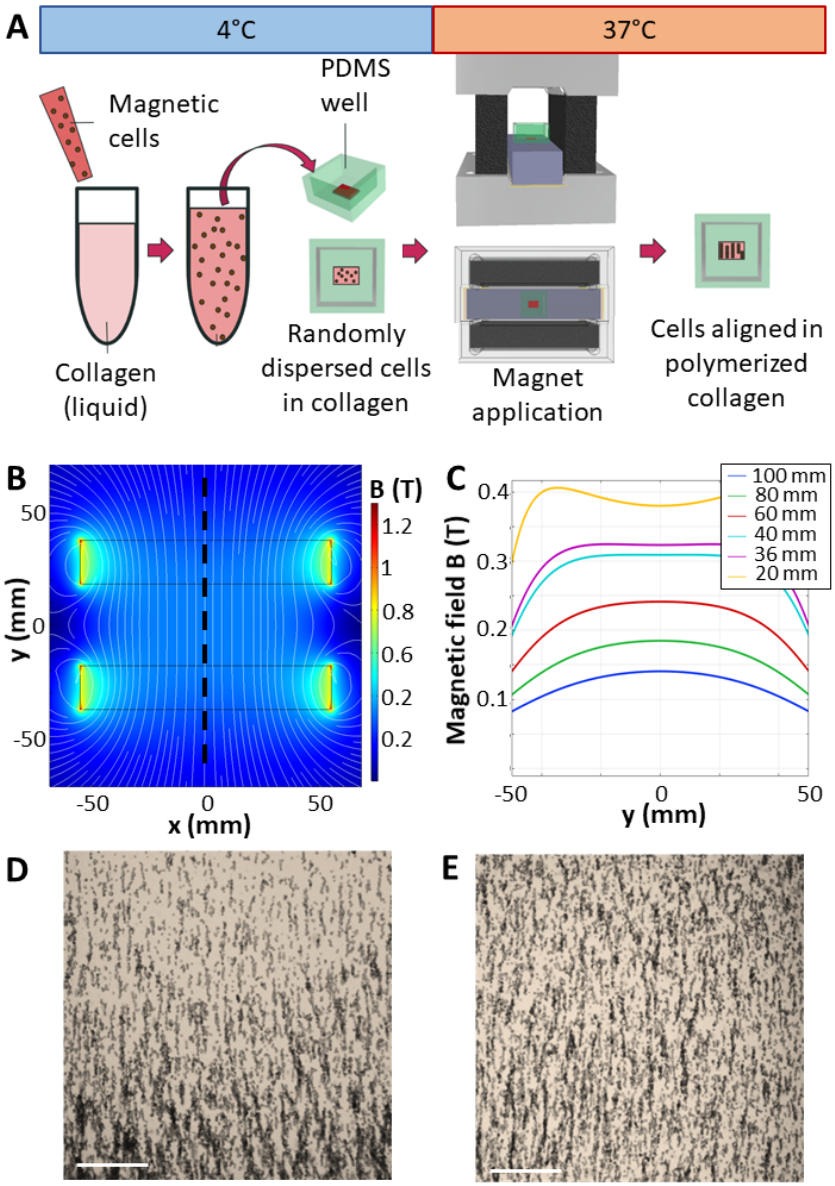

Figure 3.2. Aligning cells in a uniform magnetic field. *(A) Illustration of the alignment procedure and set-up. (B) Finite elements simulations (COMSOL) of the magnetic field over the z-slice (z=0) passing through the center of the magnets when they are spaced with 3.6 cm. (C) Magnetic field over the line (z=x=0) that passes through both magnets' center (in dashes in (B)) for distances between the magnets ranging from 10 to 2 cm. (D) Image of magnetic cell alignment when the magnets are 10 cm apart and the gradient is not optimized showing cells*

attracted towards the magnets. (E) Images of the magnetic cell alignment when the gradient is optimized with magnets 3.6 cm apart, showing cells chains uniformly distributed. (Scale bars = 200 µm). The direction of the magnetic field lines (and subsequent cell alignment) is from top to bottom in ***Chapter 3****.*

3. Magnetic cell alignment varies with cell labeling and concentration

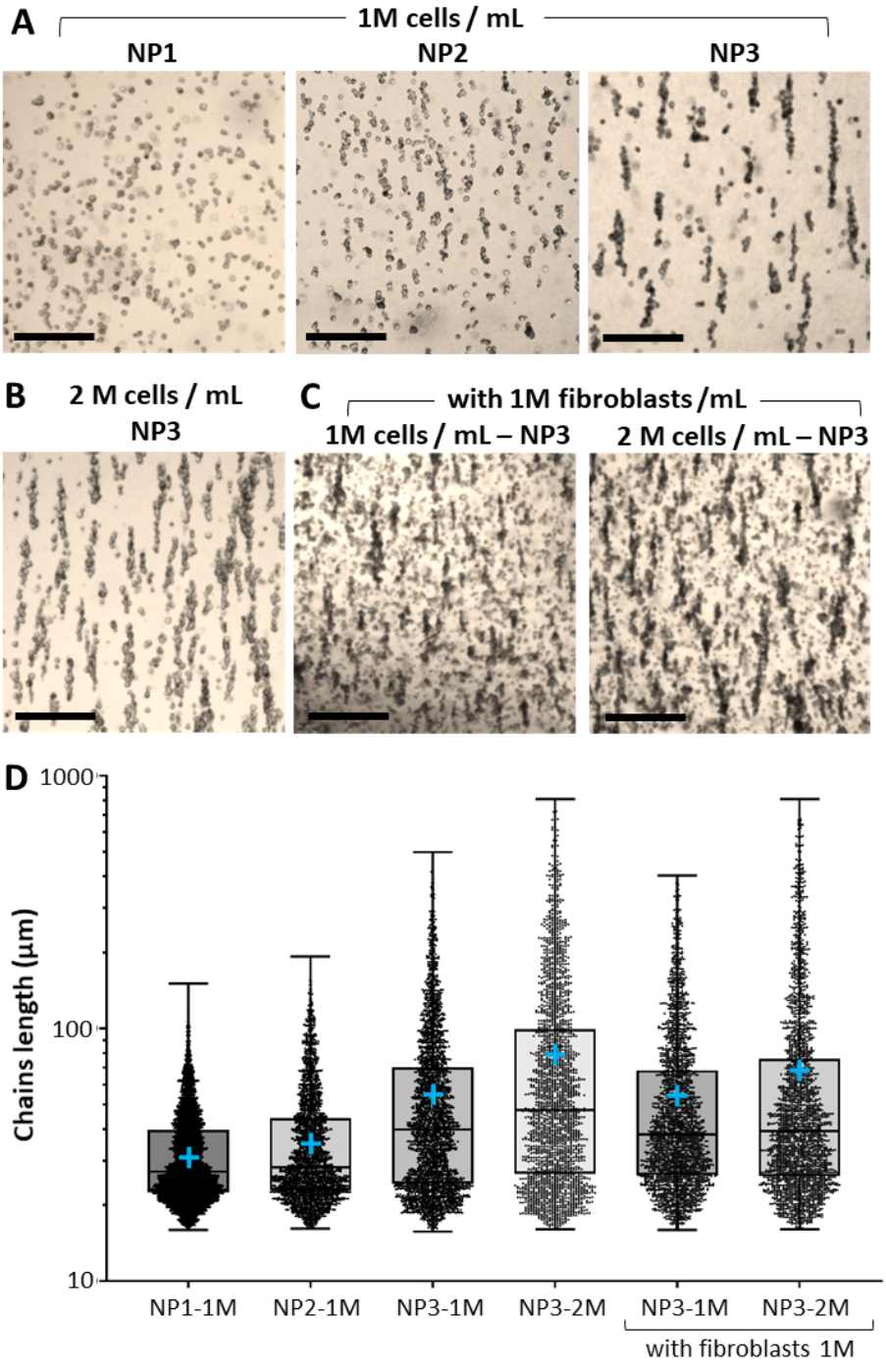

Figure 3.3. Impact of the magnetic labeling, the cell concentration and co-culture on cell chain length. *(A) Images of cells labeled with NP1, NP2 and NP3 and aligned in hydrogel at a concentration of 1 million (1M) cells per mL. (B) Cells labeled with NP3 and aligned at a concentration of 2 million (2M) cells per mL. (C) Cells labeled with NP3 and aligned in hydrogel with 1 million per mL fibroblasts at concentrations of 1 and 2 million per mL magnetic muscle cells. (D) Boxplots of the distributions of chain length for the 6 conditions, showing that the more labeled and the more concentrated the cells are, the longer the cell chains become. Data were obtained over three distinct experiments per condition, with overall more than 2000 chain lengths measured. (Scale bars = 200 µm)*

Using this magnetic alignment approach, we were able to form chains made of cells with length ranging from a few tens to hundreds of micrometers (Fig. 3.3). Figure 3.3A shows the effect of cell magnetization on cell alignment. The three labeling protocols - NP1, NP2 and NP3 - were used, consisting of respectively one, two or three consecutive days of cell labeling with an iron concentration of 2 mM during 30 min, and leading to an iron content ranging from 7 pg per cell (NP1) to 20 pg per cell (NP3). Magnetically labeled cells were then seeded in the hydrogel solution at a concentration of 1 million cells per mL, poured at 4 °C in the PDMS chips, and rapidly subjected to the magnetic field at 37 °C to induce gel polymerization. Figure 3.3A evidences that for the lower iron content per cell (NP1) cells are barely aligned while for the higher (NP3) most of the cells are organized within distinctive chains. This simply mirrors the balance of forces (drag force against dipole-dipole force) experienced by the cells, magnetic dipole-dipole force being proportional to the magnetic cell moment squared, and thus to the quantity of magnetic material within cells (squared as well). As a result, the chain length increases significantly with iron loading, with average values of 59 ± 2 µm, 72 ± 3.5 µm, and 104 ± 12.8 µm for NP1, NP2, and NP3 labeling conditions, respectively (Fig. 3.3D).

The effect of the initial cell concentration on chain formation was next investigated (Fig. 3.3B). As the dipole-dipole force decreases proportionally with the distance between the dipoles to the power of 4, we can expect the distance between cells, and therefore the cell concentration, to be a critical parameter for chain formation. The results show that doubling the cell concentration to 2 million cells/mL with NP3 labeling leads to an increase of the average chain length from 104 ± 12.8 µm to 142.8 ± 8.2 µm (Fig. 3.3D).

The ECM of a skeletal muscle is a dynamic structure which is continuously remodeled by muscle cells but also by stromal cells and in particular fibroblasts, which also play an important role in myogenesis[521,522]. This complexity must be considered when developing a 3D muscle tissue on chip. To recapitulate this feature, it was important to verify that magnetic alignment could still be achieved in the presence of non-magnetic fibroblasts. Fibroblasts were mixed with the magnetically labeled muscle cells before seeding on the chip. Figure 3.3C illustrates this co-culture condition, with one cell type (muscle cells) organized anisotropically and the other (fibroblasts) randomly dispersed within the gel. The presence of fibroblasts does not impede muscle cell chain formation but slightly decreases the average value of the chain length, to 93.7

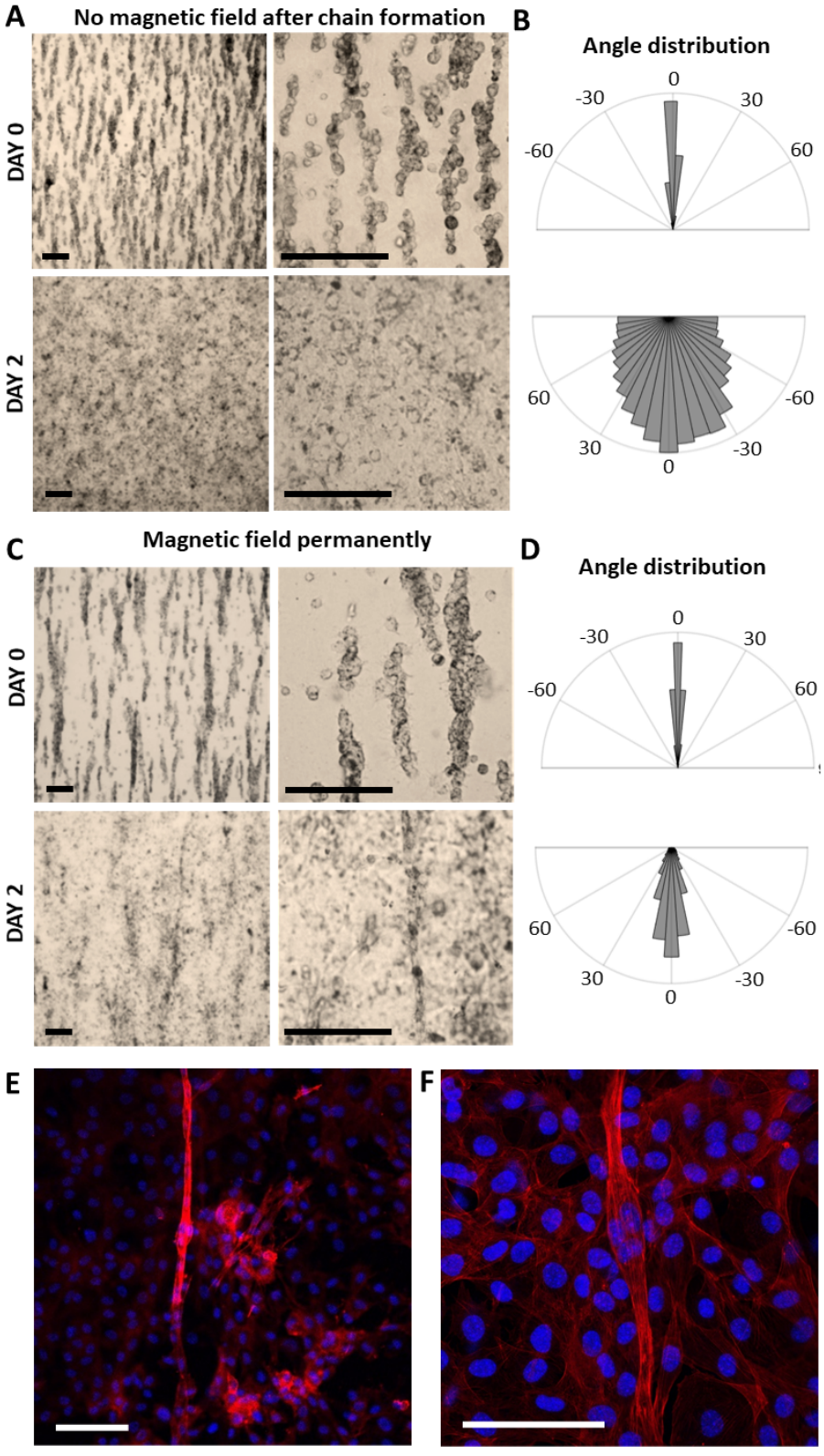

Figure 3.4. Evolution of the directionality of cell chains over time. *(A,B) Condition without magnetic field and (C, D) condition where the chips were kept between the magnets during the whole observation time. (A, C) Images of the cell chains at day 0 and day 2 after cell chain formation. (B,D) Angle distribution within the samples at day 0 and day 2 after cell chain formation. Angle distribution was measured throughout time on 3 distinct samples for each*

condition. (E,F) Confocal images of samples kept between the magnets all the time; actin stained in red and nuclei in blue, after 8 days of differentiation. (Scale bars = 100 µm)

± 12.8 µm (respective to 104 µm without fibroblast) and 128.2 ± 20.6 µm (142.8 µm without fibroblasts), for 1 million and 2 million muscle cells per mL, respectively (Fig. 3.3D). The 3D magnetic alignment approach can therefore accommodate and co-culture different cell types, both magnetic and non-magnetic, while preserving cell alignment. All conditions are represented in Figure 3.3D, as boxplots including all chains analyzed (over 2000). It clearly shows an important dispersion of the chain length distribution, with an average polydispersity of 0.9 ± 0.3 over all conditions.

4. Magnetic cell alignment fades over culture time

We next examined how the cells alignment evolved with time. Already after only one day of culture, muscle cells start colonizing the gel and progressively lose alignment. It is shown in Figure 3.4, within two days of culture, by typical brightfield images, and analysis of the distribution of cell chain angles. In Figures 3.4A-B, anisotropy is no longer present, with an almost homogeneous distribution of the angles after two days of culture. To try to preserve this anisotropy, and further promote cell fusion in the chain direction, the chips were maintained in between the magnets during the whole culture (Fig. 3.4C). While many cells were still escaping chaining, the magnetic field partially preserved some cell alignment, with a narrower angle distribution (Fig. 3.4D). After 8 days of culture in differentiation medium, the few cells that maintained their alignment were able to fuse and generate myotubes (Fig. 3.4E-F). Overall, these results showed that the magnetic alignment of individual cells for short or extended periods of time is not sufficient to maintain the anisotropy over time, although some cell fusion events can be observed to a limited extent when the magnetic field is maintained all the time.

5. High-throughput production of magnetic spheroids using micropatterned NiFe attractors

To avoid the almost total loss of anisotropy in the first-aligned muscle cells on chip, we proposed to redesign the alignment method starting with magnetic spheroids instead of individual cells. Indeed, we hypothesize that (i) spheroids provide high cell density and cohesion, that should promote cell-cell interaction and differentiation; (ii) cells being initially trapped within the spheroid, it should prevent the presence of single cells between the chains that would arrange with a random cell density and orientation; and (iii) once aligned one to the other, the spheroids chain already form a pre-muscle structure with the diameter of a myofiber.

Many methods allow producing spheroids including hanging drop arrays, ultra-low attachment wells or magnetic attraction[250–253,523,524]. Most of these methods for making

spheroids, whether they are magnetic or not, generate at most a few hundreds of spheroids, usually larger than 100 µm, and require at least one day of incubation. However, magnetic alignment would actually require several thousand spheroids, and they should not be much larger than the diameter of a myofiber. Therefore, herein, we developed a magnetic patterning method to generate rapidly (a few hours) small (below 100 µm) and size-controlled magnetic spheroids at high throughput (Fig. 3.5). It is based on a microfabricated array of soft magnetic NiFe (permalloy) micropatterns that can be magnetized by an external magnetic field and generate high magnetic field gradients in their vicinity. Each pattern should thus attract magnetized cells that aggregate and round up into a cohesive spheroid (Fig. 3.5A).

The magnetic array was fabricated by combining photolithography and electroplating on glass slides[525]. Two sizes of the NiFe structures were achieved, with a cylindrical shape of 50 µm in height and 50 or 100 µm in diameter, regularly spaced of 100 µm from each other (Fig. 3.5B). To ensure biocompatibility and avoid cell adhesion on the substrate, the magnetic patterns were spin-coated with PDMS and treated with anti-adhesive solution prior to each spheroid production. Magnetic cells were then put in contact with the patterns, at a density of 35, 70, and 140 cells per single micropattern. The magnetic field gradient was calculated through finite-element simulations in 3D using COMSOL Multiphysics 5.5 (Magnetic Field No Currents module). The magnetic properties of the materials were set as follows: a remanent flux density of 1.35 T for the permanent magnets, a permalloy (80Ni:20Fe) magnetization curve for the micromagnets, and non-interacting ($\mu_r = 0$) for other surrounding volume (PDMS, glass, air). The magnetic field gradient was extracted on a horizontal line 50 µm above the NiFe-patterned surface. It showed that the magnetic field gradient varies between 300 and 600 T/m, respectively at the center and at the edge of the pattern. For an NP3-labeled cell (21 pg of iron per cell, equivalent to a magnetic moment at saturation of 1.7×10^{-12} A.m²), this leads to an average attraction force in between 0.5 and 1 nN. 3 hours of aggregation were then sufficient to generate cohesive spheroids on top of each micromagnet (Fig. 3.5C), that can be further collected.

The first observation was that using micromagnets of 50 µm or 100 µm in diameter did not change the size of the resulting spheroids as long as the number of cells per pattern was identical. The impact of cell concentration (35, 70, and 140 cells per pattern) and magnetic labeling (NP1, NP2, and NP3 conditions) was next examined. The higher the initial cell concentration, the larger the magnetic spheroids (Fig. 3.5D): with the NP3 labeling condition, concentrations of 35 and 140 cells per pattern resulted in spheroids of 57 ± 1 µm and 97 ± 1 µm in diameter, respectively (Fig. 3.5E). Similarly, the higher the magnetic labeling, the larger the spheroids: spheroids generated with NP1, NP2 and NP3 labeled cells present an average diameter of 64 ± 1, 74 ± 2 and 97 ± 1 µm, respectively, for an initial cell concentration of 140 cells per pattern (Fig. 3.5E). Importantly, we observed many individual cells remaining in solution when generating spheroids with NP1 or NP2 labeled cells, but not with NP3. This suggests that with weakly magnetized cells, the magnetophoretic force is not sufficient to effectively attract all the cells towards the magnets.

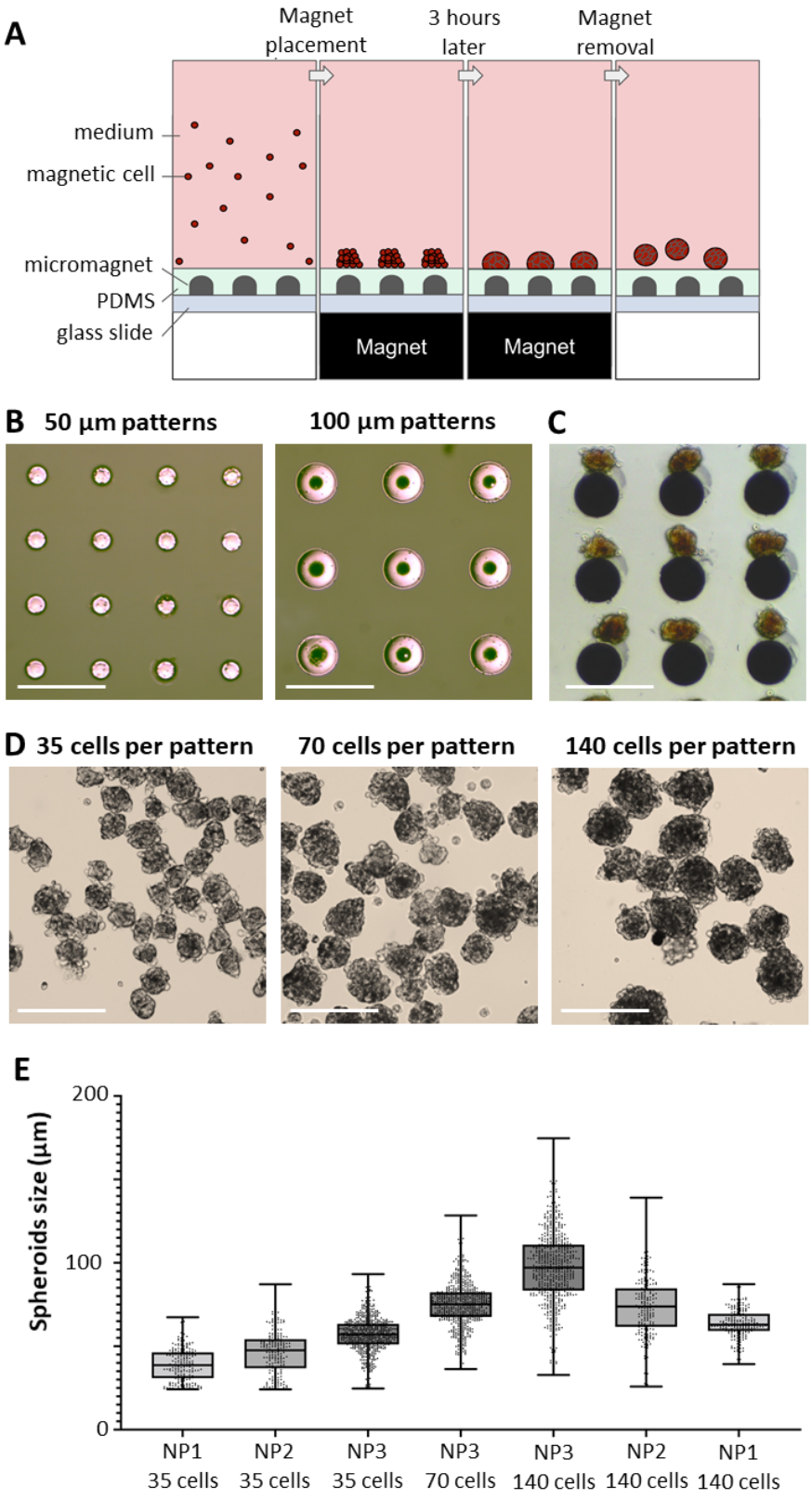

Figure 3.5. Spheroid production with magnetic micro-patterns. *(A) Illustration of the spheroid production process with the magnetic micro-patterns. (B) View from the top of the 50 and 100 µm wide magnetic nickel patterns, and (C) view from below the patterns immediately after spheroids were produced and started to move away from the patterns as the magnet was removed. (D) Images of the spheroids produced at a concentration of 35, 70 and 140 cells*

labeled with NP3 per pattern. (Scale bars = 200 µm) (E) Boxplots including all experimental data of the distribution of the spheroids' diameters for these 3 conditions (200 spheroids measured per production, with 3 productions for each condition,) and for spheroids made with cells labeled with NP1 and NP2, for 35 and 140 cells per pattern (200 spheroids measured over one production per condition).

Overall, the proposed method for generating magnetic spheroids offers easy handling, fine control over the spheroids size, as well as high-throughput production. Indeed, a micro-patterned glass slide of 75 x 26 mm^2 can produce more than 80,000 spheroids and can be easily parallelized.

6. Alignment of magnetic spheroids

Equipped with many of these highly magnetic spheroids, the next step was to evaluate the ability of our approach to magnetically align them in collagen hydrogel. The magnetic dipolar force exerted by one spheroid on another in contact is in the range of 190, 260, and 350 pN, for spheroids containing 35, 70, and 140 cells, respectively. Each spheroid thus becomes a unique building block, that could be organized within a fiber upon alignment with other spheroids. Here, the average spheroid size obtained ranges from 57 to 97 µm, which is in good agreement with *in vivo* observations of myofibers diameters[82,258].

Figure 3.6 investigates the optimal experimental conditions to generate spheroid chains for different magnetic labelings, spheroid sizes and spheroid concentrations. Concerning the influence of the magnetic labeling, it clearly appeared that, when using spheroids made of 140 cells, the strong labeling condition (NP3) achieves proper chain formation, but not the weak labeling condition (NP1) that leads to only a few chains made of 2 or 3 spheroids, with many isolated spheroids left (Fig. 3.6A). As for individual cells, an increased magnetization favors alignment. Concerning the impact of the spheroids size on chain formation, Fig. 3.6B illustrates spheroids (NP3 labeling) chaining for spheroids made of 35, 70 and 140 cells (keeping the total number of cells at 1 million per mL). Chain length increases with spheroid size, with an average length of 148 ± 3 µm and 184 ± 6 µm for spheroids made of 35 to 140 cells, respectively. Finally, similarly to individual cells experiments, an increase of spheroid concentration improved on-chip spheroids alignment. By increasing the equivalent cell concentration to 1.5 million cells/mL, an average chain length of 252 ± 11 µm was achieved, with the longest chains being up to 1 mm-long (Fig. 3.6C and 3.6E).

Eventually, the possibility to co-culture fibroblasts with the aligned spheroids was evidenced (Fig. 3.6D), the presence of non-magnetic fibroblasts randomly dispersed in the gel

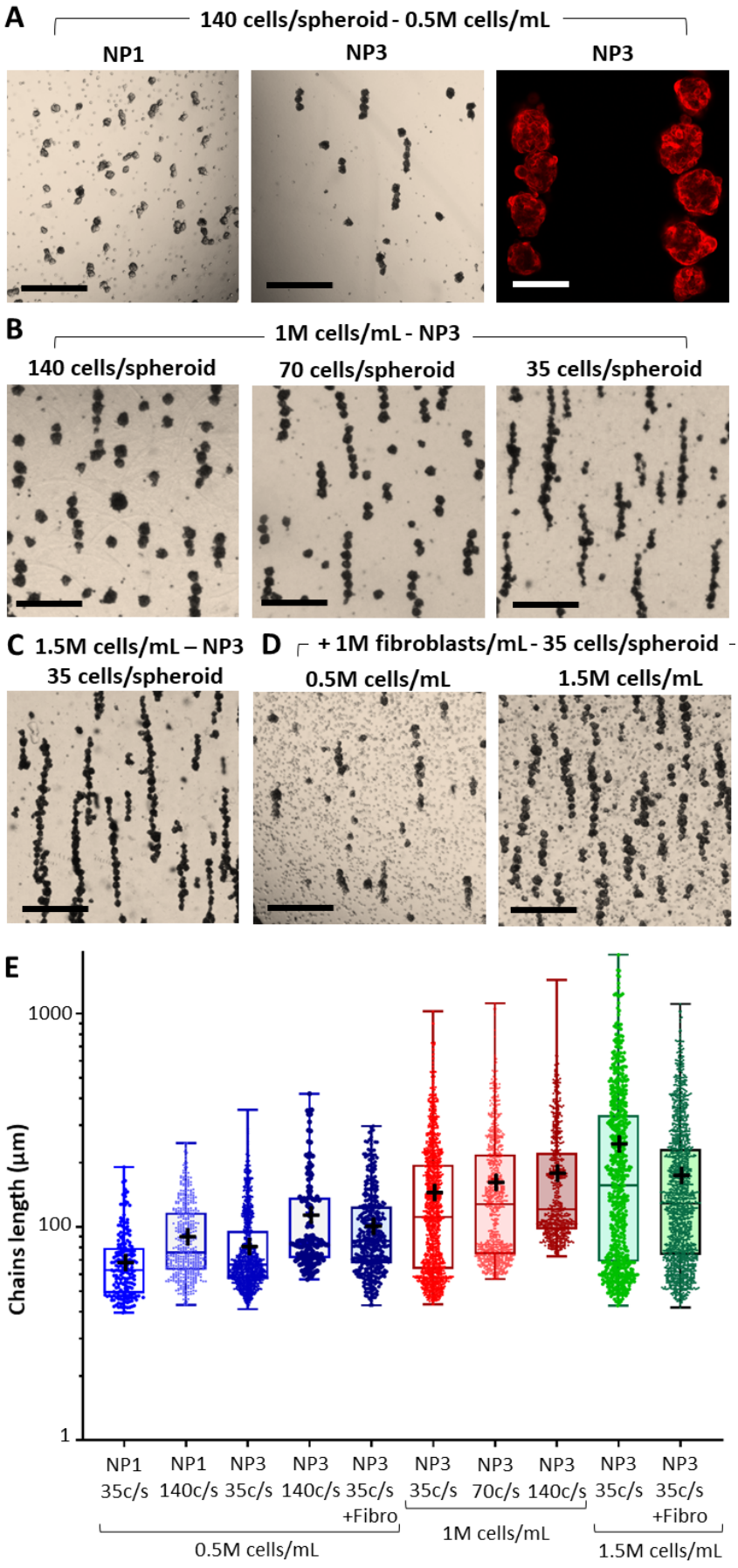
A
140 cells/spheroid - 0.5M cells/mL
NP1
NP3
NP3
B
1M cells/mL - NP3
140 cells/spheroid
70 cells/spheroid
35 cells/spheroid
C 1.5M cells/mL – NP3
35 cells/spheroid
D + 1M fibroblasts/mL - 35 cells/spheroid
0.5M cells/mL
1.5M cells/mL
E
Chains length (µm)
1000
100
1
NP1 35c/s
NP1 140c/s
NP3 35c/s
NP3 140c/s
NP3 35c/s +Fibro
NP3 35c/s
NP3 70c/s
NP3 140c/s
NP3 35c/s
NP3 35c/s +Fibro
0.5M cells/mL
1M cells/mL
1.5M cells/mL

Figure 3.6. Impact of the magnetic labeling, the spheroid size, and the spheroid concentration on the magnetic spheroid chain length. *(A) Images of the alignment of spheroids made with 140 NP1- and NP3-labeled cells per pattern at equivalent concentration of 0.5 million cells per mL, imaged with bright-field and confocal microscopy (using LifeAct transfected cells). (B) Images of the alignment of spheroids made with 35, 70 and 140 NP3-labeled cells at equivalent 1 million cells per mL concentration. (C) Image of alignment of spheroids made with 35 cells at 1.5 million cell per mL equivalent concentration. (D) Images of alignment of spheroids made with 35 NP3-labeled cells in hydrogel with 1 million fibroblasts per mL randomly dispersed fibroblasts at 0.5 and 1.5 million muscle cells per mL equivalent concentration. (Scale bars = 500 µm, except for confocal image in (A) with scale bar = 100 µm) (E) Boxplots showing all experimental data points of the chain length distributions for the 8 conditions and for the alignments of spheroids made with 35 NP1- and NP3-labeled cells (over 200 spheroids chains analyzed per condition, and up to 1000, on at least 3 different samples) .*

having no significant impact on the chain formation and length. Figure 3.6E summarizes all measurements made on single chains for each condition (over 200 spheroids chains analyzed per condition, and up to 1000, on at least 3 different samples) in the form of boxplots, showing both the median values and the large distribution.

7. Spheroid chain fusion and muscle tissue differentiation

Although creating an anisotropic cell organization within a 3D scaffold is crucial for muscle tissue engineering, it is only the first step to eventually generate mature muscle tissue in a 3D microenvironment. So, the chips containing the aligned spheroids in polymerized collagen were filled with differentiation medium to trigger muscle cell differentiation. A LifeAct transfected C2C12 cell line made possible the observation of fluorescent F-actin at both the cell and spheroid level over time. Figure 3.7 documents the chains evolution from the day of the alignment (day 0) to one (day 1) and four (day 4) days later. At day 0, just after alignment, the spheroids are distinct from each other and, even though they are aligned they do not seem to interact. However, they fuse one to the other, rapidly, within a few hours. After one day (day 1), all spheroids within the same chain become one, resembling a single elongated ellipsoid (Fig.3.7A). The persistent shapes of the individual spheroids, that were still present at day 1, were no longer visible at day 4 (Fig. 3.7A-G). This observation was consistent for all conditions: i.e., for chains generated with spheroids of different sizes as well as for different lengths of spheroid chains, from two to ten spheroids per chain (Fig. 3.7A-G). These results demonstrate that the magnetic alignment of spheroids can induce the formation of cohesive cell assembly over time thanks to spheroid fusion within the same chain.

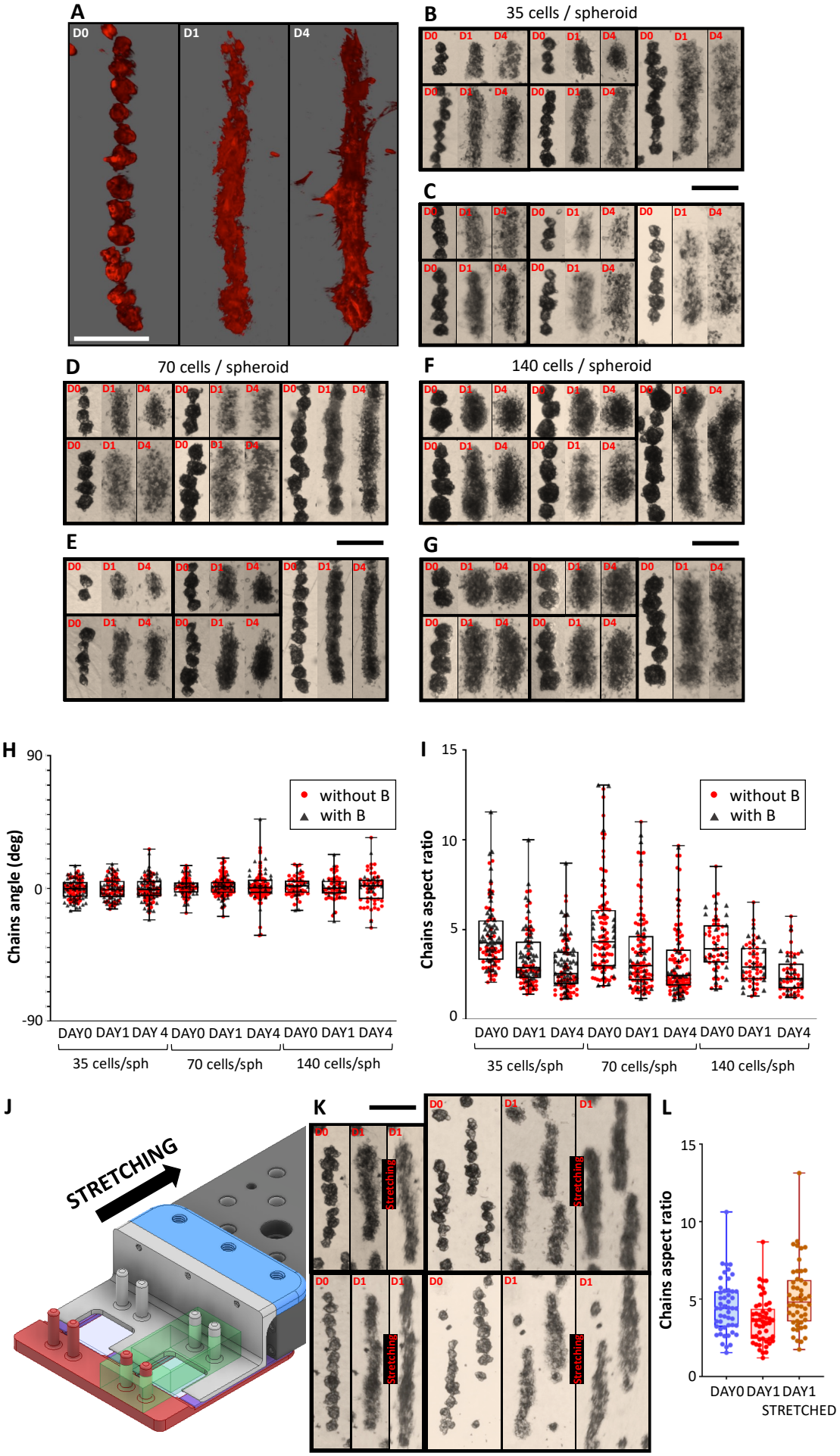
A
D0
D1
D4
B
35 cells / spheroid
C
D
70 cells / spheroid
F
140 cells / spheroid
E
G
H
Chains angle (deg)
90
0
-90
without B
with B
DAY0 DAY1 DAY 4 DAY0 DAY1 DAY4 DAY0 DAY1 DAY4
35 cells/sph
70 cells/sph
140 cells/sph
I
Chains aspect ratio
15
10
5
0
without B
with B
DAY0 DAY1 DAY4 DAY0 DAY1 DAY4 DAY0 DAY1 DAY4
35 cells/sph
70 cells/sph
140 cells/sph
J
STRETCHING
K
Stretching
L
Chains aspect ratio
15
10
5
0
DAY0 DAY1 DAY1
STRETCHED

Figure 3.7. Evolution of the morphology of the spheroid chains over time. *(A) 3D reconstructions from stacks of confocal images of the same spheroid chain made with mScarlet LifeAct cells on day 0, day 1 and day 4. (B-G) Images on day 0, day 1 and day 4 of the evolution of chains of spheroids made with NP3-labeled cells with (B,C) 35 cells per spheroid, (D,E) 70 cells per spheroid, (F,G) 140 cells per spheroid. Chains in (B,D,F) were removed from the magnets once they were aligned for 30 min, whereas chains in (C,E,G) were between the magnets from day 0 to 4. (H,I) Boxplots of the distributions of the chains (H) angle and (I) aspect ratio for chains of spheroids made with 35, 70 and 140 cells at days 0, 1 and 4, whether or not the chains were kept between magnets at all times (triangles with magnet, circles without magnet, respectively with or without B in the figure). (J) 3D design of a mechanical stretcher to deform the PDMS chips holding the collagen scaffold. (K) Images and (L) boxplots of the aspect ratio distribution of spheroid chains on day 0 and day 1 before and after stretching. At least 50 chains were studied for each condition of all graphs. (Scale bars = 200 µm)*

Spheroid fusion has been investigated to address fundamental questions about cell self-assembly or tissue organization[526,527] as well as for tissue engineering purposes[528]. A common method to promote spheroid fusion is most likely the hanging drop method[526,529] while an improved control of spheroids fusion can be achieved by an accurate positioning of spheroids within a scaffold[222]. Compared to existing approaches, the magnetic alignment of spheroids within a 3D microenvironment developed here offers new avenues to control general spheroid assembly across a large scale without needing fine control over their positioning.

All chains from all conditions (over 50 chains analyzed per condition) were quantified according to the chains angle (Fig. 3.7H), and aspect ratio (major axis over minor axis of the equivalent ellipse, Fig. 3.7I). The angle reflects the ability of the spheroid chains to keep their anisotropy over time, crucial to favor muscle cell differentiation. Figure 3.7H clearly demonstrates that all chains maintain their orientation from day 0 to day 4, with yet a notable dispersion of the angle distribution at day 4. Even though chain orientation did not vary over time, the dimensions of the chains, in particular their aspect ratio, did (Fig. 3.7I): the aspect ratio of spheroid chains decreased over time for all spheroid sizes. This can be explained by muscle cells high contractility, especially when they start differentiating. This contraction happens mostly in the direction of the chain main axis, which would be the preferred contractile direction if the cells were to form fibers in that direction. Besides, together with contraction along the chain axis, some cells also escape the chain, resulting in its enlargement.

It is worth mentioning that for half the conditions, experiments were carried out by keeping the chips in between the magnets from day 0 to day 4. Nevertheless, the permanent magnetic field did not change neither the chains orientation, nor their aspect ratio, and all data are presented within the same box plot, with black triangles denoting the permanent application of the magnetic field, while red circles correspond to chips outside of the field.

A final functionality of the design of the collagen chips is to combine magnetic alignment with mechanical stretching. A manual stretcher[530] was fabricated (Fig. 3.7J) that accommodates two chips in parallel, allowing to set and keep over time a uniaxial deformation ranging up to 20% (Fig. 3.7J-K). The chips were stretched on day 1, and deformation was transmitted to the aligned chains, as illustrated by chains imaging before and after stretching in Figure 3.7K. 50 chains were analyzed with a resulting average chain elongation of 18.8 ± 6.8%, while the chips themselves suffered a global 20% deformation. The aspect ratio of all chains analyzed are shown in Figure 3.7L, reproducing the decrease from day 0 to day 1 due to natural muscle cells contractility, but then evidencing a significant increase after stretching.

To further compare these different approaches to developing a skeletal muscle tissue on a chip, the spheroid-based samples were stained for actin and nuclei after 8 days of culture in differentiation medium and then imaged with confocal microscopy (Fig. 3.8). Figure 3.8A shows a typical chain that clearly formed a 3D tube like assembly after 8 days in differentiation medium. The cell organization within this cylindrical structure showed that in addition to the overall elongation of the structure the cells and their nuclei appear elongated. The actin filaments align along the main direction of the chain. Moreover, several multinucleated cells can be observed confirming that the differentiation process occurs.

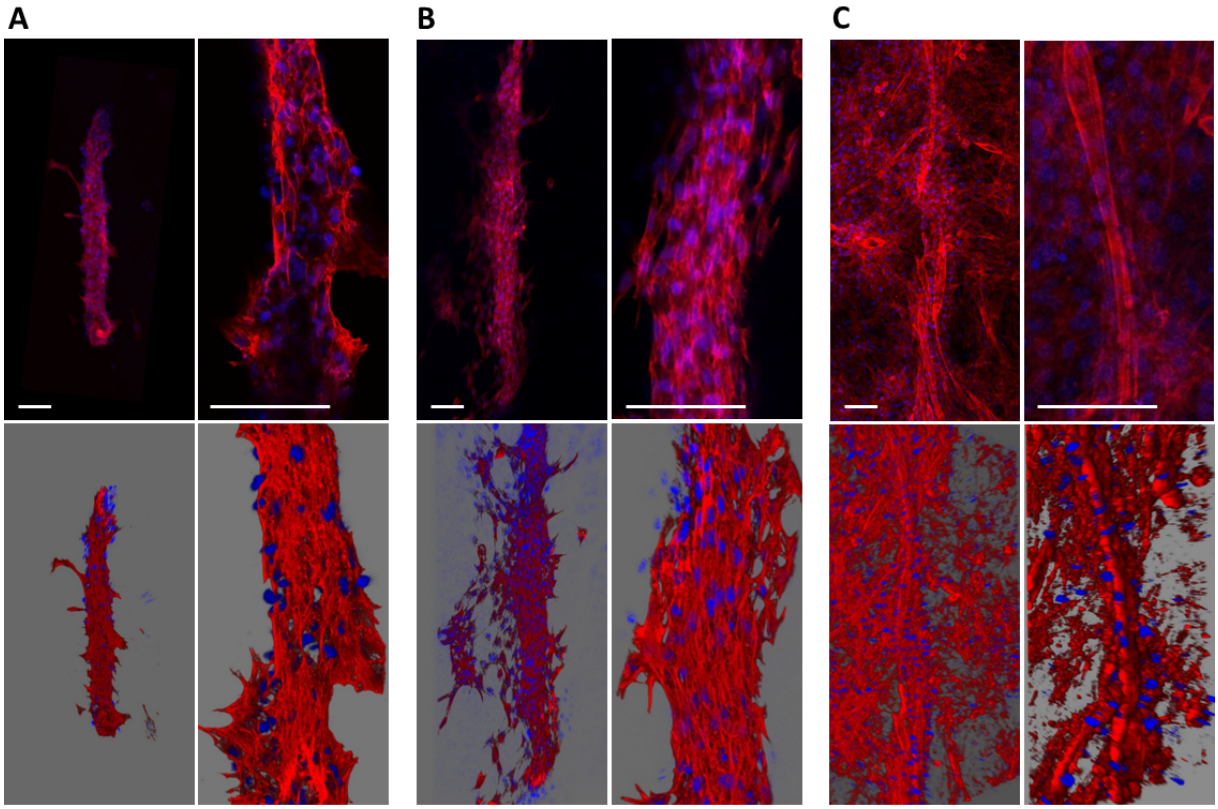

Figure 3.8. Confocal imaging of spheroid chains after several days of differentiation. *2D z-slices (top) and 3D reconstructions from z-stacks (bottom) of spheroid chains: (A) left in differentiation medium (day 7), (B) left in differentiation medium and stretched since day 1 (day*

7) and (C) of a spheroid chain where magnetic muscle cells were co-cultured with 1M/mL fibroblasts (day 5). Actin was stained in red and nuclei in blue. (Scale bar = 100 µm)

Figure 3.8B illustrates a chain that was magnetically aligned at day 0, and then stretched at day 1. Stretching did not notably affect fiber organization. After 8 days of differentiation, the overall structure remained, individual cells were elongated and oriented along the main alignment axis.

Finally, when magnetic spheroids were co-cultured with fibroblasts over the differentiation process (Fig. 3.8C), myofibers were clearly seen, the longest ones being more than 500 µm long. Bright-field microscopy showed the fibers located where the spheroid chain fused, darker in contrast than the non-labeled surrounding fibroblasts. Within these fibers, the nuclei are elongated and mostly located at the cell periphery as observed *in vivo*[531]. Both the myofibers, and the actin filaments within them, are oriented in the direction of the chain. 3D reconstitution of these confocal images finally confirmed that we succeeded in recreating three dimensional muscular fibers. Altogether, these results demonstrate that magnetically aligning spheroids in a 3D hydrogel scaffold without or with co-cultured fibroblasts, allowed generating oriented 3D myotubes.

8. Versatility of the method

Aside from muscle tissue, many living tissues present an anisotropic organization. Therefore, the two-fold magnetic method was applied to two other cell types, to investigate whether it can be a versatile tissue engineering tool (Fig. 3.9). It was tested on mice fibroblasts (Fig. 3.9A), which so far had only been used as non-magnetic cells for co-culture. The fibroblasts were labeled with the NP3 labeling and were used for making spheroids through magnetic patterning. Spheroids were successfully formed by incubating fibroblasts 3h over the magnetic patterns, with on average 35 cells per pattern. The spheroids were successfully created, with an average diameter of 70 µm. They could then be aligned, and after one day they formed single long fibers, with peripheral cells starting to colonize the gel. The method can therefore be applied to connective tissue, such as tendons and ligaments, that exhibit anisotropic structures as well[532,533]. The magnetic engineering method was next applied to human mesenchymal stem cells (hTERT) (Fig. 3.9B-C). Spheroids were easily formed by magnetic patterning, starting from 35, 70 and 140 cells per pattern, and leading to spheroids of average diameters of 73, 92, and 107 µm, respectively. Upon magnet application, they aligned and formed after one-day well-defined fiber-like structures, that could be further used for the regenerative potential of stem cells.

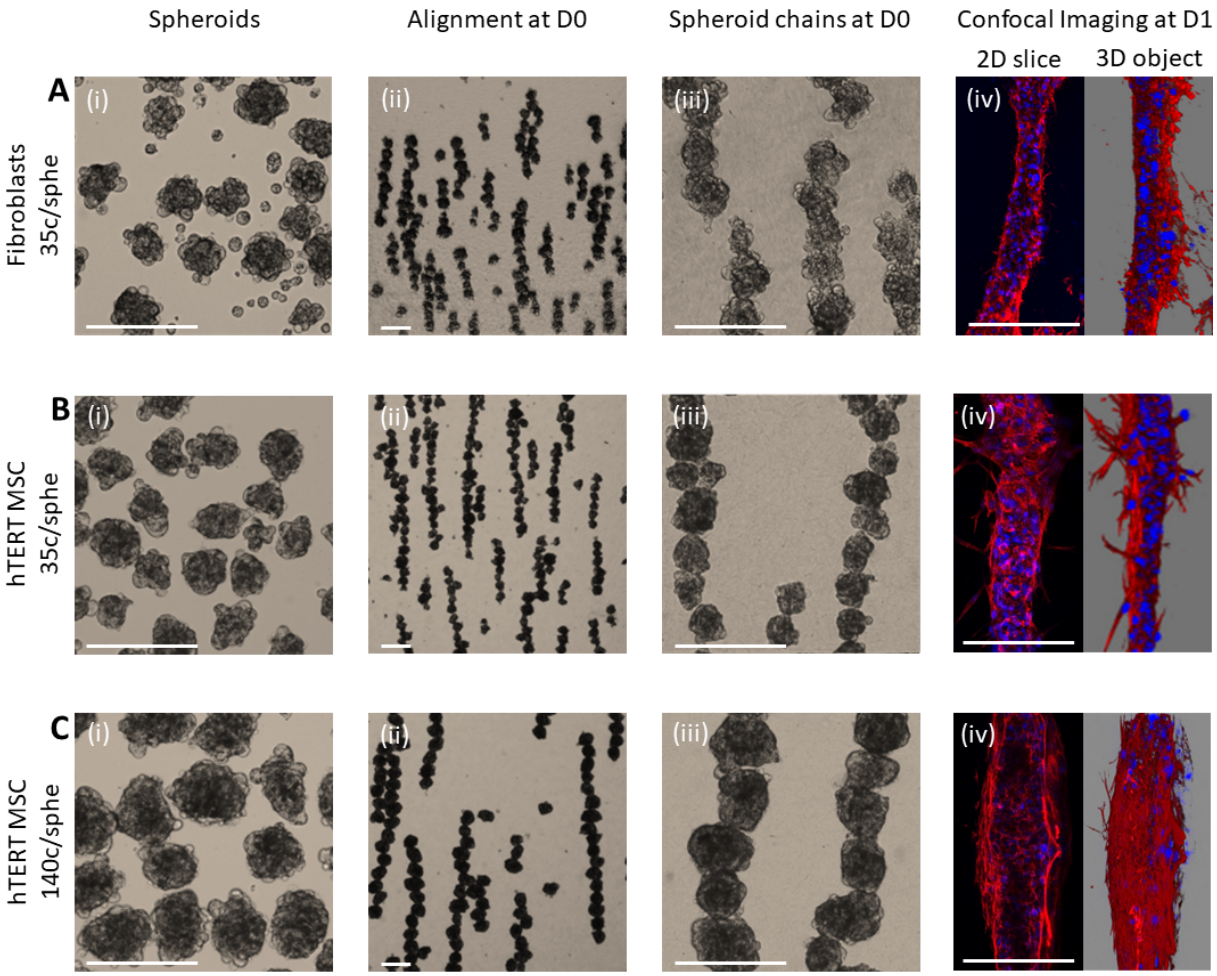

Figure 3.9. Magnetic alignment of spheroids made from fibroblasts or stem cells. *Spheroid making and alignment procedures applied to spheroids with (A) 35 fibroblasts per spheroid, (B) 35 and (C) 140 mesenchymal stem cells (hTERT MSC) per spheroid: (i) spheroids after fabrication; (ii) spheroids chains (close-up in (iii)) just after alignment, and (iv) 2D and 3D confocal imaging of the fiber-like structures created after one-day in DMEM medium supplemented with 2% serum. (Scale bar = 200 µm)*

III. Conclusion

Finding new ways to organize cells in a 3D scaffold with remote forces is beneficial to make tissue engineering progress. When it comes to skeletal muscle tissue, inducing an anisotropic organization is key to induce proper cell differentiation. In this work, two magnetic-based approaches are presented and exploited to develop an innovative approach for tissue engineering and in particular for organ-on-chip development. The first approach allows to generate at high throughput magnetic spheroids as tissue building blocks, while the second one offers a new way to align magnetic cells or spheroids along a strong uniform magnetic field. Combined, the two-step process enabled the creation of anisotropic myotubes oriented in the magnetic field direction. The magnetic labeling had to be optimized upstream, producing highly magnetic cells, having internalized up to 20 pg of iron per cells, with no impact on cell metabolic activity or capacity to differentiate. With these magnetic cells, the spheroid magnetic patterning technique offers a high yield of spheroid production with a good control over their size. Magnetic cells or spheroids made of dozens of them could then be aligned in 3D in a thermoresponsive collagen gel between two strong magnets specifically positioned at a distance avoiding any magnetic field gradient. Once the gel polymerized, the cells or spheroids were trapped in this anisotropic structure of controlled size. Structures made with aligned spheroids were the only ones that maintained their anisotropy over time, demonstrating the need for building blocks made of tens of cells. Strikingly, in a matter of days, the spheroid chains fused into fiber-like structures. These fibers could also be either 20% stretched one day after their formation or co-cultured in the 3D collagen gel with randomly dispersed fibroblasts, with several myofibers formed in the direction of the alignment. Differentiation could be further improved by investigating other stretching conditions, complementing differentiation medium with growth factor or even electrical stimulation. Co-culture of neurons could also be studied in order to recapitulate the in vivo architecture of muscle tissue more faithfully. Moreover, we showed that both the magnetic spheroid making and alignment methods can be applied to other cell types, such as fibroblasts and mesenchymal stem cells, where spheroids were easily fused, forming fiber-like structures.

This work demonstrates that combining magnetically assisted 3D strategies with organ-on-chip technology is beneficial for the fabrication of anisotropic fiber-like tissue engineered constructs, at centimeter scale, with fiber diameter of controlled size in the 10-100 µm range.

IV. Experimental procedures

Cell culture:

Mouse myogenic C2C12 cell line was obtained from ATCC and cells were cultured following conventional procedure in a growth medium made of DMEM (Gibco) supplemented with 10% v/v fetal bovine serum (Thermofisher) and 1% v/v penicillin/streptomycin (Thermofisher). The medium was changed every two days and cells were passed for confluency reaching 50% to 80% using TrypLE dissociation agent (Gibco). In experiments meant to induce cell differentiation, cells were used up to passage 10, otherwise they were used up until passage number 20. hTERT human mesenchymal stem cells (AM-T0523 Immortalized Human Bone Marrow, Euromedex), NIH3T3 fibroblasts (ATCC) were cultured in the same conditions. C2C12 cells with fluorescent actin were designed by cell transfection using the PEI MAX reagent (Polysciences). The pLVX-LifeAct-mScarlet plasmid was used for viral transfection, infecting C2C12 cells and creating a stable C2C12 LifeAct-mScarlet cell line.

Magnetic cell labeling:

Iron oxide (maghemite) superparamagnetic nanoparticles were used to magnetically label C2C12 cells. The nanoparticles were produced by iron salts co-precipitation, resulting in an average diameter of 8 nm and a polydispersity index of 0.37 and were coated with citrate ions to preserve their stability in an aqueous solution at pH 7 by electrostatic repulsions. Besides, the negative surface charge (zeta potential = -35 mV) also favors the cellular internalization. They were selected as some of the most used maghemite nanoparticles for biomedical applications[422,534,535], whose properties such as magnetization, hydrodynamic sizes, and stability, have been previously characterized in solution and within cells[518,519]. Prior to use, the stock solution of magnetic nanoparticles (2 M of iron) was sterilized by filtration through a 200 nm filter. The magnetic labeling was then performed by incubating the cells with a nanoparticle solution diluted in culture medium RPMI in which 2 mM free citrate was added to avoid nanoparticle precipitation. The pH of the RPMI medium was not affected by the addition of citrate or the nanoparticles. Nanoparticles uptake was tested for different incubation times (from 15 min to 18 hours) at [Fe]=2 mM, and different iron concentration (from 0.5 to 64 mM) for 30 min duration. Besides, a multi-step incubation was set-up, corresponding to 1, 2, or 3 30 min incubations at [Fe]=2mM. The first labeling condition (one single incubation) was named NP1. The two other labeling conditions, named NP2 and NP3, consisted in performing the NP1 labeling every day for two or three days respectively. All incubations were performed at 37 °C, and cells were rinsed afterwards in RPMI and placed back in C2C12 growth medium for at least 1 h prior to any further operations.

Quantification of internalized iron oxide by magnetophoresis:

Magnetophoresis was performed to measure the magnetization of the labeled cells, and by extension the amount of internalized iron oxide[422]. Cells suspended in PBS were placed next to a permanent magnet, generating a field B = 0.145 T and a gradient grad(B) = 17 $T.m^{-1}$. This way, the magnet attracted magnetically labeled cells, and cell migration was imaged through bright-field microscopy. The movies were then analyzed to measure cell radii and velocities, from which the magnetic force was determined by calculating the force balance with respect to Stokes drag law. The mass of iron oxide within cells was then determined from the magnetic moment calculated using the determined cellular magnetic force. For a cell of diameter d and velocity v, the mass of internalized iron is $m_{Fe} = \frac{M(Fe_2)}{M(Fe_2O_3)} \frac{\rho}{M_v} \frac{3\pi\eta dv}{grad(B)}$ with $M(Fe_2)$ and $M(Fe_2O_3)$ the molar masses of Fe_2 and Fe_2O_3 respectively, M_v the density of magnetic moment of a nanoparticle in a field of 0.145 T, ρ the density of a nanoparticle and η the viscosity of water. 200 single cell motions were analyzed for each single measurement, and the measure was made in triplicate.

Alamar Blue metabolic assay:

The metabolic activity of the magnetically labeled cells was quantified using the Alamar Blue assay and compared with non-magnetic control cells. The Alamar Blue reagent was incubated (10% in DMEM) with cells cultured in 96-well plate for 1 h (100 µL per well) and was read with a fluorescence plate reader (Enspire, Perkin Elmer) at 570 nm excitation wavelength and 585 nm detection wavelength following the vendor's instructions.

LIVE/DEAD assay:

The cytotoxicity of the magnetic labeling was tested using a LIVE/DEAD cell imaging kit (488/570, Invitrogen). The LIVE/DEAD reagents were incubated with cells in a 24-well plate for 15 min. The wells were then imaged with confocal microscopy with a 488 nm excitation wavelength for the live cells and a 570 nm excitation wavelength for the dead cells. The live cells appeared in green while the dead cells appeared in red, making it possible to count the proportion of dead cells.

Fabrication of the magnetic micro-patterns:

The magnetic micro-patterns were fabricated on a glass slide by NiFe electroplating through a photoresist mould[525]. Glass slides (Corning) were cleaned with acetone and isopropanol, after which a Ti-Cu seed layer (Ti 10 nm, Cu 100 nm) was deposited by magnetron sputtering (Plasmionique) to render them electrically conductive. TI-Prime (Microchemicals) was applied as an adhesion promoter, and an epoxy-based negative photoresist (AZ 125nXT, Microchemicals) was spun to a thickness of 70 µm, exposed through a chromium mask and

developed, leaving bare copper only where the magnetic patterns were to be grown. NiFe (80:20) deposition was performed by electroplating in a bath containing NiSO4 (250 $g.L^{-1}$), FeSO4 (5 $g.L^{-1}$), boric acid (25 $g.L^{-1}$), saccharin (2 $g.L^{-1}$) and sodium dodecyl sulfate (0.1 $g.L^{-1}$) at 30 °C under magnetic stirring. A current density of 7 $mA.cm^{-2}$ was applied between the substrate and a pure nickel anode (Goodfellow), leading to a growth rate of 4 $\mu m.h^{-1}$. When a thickness of 50 µm was achieved, the photoresist and copper layers were dissolved in TechniStrip P1316 (Technic) at 70 °C. A 100 µm PDMS layer (Sylgard 184, curing agent ratio 1:10 w/w) was then spincoated on the substrate and cross-linked for 2 hours at 70 °C, after which PDMS wells were bonded using oxygen plasma (Diener Pico) and UV-sterilized.

Magnetic spheroid formation using the magnetic micro-patterns:

The wells of the magnetic micro-patterns plate were first treated with an anti-adherence rinsing solution (Stemcell Technologies) for 1 h at room temperature and rinsed with PBS. The wells were filled with differentiation medium into which magnetic cells were suspended, the cell concentration being adjusted to control the number of cells per magnetic spot. The plate was then placed onto a magnet (110.6 x 89 x 19.6 mm^3, with remanence Br = 1.35 T, Ref. Q-111-89-20-E, Supermagnete) leading to the aggregation of cells on top of each magnetic spot. After a 3 h incubation at 37 °C, the plate was taken off the magnet, and the so formed spheroids were harvested and resuspended in differentiation medium.

PDMS chips fabrication:

Two chip designs were used: a first one for static long-term observation, and a second one for mechanical stretching. Both designs were made of PDMS (Sylgard 184) with a prepolymer/curing agent ratio of either 10:1 w/w for static experiments or 20:1 w/w for stretching experiments to increase elasticity. PDMS chips with a 1 cm deep 2 by 2 cm reservoir with a central well (10 by 7 mm rectangle, 1 mm deep) were fabricated by moulding onto custom brass moulds prepared by micromilling (Minitech) as described in a previous work[530]. For the static experiments, the PDMS at the bottom of the central wells was cut out and the chips were then plasma bonded on glass coverslips. For mechanical stretching, the PDMS bottom was kept, and additional holes were added to the sides of the chips, which were then clamped onto a custom mechanical stretcher based on a manual translation stage (Thorlabs). All the chips were then subjected to an APTES (3-Aminopropyl)triethoxysilane (Sigma-Aldrich) and Glutaraldehyde (Sigma-Aldrich) treatment to promote covalent anchoring of collagen to PDMS as described previously[536]. The PDMS chips were then UV-sterilized immediately prior to cell and hydrogel scaffold seeding.

Seeding of cells or spheroids in PDMS chips with collagen/Matrigel scaffold:

A hydrogel scaffold solution was prepared at 4 °C, containing 2 $mg.mL^{-1}$ of rat tail collagen type I (Corning, stock pre-equilibrated at pH 7 with NaOH), 10% v/v of matrigel matrix (Corning), 1x PBS, and 40% v/v of differentiation medium. The hydrogel scaffold solution was then mixed with cells or spheroids before being seeded in PDMS chips and left to polymerize for 30 min in an incubator at 37 °C.

Cell differentiation:

To promote cell differentiation after seeding in the collagen/Matrigel scaffold, a differentiation culture medium made of DMEM (Gibco) containing 1% v/v horse serum (Thermofisher) and 1% v/v penicillin/streptomycin (Thermofisher) was used.

Magnetic alignment of cells or spheroids:

After seeding the cells (or spheroids) mixed with the cold hydrogel scaffold solution in the PDMS wells, the chips were quickly placed between two iron boron magnets (110.6 x 89 x 19.6 mm^3, with remanence Br = 1.35 T, Ref. Q-111-89-20-E, Supermagnete) in an incubator at 37 °C. Between the magnets, the labeled cells acquire a magnetic moment and align due to the dipole-dipole force, while the 37 °C temperature initiates the collagen and matrigel polymerization around the aligned biological objects. The magnets were kept 3.6 cm apart (although a 10 cm distance was also tested in Figure 3.2) using custom aluminum parts machined by Protolabs. COMSOL Multiphysics (Magnetic Field No Currents module) simulations were performed to determine the optimal distance between magnets to minimize the magnetic field gradient while keeping a high field intensity.

Fluorescent cell staining:

Prior to staining, the culture medium was removed, and the chips were incubated in 4% PFA v/v in PBS for one hour at room temperature to perform cell fixation and washed 3 times with PBS. Collagen samples were detached from the chips and left an hour at 4 °C in a blocking solution composed of 4% w/w BSA (Sigma) and 0.5% v/v Triton X-100 (Fisher) in PBS. The samples were rinsed 3 times with PBS. Each sample was then left overnight in 2 mL of staining solution (blocking solution with 1:1000 of Thermofisher Phalloidin AlexaFluor 488 and 1:300 Invitrogen DAPI) at 4 °C for protein staining. The next day, the samples were rinsed 2 times with PBS at room temperature. The chips were stored in PBS at 4 °C until imaged.

Confocal imaging:

Samples were imaged using a Leica DMi8 inverted confocal microscope. Either a 10X air objective or a 25X water immersion objective were used. Collagen samples were placed using tweezers onto a fluorodish and laid flat for imaging.

Perls staining of intracellular iron:

Perls' Prussian blue staining reveals iron within labeled cells in blue. The cells were fixed as was done for confocal imaging. They were then further stained for 5 min using 0.5 g of potassium hexacyanoferrate (II) (Sigma) dissolved in 10 mL of distilled water mixed with 10 mL of Hydrochloric Acid 1N (Fisher Chemical). Counterstaining was next performed using 0.5 g of Nuclear Faster Red (Fisher Chemical) with 10 g of Aluminum sulfate hydrate dissolved in 200 mL of demineralized water.

Transmission electron microscopy imaging:

Cells were fixed for an hour in a solution made of 0.1 mol/L sodium cacodylate buffer (Sigma-Aldrich) supplemented with 5% glutaraldehyde. Rinsing (two times) was performed in 0.1 mol/L sodium cacodylate buffer, and samples were then contrasted with 0.5% Oolong Tea Extract (OTE), after that postfixed with 1% osmium tetroxide, and finally embedded in epoxy resins. Ultrathin slices (70 nm) were sectioned, counterstained with lead citrate, and imaging was achieved with a Hitachi HT 7700 at 80 kV (INRAE, UMR 1313 GABI, MIMA2-Plateau de Microscopie Electronique, 78352 Jouy-en-Josas, France).

Image and statistical analysis:

Magnetophoresis measures were performed on 200 cells per experiment, with 3 experiments per condition, by measuring their speed and diameter using Fiji. Results were presented in Figure 3.1 as mean ± standard deviation.

Evolution of the angle distribution after individual cell alignment was measured using Fiji's OrientationJ plugin on three different samples for each condition.

Chains and spheroids' sizes, elongation and angle were obtained with Fiji's Analyze particles module.

Spheroid sizes were measured over 3 productions for the NP3 labeled conditions and 1 production for the other conditions, with 200 spheroids measured per production.

Chain lengths were measured over 3 different samples per condition, with overall at least 2000 chains measured for individual cell chains, and overall, 200 to 1000 chains measured for spheroid chains. As the size and the number of objects aligned changes not only the length of

the chains but also the overall number of chains in one sample, not all conditions have the same number of chains per sample. For the spheroid chains, all the chains of each sample were measured, but some only have 200 while others have more than 1000.

Chains' elongations and angle throughout time were measured on at least 50 different chains per condition.

Statistical representations were performed using GraphPad Prism 8 (GraphPad Software, La Jolla, California).

Chapter 4

Magnetic printing and actuation of stretchable muscle tissue

Context and motivations

This first study introduced an innovative approach to magnetically align cells or spheroids of various sizes, making it possible to engineer tissues with a wide range of microfeatures. As spheroid chains were able to fuse together and preserve their anisotropy over time, muscle maturation was improved, even more so when tissues were stretched or co-cultured with fibroblasts, but it could still be further enhanced. In addition to the variability between spheroid chains, this motivated the new study presented in **Chapter 4**. Its goal is to develop a magnetic-based approach to engineer muscle constructs better suited for enhanced myogenesis and reproducibility. Our initial enquiries on muscle tissue stretching, along with current research on the impact of mechanical stimulation on muscle differentiation[46,261,265–267,272,280], also guided us to further focus on a system capable of mechanical stimulation.

This led us to revisit a magnetic stretcher system previously introduced within our lab. Two flat magnetic microtips facing one another were used to trap magnetically labeled embryonic stem cells. The cellular aggregate between the two magnets could be stimulated by cyclically moving back and forth one of the magnetic tips, which eventually resulted in its differentiation towards the cardiac pathway[57]. We aimed to apply a similar approach to skeletal muscle tissue. However, with flat magnetic microtips the trapped tissue is as large as the surface of the microtips, resulting in a cubical shape with no particular elongation nor alignment. In order to obtain a more elongated structure, flat magnetic microtips were replaced with magnetic needles meant to focus the magnetic forces and create a much narrower path for the field lines, and therefore the tissue. In preliminary work, flowing cells towards the magnetic needles led to the formation of spheroids around each needle, and if the spheroids were large enough and the needles close enough, the two cell aggregates could fuse into a “peanut” shaped tissue. While this tissue showed slightly more elongation than the one made with flat magnetic microtips, it was far from the aspect ratios observed in skeletal muscle tissue and displayed very little aptitude for stretching.

Therefore, instead of directly trapping individual cells, we explored the potential of preforming tissues in an anisotropic shape before placing them between magnetic needles. This led us back to the NiFe patterns we used to engineer spheroids in the previous study. We realized that with the same technique we made 100 µm circular dots, we could make much larger and more complex patterns. As we discovered that these patterns could in fact be used to generate tissues with precise geometries out of magnetically labeled cells, we aimed to show that this next generation magnetic patterning technique could be used for magnetic bioprinting of skeletal muscle tissue.

One major difference with most current approaches for skeletal muscle tissue engineering is the absence of a scaffold. In non-magnetic platforms, the matrix is often used to mould or generally control the shape of the tissue[42–44]. Skeletal muscle being a tissue with a rather low content in extracellular matrix, usually below 10% [174], this can be difficult to achieve in matrix-based approaches. However, most platforms involving magnetically labeled cells use magnetic forces to shape tissues, bypassing the need for a scaffold[333]. One of our goals in this

study is also to show that the magnetically printed tissues are still able to achieve proper myogenesis, even without the presence of scaffold.

To engineer more physiologically relevant models, once our approach was optimized for C2C12 mouse myoblasts, we chose to transpose it to myoblasts derived from human iPS cells. This cell type has only recently been investigated in skeletal muscle tissue engineering [262,268,269], and little is known on the impact mechanical stimulation can have on them. And yet, as iPS cells can be induced from any skin or fat tissue and easily proliferate, they represent a great source of biological material for personalized regenerative medicine. This further motivated us to investigate how this more complex cell type would react to our approach.

In addition to optimizing the shape of the tissue for anisotropic muscle differentiation, the specific wrench shape chosen for the bioprinted skeletal muscle tissues was adapted empirically through a process of trial and error to optimize its remote magnetic actuation. Indeed, as we have shown, multiple studies have attempted to engineer cellular tissues that can be actuated remotely with magnetic forces. Such magnetic actuation can be used to induce bending[458], folding and unfolding motions[437,470], or even helicoidal movement[377] on demand. In our case, the main purpose of magnetic actuation is to improve the magnetic trapping of the tissues. Using both magnetic patterning and magnetic actuation is also another example of how magnetic based techniques can be combined to leverage the magnetic properties of a tissue to their full extent

This context underpins the study described in **Chapter 4**. It is adapted from a submitted manuscript currently under revision for publication. A preprint version is available on BioRxiv[537].

Supplementary figures and tables are available in Appendix A.

Abstract

While the link between tissue organization, stimulation, and function is now acknowledged as crucial for tissue development, engineering tissues with precise, long-lasting shapes and the capability for mechanical stimulation remains challenging. This study addresses this challenge by developing a next-generation magnetic bioprinting approach to create anisotropic, shape-controlled, scaffold-free, and stretchable skeletal muscle constructs. Murine skeletal muscle cells and human induced pluripotent stem cell-derived myoblasts, labeled with iron oxide nanoparticles, were magnetically bioprinted into wrench-shaped tissues. Their magnetic properties allowed these tissues to be clipped onto magnetic needles, preserving their shape over two weeks of culture while promoting anisotropic differentiation and myoblast fusion. Additionally, the magnetic tissues could be stretched by up to 100%, enhancing their anisotropy and improving muscle maturation. This magnetic toolbox demonstrates significant advancements in muscle tissue engineering, as evidenced by enhanced indicators of myoblast differentiation, including cell fusion, increased myogenic maturation and contractility. These findings highlight the potential of magnetic-based techniques for developing advanced muscle-on-chip systems and other complex tissue constructs.

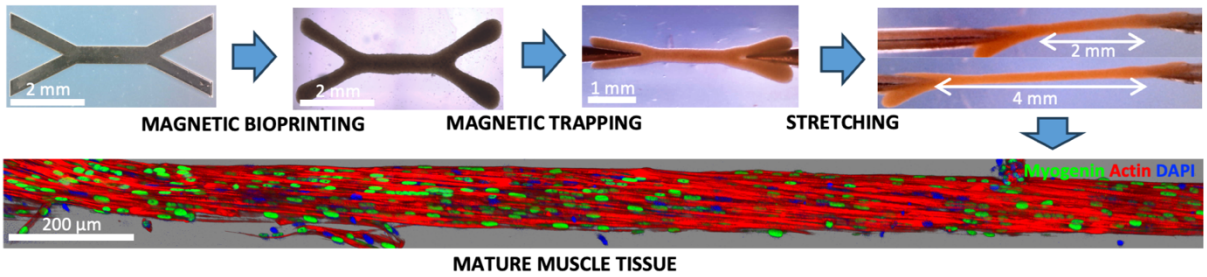

Visual table of contents of Chapter 4

I. Introduction

Due to the inability of monolayer cell cultures to accurately replicate the complexity of tissues, there is an increasing need for systems that can fully capture the *in vivo* tissue organization[13,14]. This challenge is currently being addressed through the development of organ-on-chip and bioprinting technologies. Microfluidic systems, used to create organs-on-chips[38,363,538–542], enable culturing cells in chambers that mimic the *in vivo* microenvironment, typically within a three-dimensional (3D) scaffold, to achieve a high level of control in recapitulating certain organ functions, in drug screening and to dissect tissue biology. However, current organ-on-chip approaches still lack control over the overall tissue shape, which remains a critical challenge in tissue engineering[11,31,32,63]. In contrast, bioprinting addresses the essential link between tissue shape and function[543,544] by allowing precise control over tissue geometrical cues. Bioprinting typically involves the use of bioink filled with cells, which is either extruded[42,43] or photopolymerized[44] in the desired shape. Despite their advantages, bioinks can be physiologically limiting and restrict cell density and cell-to-cell interactions. Furthermore, while bioprinting methods can accurately control the initial shape of bioprinted tissues, they do not guarantee the maintenance of this geometry throughout tissue maturation.

And yet, many tissues, such as skeletal muscle tissue[25], require both strong geometrical cues[545] and a densely packed cellular network over an extended period for proper tissue maturation[546]. Myogenesis occurs when a dense network of myoblasts, mononucleated muscle precursor cells, fuse together to form parallel giant multinucleated myofibers. This geometry is crucial for optimal maturation and functional force generation *in vivo.* The increasing contractility of differentiating cells also induces significant stresses that can deform engineered *in vitro* tissues, thereby limiting their maturation and, consequently, their physiological relevance.

Preserving the original anisotropic geometry of the tissue is therefore essential for skeletal muscle constructs. Aside from 2D systems on anisotropic substrates[64], most muscle-on-chip models constrain the tissue by anchoring it between two pillars[260–264]. Such an approach favors the maintenance of 3D anisotropy and can facilitate contractibility measurements through post deflection[262,263,547]. However, these systems generally require the use of a scaffold to maintain anisotropy. Additionally, achieving consistent reproducibility and precise shape control over time remains challenging.

The advent of magnetic-based tissue engineering techniques has recently introduced new possibilities for creating complex, scaffold-free tissues. Magnetic forces can effectively direct the organization of cells that have internalized magnetic nanoparticles[46,47]. Previously used for theragnostic purposes - such as imaging contrast agents, drug delivery vectors and anticancer hyperthermal therapies[48,49], these nanoparticles have also shown promise in remotely controlling cells within a tissue engineering context. Initiated by magnetic sheet engineering[52], magnetic bioprinting approaches have successfully created matrix-free tissues in specific shapes[46,55,59,60]. However, these magnetic tissues have not yet achieved the complexity seen in

bioprinting. Nevertheless, magnetic remote actuation has proven remarkably effective for 3D spheroid assembly[46,53], mechanical stimulation[54], and trapping cell aggregates[55–57].

Herein, we present a next generation magnetic bioprinting approach for skeletal muscle constructs, engineered to be anisotropic, shape-controlled, scaffold-free, and with inherent capacity for physical stimulation. Indeed, functionalizing the shape of the tissues enabled magnetic actuation, allowing them to be remotely clipped onto two magnetic needles while preserving their shape over time, and enabling controlled stretching. Once optimized with C2C12 mouse myoblasts, this "clip-on" two-fold magnetic process was successfully applied to myoblasts derived from human induced pluripotent stem cells (M-hiPSC). In both cases, stretching the tissues improved their maturation and differentiation, resulting in the rapid formation of fascicle-like skeletal muscle tissue.

II. Results

1. Magnetic bioprinting of wrench-shaped 'clip-on' muscle tissues

C2C12 mouse myoblasts were magnetically labeled by incubating them sequentially with maghemite nanoparticles. As demonstrated in the previous study[46], this process led to the internalization of approximatively 20 pg of iron per cell through endocytosis[417], without affecting the cells viability.

The maghemite nanoparticles are superparamagnetic: upon internalization, they enable the remote control of the cells using magnetic forces without any residual magnetism once the magnetic field is removed. Our approach aims to create a magnetic muscle tissue with controllable anisotropy and shape that can be further manipulated by magnetic forces for stretching stimulation. We envisioned a wrench-shaped form (Fig. 4.1A) with the ends designed as two clamps to clip onto magnetic attractors, such as needles, which could then be moved to enable stretching. To create the shape, we conceived a magnetic patterning strategy that could potentially replace the printing pattern during bioprinting. We employed photolithography and electrodeposition to create soft NiFe (permalloy) micropatterns in any desired shape (Supplementary Fig. 4.1A-B). The selected wrench-shaped pattern (Fig. 4.1A) features a 500 µm-wide and 2mm-long central fiber that mimics the anisotropic muscle structure and two clamps for functional purposes, while remaining large enough for effective manipulation. Once the pattern is positioned between two strong magnets (Supplementary Fig. 4.1C), where the magnetic field is uniform, it magnetizes, generating a high magnetic gradient around the pattern, as demonstrated by finite element simulations (Fig. 4.1B, Supplementary Fig. 4.1D-L).

By placing a suspension of magnetically labeled cells in a well, positioned on top of the patterns, cells are exposed to high magnetic forces at the bottom of the well. Simulations indicate that the magnetic gradient there varies between 40 and 800 $T.m^{-1}$, resulting in forces ranging from 0.05 to 1.5 nN on a single cell (with a magnetic moment at saturation of 1.7×10^{-12} $A.m^2$ that has been reached since the field between the magnets is of about 300mT and saturation of these nanoparticles is achieved after 150 mT[518]). These forces caused the cells to migrate and align with the shape of the patterns within seconds. The cells were maintained under the magnetic field for three hours to ensure cohesiveness. As a result, the tissues could be easily collected once the patterns were removed from the magnetic field (Fig. 4.1C). Thus, this magnetic bioprinting technique results in the rapid formation of cohesive tissues in the exact shape of the magnetic patterns (Fig. 4.1D). Unlike most other bioprinting methods, which typically rely on a gel or matrix, the resulting tissue is composed solely of cells. Importantly, LIVE/DEAD assays on freshly patterned tissues (Fig. 4.1E, Supplementary Fig. 4.2) demonstrated that this magnetic bioprinting process does not induce cell death, with 94 ± 2% of live cells after tissue formation. Interestingly, while cells follow the 2D pattern, the resulting tissue is three-dimensional (3D) (Fig. 4.1F-G, Supplementary Fig. 4.3), with cells aggregating in a densely packed manner on top of one another, resulting in a 3D type of bioprinting. Varying the cell density from 10^5 to 4×10^5 cells per mm^2 of pattern resulted in an increase in the width

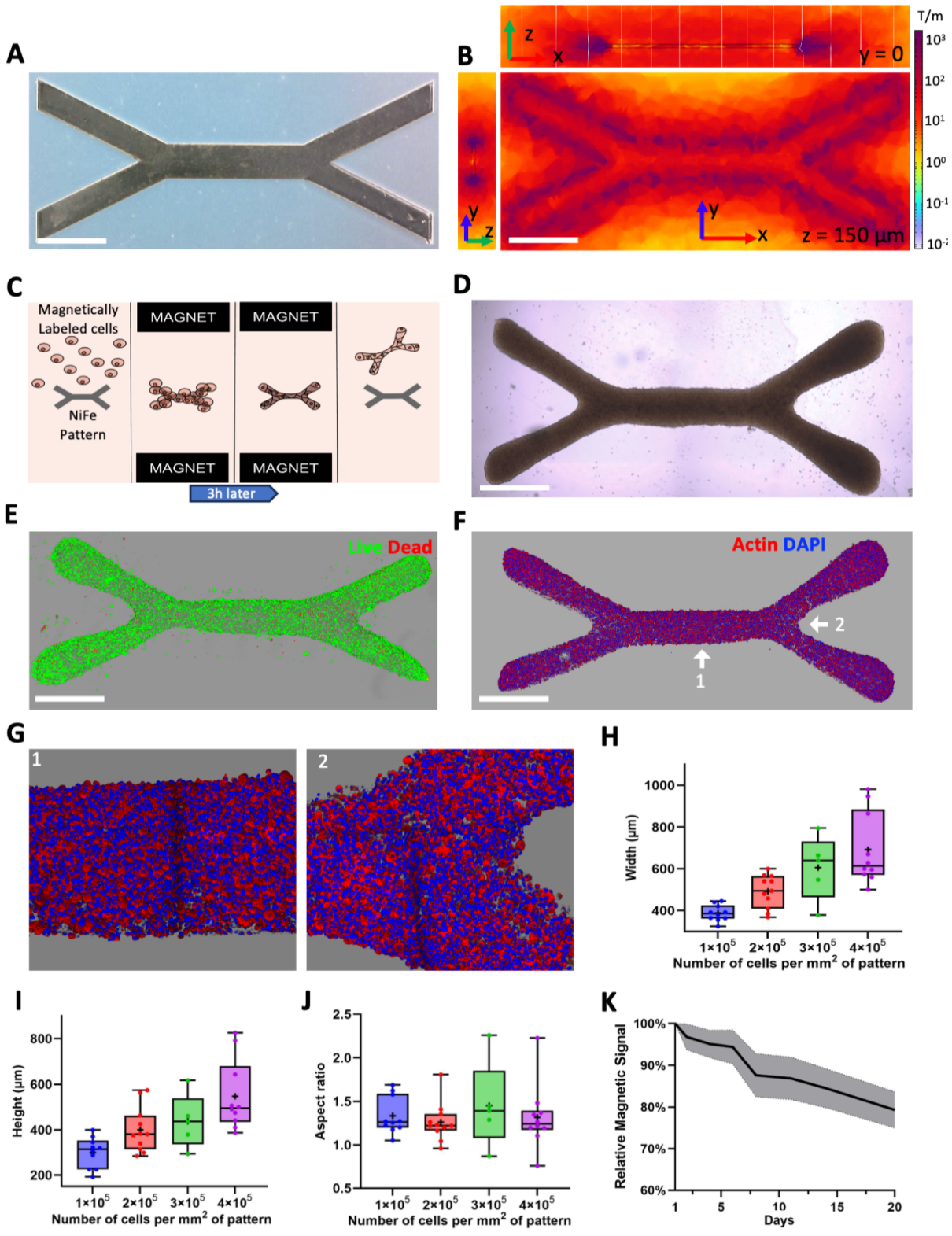

Figure 4.1. Magnetic micropatterns generate viable, shape-controlled 3D tissues. *(A) Wrench-shaped magnetic micropattern. (B) Magnetic field gradient generated when the pattern is placed between two strong magnets. (C) Patterning procedure. (D) Typical bright-field image of a magnetically bioprinted tissue. (E) 3D reconstitution from confocal imaging of a LIVE/DEAD assay on a tissue immediately after patterning (live cells in green, dead cells in red). (F-G) 3D reconstitutions from confocal microscopy of a tissue (actin in red, nuclei in*

blue): (F) whole tissue, (G) zoomed-in views of zones 1 and 2. (H-J) Boxplots of the (H) width, (I) height and (J) aspect ratio of the section of the central fiber of the tissue after patterning (whiskers as min and max, box as the interquartile range, center line as median and mean as +). (K) Variation of the magnetic signal of bioprinted tissues with time (n=9) plotted relative to the signal on day 1 until day 20. (Scale bars = 1 mm)

and height of the central fiber, which on average grew from 388 µm and 300 µm to 692 µm and 547 µm, respectively (Fig. 4.1H-I). Cell densities can therefore be used to control the thickness of the tissue, while the ratio between width and height remains constant (Fig. 4.1J). In the following experiments, tissues were created with a cell density of 10^5 cells per mm^2 of pattern, as this density minimizes the number of required cells and results in tissues that closely match the size of the pattern without compromising oxygen and nutrient diffusion within the tissue[548].

The magnetic properties of the bioprinted tissues were monitored over time, as they are central to the entire magnetic bioprinting process. Additionally, for potential future clinical applications, it is important to eventually eliminate the presence of nanoparticles within the tissues through cellular assimilation involving iron metabolism[417]. To investigate whether such assimilation could take place in the bioengineered magnetic muscular tissues, bioprinted tissues were cultured in non-adherent 500µL tubes and their magnetic signals were regularly measured using a benchtop magnetometer[254]. Consistent with previous studies indicating that cells degrade magnetic nanoparticles over time[254,417], the samples exhibited a linear decrease in the magnetic signal with a total loss of about 21% from day 1 to day 20 (Fig. 4.1K).

2. Trapping the magnetic-printed muscle tissue between two magnetic needles

Once removed from the pattern, each tissue is transferred into one of the eight microfabricated chambers of a chip filled with differentiation medium and made of a soft silicone – Ecoflex material (Fig. 4.2A, Supplementary Fig. 4.4), which will allow stretching later on. Each compartment contains two steel needles facing one another at a 2 mm distance, magnetized by a pair of adjacent magnets attracting each other. The magnetic field gradient (Fig. 4.2B) is focused on the tips of the needles: when a tissue is pipette-deposited in the center of a chamber containing the two facing needles, it immediately attaches to the needles with its two clamps (Fig. 4.2C), transforming the muscle construct into a clip-on tissue. Remarkably, the clip-on process is both efficient and reproducible, with a nearly 100% success rate (Fig. 4.2D).

After the tissues are magnetically trapped, they are left to adhere overnight to the needles, with the permanent magnets in place to maintain the attraction forces. It is important to note that these forces are present only near the tips of the needles while the magnetic gradient is close to 0 between the needles. For reference, at a distance of 100 µm from the tips,

simulations indicate that a single magnetized cell experiences an 8000 $T.m^{-1}$ gradient (Fig. 4.2B, Supplementary Fig. 4.5A), resulting in an attractive force of approximately 15 nN on each cell, considering that nanoparticles saturation above 150mT is achieved in cells closer than 400 µm from the needle tips (Supplementary Fig. 4.5B). The next day, the magnets are removed, releasing the initial magnetic forces that facilitated tissue placement, initial attachment, and cohesiveness of the tissue clamps. Since the needles are coated with polydopamine and collagen, tissues remain attached to their respective anchor needles.

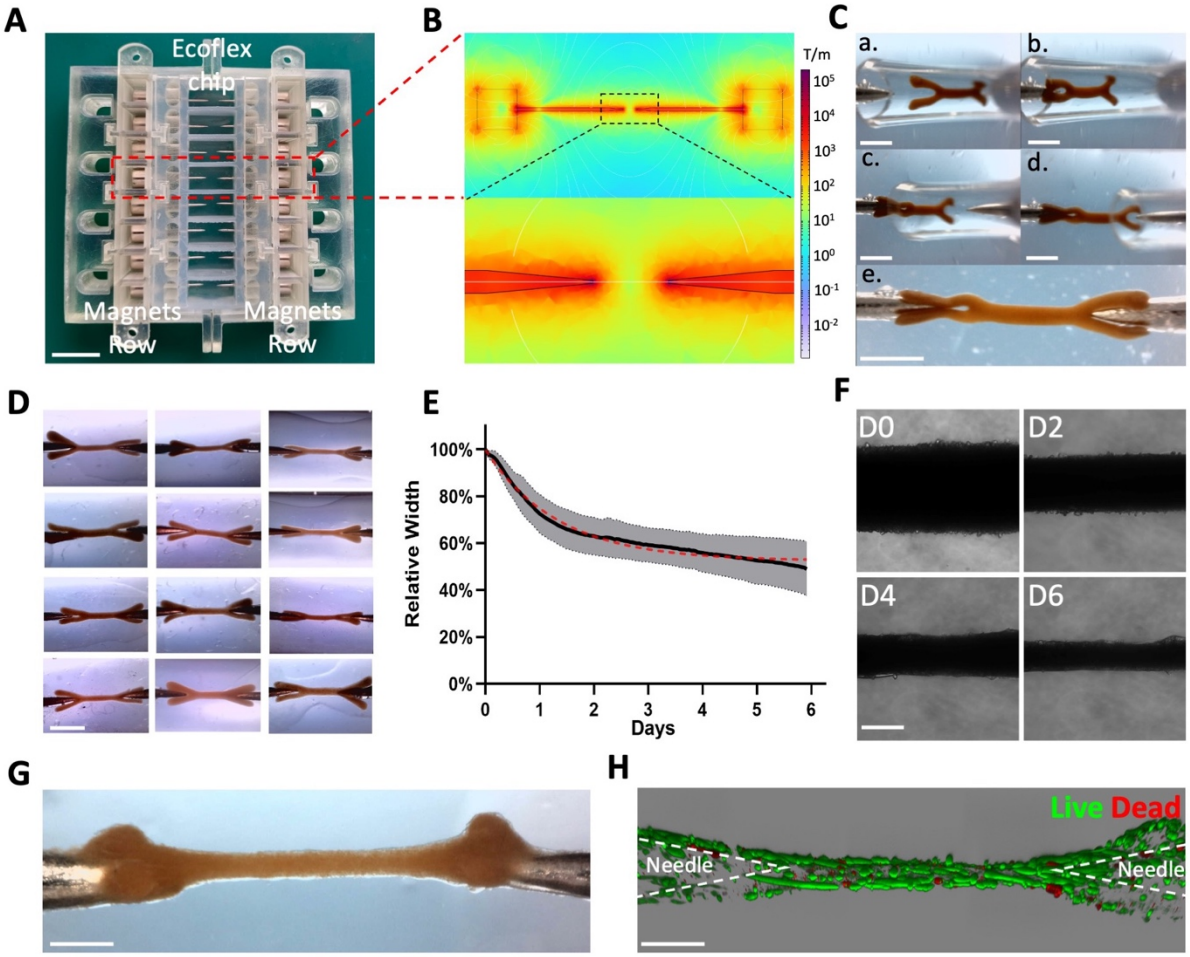

Figure 4.2. Tissue shape is preserved by magnetic trapping. *(A) Ecoflex chip (schematics in supplementary Fig. 4.4B) with 8 compartments of magnetized needles and the adjacent magnet holders (schematics in supplementary Fig. 4.4C). (Scale bar = 2 cm) (B) Magnetic field gradient around the magnets and needles, with a close-up between two needles. (C) Trapping procedure to clip a tissue on two needles. (Scale bar = 1 mm) (D) Tissues made from C2C12 cells clipped on needles. (Scale bar = 2 mm) (E-F) Evolution of the central fiber's width (E) plotted relative to the width on day 0 over 6 days (n=4) and (F) illustrated with bright-field microscopy. (Scale bar = 200 µm) (G-H) Fiber made from C2C12 cells imaged after 6 days of differentiation (G) from the top with a binocular magnifier and (H) with confocal imaging after a LIVE/DEAD assay (live cells in green, dead cells in red). (Scale bar = 500 µm)*

As soon as muscle differentiation is initiated on day 0 by replacing the medium with differentiation medium, the central fibers of the trapped tissues exhibit significant thinning over the following days (Fig. 4.2E-F, Supplementary Fig. 4.6). This thinning initially occurs at an approximately linear rate before gradually plateauing. This evolution can be described by a decreasing exponential curve, characterized by a time constant of approximately 30 hours. Tissues are maintained between the needles for a maximum of 14 days. Thanks to the magnetic trapping and subsequent cellular adhesion, the overall tissue anisotropy is systematically preserved (Fig. 4.2G, Supplementary Fig. 4.7). In contrast, similar tissues cultured in a non-adherent well, free from constraints, quickly lose their shape and eventually become more spherical (Supplementary Fig. 4.7D) to minimize surface tension. Importantly, tissues cultured on the needles for 6 days exhibited almost no cell death with 94 ± 2% of live cells, even at the needle sites, demonstrating the long-term viability of the trapping procedure (Fig. 4.2H, Supplementary Fig. 4.8).

3. Preserving tissue anisotropy for myogenesis

The muscle differentiation is initially assessed by examining internal C2C12 cell reorganization. Figure 4.3A and Supplementary Figure 4.9 show that on day 0 cells are round, mononucleated and organized isotropically. Over time, they progressively fuse together and become increasingly elongated and aligned in the direction of the overall tissue (Fig. 4.3B-C, Supplementary Fig. 4.10A-C, 4.11A-B and 4.12A-C). By day 6, the central fiber of the tissue resembles a fascicle, with giant fused myotubes all aligned in the same direction (Fig. 4.3D-E, Supplementary Fig. 4.13A-D). Regarding cell fusion, from the original population of myoblasts at day 0, only 36% remain mononucleated on day 6, while the remaining 64% fused to form multinucleated myotubes with at least two nuclei (Fig. 4.3F). Notably, 28 % of the original myoblasts developed into multinucleated cells with more than 10 nuclei, some of which contained over 60 nuclei and approached millimeter-scale sizes (Supplementary Fig. 4.14A). At this stage, 53% of the actin filaments are oriented within ± 15° of the fiber's direction, compared to only 18% on day 0. C2C12 cells cultured in 2D showed no overall anisotropy at day 6, and no matter the direction chosen, the percentage of actin filaments within a ± 15° range did not exceed 21% at best (Fig. 4.3G, Supplementary Fig. 4.15A-C). Intriguingly, while the 3D tissues become increasingly anisotropic over time (Fig. 4.3G), some samples on day 6 show a slight shift in the direction of cell alignment. 3D reconstruction reveals that these cells appear to be twisting along the tissue axis, possibly to better distribute forces within the tissue. This shift appears to slightly persist in tissues cultured up to 14 days. However, overall, from day 4 to day 14, the distribution of actin filaments alignment remains mostly constant, with 47% of the filaments still aligned within ± 15° of the fiber's direction on day 14. One noticeable change observed in samples cultured for two weeks (Fig. 4.3H) is the width of the multinucleated myotubes. The average width of myotubes with more than 10 nuclei on day 6 is 35 µm, compared to 11 µm for mononucleated myoblasts on day 0, and further increases to 42 µm after 2 weeks (Fig. 4.3I).

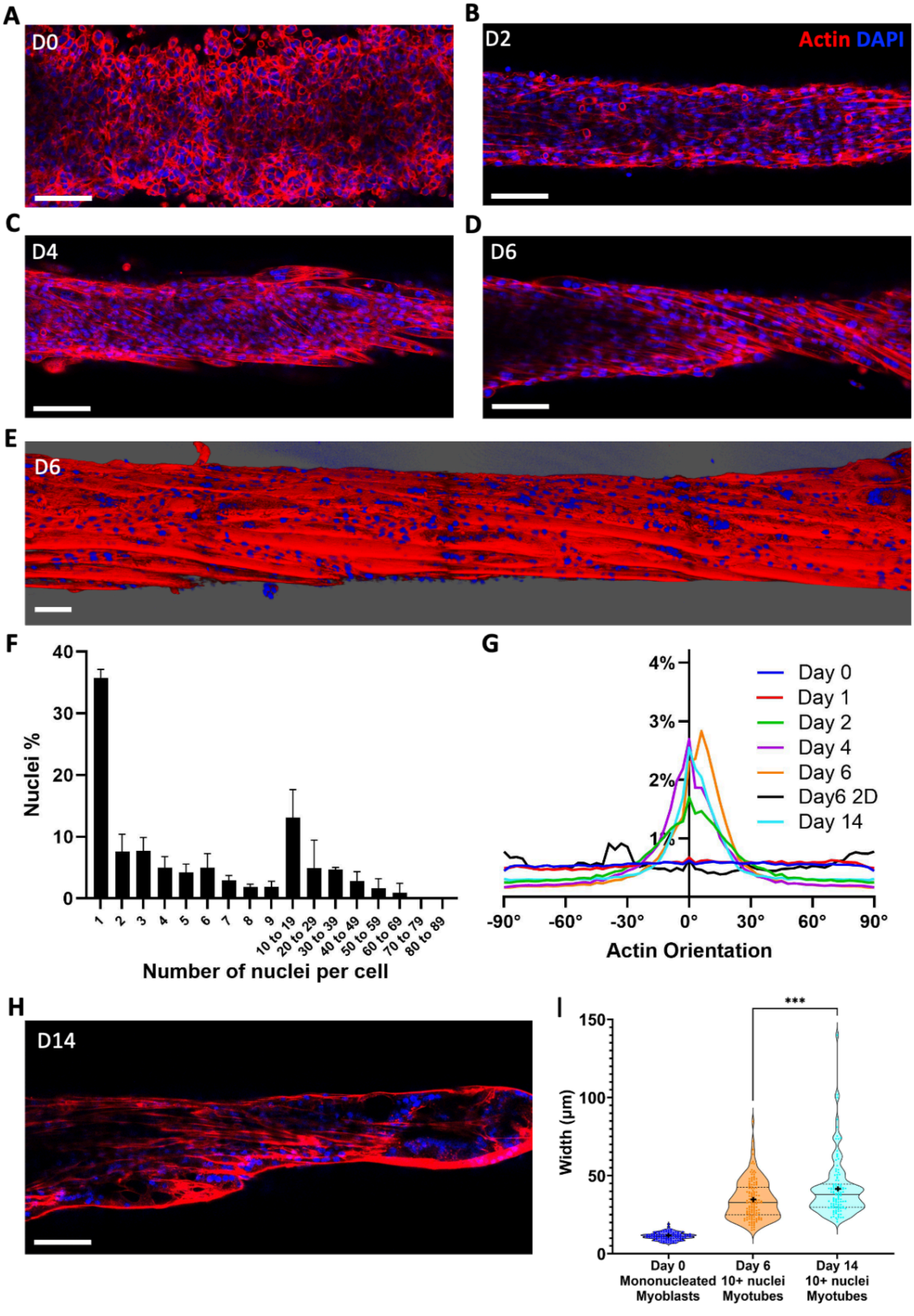
A
D0
B
D2
Actin DAPI
C
D4
D
D6
E
D6
F
Nuclei %
40
30
20
10
0
1
2
3
4
5
6
7
8
9
10 to 19
20 to 29
30 to 39
40 to 49
50 to 59
60 to 69
70 to 79
80 to 89
Number of nuclei per cell
G
4%
3%
2%
1%
Day 0
Day 1
Day 2
Day 4
Day 6
Day6 2D
Day 14
-90°
-60°
-30°
0°
30°
60°
90°
Actin Orientation
H
D14
I
***
150
100
50
0
Width (µm)
Day 0
Mononucleated
Myoblasts
Day 6
10+ nuclei
Myotubes
Day 14
10+ nuclei
Myotubes

Figure 4.3. Constraining the tissue induces anisotropic differentiation and cell fusion. *(A-D) Confocal imaging of a z-slice of the internal cellular structure of a tissue made from C2C12 cells on (A) day 0, (B) day 2, (C) day 4 and (D) day 6. (E) 3D reconstruction from confocal imaging of a fiber on day 6 (actin in red and nuclei in blue). (F) Distribution of nuclei fusion in terms of nuclei percentage on day 6 in the 3D tissues (quantified for 3 samples, 9216 nuclei in total). (G) Distribution of actin filaments orientation in 3D tissues on day 0 (n=3), day 1 (n=4), day 2 (n=3), day 4 (n=4), day 6 (n=5), day 14 (n=4) and in 2D on day 6 (n=3). For each condition, the curve represents the average distribution across all samples. (H) Confocal imaging of a z-slice of the internal cellular structure of a tissue made from C2C12 cells on day 14. (I) Distributions of the widths of mononucleated myoblasts in tissues that were just bioprinted on day 0, and of myotubes with more than 10 nuclei in 3D tissues cultured between two needles for 6 (n=3) and 14 days (n=4). Each data point on the graph represents the measurement of one cell width. (Scale bars = 100 µm)*

4. Stretching improves muscle differentiation

Mechanical cues are omnipresent in skeletal muscle tissue maturation[549–552], and muscle development and functionality largely depend on being subjected to mechanical stretching constraints. The advantage of the magnetic tissue trapping system is its ability to stretch the anisotropic magnetic tissue between the needles at will. To achieve this, the chip containing the eight compartments was mounted on a translation stage with 3D-printed parts (Fig. 4.4A, Supplementary Fig. 4.16), allowing the distance between the needles to be increased, thereby stretching the clamped tissues. Tissue constructs were stretched by up to 100% in a single step on day 1. Remarkably, the central fiber can double in length without detaching or breaking (Fig. 4.4B), leading to an immediate reorganization of the tissue on day 1 (Fig. 4.4C). Cells that are still isotropically organized in the absence of stretching (Fig. 4.4D, Supplementary Fig. 4.10A-C) rapidly elongate and align when the tissue is stretched by 50% (Fig. 4.4E, Supplementary Fig. 4.10D-G), with even more pronounced alignment at 100% strain (Fig. 4.4F, Supplementary Fig. 4.10H-J). At 100% stretching on day 1, the distribution of actin filament orientation resembles that observed on day 6 without stretching, with 52 % of the actin filaments oriented within ± 15° of the fiber. This indicates that stretching places the tissue in conditions that match a more advanced stage of differentiation.

As the stretched tissues continue to mature over time (Supplementary Fig. 4.11C-J and 12D-H), they not only become thinner by day 6 (Fig. 4.4G-I, Supplementary Fig. 4.6, 4.13E-K, and 4.17), but also display better alignment and cell fusion compared to tissues that were not stretched. Furthermore, twisting was no longer observed under stretching, and the distribution of actin filament orientation became narrower, with 66 % of the filaments aligned within ± 15° of the fiber on day 6 (Fig. 4.4J). Conversely, tissues cultured in a non-adherent well, totally free from constraints, exhibit no anisotropy in actin orientation (less than 19% of the filaments within ± 15° no matter the reference direction chosen) and show minimal fusion (Supplementary Fig. 4.15D-I). In tissues stretched by 100%, on day 6, 24% of the original

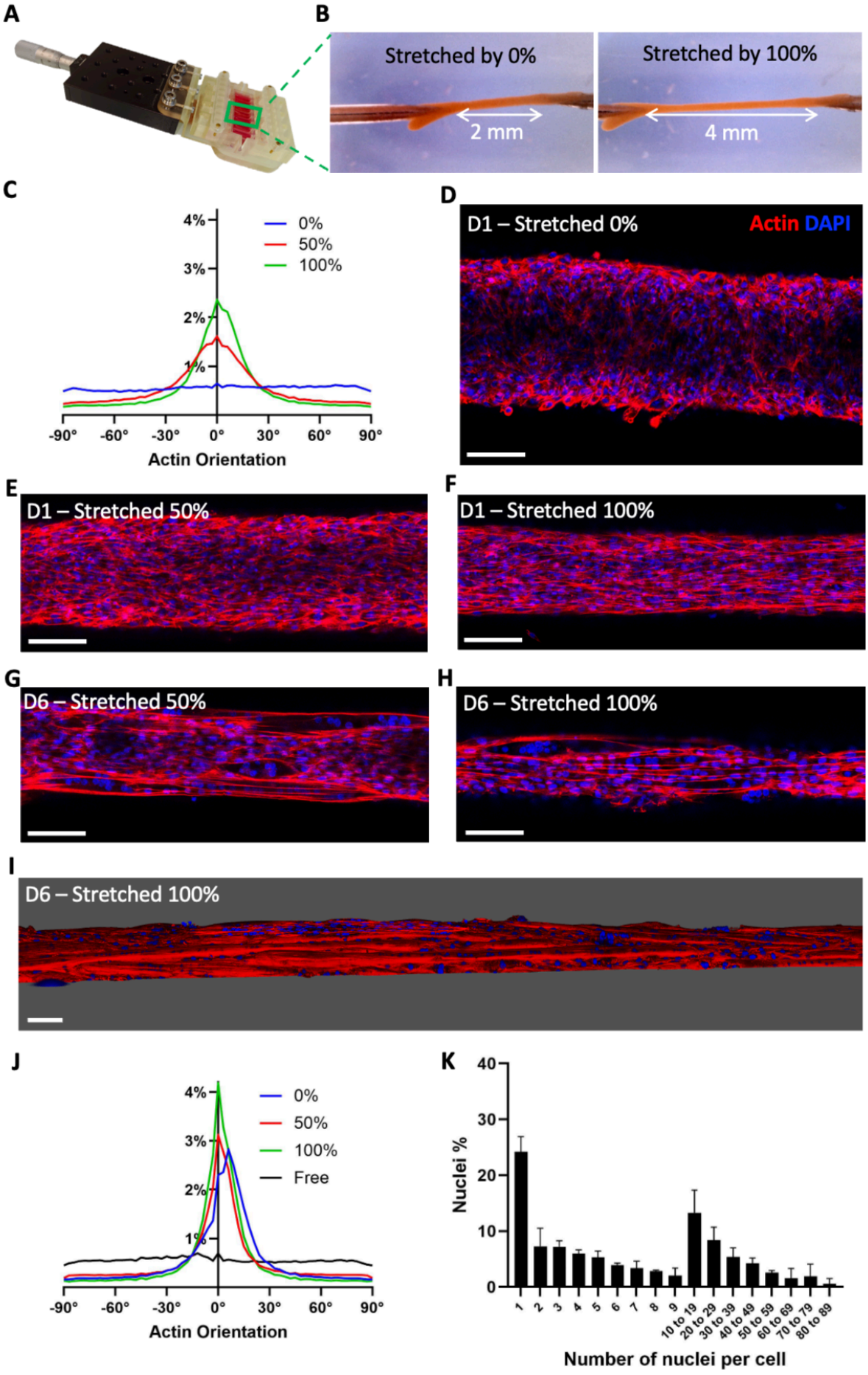
A
B
Stretched by 0%
2 mm
Stretched by 100%
4 mm
C
4%
3%
2%
1%
0%
50%
100%
-90°
-60°
-30°
0°
30°
60°
90°
Actin Orientation
D
D1 – Stretched 0%
Actin DAPI
E
D1 – Stretched 50%
F
D1 – Stretched 100%
G
D6 – Stretched 50%
H
D6 – Stretched 100%
I
D6 – Stretched 100%
J
4%
3%
2%
1%
0%
50%
100%
Free
-90°
-60°
-30°
0°
30°
60°
90°
Actin Orientation
K
Nuclei %
40
30
20
10
0
1
2
3
4
5
6
7
8
9
10 to 19
20 to 29
30 to 39
40 to 49
50 to 59
60 to 69
70 to 79
80 to 89
Number of nuclei per cell

Figure 4.4. Anisotropy and cell fusion are enhanced by stretching the tissues. *(A-B) Stretching system used to stretch (A) the chips and therefore (B) the tissues. (C) Distribution of the actin filaments orientation in tissues stretched by 0% (n=4), 50% (n=5) and 100% (n=4) on day 1. For each condition, the curve represents the average distribution across all samples. (D-H) Confocal imaging of a z-slice showing the internal structure of a C2C12 tissue on day 1 stretched by (D) 0%, (E) 50%, or (F) 100% and on day 6 after (G) 50% and (H) 100% stretching since day 1 (actin in red and nuclei in blue). (I) 3D reconstruction from confocal imaging of a tissue on day 6 stretched by 100 %. (J) Distribution of the actin filaments orientation on day 6 in trapped 3D tissues stretched since day 1 by 0% (n=5), 50% (n=3) and 100% (n=4) and in 3D free-floating tissues cultured free of constraints (n=3). For each condition, the curve represents the average distribution across all samples. (K) Distribution of nuclei fusion in terms of nuclei percentage at day 6 in 3D tissues stretched by 100% (quantified for 3 samples, 12522 nuclei in total). (Scale bars = 100 µm)*

myoblasts are still mononucleated while 76% have fused into myotubes (Fig. 4.4K), representing a significant improvement compared to non-stretched tissues. Stretching also increased the proportion of nuclei belonging to cells with more than 10 nuclei, reaching 38%. Maximum cell fusion and elongation are also improved, with some cells containing over 80 nuclei and measuring up to 2 mm in length (Supplementary Fig. 4.14B).

To further assess the mechanical stresses in the trapped tissues and examine their role in myogenesis, we embedded within the tissues deformable 42 ± 5 µm spherical polyacrylamide beads coated with fluorescent poly-L-lysine for cell adhesion (Fig. 4.5A-5D, Supplementary Fig. 4.18). These deformable beads were previously used to measure internal stresses in tissues, such as in zebra-fish embryos[553]. Confocal imaging provided the aspect ratio (Fig. 4.5E) and orientation of the beads relative to the direction of the tissue (Fig. 4.5F). Notably, stretching the tissue on day 1 increases the aspect ratio of the beads to 1.80 ± 0.14, and the orientation distribution of the beads becomes more aligned with the tissue direction. Remarkably, the aspect ratio of beads in non-stretched conditions on day 6 was 1.88 ± 0.31, close to the 1.80 value found at day 1 immediately after stretching, confirming that stretching places the tissue in a more advanced maturation stage, at least from a mechanical point of view.

Generation of contractile force and calcium transients in response to chemical stimulation is also a key functional signature of skeletal muscles. To complement the mechanical characterization provided by the beads with information on functionality, calcium imaging was performed on tissues with and without the addition of acetylcholine (ACh), a neurotransmitter that induces an influx of calcium ions in skeletal muscle, triggering contraction[268]. For optimal visualization, tissues were detached from the needles and imaged with a spinning-disk microscope. While the calcium signal in cells from tissues imaged immediately after bioprinting (day 0) remained constant, the tissues exhibited some fluctuations in their calcium activity after 6 days of culture (Fig. 4.5G), even without ACh. After treating them with 1 mM of ACh, the control samples on day 0 showed no response, except for a slight

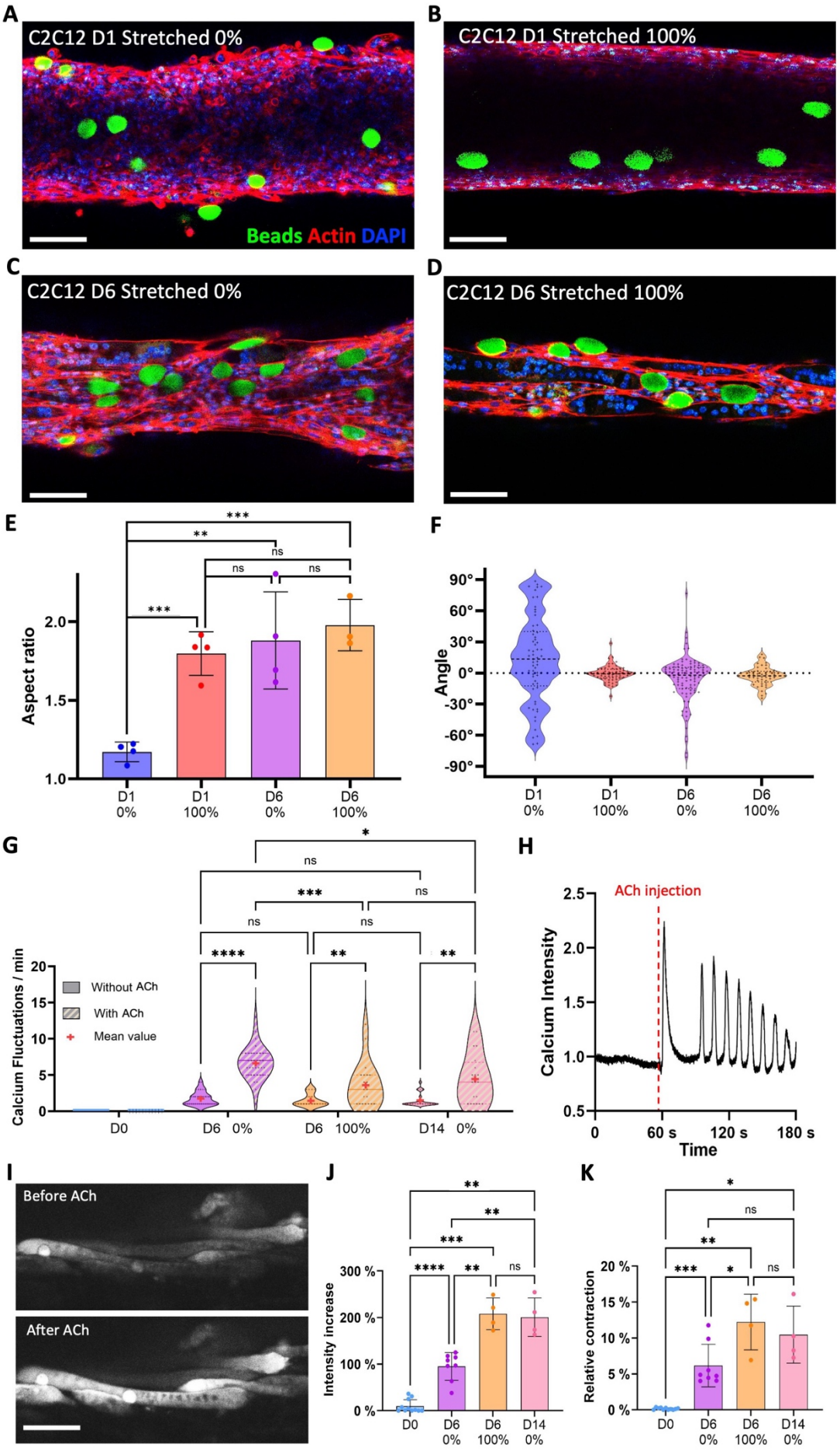
A
C2C12 D1 Stretched 0%
Beads Actin DAPI
B
C2C12 D1 Stretched 100%
C
C2C12 D6 Stretched 0%
D
C2C12 D6 Stretched 100%
E
Aspect ratio
D1 0%
D1 100%
D6 0%
D6 100%
F
Angle
G
Calcium Fluctuations / min
Without ACh
With ACh
Mean value
D0
D6 0%
D6 100%
D14 0%
H
ACh injection
Calcium Intensity
Time
I
Before ACh
After ACh
J
Intensity increase
K
Relative contraction

Figure 4.5. Deformable beads and calcium imaging reveal stresses and contractility are similar in early stretched tissues and differentiated tissues. *(A-D) Confocal images of polyacrylamide beads in tissues made from C2C12 cells on day 1 stretched by (A) 0% and (B) 100%, and on day 6 with an initial stretching of (C) 0% and (D) 100% (beads in green, actin in red and nuclei in blue). (E) Aspect ratio and (F) distribution of the orientation of beads in tissues on days 1 and 6 whether they were stretched by 0% or 100%. Data points represent the average bead aspect ratio within one sample, and the angles of all beads across all samples. (G) Distribution of the frequencies of cellular calcium fluctuations in tissues on day 0, day 6 (whether they were stretched by 0% or 100%), and day 14 (non-stretched) before and just after treating them with 1 mM of ACh. For each tissue, measurements were taken from 5 different cells exhibiting fluctuations, before and after ACh treatment, and each of these measurements was represented as one point on the plot. Samples on day 0 showed no fluctuations, but a line at 0 was placed for reference. (H) Kymograph of the calcium signal in a cell and (I) spinning disk microscope imaging from a non-stretched tissue on day 6 before and after exposure to 1 mM of ACh. (J) Relative increase of signal intensity and (K) tissue contraction after treating tissues collected on day 0, day 6 (whether they were stretched by 0% or 100%) and day 14 (non-stretched) with 1 mM ACh. (Scale bars = 100 µm)*

increase in signal (Supplementary Fig. 4.19A). However, in 6- and 14-day-old tissues, ACh treatment not only induced increased calcium fluctuations, as shown in the kymographs in Figure 4.5H and supplementary Figure 19, but also enhanced the overall intensity of the calcium signal within the tissues (Fig. 4.5I-5J) and triggered tissue contraction (Fig. 4.5I and 5K). While the frequency of fluctuations increased the most in non-stretched tissues on day 6, with an average of 6.7 fluctuations per minute (Fig. 4.5G), both the relative increase in signal intensity and tissue contraction following ACh treatment were twice as high in stretched tissues. Notably, non-stretched tissues cultured for 14 days exhibited responses closer to those of stretched tissues, supporting the hypothesis that stretching could help tissues reach later stages of differentiation faster. One possible explanation for the greater increase in fluctuations in non-stretched tissues is that in stretched tissues, while some cells exhibited increased calcium fluctuations (Supplementary Fig. 4.19B), others showed significantly higher calcium intake (Supplementary Fig. 4.19C). This could lead to tetanic contraction and suggests that stretched tissues may be more sensitive to ACh.

5. Transposing to myoblasts derived from human induced pluripotent stem cells

The two-fold method of magnetic bioprinting and tissue trapping was then applied to myoblasts derived from human induced pluripotent stem cells (hiPSC) to validate its effectiveness in a more clinically relevant model. A transgene-free differentiation protocol was used to generate a homogenous population of myogenic progenitor cells from a healthy hiPSC

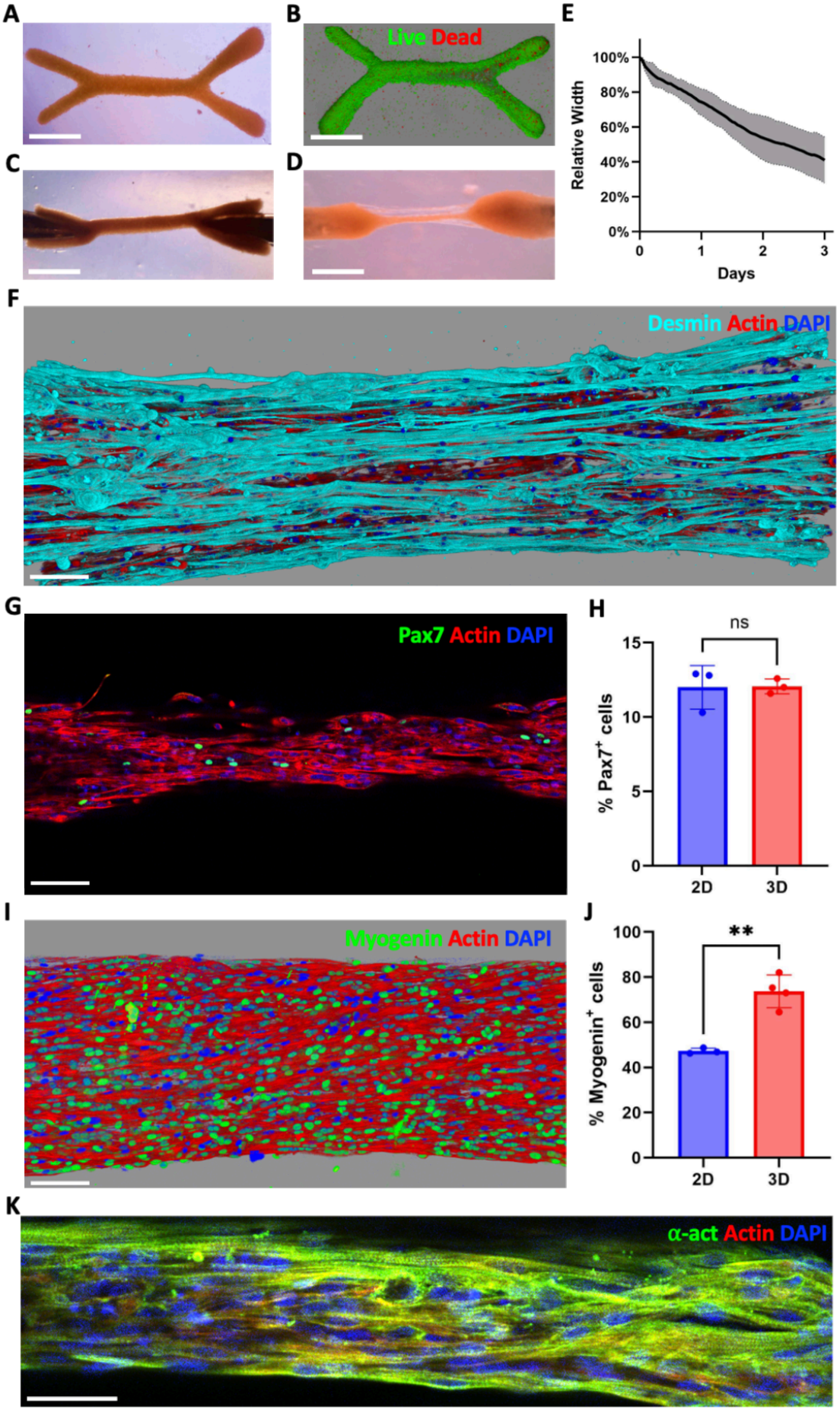
A
B
Live Dead
C
D
E
Relative Width
100%
80%
60%
40%
20%
0%
0
1
2
3
Days
F
Desmin Actin DAPI
G
Pax7 Actin DAPI
H
ns
% Pax7+ cells
15
10
5
0
2D
3D
I
Myogenin Actin DAPI
J
**
% Myogenin+ cells
100
80
60
40
20
0
2D
3D
K
α-act Actin DAPI

Figure 4.6. Differentiation is improved in 3D tissues bioprinted from M-hiPSC. *(A-D) Wrench shaped tissue patterned with M-hiPSC imaged (A) after patterning, (B) with confocal imaging after LIVE/DEAD assay (live cells in green, dead cells in red), trapped between needles on (C) day 0 and (D) day 6. (Scale bar = 1 mm) (E) Evolution of central fiber's width from day 0 to day 3 (n=3). (F) 3D reconstructions from confocal imaging of a 6-day-old tissue immunostained in cyan for desmin. (G) Confocal imaging of a 6-day old tissue immunostained in green for Pax 7 and (H) proportions of Pax 7 positive cells. (I) 3D reconstruction from confocal imaging of a 6-day old tissue immunostained in green for myogenin and (J) proportions of myogenin positive cells. (Scale bar = 100 µm) (K) Confocal imaging of a 6-day old tissue immunostained in green for alpha-actinin. (Scale bar = 50 µm) (Actin in red, DAPI in blue).*

line within 4 weeks. Magnetic labeling of these hiPSC-derived myogenic cells resulted in each cell internalizing approximately 17 pg of iron (Supplementary Fig. 4.20). Figures 4.6A and 4.6B, along with supplementary Figure 4.21 demonstrate that M-hiPSC can be magnetically bioprinted and that the resulting tissues are viable (94 ± 2% of live cells). These tissues derived from M-hiPSC could be clipped onto the magnetic needles (Fig. 4.6C) and successfully cultured for 6 days (Fig. 4.6D, Supplementary Fig. 4.22), proving the successful transposition of the technique to M-hiPSC. The central fibers once again exhibited a decrease in width over time (Fig. 4.6E), however this reduction was more pronounced than in tissues derived from mouse myoblasts, reaching about 40% of their original width after 3 days, compared to approximately 60% in the latter (Fig. 4.2E).

Immunostainings were performed on day 6 to assess specific skeletal muscle markers. Figure 4.5F and Supplementary Figure 4.23A-E confirmed the presence of desmin, a muscle-specific protein[554], throughout the tissue, as well as myosin heavy chains (Supplementary Fig. 4.24A). Pax7, an indicator of satellite-like cells essential for muscle development and repair[555],was found in 12.1 ± 0.5% of cells in the 6-day-old 3D tissues (Fig. 4.6G-H, Supplementary Fig. 4.25A-B), a proportion similar to that observed in 2D controls (Supplementary Fig. 4.26). To evaluate the number of myoblasts that started differentiating in the tissues, myogenin, a transcription factor for muscle differentiation[556], was analyzed (Fig. 4.5I, Supplementary Fig. 4. 27A-C and 4.28A-B). On day 6, 73.7 ± 7.2% of cells were positive for myogenin, representing a significant increase compared to 2D controls (Fig. 4.6J, Supplementary Fig. 4.29). To gain deeper insight into the internal architecture of the cells, Figure 4.6K and Supplementary Figure 4.30 show the alpha-actinin filaments, which highlight the presence of striations - the hallmark of the sarcomeres[557], the contractile units of muscle tissue. Finally, about half of the 3D samples showcased sporadic spontaneous contractions by day 6, further validating the presence of the contractile apparatus in the muscle cells.

The deformation of elastic beads embedded in tissues made of M-hiPSC (Supplementary Fig. 4. 31A-H) also evidenced the stresses the cells were developing within the

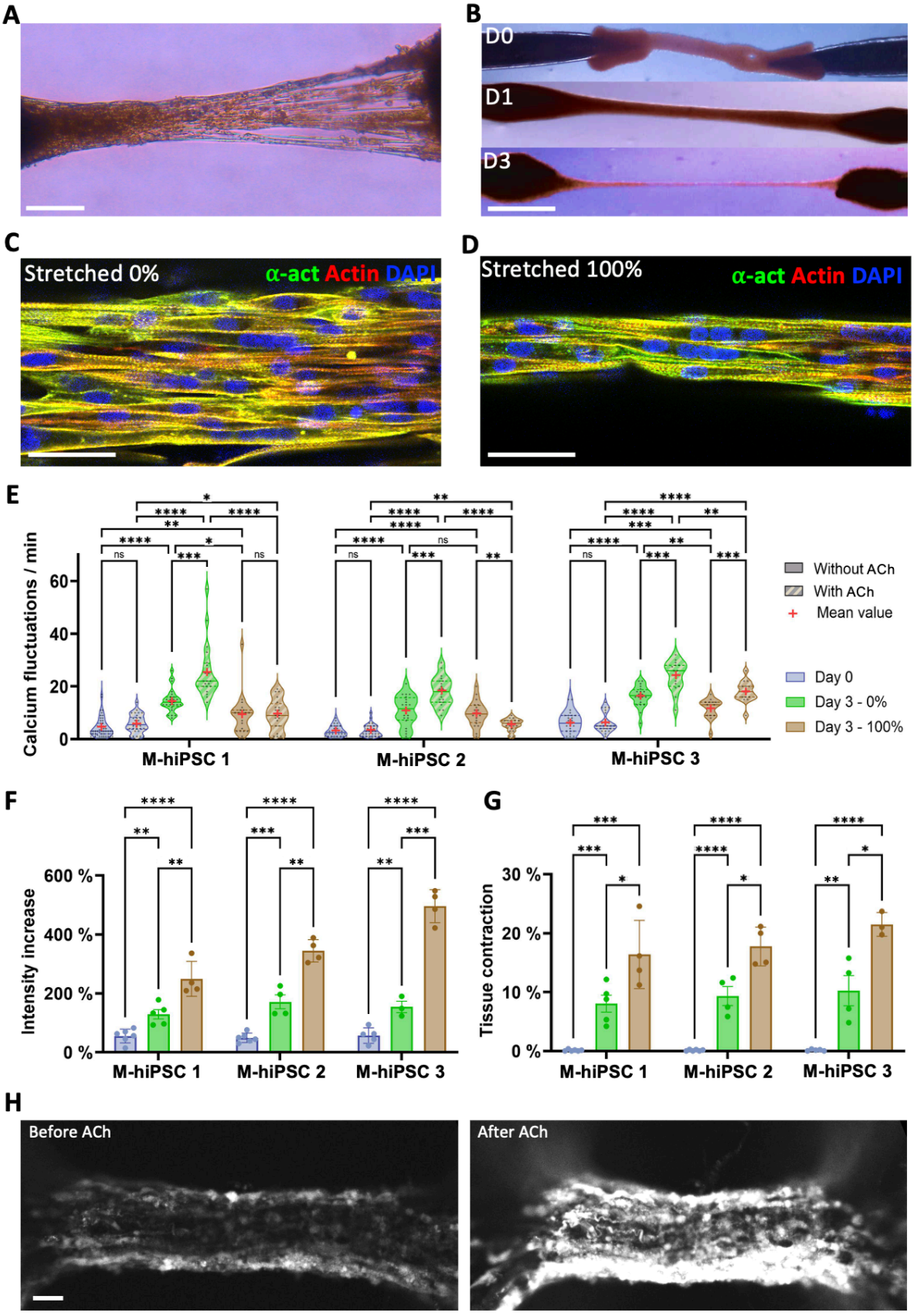

Figure 4.7. Stretching tissues made from the three different M-hiPS cell lines increases tissue contractility. *(A) 3D tissue made with M-hiPSC-1 on day 3. (Scale bar = 200 µm) (B) Trapped*

tissue on day 0, and after 100% stretching on days 1 and 3. (Scale bar = 1 mm) (C-D) Confocal imaging of 3-day-old M-hiPSC 1 tissues immunostained in green for alpha-actinin with (C) 0% and (D) 100% stretching. (E) Distribution of the frequencies of calcium fluctuations in M-hiPS cells from tissues on day 0 and on day 3 whether they were stretched by 0% or 100%, before and just after treating them with 1 mM of ACh. For each tissue, measurements were taken from 5 different cells exhibiting fluctuations, before and after ACh treatment, and each of these measurements was represented as one point on the plot. (F) Relative increase in signal intensity and (G) tissue contraction after 1 mM ACh treatment in tissues collected on day 0 and day 3 whether they were stretched by 0 or 100%. (H) Spinning-disk microscope imaging on day 3 of a M-hiPSC 2 tissue stretched by 100%, before and after exposure to 1 mM of ACh. (Scale bar = 50 μm)

tissues over time. Although the beads exhibited the highest aspect ratio (Supplementary Fig. 4.31I) and anisotropy (Supplementary Fig. 4.31J) on day 6, most of their deformation along the tissue's axis appeared to occur within the first 3 days of differentiation.

6. Stretching improves functionality and specialization

Interestingly, some samples exhibited sporadic spontaneous contractions as early as day 3. Combined with the rapid thinning of the tissue (Fig. 4.7A) and the significant deformation of the beads by day 3, this points to fast differentiation. We thus investigated the effect of stretching on tissues cultured for 3 days, across three different M-hiPS cell lines (referred to as M-hiPSC 1, for the first cell line studied, 2 and 3 for the two additional ones). Magnetic trapping of tissues bioprinted with M-hiPSC 2 and 3 are illustrated in Supplementary Fig. 4.32. Tissues made from all three M-hiPS cell lines were successfully stretched by 100% on day 1 (Fig. 4.7B) and formed thin fascicle like structures by day 3. Alpha-actinin striations were observed in all conditions at day 3 (Fig. 4.7C-D), indicating that the contractile apparatus is already in place after 3 days, which was further assessed through calcium imaging. On day 0, fluctuations were present in all cell lines, with an average frequency within flickering cells of 4.7 fluctuations per minute (Fig. 4.7E, Supplementary Fig. 4.33A). This value significantly increased after 3 days, reaching 13.9 and 10.2 fluctuations per minute for samples stretched by 0% and 100%, respectively (Fig. 4.7E, Supplementary Fig. 4.33B). Upon 1 mM ACh treatment, fluctuations consistently increased for non-stretched tissues, reaching more than 20 fluctuations per minute on average at day 3. ACh treatment also led to an increase in signal intensity (Fig. 4.7F, Supplementary Fig. 4.33C) and contraction (Fig. 4.7G-H) of all 3-day old tissues, with effects being twice as high on average in stretched tissues compared to non-stretched tissues.

Immunofluorescence staining and confocal imaging were next performed to better characterize 3-day-old tissues. Cells are expressing desmin (Fig. 4.8A-C, Supplementary Fig. 4.23F-Q) and myosin heavy chains (Supplementary Fig. 4.24B-D) in all conditions. Stretching then appears to significantly impact the populations of myogenin positive (Fig. 4.8D-F, Supple-

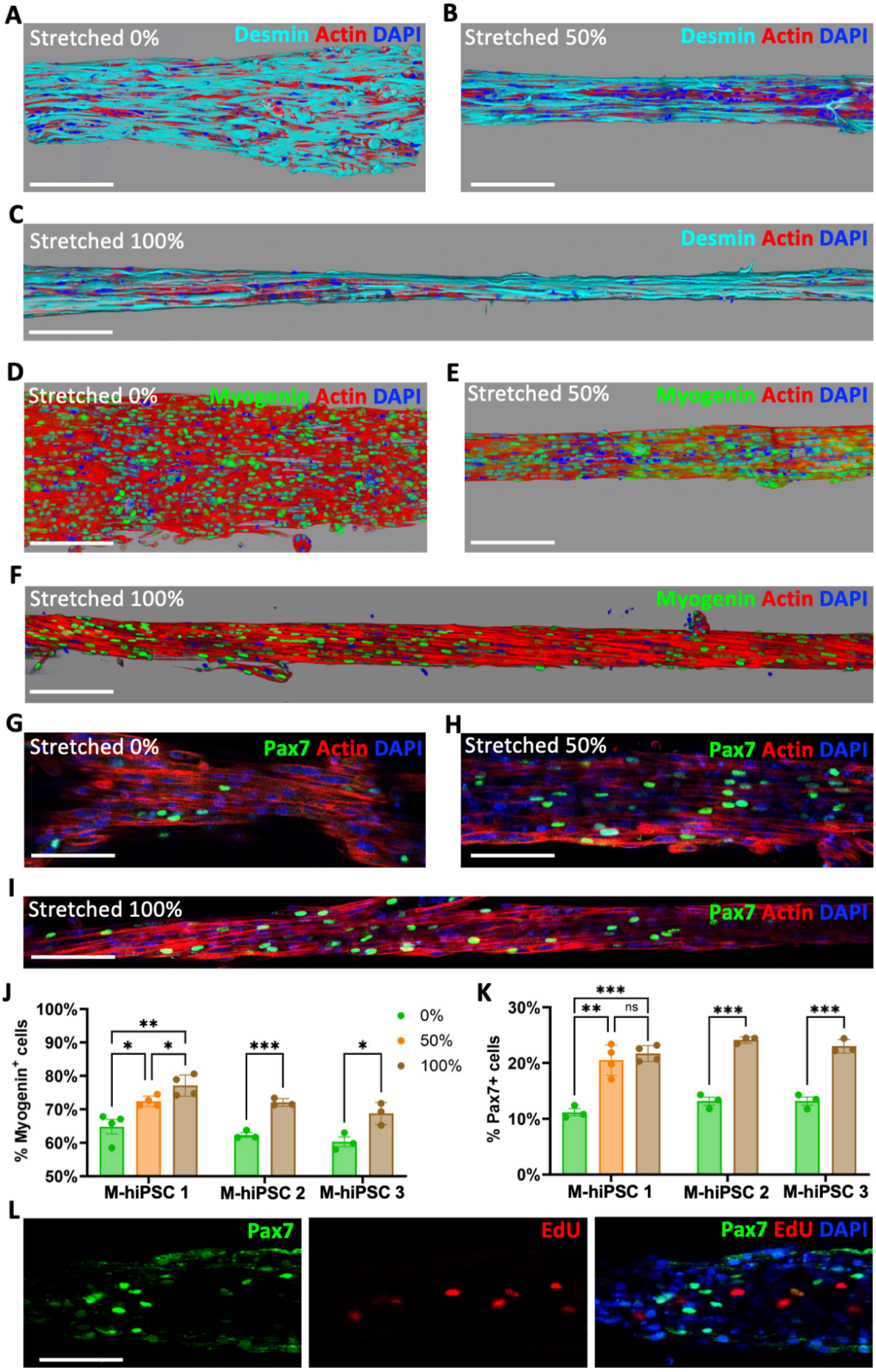
A
Stretched 0%
Desmin Actin DAPI
B
Stretched 50%
Desmin Actin DAPI
C
Stretched 100%
Desmin Actin DAPI
D
Stretched 0%
Myogenin Actin DAPI
E
Stretched 50%
Myogenin Actin DAPI
F
Stretched 100%
Myogenin Actin DAPI
G
Stretched 0%
Pax7 Actin DAPI
H
Stretched 50%
Pax7 Actin DAPI
I
Stretched 100%
Pax7 Actin DAPI
J
% Myogenin+ cells
100%
90%
80%
70%
60%
50%
**
*
*
***
*
0%
50%
100%
M-hiPSC 1
M-hiPSC 2
M-hiPSC 3
K
% Pax7+ cells
30%
20%
10%
0%
***
**
ns
***
***
M-hiPSC 1
M-hiPSC 2
M-hiPSC 3
L
Pax7
EdU
Pax7 EdU DAPI

Figure 4.8. Stretching tissues made from M-hiPSC increases the number of myogenin and Pax7 positive cells. *(A-C) 3D reconstructions from confocal imaging of 3-day-old M-hiPSC 1 tissues immunostained in cyan for desmin with (A) 0%, (B) 50% and (C) 100% stretching. (D-F) 3D reconstructions from confocal imaging of 3-day-old M-hiPSC 1 tissues immunostained in green for myogenin with (D) 0%, (E) 50% and (F) 100% stretching. (Scale bar = 200 µm) (G-I) Confocal imaging of 3-day old M-hiPSC 1 tissues immunostained in green for Pax 7 with (G) 0%, (H) 50% and (I) 100% stretching. (Actin in red, nuclei in blue). (J-K) Proportions of (J) myogenin positive cells and (K) Pax7 positive cells on day 3 in tissues made from all three M-hiPS cell lines whether they were stretched by 0%, 50% or 100% since day 1. (L) Confocal imaging of the different color channels of a 3-day old M-hiPSC 1 tissue stretched by 100% with proliferative cells labeled with EdU and then immunostained for Pax 7 (Pax7 in green, EdU in red, nuclei in blue). (Scale bar = 100 µm)*

mentary Fig. 4.27D-O and 4.28C-K) and Pax7 positive (Fig. 4.8G-I, Supplementary Fig. 4.25C-J) cells. In tissues made from M-hiPSC 1, the number of myogenin positive cells at day 3 increases with stretching, rising from 64.8 ± 4.3% without stretching to 77.1 ± 3.2% with 100% stretching (Fig. 4.8J), and stretching doubles the number of Pax7 positive cells, which goes from 11.2 ± 1.1% without stretching to 21.7 ± 1.5% with 100% stretching (Fig. 4.8K). These increases were also observed in M-hiPSC 2 and 3 (Fig. 4.8J-K). EdU staining confirmed that most Pax7 positive cells in stretched samples are quiescent (Fig. 4.8L), with only 9.9 ± 2.7% proliferative cells among Pax7-positive cells across the three cell lines, which is similar to the 7.9 ± 1.3% in non-stretched 3-day old samples and 9.6 ± 0.9% at day 0. This further reinforces the idea that stretching not only increases the number of cells starting to differentiate but also promotes the presence of satellite-like cells.

Finally, gene expression analysis was performed on day 3 on M-hiPSC 1 cells to quantify the levels of four different isoforms of myosin heavy chains: one embryonic form (Myh3), one neonatal form (Myh8) and two adult forms (Myh1 and Myh2) (Supplementary Fig. 4.34). Although significant differences were not observed between all conditions, both the embryonic and neonatal isoforms displayed increasing trends in non-stretched 3D samples and decreasing ones in tissues stretched by 100%. Without stretching, Myh1 expression was similar in 2D and 3D, while Myh2 was slightly lower in 3D. However, stretching led to increasing trends in the expression of these two adult isoforms of myosin, with significant differences for Myh2 in tissues stretched by 100%.

III. Discussion

In this work, we demonstrate the engineering of 3D mature muscle tissue using magnetic forces. These forces serve (1) to precisely bioprint the tissue into any desired shape without the need for a supporting matrix, and (2) to maintain its shape or even stretch it, thereby promoting muscle maturation.

The next-generation magnetic bioprinting method with high-resolution NiFe patterns produces shape-controlled 3D tissues in just 3 hours. The use of NiFe patterns as customized magnets enhances previous magnetic bioprinting methods[46,55,59,60] by providing improved control over the geometry and competes effectively with traditional bioprinting approaches[42–44] enabling precise shape control. Despite the significant advancements brought by bioink-based bioprinting to 3D tissue engineering, it still faces limitations, such as external stresses applied to cells during the printing process and the lack of physiological relevance of certain bioinks. Additionally, matrix can limit cell density[261], posing a challenge when differentiating muscle precursor cells into muscle fibers. Magnetic bioprinting offers distinct advantages. Although the absence of matrix makes tissue cohesion more challenging and necessitates the use of a higher number of cells, this approach allows the creation of tissues composed of densely packed cells. This high cell density reduces the dependency on an extracellular matrix, relying instead on adhesive molecules produced by the cells themselves. Consequently, magnetic bioprinting enables the fabrication of tissues that more closely mimic the cellular composition and density of native tissues.

The magnetic properties of the cells were not only used for bioprinting tissues with controlled geometry but also for trapping the tissue between two magnetic attractors. This magnetic clipping function complements remote magnetic actuation techniques, which have primarily been applied for targeting therapeutic agents, controlling cell migration[47,558,559] or triggering mechanotransduction[54–56]. One major advantage of magnetic clipping is its ability to maintain the tissue's geometry over time. Preserving the anisotropy of a tissue, such as muscle, is crucial for its function, but remains challenging[31] for contractile tissue, as evidenced in Supplementary Figures 4.7D and 4.15D-I without the clipping function. Systems where the tissue is moulded in a tube or extruded typically provide good anisotropy over the entire tissue[224,258]. However, moulded gels can be colonized[46], may not be biomimetic, or are simply used as sacrificial moulds[258]. The magnetic clipping approach shares similarities with systems where tissue matures around two posts[42,260–267,269–272,280]. This post-method, introduced over two decades ago[261], has become a stapple of muscle tissue engineering. Despite numerous variations, few alternative approaches have emerged, aside mostly from bioprinting[43] and tube moulding[224,258] (Table 4.1). All these methods rely on extracellular matrix for tissue cohesion. For those that do not, only tissues at much smaller scale - typically in the range of a few hundred micrometers[263] - have been successfully achieved (Table 4.1). Thus, having a novel method to

produce scaffold-free tissues at the centimeter scale with precise control over both their initial and final shape using remote magnetic actuation could be beneficial for skeletal muscle tissue engineering. This is particularly advantageous when tissue maturation can be further enhanced through stretching.

The magnetic approach proposed here has successfully enabled the engineering of skeletal muscle tissue with a high level of differentiation within a few days, both with immortalized C2C12 cells and even with M-hiPS cells. This cell type has only recently been used to create 3D constructs[262,268,269]. Here, indicators of differentiation after a week, such as the presence of myogenin-positive cells, were markedly higher to those observed in M-hiPS 2D cultures. Human iPS-derived muscle cells exhibited spontaneous contractions after just three days of culture in our system, when they are usually reported after at least a week[268]. Functionality was assessed by calcium imaging in absence or presence of acetylcholine, with responses within just 3 days, comparable to those reported in other studies[268,270] after more than a week with higher ACh concentrations. Other studies have also investigated functionality by examining the force response upon electrical stimulations[260,262,267–272] (Table 4.1), which could also be explored in combination with mechanical stimulation in our system for future studies. Importantly, high levels of maturation in our systems as early as day 3 were further evidenced by the high percentage of myogenin-positive cells and the presence of clear sarcomeric striations in most cells. This crucial feature of muscle differentiation is usually expected after one week[268,269,272] and is not always reported in muscle constructs[42,260,265,267,280]. One study[268] showed that about 20% of nuclei belonged to striated cells after a week of culture, and 50% after 2 and 4 weeks. In contrast, we achieved here high levels after only 3 days of maturation.

Furthermore, stretching significantly enhanced maturation, with alignment and differentiation improving in tissues stretched by 100%. Indeed, stretching further increased both the populations of myogenin and Pax7 positive cells after only two days in tissues generated from M-hiPSC. While the role of stretching on muscle cell differentiation has mostly been studied with C2C12 cells[46,265–267,280] and with primary human skeletal muscle cells[261,272] (Table 4.1), its impact on myoblasts derived from hiPS cells remains to be fully explored. This study shows that stretched samples from hiPS-derived myoblasts exhibit levels of myogenin positive cells similar to the ones observed after 2 weeks of culture in another study[268]. Moreover, the number of Pax7-positive cells doubles in stretched tissues compared to non-stretched ones at day 3, despite being quiescent and likely satellite-like. This, to the best of our knowledge, has not been observed before and would require further investigation to understand the impact of mechanical stress on Pax7 positive, and more specifically satellite, cells. The enhanced response to ACh in stretched samples also highlights the significant role of mechanical cues in myogenesis, with stretched samples contracting by approximately 20% - twice more than non-stretched samples - when stimulated with ACh after just 3 days. It is important to note that 100% stretching is far beyond physiological levels, especially in comparison to other approaches that rarely exceed 20% stretching (Table 4.1). However, in the context of *in vitro*

Ref.[a]	Cell type[b]	Days[c]	Tissue engineering Approach	Scaffold	Size[d] (mm)	Mechanical stimulations	Other Stimulations	Force evaluation
[42]	Mouse mesoangioblasts - Muscle-derived human mesenchymal stem cells	30	Extrusion of photopolymerized fiber on C-shape support	PEG-Fibrinogen (8 $mg.mL^{-1}$), 0.1% $w.v^{-1}$ Irgacure 2959	40	No	No	No
[43]	Human muscle progenitor cell	9	Extrusion based bioprinting with sacrificial gelatin bioink	Fibrinogen (20 $mg.mL^{-1}$), gelatin (35 $mg.mL^{-1}$), hyaluronic acid (3 $mg.mL^{-1}$), 10% (v/v) glycerol	15	No	No	No
[260]	Primary rat myoblasts	42	Seeding cells on a fibrin gel with two anchors	500 µL medium with thrombin (10$U.mL^{-1}$) with 200µL fibrinogen (20 $mg.mL^{-1}$)	12	No	Electrical (15 V, 1.2 ms single pulse & 1 s train of 1.2 ms 10-150 Hz pulses)	Force transducer
[261]	Primary human skeletal muscle cells	16	Casting a cell-loaded gel in a well with two pins	Collagen I (0.8 $mg.mL^{-1}$), Matrigel (1:6 v/v)	25	10% / 4 days strain & later cycles of 3 sets of 5 2 s pulses (5% strain for 2 days, 10% for 2 days, 15% for 4 days)	Cytochalasin D (2-5 µM)	Force transducer
[262]	C2C12 - M-hiPS cells	28	Injection of cell loaded gel in microfluidic chamber with two pillars, with motor neuron spheroid in another chamber	Collagen I (2.4 $mg.mL^{-1}$), Matrigel (10%)	1.5	No	Electrical (0.5-4Hz, 12V) Glutamic acid (0.1-5mM), tetrodotoxin (1 µM), bosutinib (100 µM) & rapamycin (200 nM)	Pillar deflection
[263]	Immortalized (healthy and pathological) and primary human myoblasts	14	Seeding cells on pillars micropatterned with Matrigel	No matrix	0.2	No	ACh (20 µM)	Pillar deflection
[264]	C2C12 cells modified for optogenetic control	21	Injection of a cell loaded gel in a well with two pillars	Collagen I (2$mg.mL^{-1}$), Matrigel (10%)	1	No	Optogenetic (1.5 W collimated blue light or 300 W lamp with 472 nm filter)	Pillar deflection
[46]	C2C12	7	Magnetic alignment of cells and spheroids in a gel	Collagen I (2 $mg.mL^{-1}$), Matrigel (10%)	10	20% strain	No	No
[224]	C2C12	28	Seeding cells in a microfluidic tube moulded in a collagen gel	Collagen I (6 $mg.mL^{-1}$)	4	No	No	No
[258]	C2C12	14	Moulding a cell laden gel in a microfluidic tube in a sacrificial gel	Fibrinogen (5 $mg.mL^{-1}$), Thrombin (1 $U.mL^{-1}$),Matrigel (20% v/v)	5	No	No	No

Ref.[a]	Cell type[b]	Days[c]	Tissue engineering Approach	Scaffold	Size[d] (mm)	Mechanical stimulations	Other Stimulations	Force evaluation
[280]	C2C12	13	Seeding cells onto DegraPol® strips	DegraPol® strips	31	48 h stretching at 0.02 mm/h, then cycles of 3 sets of 5 1 mm 2 s pulses; Max. strain: 6.7%	No	No
[265]	C2C12	8	Casting a cell-loaded gel in a cylindrical shape with two anchors	Fibrinogen (3 $mg.mL^{-1}$), aprotinin (5 $mg.mL^{-1}$) mixed 1:1 with thrombin (2 $U.mL^{-1}$)	15	50% strain	No	No
[266]	C2C12	9	Moulding a cell-loaded gel in a ring shape and mounting it onto spools	Fibrinogen (20 $mg.mL^{-1}$), thrombin (0.6 $U.mL^{-1}$)	33	Cycles of 10% strain for 6 h, 18 h at 3%, for 6 days	No	No
[267]	C2C12	16	Casting a cell-loaded gel in a well with two pillars	85% collagen I (2 $mg.mL^{-1}$)	24	15% / 1h strain, 15% for 2h and then 0%	Electrical (3.6 V/mm 1.2 ms pulse & 1s 100 Hz)	Force transducer
[268]	Muscle progenitor cells induced from hiPS cells - Primary human muscle cells	28	Casting a cell-loaded gel in semi-cylindrical mould and anchoring it to nylon frame	Fibrinogen (4 $mg.mL^{-1}$), Matrigel (20% v/v), thrombin (0.2$U.mg^{-1}$)	7	No	Electrical (40 V/cm, 10 ms pulse & 1s 5-40 Hz) ACh (10mM)	Force transducer
[269]	Muscle progenitor cells induced from hiPS cells - Primary human myoblasts	7	Casting a cell loaded gel in a chamber with pillars	Fibrinogen (1-2 $mg.mL^{-1}$), Matrigel (20% v/v), Thrombin (0.8$U.mL^{-1}$)	11	No	Electrical (2.45 V, 1 or 20 Hz) Caffeine (100 µM), verapamil (10 µM), cardiotoxin (1.2 µM), chloroquine (100 µM)	Pillar deflection
[270]	Primary human myoblasts	14	Casting a cell loaded gel in wells of a 96-well plate with PDMS pillars	Fibrinogen (4 $mg.mL^{-1}$, 40% v/v), GeltrexTM (20% v/v), thrombin (0.2 $U.mL^{-1}$)	4	No	Electrical (10 V/cm, 0.5-20 Hz) Dexamethasone, IGF -1, cerivastatin (1-100 nm), gemcitabine (32-320 µM), d-tubocurarine (25 µM), ACh (2 mM), Irinotecan (16-72 µM)	Pillar deflection
[271]	Primary rat skeletal myocytes	28	Casting a cell loaded gel in circular mould, later transferred to holders	collagen I (0.4 mg), Matrigel (10% v/v)	8	Mechanical "crush" injury	Electrical (4 ms, 2.5-100Hz) 25 $µg.mL^{-1}$ cardiotoxin, 0.5 µmol/L γ-secretase inhibitor, 5 µmol/L IWR-1, 1 µmol/L CHIR99021, 100 mol/L Oxytocin, 100 nmol/L Angiotensin-II	Force transducer
[272]	Primary human myoblasts	14	Casting a cell loaded gel in a chamber with pillars	Collagen I (3.3 $mg.ml^{-1}$), Matrigel (22%, v/v)	1	No	Electrical (5ms, 1-20 Hz square impulses, 20 mA) Optogenetic (2 h/day, 200 ms light pulse every 5s)	Pillar deflection
*	C2C12 - M-hiPSC	14	Magnetic bioprinting and trapping	No matrix	8	100% strain	ACh (1 mM)	Deformable beads

[a]Reference of the study presenting this construct

[b]Skeletal muscle cell types or cell types meant to mature towards muscle tissue in the construct. Unless mentioned, cells were not pathological.

[c]Maximum *in vitro* culture time of muscle cells in 3D system (in days)

[d]Maximum dimension of the construct achieved (in mm)

* Present study

Table 4.1. Table comparing various parameters of the different skeletal muscle tissue engineering constructs referenced in this study

tissue engineering, such a high strain could offer beneficial effects, and it does not require complex stretching machinery and protocols like other methods[265–267,280].

Due to its simplicity, our system does not offer direct force measurement through a force transducer[260,261,267,268,271] or pillar deflection[262–264,269,270,272]. To assess the mechanical environment of the cells, we proposed an approach for stress evaluation in muscle tissue, originally developed for zebrafish embryos[553], using deformable polyacrylamide beads embedded in the tissue. These beads revealed that stretching the tissues led to stresses and a mechanical state, similar to those in mature tissues, which could help explain why stretching enhances myogenesis and increases the number of Pax7-positive cells.

The magnetic approaches presented here could be further complexified for various biological applications, including disease modeling and drug screening, and could provide insights into the neuromuscular junction once innervated. For instance, magnetic bioprinting could be employed to create complex and precisely tuned cellular architectures, with innervation or vascularization integrated with the magnetic muscle constructs in co-culture approaches. More complex magnetic systems, such as those incorporating Halbach configurations to precisely control the magnetic field and gradient, could potentially be used to directly stimulate the cells through magnetic forces. The rapid magnetic bioprinting process and its ability to generate large and complex tissues also offer promising opportunities for graft development. Nanoparticles within the grafts could serve as MRI contrast agents for real-time monitoring. Magnetic stents, akin to the magnetic needles, could enable precise *in vivo* positioning, while magnetic actuation could dynamically adjust graft shape or movement during and after implantation, potentially reducing invasiveness and improving surgical outcomes. Post-implantation, magnetic forces could also guide cell migration and enhance tissue integration.

IV. Experimental procedures

Cell Culture:

C2C12 cells were cultured in proliferation medium consisting of DMEM (Gibco) supplemented with 10% FBS (Dutcher) and 1% Penicillin-Streptomycin (Thermofisher).

M-hiPS cells were cultured in DMEM with 1000 mg/L D-Glucose (Stem Cell Technologies) supplemented with MyoCultTM-SF expansion 10X supplement (human, Stem Cell Technologies) and 0.1% Penicillin-Streptomycin on flasks coated with Matrigel (Corning). Both cell types were passaged once confluency reached between 50 and 80%, without exceeding passage 5.

Myogenic differentiation of hiPSCs:

The three hiPSC lines used in the study were derived by Phenocell® using the Epi Episomal iPSC Reprogramming Kit (ThermoFischer) from three different patient cell lines (Supplementary Table 4.1). Informed consents were obtained from all the patients included in this study, complying with the ethical guidelines of the institutions and with the legislation requirements of the country of origin. Experimental protocols were approved by the French minister of health (2019-A02599-48).

hiPCs were used at passages P15-P20, maintained in StemMACS iPS-brew XF medium (Miltenyi Biotec) in vitronectin (Gibco)-coated culture dishes and were routinely tested for Mycoplasma contamination using a commercially available kit (MycoAlert, Lonza).

hiPSC skeletal muscle differentiation experiments were performed using media A, B, C, and D from the commercially available STEMdiff™ Myogenic Progenitor Supplement Kit (Stem Cell Technologies). Briefly, hiPSC colonies were dissociated into single cells with Tryple Express (Thermo Fischer Scientific) and seeded onto Matrigel (Corning)-coated 6-well plates at a density of 20,000 cells/cm² in medium A for 2 days. Cells were then switched to medium B (days 2-4), medium C (days 2-4) and medium D (days 6-30) with a daily medium change.

Day 30 skeletal myocytes were dissociated with Tryple Express and 285µg/mL Collagenase IV (Stem Cell Technologies) for 10 minutes, filtered on a 70 µm strainer and replated on Matrigel-coated flasks at a density of 15,000 - 20,000 cells/cm² in MyoCult™-SF Expansion Medium with 10 µM Y-27632 (Stemgent). When the culture reached 60 - 80% confluency, myogenic progenitors were harvested and cryopreserved.

Terminal differentiation:

C2C12 differentiation was triggered by switching their culture medium to differentiation medium, consisting of DMEM (Gibco) supplemented with 1% Horse Serum (Thermofisher) and 1% Penicillin-Streptomycin (Thermofisher).

M-hiPSC were differentiated into mature muscle cells using the MyoCult™ Differentiation Kit (human, Stem Cell Technologies) supplemented with 0.1% Penicillin-Streptomycin.

In both cases, growth medium was switched with differentiation medium on day 0, immediately after the cells were magnetically bioprinted.

Magnetic Labeling:

Cells were magnetically labeled with superparamagnetic maghemite iron oxide nanoparticles coated with citrate[46,422]. The nanoparticles were synthesized using the standard procedure of iron salts co-precipitation. In brief, 3 g of $FeCl_3$ were mixed with 8.1 g of $FeCl_2$ in 5 mL deionized water, supplemented with 25 % ammonium hydroxide as precipitating agent to achieve and alkaline pH of 10. The solution was heated to 90 °C for 20 minutes, then magnetically decanted, washed with acetone, washed with water, and centrifuged (8000 rpm for 10 min). The pellet was resuspended in 10 mL of deionized water. Subsequently, 2 g of citrate, dispersed in 20 mL of deionized water, was added to the solution, and the mixture was further heated at 90 °C for 1 hour. This final step is crucial for both the oxidation of nanoparticles into maghemite and the citrate coating which ensures colloidal stability. The nanoparticles diameter was measured by transmission electron microscopy to be 8 ± 1.7 nm. Citrate absorption was effective, resulting in a final negative zeta potential -35mV. The nanoparticles exhibited a saturation magnetization of 65 emu/g, without any hysteresis in the magnetization curve. Before administering the nanoparticles to cells, the stock solution was filtered-sterilized through a 200 nm filter.

C2C12 cells were labeled by incubating them in an RPMI (Gibco) solution containing nanoparticles at a concentration of 2 mM iron and 2 mM citrate. The citrate was included to prevent nanoparticle precipitation without affecting the solution's pH. Incubation was performed for 30 minutes once daily over three days preceding magnetic bioprinting, as previously described[46]. During this process, cells progressively internalized the nanoparticles through the endocytic pathway.

The labeling procedure was modified for M-hiPS cells, as prolonged exposure to the 2 mM iron and 2 mM citrate solution caused cell detachment. These cells were labeled with the same nanoparticle solution, but for 15 minutes once daily over two days preceding magnetic bioprinting. To further enhance nanoparticles uptake, nanoparticles dispersed at 0.2 mM iron were also added to the cells' regular culture medium at 0.2 mM iron overnight between the two labeling sessions.

Magnetophoresis to quantify iron internalization:

To measure the amount of iron internalized by the cells, magnetophoresis was performed[422]. Magnetically labeled cells were resuspended in PBS and the solution was placed next to a permanent magnet with a magnetic field B = 0.145 T and a gradient grad(B) = 17 $T.m^{-1}$. By

recording the cells' displacement towards the magnet and measuring their speed and diameter, the magnetic force applied to each cell was inferred, as it balances the Stokes drag force. This allowed for the determination of the magnetic moment and, consequently, the amount of iron internalized by each cell.

Magnetic signal measurement:

After bioprinting, tissues were cultured in differentiation medium in 500 µl Eppendorf tubes. The tubes fit in a bench-top magnetometer which was regularly used to measure magnetic signal of the tissues. The device assesses the magnetic response of the tubes content when exposed to two alternating fields, providing a value proportional to the amount of magnetic material within the sample. The details of the principle of this magnetic technique and its application are explained in reference[254].

Nickel iron pattern fabrication:

A 70 x 50 mm^2 Corning glass slide was covered with a Ti-Cu layer (Ti 10nm, Cu 100nm) through magnetron sputtering (Plasmionique). The resulting conductive layer was spincoated with TI-Prime (Microchemicals) and then with 70 µm of AZ 125nXT photoresist (Microchemicals). Photolithography with a chromium mask would then remove the resist in the shapes and positions of the desired patterns. These holes, where the copper was exposed, could be used as moulds to grow NiFe (80:20) patterns through electrodeposition[46,56,465]. The substrate was immerged in a magnetically steered 30 °C electroplating bath with 250 $g.L^{-1}$ $NiSO_4$, 5 $g.L^{-1}$ $FeSO_4$, 25 $g.L^{-1}$ boric acid, 2 $g.L^{-1}$ saccharin and 0.1 $g.L^{-1}$ sodium dodecyl sulfate. With the substrate acting as a cathode and a pure nickel anode (Goodfellow), a 7 $mA.cm^{-2}$ current density resulted in NiFe growing by about 3 $\mu m.h^{-1}$ on the exposed copper on the substrate. Once the NiFe deposit reached a height of about 50 µm, the resist and surrounding copper were removed using TechniStrip P1316 (Technic) at 70 °C. The patterns were then protected by spincoating the substrate with a 100 µm layer of PDMS (Sylgard 184, 1:10 curing agent). Multiple wrench-shaped patterns were made on the same glass slide, and they were usually regrouped in groups of 6, packed together to fit in a 16 mm wide circle.

Magnetic bioprinting:

Wells to support magnetic tissue formation were prepared from 1 cm thick PDMS (Sylgard 184, 1:10 curing agent) by punching out discs with an inner diameter of 16 mm and an outer diameter of 20 mm. These hollow disks were plasma-bonded to 100 µm-thick 22 x 22 mm^2 VWR coverslip to create the wells.

Each well was treated with anti-adherence solution (StemCell Technologies) for 1 hour and then placed on top of a group of 6 patterns. Magnetically labeled cells were detached using TrypLE

Express 1X (Gibco) and resuspended in differentiation medium. Each wrench-shaped pattern has an area of 4.3 mm^2. To achieve a density of 10^5 cells per mm^2 of pattern, 2.6×10^6 cells are needed for 6 wrench-shaped patterns. 500 µL of the cell suspension containing 2.6×10^6 cells were added to each well. The wells on top of the patterns were then immediately positioned in between two strong magnets (110.6 × 89 × 19.6 mm^3, remanence Br = 1.35 T, Ref. Q-111-89-20-E, Supermagnete), spaced by 3.6 cm to minimize the gradient between them. This system, presented in Supplementary Figure 4.1C, was left for 3 hours in this configuration to allow the magnetic bioprinting process to occur.

Chip Fabrication:

Chips were fabricated by casting transparent Ecoflex (00-31 Near Clear, Smooth-on) in 3D-printed moulds (Supplementary Fig. 4.4), into which needles were previously inserted in dedicated holes. After curing for 3 hours at 75 °C, the needles were removed, and the chips were unmoulded. Nickel-plated steel needles (0.6 mm wide, Bohin) were coated three times with transparent nail polish to prevent rusting in cell culture medium and then dried overnight at 120 °C to remove any traces of solvent. These needles were placed into the chips' pre-made holes so that two needles in each compartment faced each other at a distance of 2 mm. Once inserted, the needles were bonded to the chip using Loctite SI 5398 adhesive in the holes designated for stretching clamps. The needles were then coated with polydopamine by plasma-treating the chips and then filling the compartments with 5 mg/mL dopamine hydrochloride (Thermo Scientific) in Tris-HCL buffer (pH = 8.5). After 3 hours, the compartments were rinsed with PBS. The activated surface of the needles was then coated with 0.2 mg/mL collagen I (Corning, rat tail) in PBS for C2C12 cells or Matrigel for M-hiPSC for 2 hours at room temperature, while the magnetic bioprinting process was conducted in parallel. Just before removing the substrate from the magnets, the chips were rinsed with PBS and filled with warm differentiation medium.

Magnetic Trapping of a wrench shaped tissue:

A row of 8 N48 Neodymium magnets with a diameter and height of 6 mm (Supermagnete, S-06-06-N) was placed on each side of the chip in 3D-printed slots, with one magnet aligned per needle. All magnets were oriented identically so that adjacent magnets repelled each other while the pair of magnets magnetizing needles facing each other attracted one another, creating magnetic field lines that extended from one needle tip to the other. After removing the substrate from the magnets, the six tissues within a well would either detach spontaneously or could be gently detached by applying a flow with a micropipette. The cohesive tissues were then aspirated using a 5 mL pipette and released in one of the chip's compartments, in between the two needles where the tissue would clip onto. After incubating the tissue overnight, the magnets were removed for the rest of the maturation period.

Stretching:

Once the tissue had adhered to the needles overnight, the samples could be stretched. A pair of 3D-printed clamps was used to secure the chip onto a translation stage (Thorlabs). Stretching the chip increased the distance between the two needles, thereby stretching the tissue. Stretching the chip by 2 mm resulted in an approximate 1 mm increase in the distance between the needle tips, equivalent to 50% stretching. Stretching by 4 mm led to a 2 mm increase between the needle tips, corresponding to 100% stretching.

Tissue Fixation and Staining:

Culture medium was removed from the chips and replaced with 4% Paraformaldehyde (v/v) in PBS. Samples were incubated for two hours at room temperature while they were still attached to the needles, and, when applicable, in a stretched position. This allowed to preserve the exact configuration of the samples prior to fixation, and upon detachment from the needles using tweezers, their original shape was maintained. After rinsing the samples three times with PBS, they were incubated for 1h in blocking solution with 4% w/w BSA (Sigma) and 0.5% v/v Triton X-100 (Fisher) in PBS. Following another PBS rinse, the samples were incubated overnight at 4 °C in blocking solution with 1:1000 Phalloidin AlexaFluor 555 (Thermofisher) and 1:300 DAPI (Invitrogen). For further immunostaining, samples were immersed in a saturation solution containing 1% (w/w) BSA and 0.3% (v/v) Triton X-100 in PBS, for one hour at room temperature. After rinsing with PBS, samples were incubated overnight in saturation solution with the desired primary antibodies: 1:200 Desmin (goat, R&D, AF3844), 1:100 Pax7 (mouse, DHSB, Pax7-c), 1:100 MF20 (mouse, DHSB, MF20-c), 1:200 Myogenin (mouse, DHSB, F5D), or 1:500 Alpha-Actinin (mouse, Sigma, A7811-.2ML). After washing with PBS, samples were incubated overnight in saturation solution with secondary antibodies, 1:750 donkey anti-goat 647 (Thermofisher Scientific, A32849) and 1:750 donkey anti-mouse 488 (Thermofisher Scientific, A-21202), and then washed with PBS. In the case of samples stained with EdU to detect proliferative cells, they were first incubated with 10 µM EdU in culture medium for 2 hours before fixation. Once fixed, EdU incorporation was revealed using the Click-iT™ reaction cocktail from the Click-iT™ EdU Cell Proliferation Kit (Invitrogen). Afterward, samples were labeled with Hoechst dye and then incubated with antibodies, as previously described.

LIVE/DEAD Assay:

The impact of the magnetic bioprinting and trapping over time on cell viability was assessed with LIVE/DEAD cell imaging kit (488/570, Invitrogen). Tissues that had just been patterned were transferred to a well of a 48-well plate filled with the reagents. For tissues suspended between the needles, the cell culture medium was replaced by the reagents. Tissues were incubated for 30 minutes and then imaged via confocal microscopy. Non-trapped tissues were first transferred to a fluorodish for imaging, while trapped tissues were imaged in situ within

the chip, through the Ecoflex near-clear bottom layer. Live cells were visualized in green using a 488 nm excitation wavelength and dead cells were visualized in red using a 552 nm excitation wavelength.

Microscopy:

Fixed samples were positioned flat onto a fluorodish using a micropipette and tweezers. They were then imaged with a 25x water immersion objective on a Leica DMi8 inverted confocal microscope. Live microscopy was conducted within the incubator using a CytoSmart Lux 3 FL system. For imaging samples or systems from above, a DinoEye camera adapted to a Stemi 508 Greenough Stereo Microscope was used. Calcium imaging was performed using a Spinning Disk microscope, which allows for image acquisition at 100ms intervals.

Gene expression analysis:

Tissues were detached from the needles using tweezers. The central fiber of the tissue was cut and flash-frozen dry at -80 °C. Total RNA was isolated using the RNeasy Micro Kit (Qiagen) and cDNA was synthesized using SuperScript III (Invitrogen) according to the manufacturer's instructions. Quantitative real-time PCR was performed in triplicate using a QuantStudio 12K Flex RT-PCR system (Applied Biosystems) with the Luminaris HiGreen qPCR Master Mix (Thermo Fisher Scientific). Primer sequences are listed in Supplementary Table 4.2. Experiments were performed with at least three replicates per condition and expression levels were normalized to 18S. Relative expression compared to 2D gene expression levels at day 0 was determined by calculating the $2^{-\Delta\Delta Ct}$. If no signal was detected at the end of the qPCR process, the Ct was set to 46, which was the maximum number of PCR cycles performed. For genes with very low or undetectable expression in control samples at day 0, this approach can result in very high fold changes at day 3, reflecting the gene's activation during differentiation.

Magnetic field simulations: Simulations to determine the magnetic field and gradient around the NiFe patterns during magnetic bioprinting and the needles during the magnetic trapping process were performed using COMSOL Multiphysics (Magnetic Field No Currents module, Licence number 6464550).

Designing and printing 3D parts:

The moulds, chips and various 3D-printed parts used in our set up were designed using Autodesk® Inventor® (Supplementary Fig. 4.4 and 16). These designs were then 3D printed using a Digitalwax 028J Plus® 3D printer (DWS).

Fabrication of fluorescent polyacrylamide beads:

Beads were fabricated by adapting previously established protocols[553,560]. Briefly, an aqueous solution containing 0.63% w/w Acrylamide (Sigma A4058), 1.13% w/w Bis-acrylamide molar ratio 19:1 (Sigma A9926), 10 mM of Tris buffer pH7.5 and 0.15% v/v ammonium persulfate, and an HFE 7500 fluorinated oil solution with 0.4% v/v TEMED (Sigma), 1% w/v FluoroSurf surfactant (Emulseo) and 0.1% w/v N-hydrosuccimide ester (Santa Cruz Biotechnology Inc.) was prepared, vortexed and filtered. Using a microfluidic chip similar to the one used in the original study[560], the acrylamide solution was flowed through 20 x 35 μm^2 channels at 300 µL/h. This flow was disrupted by an 800 µL/h flow of the oil solution, resulting in the formation of an emulsion of acrylamide droplets in oil. This emulsion was then collected in an Eppendorf tube with mineral oil and incubated at 60 °C for 16 hours. The following day, the bottom and top layers of HFE and mineral oils were removed. The emulsion was then washed at least 3 times with 20% Perfluoro-octan-1-ol in HFE oil, at least two times with Hexane with 1% (w/v) Span-80, and finally with three washes with PBS. This process resulted in the formation of spherical deformable polyacrylamide beads with an average diameter of 42 ± 5 µm. The beads were then incubated overnight in a rotating Eppendorf tube with 0.1 mg/mL FITC-labeled poly-L-lysine (Sigma) in sterile 50 mM HEPES (pH 8.2). Finally, the beads were washed with PBS.

Just before bioprinting the tissues, the beads were mixed into the cell suspension at a concentration of one bead per 500 cells. Although the beads were not magnetic, they became easily embedded in the tissues during the bioprinting process.

Calcium imaging and Acetylcholine assays:

Tissues were incubated with Fluo-4, AM, a cell-permeant dye (Thermofisher Scientific), in HBSS buffer, for one hour. After incubation, tissues were rinsed with HBSS buffer and differentiation medium, and then transferred in 240 µL of differentiation medium in a 96-well plate for imaging. For tissues trapped between needles, they were carefully detached from the needles and allowed to recover and stabilize for 5 minutes before imaging. Samples were imaged using a Spinning-Disk microscope with a 488nm laser, capturing images every 100 ms for a total duration of 3 minutes. Approximately one minute into the imaging session, 60 µL of a 5 mM acetylcholine (ACh) solution was added to the well, achieving a final concentration of 1 mM ACh without causing excessive movement of the tissue.

Image analysis:

Image analysis was performed using Fiji. The orientation distributions of actin were analyzed with the Directionality plugin, normalized, and plotted as probability distribution curves, where the proportion of filaments between two angles corresponds to the area under the curve between those angles. 3D segmentation to measure the numbers of nuclei per cell and their lengths was

performed manually using the ROI manager tool. Bead deformation was quantified using a simple model by fitting ellipses to the bead projections. Aspect ratio and orientation of the ellipses were extracted using the Analyze Particles tool. Frequencies of calcium fluctuations were measured in five cells exhibiting fluctuations from each sample without ACh, and within 2min following ACh injection. Cells that did not exhibit fluctuations were excluded from the analysis. The relative increase in calcium signal intensity was calculated between the intensity just before ACh addition and the maximal intensity after addition, normalized by the background intensity. Intensity increase was assessed over a large area of the tissue, rather than focusing on individual cells. The numbers of myogenin- and Pax7-positive cells were counted manually using the Cell Counter plugin.

Statistical analysis:

Data were processed using Microsoft Excel and represented using GraphPad Prism 8 (GraphPad Software, La Jolla, California). Values were averaged from at least three independent replicates. Errors bars represent ± standard deviation. Significant differences between two conditions were evaluated using two-tailed unpaired Student's t-tests with a 95% confidence interval, except for frequencies of calcium fluctuations which were evaluated with two-tailed unpaired Welch's t-tests which do not assume equal standard deviations. Statistical significance is indicated with * for P value < 0.05, ** for $P < 0.01$, *** for $P < 0.001$ and **** for $P < 0.0001$.

Chapter 5

Controlling and probing the geometrical and mechanical properties of magnetically bioprinted tissues

Context and motivations

By engineering mature skeletal muscle tissue, this previous study demonstrated the potential of a next generation magnetic tissue engineering toolbox, especially magnetic bioprinting. The upcoming third and final study of this manuscript presented in **Chapter 5** aims to further explore what this magnetic bioprinting technique has to offer, while also investigating the properties of magnetically printed tissues. In particular, the interplay between function, geometry and mechanical cues in morphogenic processes inspired us to use magnetically printed tissues for biomechanical research purposes.

The added value of this magnetic bioprinting technique lies in its ability to engineer much more complex tissue shapes than previous magnetic patterning techniques. Most of them are restricted to basic magnet shapes such as rods, rectangle, disk or rings [46,55,59,60]. A few do achieve more variations, but they are still limited in the type or size of possible shapes [432,439]. And most of the time, cells are patterned onto a 2D substrate without expecting to form a 3D tissue[416]. Indeed, most magnetic approaches aiming to engineer 3D tissues usually rely on assembly techniques and are even more limited than patterning approaches when it comes to possible geometries[53,58,293,329,375]. Therefore, the magnetic bioprinting technique presented in the previous study has the potential to really advance magnetic patterning and maybe even compete with current bioprinting platforms, which we aim to uncover in the next study.

Although magnetic bioprinting can generate a wide range of geometries, one of the main concerns that will be addressed is how to preserve this geometry over time. We previously showed that wrench shaped tissues tend to curl into a spherical shape after a week but trapping them maintains their original shape despite morphogenic processes. However, wrench shaped tissues were specifically designed to be trapped. It is therefore important to investigate how other shapes evolve and what strategies can be employed to prevent or at the very least guide any morphological changes.

This is essential to investigate how geometrical constraints impact maturation[9,10,32]. The wrench shape was optimized to facilitate both tissue trapping and anisotropic myogenesis. Conversely, this also raises the question of how muscle maturation would proceed in a non-physiological geometry, which we want to address now.

The versatility of magnetic bioprinting is not limited to the shape of the printed tissues but also extends to co-culture systems. In a couple of previous magnetic based approaches, precise placement of multiple cell type has been achieved through sequential steps, either by patterning one cell type after the other [430,431], sometimes changing the magnetic field in between, or by magnetically positioning spheroids one by one [248,314]. We want to explore what happens with our platform when bioprinting multiple cell types at the same time, and if there is a way to create heterogenous distributions of multiple cell types, notably by varying the magnetic labeling of the cells.

Regarding mechanical stimulation of the printed tissues, so far, we have only applied step-like deformations. This is because the stretching system in the past two studies was

manually operated. In order to keep up with current skeletal muscle engineering platforms capable of automatized stretching[46,261,265–267,272,280], and to expand the range of our biomechanical investigations, we have upgraded our stretching system by motorizing and automatizing it.

As we will see, this will be very useful to test the mechanical properties of the printed tissues. While the previous study was mainly focused on optimizing muscle differentiation, here we chose to use various automatized protocols to investigate tissue cohesion, resistance to deformation, and material fatigue, which has mostly been studied on cell monolayers so far[561,562]. If magnetically printed tissues are to be further stimulated or manipulated for possible biomedical or bioengineering applications, evaluating their material properties is an essential first step, one that we chose to investigate in this third and final study.

Investigating these open questions surrounding magnetic bioprinting and the functional performance of printed tissues is what motivated this final study, which is in preparation for submission.

Supplementary figures are available in Appendix B.

Abstract

Mechanical and geometric cues play a crucial role *in vivo*, regulating both morphogenetic processes and proper tissue function. This is particularly evident in skeletal muscle, where aligned architecture is essential for myogenesis and functional force generation. However, precisely engineering tissue geometry at both macroscopic and microscopic scales while simultaneously controlling internal mechanical forces remains a significant challenge. In this study, we introduce a magnetic tissue engineering platform based on a magnetic bioprinting technique, enabling precise control of biophysical cues that guide *in vitro* tissue morphogenesis. Applied here to skeletal muscle, this approach allows for the rapid fabrication of cohesive tissues in any desired shape using cells labeled with magnetic nanoparticles. Additionally, multiple cell types can be incorporated and spatially organized within the same construct through magnetic segregation. Optimizing tissue geometry further enables magnetic actuation, including the ability to trap and maintain tissue shape over time. Furthermore, this magnetic platform facilitates the investigation of how tissue architecture influences mechanical properties, such as resistance to rupture. Overall, this study highlights the significant potential of magnetic bioprinting and stimulation for controlling tissue morphology and advancing biomechanical research.

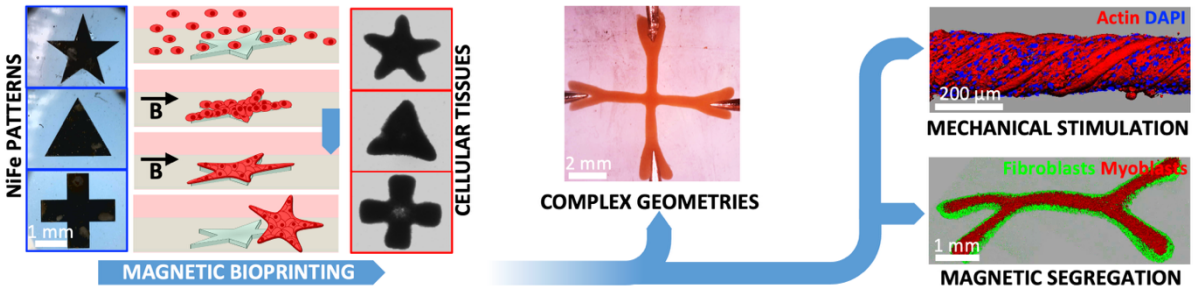

Visual table of contents of Chapter 5

I. Introduction

As soon as embryogenesis begins, cells are subjected to mechanical and geometrical constraints that guide morphogenesis[9,10]. Coupled with biochemical signals, these structural cues diverge locally, directing cells to differentiate in a spatially dependent manner and ultimately shaping the different organs of the body[563]. Understanding and replicating these morphogenic processes has become essential for developing systems that accurately recreate *in vitro* the complex *in vivo* tissue organization. Advances in regenerative medicine have motivated efforts to engineer physiologically relevant tissues at large scale[563], while microphysiological systems[38,224,363,364,380,538–542], such as organs-on-chips, have successfully reproduced key aspects of tissue microenvironments. However, achieving full control over a tissue's macroscopic shape, internal cellular organization, and mechanical forces remains challenging, particularly at larger scales[11,31,32].

Several approaches have been developed to impose tissue geometry, including matrix moulds, to shape cells or tissues[224,258,259,364], and bioprinting, where cells are seeded into a biocompatible scaffold that is either extruded[42,43,564] or photopolymerized[44] in a controlled geometry. These platforms enable the fabrication of complex tissue architectures, sometimes even accurately replicating the overall geometry of entire tissues and even organs[466]. Despite these advancements, scaffold-based approaches have limitations. They can restrict cell density[261], and while the initial geometry is precisely controlled, the dynamic evolution of the tissue's internal cellular architecture and stresses remains challenging to regulate. These structural and mechanical cues are essential to morphogenesis. Skeletal muscle tissue provides a clear example, as alignment is present at every scale - from the entire organ spanning from tendon to tendon to actin-myosin complexes within multinucleated myofibers, all oriented in the direction of muscle contraction[25,26]. This uniform alignment optimizes force generation and enables movement. Moreover, aligned geometry and mechanical forces are not only functionally coupled, but are also essential in myogenesis, where mononucleated myoblasts fuse together to form aligned myotubes. Such coupling of structural and biomechanical cues plays a crucial role in many other tissues and physiological processes. This includes the development and function of smooth[565] and cardiac muscles but extends well beyond muscle tissue. For instance, endothelial cells in tubular tissues display a specific apical-basal polarity and respond to fluid shear stresses[363]. Similarly, gut organoid development, particularly the formation of crypt-villus structures, has been shown to improve under cyclic mechanical stretching[566]. These examples underscore the widespread significance of mechanical and geometric cues in tissue formation and function.

Replicating *in vivo* dynamic mechanical stresses has therefore become a key challenge in tissue engineering. Different strategies have been developed to mimic the physiological conditions, including pressure-controlled flows in microfluidic devices[259,363], or engineered systems to constrain, compress or stretch[46,57,265–267,280,530] tissues.

A promising strategy for controlling both structural and mechanical cues in tissue engineering involves the use of magnetic forces. Iron oxide nanoparticles, widely used in

imaging (e.g. as MRI contrast agents) and therapeutic (e.g. for drug delivery or hyperthermia treatment) applications[48,49], can be efficiently internalized by various cell types via the endocytic pathway[46,47], without impairing cellular functions. Once internalized, these nanoparticles enable remote cellular manipulation through external magnetic fields, providing a non-invasive means of exerting precise mechanical forces on cells. Building on this principle, magnetic tissue engineering approaches have emerged, beginning with the development of magnetically produced cell sheets[52]. This technology was subsequently adapted to generate simple tissue geometries, such as rods, spheroids or rings[46,55,59,60], with the added potential for remote magnetic manipulation[46,53–57]. However, the full potential of magnetic tissue engineering remains untapped, particularly in achieving more complex tissue architectures and in precise dynamic biomechanical control.

To address these challenges, we developed an innovative magnetic tissue engineering platform that enables precise, remote control over both tissue geometry and biomechanics. A key feature of this platform is a magnetic bioprinting approach capable of generating tissues of arbitrary shapes while maintaining control at both macroscopic and microscopic levels. We demonstrate that optimizing tissue geometry enhances the potential for further magnetic actuation, enabling shape retention over time. Using skeletal muscle as a proof of concept, we show that this platform allows for the controlled evolution of tissue shape, as well as the internal organization of cells, including their orientation and spatial positioning via magnetic segregation. Additionally, this system allows for the assessment of tissue mechanical properties, specifically resistance to fracture, which is found to be dependent on the variations of stimulation parameters, including the speed, amplitude, and duration of the applied stress, as well as the cell type used.

II. Results

1. Versatile magnetic bioprinting for custom tissue architecture

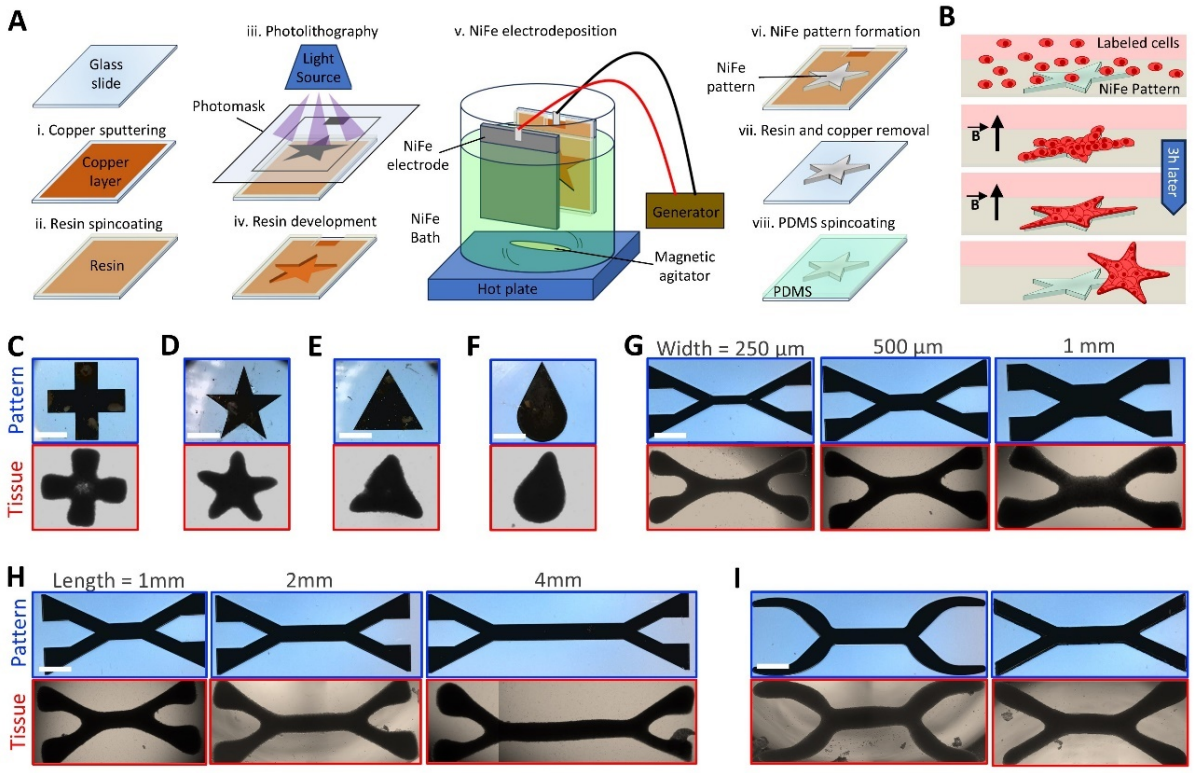

Figure 5.1. Magnetic bioprinting of cellular tissues with customizable geometries*. (A-B) Schematics of (A) the NiFe pattern fabrication process and (B) the magnetic bioprinting process. (C-F) Magnetic patterns (top) and the resulting printed tissues made of C2C12 cells (bottom) in the shapes of (C) a cross, (D) a star, (E) a triangle, and (F) a droplet. (G-I) Wrench-shaped magnetic patterns (top) and the resulting printed tissues (bottom) demonstrating variations in central fiber (G) width, (H) length, and (I) clamp shape. (Scale bar = 1mm).*

Magnetic tissue engineering, particularly magnetic bioprinting, requires both magnetically labeled cells and precisely controlled magnetic fields to organize them. To achieve the magnetic labelling, C2C12 mouse myoblasts cells were exposed to superparamagnetic iron oxide nanoparticles at a 2 mM iron concentration for 30 minutes, once daily, over the three days prior to printing. This labeling procedure, referred to as NP3, allows cells to internalize approximately 20 pg of iron per cell via the endocytic pathway, as previously described[46], therefore enabling their remote actuation through magnetic forces. To precisely control the magnetic field distribution, NiFe micropatterns with the desired geometry were fabricated using photolithography followed by NiFe electrodeposition onto a copper-coated glass slide (Fig. 5.1A). NiFe patterns grow onto the exposed copper regions defined by photolithography while the remaining substrate is protected by a resin layer, forming 50 µm-thick patterns that replicate

the exact same shape of the photomask design[465]. Next, to perform magnetic bioprinting, a suspension of magnetically labeled cells is deposited onto these micropatterns, and the system is exposed to a strong magnetic field generated by two opposing magnets positioned to minimize field gradient. While the NiFe patterns are not magnetic on their own, they act as magnetic concentrators when exposed to the external magnetic field, locally amplifying magnetic forces and directing the cells towards them[46]. After a 3h incubation period and subsequent removal from the magnetic field, the cell aggregates should self-organize into cohesive tissues that replicate the pattern geometry (Fig. 5.1B). This was demonstrated using patterns of various shapes, including crosses (Fig. 5.1C), stars (Fig. 5.1D), triangles (Fig. 5.1E) or droplets (Fig. 5.1F). More complex structures, such as wrench-shaped geometries, could also be fabricated, with the ability to modulate key geometrical features of the printed tissues, such as width (Fig. 5.1G), length (Fig. 5.1H), and the shape of the clamps at each extremity (Fig. 5.1I). These results highlight the versatility of the magnetic bioprinting technique for engineering tissues with customizable shapes and dimensions. [46]

2. Tissue maturation drives contraction towards spherical geometry

Once the magnetic field is removed, the printed tissues readily detach from the patterns, facilitating their collection and manipulation. However, it also means they are not constrained anymore. While magnetic bioprinting ensures precise control over tissue shape at the time of printing (day 0), maintaining this shape over time proved significantly more challenging, especially for contractile cells such as myoblasts. When left free-floating in a non-adherent dish, the tissues gradually transition into a spherical shape, likely due to the overall tissue surface tension and cellular contractility. Since preserving tissue geometry over time is crucial, this "spherification" process needed to be investigated, and strategies to prevent it had to be developed. To address this, we focused on cross-shaped tissues, as their geometry is very distinct from that of a circle and can be easily modulated. The first strategy to mitigate shape loss was to vary tissue scale. Cross-shaped NiFe patterns were made with branch lengths of 1, 2 and 4 mm, all 500 μm wide. While the magnetic bioprinting process successfully generated these larger centimeter-scale tissues, they invariably transitioned towards a circular shape (Fig. 5.2A, Supplementary Fig. 5.1A). Smaller crosses compacted by retracting their branches toward the center, whereas larger ones folded onto themselves before rounding up. Quantification of the projected tissue area over six days (Fig. 5.2B) revealed an exponential decay, with a time constant of approximately 1.5 days across all cross sizes. Further analysis of tissue circularity (Fig. 5.2C) and solidity (Fig. 5.2D) confirmed a progressive evolution toward a convex sphere at the same time as they become more and more compact.

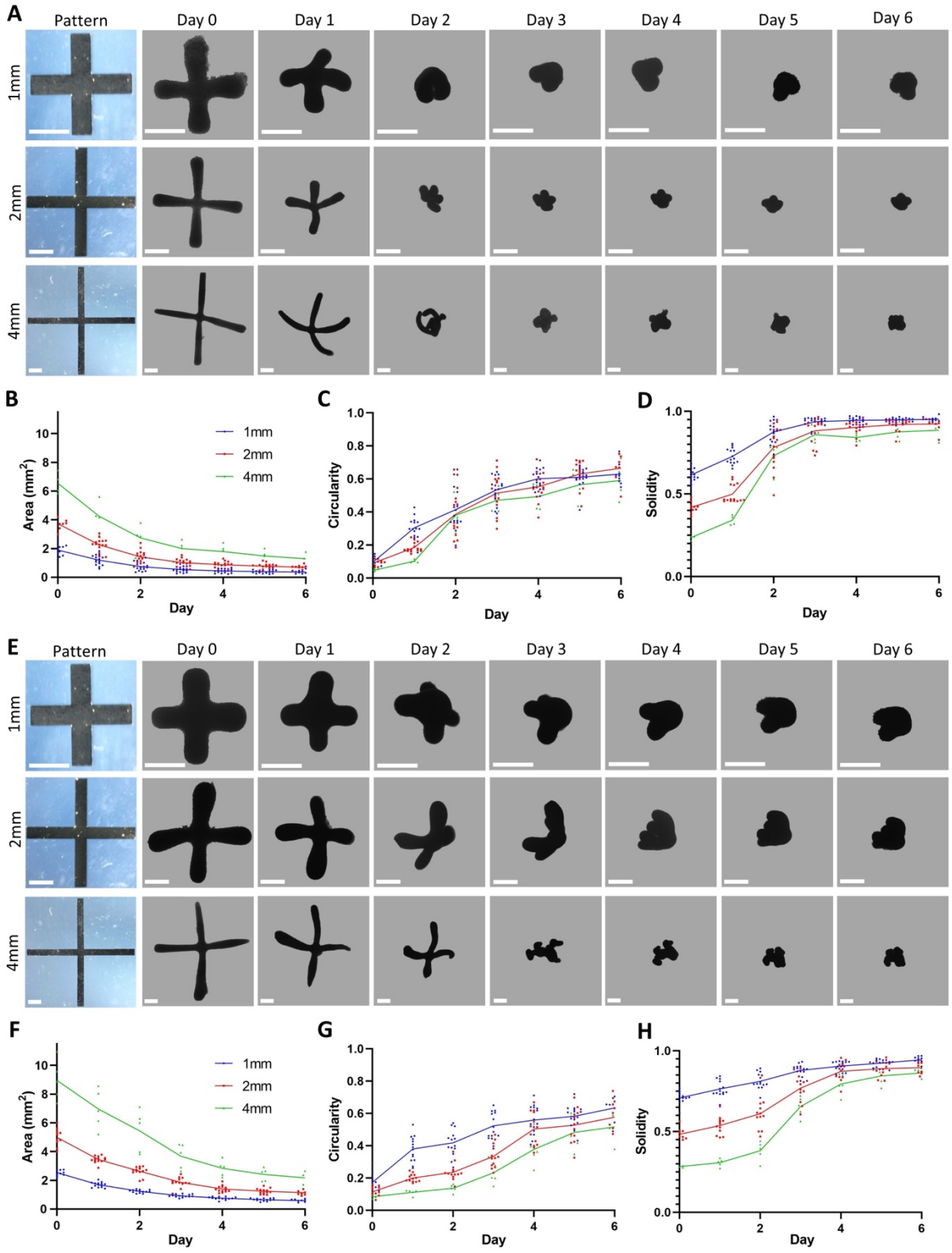

Figure 5.2. Cross-shaped tissues naturally mature toward a spherical shape*. (A) Brightfield images from day 0 to day 6 of free-floating tissues printed using cross patterns with branch lengths of 1, 2 and 4 mm, at a cell density of 100,000 cells per mm² of pattern. Evolution of their (B) area, (C) circularity and (D) solidity over time. (E) Brightfield images from day 0 to day 6 of free-floating tissues printed using the same cross patterns but with a higher cell density*

of 200,000 cells per mm² of pattern. Evolution of their (F) area, (G) circularity and (H) solidity over time. Images of the tissues were segmented to remove the background. (Scale bar = 1 mm).

As an alternative strategy to better maintain their initial shape, we increased tissue thickness rather than length. To achieve this, the tissues that were previously printed at a cell density of 100,000 cells per mm^2 of NiFe pattern were now printed at twice this density, resulting in thicker tissues (Fig. 5.2E, Supplementary Fig. 5.1B). While the thickness increase extended the time constant to up to three 3 days, the area still shrank exponentially (Fig. 5.2F) with these tissues reaching the same levels of circularity (Fig. 5.2G) and convexity (Fig. 5.2H) of the thinner tissues.

Since modifying tissue geometry only appeared to slow down, rather than prevent shape transformation, other strategies to preserve the 3D architecture were explored - specifically, maintaining the shape by applying the magnetic force continuously during maturation or embedding the tissue within a matrix. In the initial bioprinting process, tissues were collected after three hours of exposure to the magnetic field, forming a structure that precisely matched the underlying NiFe patterns (Fig. 5.3A-B). Given that the pattern-mediated magnetic forces drive cell assembly, maintaining the tissues under these forces over longer periods of time might help to preserve their shapes. However, when tissues remained on the patterns placed within the magnets for six days, they still lost their original geometry, eventually compacting into spherical aggregates on top of the patterns (Fig. 5.3C-D). This suggests that the contractile forces driving shape transition are stronger than pattern-induced magnetic forces, previously evaluated at approximately 1nN on a single cell[465].

A distinctive feature of magnetic bioprinting is its scaffold-free nature, setting it apart from most other bioprinting technique[42–44,564]. While the absence of supportive matrix allows for greater flexibility in tissue assembly, it also means that tissues lack external structural reinforcement. We therefore investigated whether embedding printed tissues in a hydrogel matrix could help preserve their shape. To test this, tissues were bioprinted as usual, but instead of being cultured free-floating in medium, they were embedded in a 2 $mg.mL^{-1}$ collagen matrix (Fig. 5.3E). After 24 hours, cells at the tissue periphery began invading the gel (Supplementary Fig. 5.2), but the main structure remained cohesive and simply detached from the gel, leaving an imprint of its original shape within the collagen matrix on day 6 (Fig. 5.3F). While embedding in collagen modestly slowed shape transformation for small cross-shaped tissues (area, Fig. 5.3G; circularity, Fig. 5.3H; and solidity, Fig. 5.3I), larger ones retained their shape better than those observed in free-floating tissues (Fig. 5.3J-K). Although they also detached from the matrix and compacted, the matrix prevented the large structures from folding onto themselves. However, despite this macroscopic improvement, confocal imaging revealed a misalignment between microscopic cellular organization and tissue geometry. Instead of aligning along the branches of the cross, myoblasts oriented perpendicular to them (Fig. 5.3L-M). Since myoblast alignment is crucial for proper differentiation and fusion, and they typically align with macroscopic geometry *in vivo,* this discrepancy suggests that the matrix alone is

insufficient to fully preserve and control both the shape and internal architecture of magnetically printed tissues.

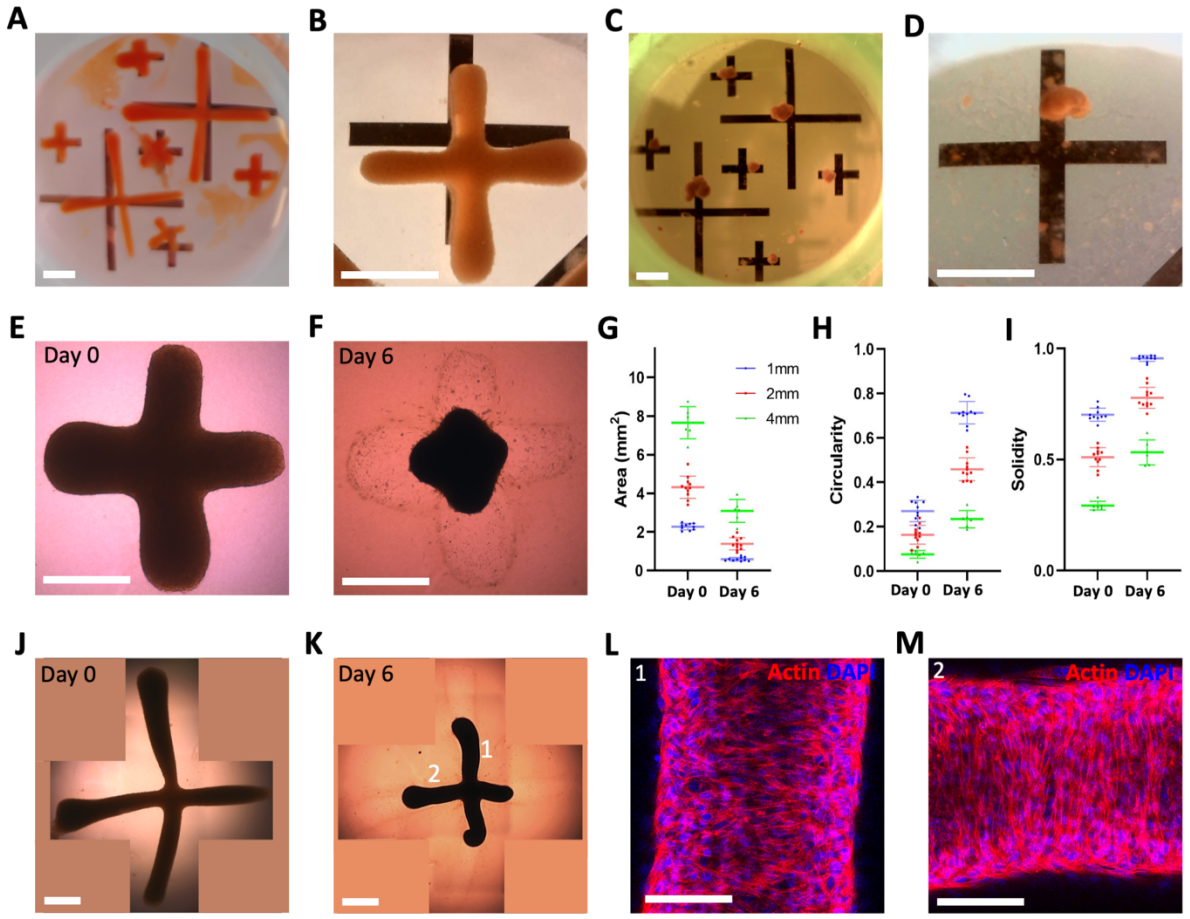

Figure 5.3. Tissue shape cannot be fully preserved by magnetic patterns or a collagen matrix*. (A-B) Tissues remaining on top the patterns in a bioprinting well after 3 hours and (C-D) 6 days between magnets, shown at both whole-well scale and at the level of a cross with 2 mm branches. (Scale bar = 2 mm) (E-F) Brightfield images of a tissue made with cross patterns with 1 mm branches and 200,000 cells per mm² of pattern, trapped in a collagen matrix, on (E) day 0 and (F) day 6. (G) Area, (H) circularity, (I) solidity of tissues made with 1, 2 and 4 mm-long branches and 200,000 cells per mm² of pattern on days 0 and 6. Brightfield of a tissue made with cross patterns with 4 mm branches and 200,000 cells per mm² of pattern, trapped in a collagen matrix, on (J) day 0 and (K) day 6. (Scale bar = 1mm) Tissues were not segmented to show the deformation of the matrix. As tissues were reconstructed from multiple frames, blank parts were filled with a uniform background color. (L-M) Confocal images of slices of two perpendicular branches of a cross-shaped tissue trapped in collagen on day 6, with nuclei in blue and actin in red. (Scale bar = 100 µm)*

3. Magnetic trapping stabilizes tissue architecture

While the magnetic forces exerted by the patterns were insufficient to balance the contraction forces, properly focused magnetic forces could still serve to mechanically constrain the tissues. To achieve this, cross-shaped patterns were redesigned to include clamps at the end of each branch to engineer clip-on cross-shaped tissues (Fig. 5.4A and Supplementary Fig. 5.3), enabling magnetic entrapment by gripping onto four magnetized needles. Chips made of Ecoflex were specifically designed for that effect, featuring needles at 90° angles and directed toward the chip's center. Each needle was magnetized by an adjacent external magnet (Fig. 5.4B). Simulations indicated that the specific arrangement of the external magnets had little effect on the magnitude of the magnetic field gradient near the needles, which remained of about 10^4T/m (Fig. 5.4C and Supplementary Fig. 5.4). This resulted in forces of approximately 10nN on NP3-labeled cells in the vicinity of the needles, whereas forces would progressively tend to 0 at the center of the chip. However, the magnet configuration influences the orientation of the magnetic field. An alternating arrangement of north and south poles generated a cross-like pattern between the needles. This configuration was chosen based on the expectation that magnetically printed tissues would align along the field lines. This was verified empirically: cross-shaped tissues transferred into the chip immediately reoriented themselves and clipped onto the needles (Fig. 5.4D). Furthermore, the collagen coating applied to the needles facilitated tissue adhesion. After overnight incubation, the tissues remained securely attached to the needles even after the external magnets were removed. This approach effectively constrained tissue movement while preserving the initial printed geometry.

As the tissues were cultured within the chips in differentiation medium, some successfully retained their shape for 6 days (Fig. 5.4E). However, this only happened in a subset of cross-shaped tissues with 2 mm-long branches and printed with 200,000 cells per mm^2 of pattern. Crosses with lower cell density could experience structural failure, with one (Fig. 5.4F) or two (Fig. 5.4G) branches breaking after a couple of days. Given that myoblasts tend to align to fuse while simultaneously generating uniform forces in the same direction, it is likely that increased contractility in two different directions induced shear stress, eventually leading to tissue rupture. It suggests an intrinsic tendency of the tissues to reorganize into a more physiologically relevant uniaxial geometry.

Increasing the initial cell density from 100,000 to 200,000 cells per mm^2 improved tissue cohesion and reduced the likelihood of breakage. However, it also makes the tissue more likely to detach from the needles, as it would be expected that the adhesion area remains constant despite the increased cellular tension of thicker tissues. To mitigate this issue, additional NP3-labeled C2C12 cells were pipetted towards the magnetized needles, forming a reinforcing shell around each clamp. This approach effectively strengthened both the tissue structure and its attachment points, enabling the stable culture of clip-on cross-shaped tissues without breaking for at least one week, with a reproducibility rate exceeding 80%, even for crosses with 4 mm-long branches (Fig. 5.4H-I).

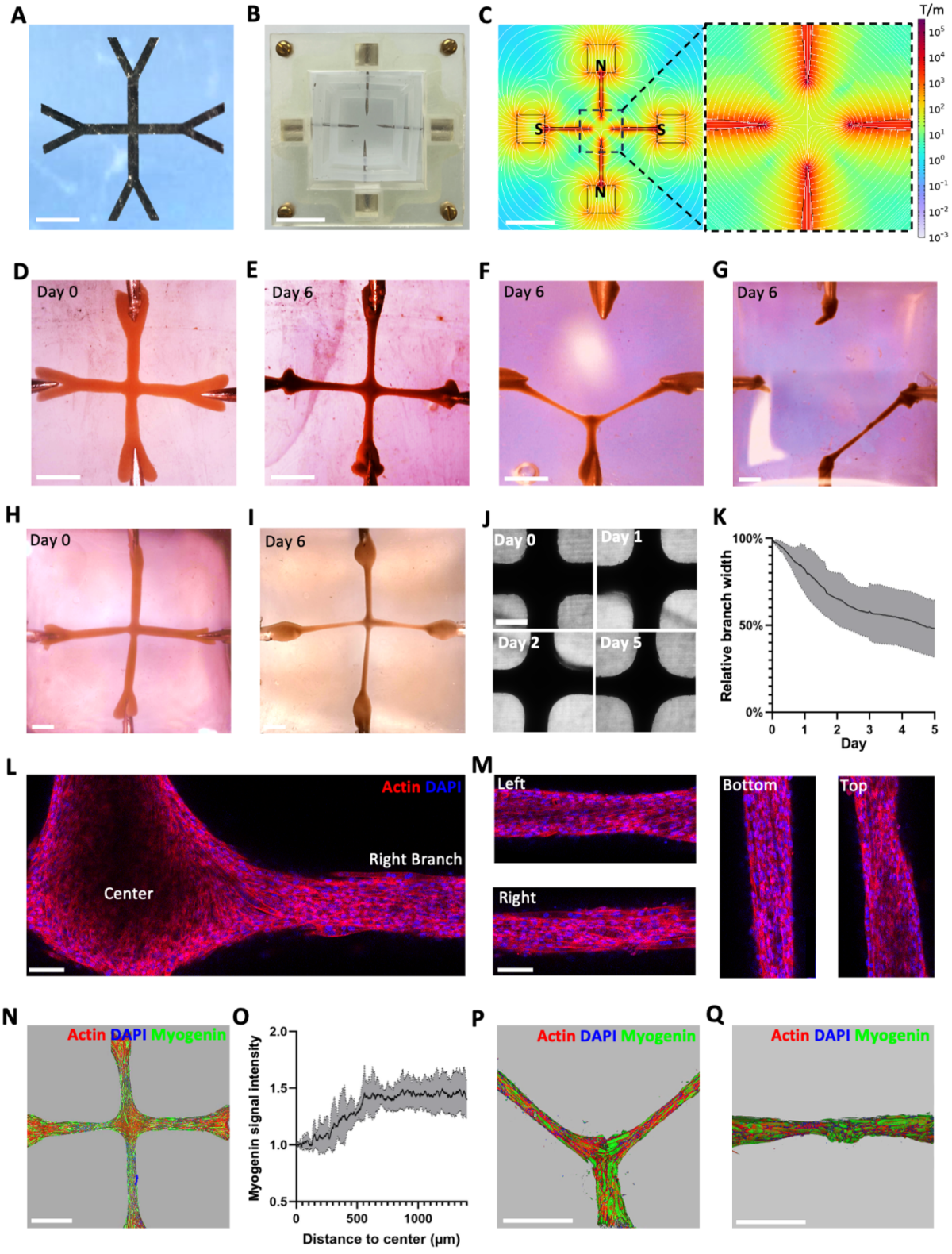

Figure 5.4. Clip-on cross-shaped tissues maintain their shape over time. *(A) Clip-on cross-shaped pattern. (Scale bar = 2 mm). (B) Custom-designed chip for trapping the tissue, with (C) the corresponding magnetic field gradient and lines when magnets polarities (S for South and N for North) were alternated. (Scale bar = 1 cm). (D-E) Magnetically trapped tissue generated from clip-on cross patterns with 2mm-long branches and 200,000 cells per mm² of pattern, shown on (D) day 0 and (E) day 6. (F-G) Examples of broken magnetically trapped tissues*

produced from clip-on cross patterns using a lower density of 100,000 cells per mm^2 of pattern, with (F) 2 mm and (G) 4 mm-long branches. (H-I) Magnetically trapped tissue formed from clip-on cross patterns with 4 mm-long branches and 200,000 cells per mm^2 of pattern, with reinforced clamps, shown at (H) day 0 and (I) day 6 (Scale bar = 2 mm). (J-K) Evolution of branch width in cross-shaped tissues from day 0 to day 5, shown in (J) brightfield microscopy images and (K) plotted relative to the initial width (n=3) (Scale bar = 500 µm). (L-M) Confocal imaging of actin filaments in (L) the central region and (M) the 2 mm-long branches of a clip-on cross-shaped tissue on day 6. (Scale bar = 100 µm) (N-O) Spatial distribution of myogenin within a cross-shaped tissue with 2mm-long branches on day 6, visualized in (N) a confocal 3D reconstruction and (O) plotted after normalization as a function of the distance from the center (n=5). (P-Q) 3D confocal reconstructions of 6-day-old trapped cross-shaped tissues where (P) one or (Q) two branches had broken. Actin is represented in red, nuclei in blue, and myogenin in green. (Scale bar = 1 mm)

With the successful stabilization of the cross geometry, it became possible to examine tissue maturation. Although the overall cross shape was maintained over time, the branches progressively became thinner (Fig. 5.4J) following an exponential decay with a time constant of approximately two days (Fig. 5.4K). While the central region exhibited no clear anisotropy (Fig. 5.4L), cells positioned further from the center displayed increasing alignment along the direction of the branches (Fig. 5.4M). Since alignment is a key factor in myogenesis, differentiation in the branches was further evidenced by fused multinucleated myotubes, and validated using myogenin staining. Myogenin, a key transcription factor in skeletal muscle differentiation, was found to be more expressed in the branches of the tissues than their centers (Fig. 5.4N), with signal intensity plateauing at about 50% above central levels (Fig. 5.4O and Supplementary Fig. 5.5).

Interestingly, in tissues where one (Fig. 5.4P) or two (Fig. 5.4Q) branches had broken, myogenin was overexpressed in the center. This suggests that the mechanical stress in this region was significant, and when combined with tissue compaction, may have favored muscle differentiation. Additionally, cell alignment and especially myotube organization at the branches' junction in these damaged tissues indicate an apparent attempt to reconnect the remaining branches.

This observation leads to an important insight: while we have demonstrated that non-physiological cross-shaped geometries can be imposed and stabilized using magnetic bioprinting, highlighting the versatility of this approach in magnetic tissue engineering, the phenomenon of a single central branch forming suggests an intrinsic property of the cells. Specifically, as myoblast alignment in a single direction is crucial for myogenesis, the cross-shaped tissues appear to be attempting to reorganize into more physiologically relevant fascicle-like structures. This natural tendency towards alignment prompted us to shift focus towards more uniaxial tissue geometries, which we believe will allow for a deeper understanding of the properties and behavior of magnetic printed tissues.

4. Magnetic trapping and stretching enable mechanical characterization of printed tissues

The chosen wrench-shaped tissue, designed with a uniaxial central fiber and two clamps, also exhibited progressive spherification over the course of a week (Fig. 5.5A and Supplementary Fig. 5.6), curling up on itself. However, this geometry not only better replicates *in vivo* tissue organization but also facilitated the tissue's magnetic trapping between two needles (Fig. 5.5B), within one of the compartments of the Ecoflex chip. More importantly, this shape allowed for a more thorough exploration of the properties of the magnetic printed tissues, which had previously only been cultured under static geometrical constraints. To introduce dynamic stresses, which are essential *in vivo*, and evaluate how magnetic printed tissues would respond, the chips were clamped onto an automated motorized stretcher (Fig. 5.5C) after an overnight incubation of the tissues on the collagen-coated needles. Stretching the chips resulted in direct mechanical deformation of the tissues without detachment in most cases, as adhesion to the needles was established during incubation. This setup provided a valuable platform for assessing the mechanical properties of printed tissues. As observed with cross-shaped tissues, printed tissues can rupture, and evaluating their resistance to rupture offers insight into their cohesion and internal organization. This is particularly relevant given that wrench-shaped tissues resemble tensile test specimens commonly used in material testing.

One of the first parameters examined was the impact of stretching speed on tissue rupture. The automated stretching system allowed tissues to be elongated at different speeds, ranging from 100% deformation over a few seconds to gradual deformation over several days, while monitoring at what point each tissue would rupture (Fig. 5.5D). Tissues stretched at a speed of 100% over two days reached over four times their original length (Fig. 5.5E) before rupture, whereas those subjected to rapid stretching could only extend to approximately twice their initial length (Fig. 5.5F). Although such strains exceed physiological levels, these results still indicate that allowing cells to adapt during stretching with a lower stretching speed enables them to withstand significantly higher strains. However, when tissues were stretched at an intermediate speed (100% over 12 minutes), those stretched only after 6 days of differentiation could barely be stretched more than 100%, whereas tissues stretched on day 1 could reach more than 200% strain (Fig. 5.5G). To confirm that this was not due to the tissues becoming thinner, from 358 ± 38 µm on day 1 to 203 ± 53 µm on day 6, rupture experiments were conducted on day 1 using tissues printed from patterns with a 250 µm-wide central fiber, which was half the width of the control (Supplementary Fig. 5.7). These tissues, with an average width of 238 ± 30 µm on day 1, exhibited similar rupture behavior to the control (Fig. 5.5G). This suggests that the increased brittleness of tissues on day 6 is a result of their maturation process and tissue reorganization, making them less capable of withstanding deformation unless they have been progressively stretched over time.

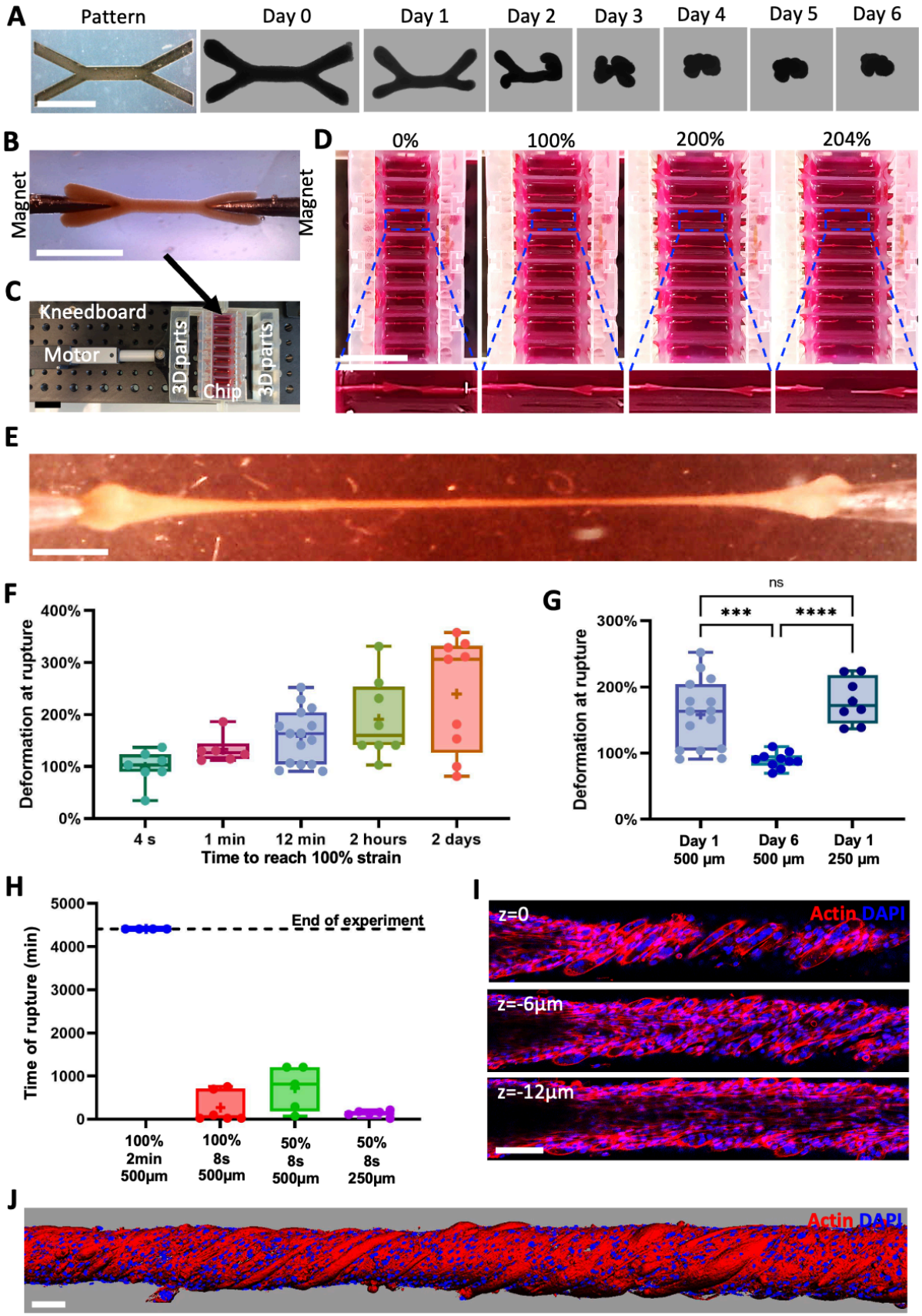

Figure 5.5. Mechanical resistance of magnetically printed tissues under stretching*. (A) Brightfield images showing the evolution of free-floating tissues printed with wrench-shaped*

patterns (100,000 cells per mm^2 of pattern) from day 0 to day 6. (B) Magnetically trapped clip-on wrench-shaped tissue on day 1. (Scale bar = 2 mm) (C) Automated stretching system and (D) progressive stretching of a chip until tissue rupture. (Scale bar = 2 cm) (E) Tissue stretched at a rate of 100% strain over 2 days on day 6, reaching four times its original length. (Scale bar = 1 mm). (F-G) Deformation at rupture of (F) 1-day-old C2C12 tissues printed with 500 µm-wide patterns, stretched at rates of 100% strain over 4 s, 1 min, 12 min, 2 hours, and 2 days, and (G) comparison of rupture deformation for tissues stretched at a rate of 100% strain over 12 min on day 1 versus day 6, printed either with 500 or 250 µm-wide patterns. (H) Time of rupture for tissues subjected to cyclic stretching from day 1 with 100% strain amplitude and 2-minute cycles (500 µm-wide patterns), 100% strain amplitude and 8-second cycles (500 µm-wide patterns), and 50% strain amplitude within 8-second cycles (500 µm- and 250 µm-wide patterns). (I) Confocal imaging of multiple z-slices and (J) 3D reconstruction of a tissue stretched from day 1 to day 4 with 100% strain amplitude 2-minute cycles. Actin is shown in red, and nuclei in blue. (Scale bar = 200 µm)

Automating the stretching system also enabled the application of more complex stretching protocols, like cyclic stretching. To complement studies focusing on physiological ranges of deformation[387–389,567–569], we applied cyclic stretching with larger amplitudes (100% and 50%) to further test the mechanical properties of the printed tissues over four days. Interestingly, tissues stretched to 100% amplitude within 2-minute cycles (ramping from 0% to 100% in 1 minute, then returning to 0% in 1 minute) did not rupture over the four-day experiment. In contrast, tissues exposed to 100% strain in 8-second cycles broke within a few hours at most (Fig. 5.5H). Reducing the amplitude to 50% more than doubled the time before rupture, indicating that while strain amplitude does play an important role, cycle duration is more critical. Additionally, tissues printed with 250 µm-wide central fibers ruptured five times faster than those with 500 µm-wide fibers, even though tissue width did not influence the maximum deformation under linear stretching. This suggests that rupture under cyclic stretching may result from material fatigue rather than exceeding the limit of deformation. Notably, tissues that did not rupture under 100% strain within 1-minute cycles displayed a distinct internal organization, with cells aligning at a 45° angle relative to the overall tissue structure (Fig. 5.5I-J). Given that they were alternately subjected to tensile forces (which align cells along the stretching axis) and compressive forces (which promotes perpendicular alignment), the 45° orientation likely represents an optimal configuration that minimizes overall stress.

5. Magnetic cell segregation enables spatial organization in co-culture tissues

After characterizing the geometrical and mechanical properties of tissues composed solely of C2C12 myoblasts, we introduced a second cell type - NiH3T3 fibroblasts - during the

bioprinting process. Myoblasts and fibroblasts were respectively mCherry and GFP Lifeact transfected to distinguish them. Additionally, the cells were magnetically labeled using two distinct nanoparticle incubation protocols: NP3 labeling or NP1 labeling (a single 30-minute nanoparticle incubation the day before bioprinting). With a single incubation, myoblasts internalized slightly more nanoparticles (8 pg per cell) compared to fibroblasts (6 pg per cell) (Fig. 5.6A). As expected, this difference became more pronounced after two additional incubations, with myoblasts reaching an average of 20 pg per cell, against 11 pg for fibroblasts.

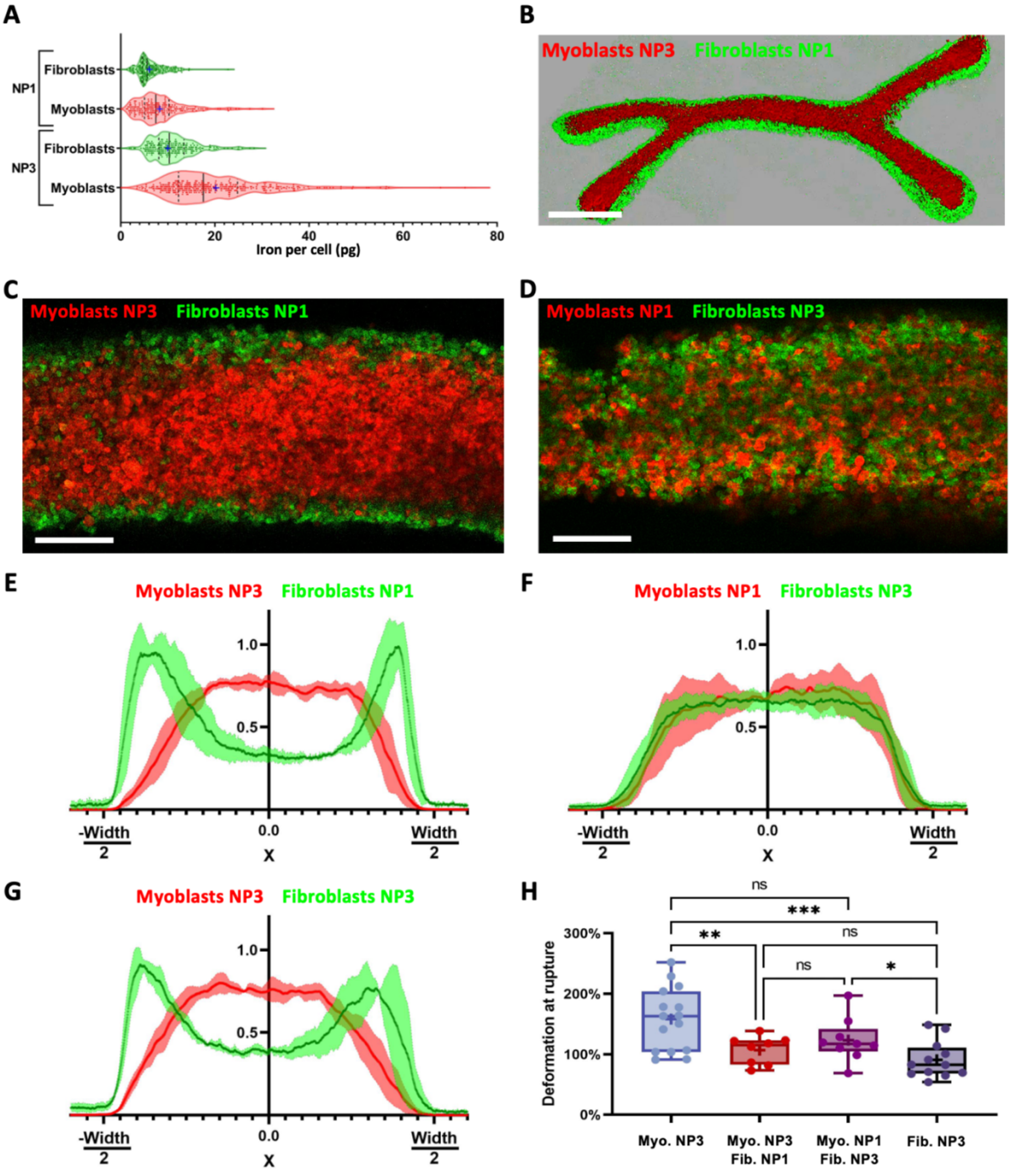

Figure 5.6. Magnetic segregation in bioprinted tissues composed of two cell types*. (A) Distributions of iron mass internalized by C2C12 myoblasts and NiH3T3 fibroblasts following NP1 or NP3 labeling. (B) 3D reconstruction from confocal imaging of a tissue printed with 50% NP3-labeled myoblasts cells and 50% NP1-labeled fibroblasts. (Scale bar = 1 mm) (C-D) Confocal z-slices of tissues printed with (C) 50% NP3-labeled myoblasts and 50% NP1-labeled fibroblasts, and (D) 50% NP1-labeled myoblasts and 50% NP3-labeled fibroblasts. (Scale bar = 200 µm) (E-G) Normalized fluorescence intensity profiles of mCherry-Lifeact myoblasts and GFP-Lifeact fibroblasts along the width of the central fiber in tissues composed of (E) 50% NP3-labeled myoblasts and 50% NP1-labeled fibroblasts (n=4), (F) 50% NP1-labeled myoblasts and 50% NP3-labeled fibroblasts (n=5), and (G) 50% NP3-labeled myoblasts and 50% NP3-labeled fibroblasts (n=4). (H) Deformation at rupture on day 1 for tissues stretched at a strain rate of 100% in 12 minutes, comparing tissues composed of NP3-labeled myoblasts, NP3-labeled fibroblasts, 50% NP3-labeled myoblasts and 50% NP1-labeled fibroblasts, and 50% NP1-labeled myoblasts and 50% NP3-labeled fibroblasts.*

When NP1-labeled fibroblasts and NP3-labeled myoblasts were mixed in equal proportion before bioprinting, their difference in magnetization led to their spatial segregation within the printed tissue. The more magnetic myoblasts accumulated primarily at the center of the structure, while the less magnetic fibroblasts localized at the periphery (Fig. 5.6B-C). This phenomenon occurs because the more magnetic myoblasts move faster and reach the whole patterned area first, while the less magnetic fibroblasts accumulate afterwards where the magnetic field gradient is strongest - along the edges of the pattern. In contrast, when the labeling was reversed (NP3-labeled fibroblasts and NP1-labeled myoblasts), the distributions of iron internalization of the two cell types were very similar, leading to a random distribution in the tissues after magnetic bioprinting (Fig. 5.6D). This segregation effect was further confirmed by fluorescence intensity profiles across tissue width which showed a distinct central localization of myoblasts when they were more magnetic and a uniform distribution when their magnetization was lower (Fig. 5.6E-F). Intermediate levels of segregation were observed when different labeling combinations were tested, depending on the relative difference in magnetization between the two cell types (Fig. 5.6G and Supplementary Fig. 5.8).

Rupture tests were performed on tissues composed solely of NP3-labeled fibroblasts, at a strain rate of 100% in 12 min. These tissues broke at much lower deformation compared to myoblast-only tissues, prompting an investigation into the mechanical behavior of mixed-cell tissues. Interestingly, tissues where the two cell types were magnetically segregated exhibited properties closer to those of the fibroblast-only condition, whereas tissues with a random distribution were more similar to myoblasts-only tissues (Fig. 5.6H). One possible explanation is that when the tissue is segregated, the weaker fibroblast region dictates the moment of rupture, as it breaks first, leading to overall failure. However, when the two cell types are homogeneously mixed, the more deformation-resistant myoblasts may help compensate for the lower mechanical strength of fibroblasts, delaying tissue rupture.

III. Discussion

In this study, we demonstrate how magnetic-based approaches, particularly magnetic bioprinting, can be used to control both the macroscopic shape and microscopic cellular architecture of engineered tissues. Reproducing specific macroscopic geometries is a key objective in 3D tissue engineering. Many approaches focus on a single predefined shape for a specific application, such as moulding collagen tubes to mimic tubular structures[364] or muscle fascicles[224,258,259] or stamping intestinal-like grooves onto matrices[380]. Bioprinting[42–44], relying on ink extrusion or photopolymerization, increases the versatility and complexity of the designs that can be created, sometimes closely resembling organs[466]. These techniques almost systematically depend on scaffolds, either preloaded with cells – subjecting them to stress during gel extrusion - or seeded post-fabrication, requiring cellular colonization over time[290,466]. Magnetic bioprinting differs by being scaffold-free, allowing unrestricted cell density. While previous studies on magnetic bioprinting have primarily achieved simple geometries[46,55,59,60] such as rods, rings or spheroids, the method introduced here enables a level of 2D complexity comparable to conventional bioprinting techniques. Additionally, tissue thickness can be adjusted to provide a degree of 3D control, though not as advanced as extrusion-based techniques. Importantly, this approach inherently imparts magnetic properties to the printed tissues, allowing them to be actuated by magnetic forces, as evidenced by their ability to clamp onto magnetic needles and undergo stretch-induced stimulation. This new set of magnetic tools resembles 4D bioprinting[570], where scaffolds can evolve in response to stimuli, sometimes even magnetic[290]. But our approach can bypass the matrix and directly control the cells.

Controlling the macroscopic shape of the tissue also influenced internal cellular organization[563]. The clearest example is the clip-on cross tissues, where cells aligned along the four branches but remained unorganized in the center. This pattern likely arises from the mechanical forces within the tissue, as cells tend to minimize deformation energy[571,572]. With one end constrained by a needle and the other connected to the center, each branch experiences traction forces that align cells along its axis, while the center, subjected to multidirectional forces, lacks a dominant orientation. This also creates shear stresses, making the center a structural weak point if the tissue is too thin. In contrast, tissues embedded in collagen were initially constrained on every external surface by the surrounding matrix. Detaching from this matrix allowed the branches to compact and develop compression forces, which led to cell perpendicular alignment. These conditions under static constraints suggest that cells in 3D tissues align based on boundary constraints, consistent with previous observations[387], but now demonstrated in a more complex geometry. Under dynamic constraints, stretching wrench shaped tissues caused C2C12 cells to adopt an oblique 45° orientation relative to the tissue and stretching direction. While traction induces parallel alignment[46] and compression leads to perpendicular alignment, the 45° orientation may represent an intermediate state that minimizes overall stress. Most studies on cyclic stretching show that cells can align perpendicularly to the stretching direction in 2D[387,568,569], while in 3D, alignment varies: cells may be

perpendicular[388,389], parallel[567], or even position-dependent - parallel in the core and perpendicular at the periphery[389]. In our constructs, outer cells twisted around the tissue, adopting an oblique orientation. This 45° orientation is uncommon in 3D tissues and may result from the high stretching amplitude (100%), whereas most studies do not exceed 20%[387]. Another key distinction is the absence of a matrix, which in traditional scaffolds provides guidance cues that reinforce alignment. Matrix remodeling can even amplify alignment over time, leading to a self-reinforcing organization[573]. By observing these diverse cellular orientations in scaffold-free tissues, we gain insight into how structural and mechanical cues - purely from cell-cell interactions - govern cell alignment. From a tissue engineering perspective, this study showcases strategies to actively shape tissue architecture and control cellular orientation in multiple directions.

Beyond cell orientation, cellular organization within tissues could also be controlled through magnetic segregation of multiple cell types. In microfluidic chips, co-culture is typically achieved by isolating different cell types in separated compartments, whereas precisely arranging multiple cell types within a single tissue remains challenging. One effective method involves extruding multiple gels, each loaded with a different cell type[574], offering versatility but adding complexity to the bioprinting process. In contrast, co-culture does not complicate magnetic bioprinting. While less versatile than extrusion-based approaches, it enables a simple and scalable way to achieve core-shell tissue organization in various geometries, which holds potential for tissue engineering. A previous study used matrix-guided moulding to create endothelial vessels surrounded by muscle cells, but only in a uniaxial configuration[259]. With the increased geometric flexibility provided by magnetic bioprinting, more complex tissues could be engineered, such as tubular networks embedded within another cell type, or multilayered structures mimicking smooth muscle layers in the intestines for instance.

Controlling both the geometry and internal organization of tissues is not only interesting for tissue engineering but also provides insight into how these parameters influence tissue mechanical properties, particularly fracture mechanics. Proper resistance to rupture is essential during development, as tissues experience a variety of stresses, and can serve to distinguish healthy from pathological tissues. It is generally assumed that under mechanical stress, a tissue stretches until the deformation exceeds the adhesion forces between cells or matrix components, at which point an initial defect forms and propagates through cell junctions, eventually to the entire tissue[575]. This failure mechanism is well documented in cell monolayers and 2D systems[561,562]. However, fewer studies have investigated it at the level of a 3D tissue. In 3D, some studies on the separation of cellular aggregates[576] have examined tissue fracture, yet primarily focusing on the cellular[577] and adhesion molecule[578] scales. Magnetic printed tissues offer a new tool to study tissue cohesion and resistance, notably thanks to their adaptable design. Our findings demonstrate that tissues of different widths (500 µm and 250 µm) showed similar

rupture distributions, confirming that deformation at failure under linear stretching is a material property independent of geometry, as previously observed in epithelial monolayers[561]. Moreover, we observed a decrease in deformability at higher strain rates, consistent with prior studies. However, we extended our analysis to much lower strain rates, including experiments lasting more than an hour, and even up to a week. At these timescales, cellular rearrangements occur, making it difficult to assess purely physical material properties, yet the trend remained: lower strain rates corresponded to higher rupture deformation. Interestingly, slow stretching appeared to condition the tissue, making it more stretchable than tissues subjected to rapid deformation after six days. Beyond strain rate effects, fracture mechanics in tissues composed of two cell types – especially when spatially segregated - has not been investigated to the best of our knowledge. The difference in rupture behavior between segregated and homogeneously mixed tissues observed in this study can be explained by a crack propagation model[575], which assumes that a crack appears when the energy needed to deform a cell exceeds the energy needed to break cell adhesion. In randomly distributed co-cultures, the more deformable myoblasts can compensate for the higher brittleness of fibroblasts, resulting in an overall intermediate mechanical response. However, in segregated tissues, fibroblast-rich regions must stretch the same extent as the rest of the tissue. Since fibroblasts are less deformable, cracks form earlier in these weaker regions and propagate through the tissue, ultimately leading to premature failure.

Regarding cyclical stretching, it is typically used in mechanostranduction studies[46,265–267,280] to promote cell differentiation. In this study, it also provided insights into the mechanics of magnetic bioprinted tissues. Indeed, despite deforming the tissues by 100%, a strain rate of 100%/min was low enough to allow cyclic stretching over multiple days, whereas a rate of 25%/s was not sustainable. This supports the idea that, unlike inert materials, tissues can repair themselves, with cells capable of re-stablishing adhesion given sufficient time[579]. For example, in *Drosophila* tissue subjected to pulsatile forces[580] myosin-mediated adhesion repair occurs within 400 seconds. Despite this regenerative ability, living tissues remain susceptible to mechanical fatigue like conventional materials[579]. Repeated sub-failure loads lead to the accumulation of micro-defects, which can propagate and cause rupture. Higher strain amplitudes increase the likelihood of such defects appearing[581], and unlike linear stretching, tissue geometry influences fatigue-induced failure - thinner constructs are more prone to breakage under cyclic loading[582].

Together, these findings highlight the need to consider both mechanical and biological factors when studying the properties of living tissues. By controlling tissue architecture at both the macroscopic and microscopic levels, as well as the mechanical strains applied, the magnetic-based approaches in this study demonstrate potential not only for tissue engineering but also for advancing our understanding of the biomechanical principles governing living tissues.

IV. Experimental procedures

Cell culture:

C2C12 cells (ATCC) were cultured in growth medium, DMEM (Gibco) with 10% fetal bovine calf serum (Dutcher) and 1% Penicillin-Streptomycin (Thermofisher).

NiH3T3 fibroblasts (ATCC) were cultured in growth medium, where bovine calf serum was replaced by calf serum (ATCC 61965-026).

Both cell types were passaged once confluency reached between 50 and 80%, without exceeding passage 5 for C2C12 and 10 for NiH3T3.

Cell Transfection:

Cell transfection was performed using the PEI MAX reagent (Polysciences) according to the manufacturer's protocol. The pLVX-LifeAct-mScarlet plasmid and the pLVX LifeAct-eGFP-P2A-puro plasmid (constructed from pLVX puro vector Clontech Catalog No. 632164) were used for viral transfection. The pLVX-LifeAct-mScarlet plasmid was employed to infect C2C12 cells, generating the C2C12 LifeAct-mScarlet stable cell line. Similarly, the pLVX-LifeAct-eGFP-P2A-puro plasmid was used to infect NIH3T3 cells, resulting in the establishment of the NIH3T3 LifeAct-eGFP stable cell line.

Magnetic Labeling:

Superparamagnetic maghemite nanoparticles, synthesized via the iron salts co-precipitation method and coated with citrate, were used to label the cells [316].

Labeling solution was prepared by mixing the nanoparticles at a concentration of 2 mM of iron and 2 mM citrate (to prevent nanoparticle aggregation) into RPMI medium (Gibco). For NP1 labeling, the cell culture medium was replaced with this nanoparticle solution and incubated for 30 minutes the day before the bioprinting procedure. For NP3 labeling, cells were incubated with the nanoparticle solution once daily for three consecutive days prior to bioprinting, as described previously[46]. These incubation protocols facilitated nanoparticle efficient internalization via endocytosis.

NiFe pattern fabrication:

Magnetron sputtering (Plasmionique) was used to deposit a conductive layer of 10nm of titanium and 100 nm of copper on a 70 x 50 mm^2 Corning glass slide. TI-Prime (Microchemicals) and then 70 µm of AZ 125nXT photoresist (Microchemicals) were spincoated on the coated side of the slide. Photolithography was then performed with a chromium mask, designed with the shape of the desired patterns. This exposes the copper in

these shapes, making it possible to perform NiFe (80:20) electrodeposition [46,56,465]. The copper covered substrate, acting as a cathode, and an NiFe anode (Goodfellow) were connected to a generator while being immersed in a 250 $g.L^{-1}$ $NiSO_4$, 5 $g.L^{-1}$ $FeSO_4$, 25 $g.L^{-1}$ boric acid, 2 $g.L^{-1}$ saccharin and 0.1 $g.L^{-1}$ sodium dodecyl sulfate bath, heated to 30 °C and magnetically stirred. Applying a current of 7 mA per mm^2 of patterns led to NiFe deposition in the holes with the exposed copper. In these moulds, NiFe patterns would grow by approximately 3 $\mu m.h^{-1}$, until patterns would be at least 50 µm-thick. The substrate would then be immersed in TechniStrip P1316 (Technic) at 70 °C to remove the copper and resist, exposing the freshly electrodeposited 50 µm-thick NiFe patterns in the same shape as the original patterns on the chromium mask. The substrate was finally spincoated with 100 µm of PDMS (Sylgard 184, 1:10 curing agent). Multiple patterns were made on the same glass substrate. They were positioned to be grouped within 16 mm wide circles, the size of the wells for the next bioprinting step.

Magnetic bioprinting process:

Wells were made by plasma-bonding 1 cm high hollow PDMS (Sylgard 184, 1:10 curing agent) disks with outer and inner diameters of 20 mm and 16 mm respectively, to a 150 µm thick 22 x 22 mm^2 VWR coverslip. After treating them with anti-adherence solution (StemCell Technologies) for 1 hour, they were placed directly on top of NiFe patterns. 500µL of a suspension of previously magnetically labeled cells, detached with TrypLE Express 1X (Gibco) was pippeted into each well. The number of cells in this volume was adapted to the total area of the NiFe patterns beneath the wells, aiming for either 10^5 or 2×10^5 cells per mm^2 of pattern. The substrate with the patterns and the wells on top was then placed in the middle of two magnets (110.6 × 89 × 19.6 mm^3, remanence Br = 1.35 T, Ref. Q-111-89-20-E, Supermagnete), positioned to attract each other but maintained at 3.6cm, a distance meant to minimize the magnetic gradient[46]. After usually 3h the system was removed from the magnets and the magnetic printed tissues were collected.

Tissue culture after bioprinting:

Following bioprinting, C2C12 cells were cultured in differentiation medium, consisting of DMEM (Gibco) with 1% Horse Serum (Thermofisher) and 1% Penicillin-Streptomycin (Thermofisher).

To investigate whether the patterns could prevent tissue compaction, some tissues were maintained on the patterns within the magnetic field for 6 days, without changing the initial configuration from day 0. For all other conditions, tissues were collected from the wells with a 5mL pipette just after removing them from the magnets and the patterns, 3 hours post-bioprinting. The tissues were then cultured for 6 days, either free floating in wells of non-treated VWR 48-well plates, magnetically trapped by needles in ecoflex chips or embedded within a 2$mg.mL^{-1}$ collagen matrix. For the latter, a layer of 100 µL of a cold collagen solution (differentiation medium with 2 $mg.mL^{-1}$ collagen (Corning, rat tail) and pH 7 adjusted with

NaOH) was put to polymerize at the bottom of a well of a 48 well plate. After placing the printed tissue on top of the polymerized collagen layer, which prevents it from sedimenting at the bottom, the supernatant was removed and a second layer of 100 µL collagen solution was added. Once polymerized after 30 min in an incubator, the tissue was fully embedded in the matrix, and the well was filled with differentiation medium.

Chip fabrication:

Ecoflex (00-31 Near Clear, Smooth-on) was poured into 3D printed moulds, designed on Autodesk inventor, with needles inserted where the final needles should be, and then placed at 75 °C for 3 hours. After withdrawing the needles, the chips could be unmoulded and nickel-plated steel needles (0.6 mm wide, Bohin) were inserted back in the chips. To avoid them from rusting in cell culture medium, these final needles were covered with 3 coatings of transparent nail polish dried overnight at 120 °C to evaporate all solvents. The chips for cross shaped tissues were designed as 15 mm wide square reservoirs with four needles aiming towards the center of the chips, at 2.25 mm or 4.25 mm from the center. The chips for wrench shaped tissues were designed with 8 parallel 14 mm long rectangular reservoirs with two aligned needles aiming towards the center and 2 mm apart. Once properly placed, the needles were fixed to the chips with Loctite SI 5398 adhesive. Next, the chips, and specifically the needles, were plasma treated, exposed to Tris-HCL buffer (pH = 8.5) with 5 mg/mL dopamine hydrochloride (Thermo Scientific) for 3 hours, and then rinsed with PBS. The polydopamine treatment is meant to activate the surface of the needles for the final coating at room temperature with a PBS solution with 0.2 mg/mL collagen I for 2 hours. This coating, timed to end at the same time as the bioprinting process, was rinsed with PBS and the chips were filled with warm medium.

Magnetic trapping process:

In each chip, each needle is magnetized by a N48 Neodymium magnet with a height and diameter of 6 mm (Supermagnete, S-06-06-N) placed on its outward end with its axis aligned with the needle. The magnets were positioned in this specific configuration by trapping them in 3D printed slots adapted for each chip. The chip for cross shaped tissues fits into a square magnet holder with a magnet slot in the middle of each side. The magnets are arranged so that their polarity alternates, meaning that two magnets facing each other repel, creating magnetic field lines in a cross shape at the center of the chip. For wrench-shaped tissues, the chip is placed between two magnet holders, each consisting of 8 rows of magnet slots, to magnetize the two needles on each side of the 8 compartments of the chip. Within one holder, magnets are oriented identically, and magnets facing one another are oriented to attract one another, creating magnetic field lines spanning from one needle tip to the other.

For clip-on cross shaped tissues, tissues were transferred from the bioprinting well to the chip with a 5 mL pipette. As the tissue folds onto itself when aspirated, it first needs to unfold, and as soon as the magnets are placed next to the needles, each clamp of the tissue clips onto one

of the four needles. For wrench shaped tissues, the magnets are already in place, and as the tissue is approached to the needles with the pipette, it magnetically clamps onto the two needles directly.

3D printed parts:

Moulds for the chips and the various parts used mostly to hold magnets and stretch the chips were designed on Autodesk Inventor and then 3D printed with a Digitalwax 028J Plus® 3D printer (DWS).

Simulations:

Magnetic field simulations were done with COMSOL Multiphysics (Magnetic Field No Currents module, Licence number 6464550).

Rupture tests:

After the tissues were incubated overnight to allow adhesion to the needles, the chips were clamped onto an automated stretching system. This system was assembled using a Thorlabs breadboard, onto which motors and 3D-printed parts were fixed. One side of a chip is connected to a part fixed to the board, while the other side is connected to the motor. As the motor retracts, the chip is stretched, which increases the distance between the needles, consequently stretching the trapped tissue. The movement of the motor is controlled from a computer, via a Raspberry Pi, with a software developed to impose any type of command to the motor. The system allows up to four independent motors to operate simultaneously on one breadboard, enabling parallel stretching of multiple samples. The chips were subjected to stretching under various conditions until the tissue within each chip ruptured. During the tests, the time of rupture and the amount of stretching (when tissues were stretched linearly) were recorded. Tissues that detached from the needles before rupturing were excluded from the analysis.

Fixation and stainings:

Tissues were rinsed in PBS, immersed in 4% Paraformaldehyde in PBS (Thermofisher) for 1h at room temperature for fixation and then rinsed again with PBS. Magnetically trapped tissues were fixed as they were in their chips to preserve their shape.

Prior to staining, tissues were placed in blocking solution, 4% w/w BSA (Sigma) and 0.5% v/v Triton X-100 (Fisher) in PBS, at room temperature for 1 hour. After rinsing them with PBS they were incubated overnight at 4 °C with 1:1000 Phalloidin AlexaFluor 488 (Thermofisher) and 1:300 DAPI (Invitrogen) in blocking solution. The next day samples were rinsed with PBS.

For myogenin stainings, samples were additionally placed at room temperature in saturation solution, PBS with 0.3% (v/v) Triton X-100 and 1% (w/w) BSA. After rinsing them with PBS, samples were immersed overnight at 4 °C with saturation solution with 1:200 myogenin primary antibody (mouse, DHSB, F5D). Following PBS rinsing the next day, samples were incubated at 4 °C overnight with 1:750 donkey anti-mouse 488 (Thermofisher Scientific, A-21202) in saturation solution. The following day, samples were rinsed with PBS.

Magnetophoresis for quantification of iron internalization:

Magnetophoresis was used to measure the amount of iron internalized by cells following incubations with magnetic nanoparticles[422]. Magnetically labeled cells in suspension in PBS were filmed after approaching them to a magnet with a magnetic field of 0.145T and a gradient of 17 $T.m^{-1}$. As the magnetic force attracting each cell towards the magnet should counterbalance the drag force, it can be calculated by measuring the speed and diameter of each cell. Knowing the magnetic field and gradient, the magnetic moment of each cell can then be inferred, from which the mass of iron internalized by each cell can be calculated.

Imaging:

After fixation and stainings, samples were placed on fluorodishes using tweezers and a pipette for imaging with a Leica DMi8 inverted confocal microscope employing either 10x air or 25x water objective. Live samples were imaged from below the chips or wells with a Leica DMi1 brightfield microscope for punctual images or within the incubator using a CytoSmart Lux 3 FL videomicroscopy system. A Stemi 508 Greenough Stereo Microscope with a DinoEye camera was used to image samples from above. For rupture tests, chips were imaged either by filming the entire chip during the stretching process (with the chip steadily fixed in a holder) or by taking pictures at regular intervals for stretching rates of 100% stretching over 2 hours and below. Chips that were filmed were stretched outside of the incubator for no more than 40 min, with a heating lamp to maintain a temperature of 37 °C. For longer experiments at slower speeds, the chips and stretching system were kept inside the incubator, except for medium changes and regular image capturing.

Image analysis:

Image analysis was performed on ImageJ. Images of larger objects were first reconstructed from multiple frames, either with the MosaicJ or the Stitching plugins.

Tissue shape and branch thickness were analyzed with the “Analyze particles” module.

To evaluate fluctuations of the intensity signal of myogenin in clip-on cross-shaped tissues, stacks of confocal images were summed for each channel, for each branch of the crosses a frame from the center of the tissue to the edge of the branch was cropped and the “Plot profile” module

was used for the myogenin and the actin channels. For each plot, the background value was subtracted and the myogenin signal was divided by the actin signal to normalize it. The plots from all branches were averaged, resulting in a mean value of the normalized myogenin signal intensity as a function of a distance to the center. To normalize all samples together, for each of them the intensity was divided by the average value within the first 50 μm from the center of the tissue.

The spatial distributions of fibroblasts and myoblasts in co-culture constructs was obtained by plotting the intensity profiles of the green and red signals along the width of the central fiber of the tissues. Both signals were then normalized in x using a python code so that the width of the tissues would be equal to 1. The minimum signal value was set to 0 and the overall signal was normalized so that the area under the curve would be equal to 1, making it easier to compare and plot the different samples together.

Statistical analysis:

Data processing was done with Microsoft Excel, and graphs were plotted with GraphPad Prism 8 (GraphPad Software, La Jolla, California). Standard deviations were used to represent error bars. Every value represented was obtained by averaging at least three independent replicates. Statistical differences were evaluated using Welch t-tests and represented with * when P value < 0.05, ** when $P < 0.01$, *** when $P < 0.001$ and **** for $P < 0.0001$.

Chapter 6

Conclusion and Perspectives

I. Achievements

Recapitulating the native structure of complex anisotropic tissues *in vitro*, such as skeletal muscle, remains one of the greatest challenges of tissue engineering. Technologies like electrospinning and bioprinting have become cornerstones of anisotropic tissue engineering, yet they still fall short of producing fully physiologically relevant tissues. Among emerging strategies, magnetic based approaches have shown considerable promise to recreate intricate *in vivo* architectures thanks to their versatility and capacity for remote manipulation. This context motivated the objectives outlined at the beginning of this manuscript: to advance magnetic-based techniques and leverage them to engineer and study anisotropic skeletal muscle tissue. Following a review of the current research landscape in **Chapter 2**, we addressed these objectives through three original contributions, achieving meaningful progress in both technological innovation and their application to skeletal muscle tissue engineering.

1. Technological advances

Throughout this manuscript, we have presented a next-generation magnetic tissue engineering toolbox that integrates all forms of magnetic based approaches first introduced in the review of **Chapter 2**: magnetic alignment, assembly, patterning and actuation.

All these approaches were made possible by an initial optimization in **Chapter 3** of the magnetic labeling protocol, enabling myoblasts to internalize up to 20 pg of iron without compromising cell viability through sequential incubations.

Magnetic alignment is also at the core of **Chapter 3**. Through simulations and empirical experimentations, we optimized the magnetic gradient and thereby enhanced the alignment of myoblasts. We were able to control the length of aligned cell-based chains by tuning their density and magnetization and showed that co-culture with non-magnetic fibroblasts could even be possible without any impact on alignment. Moreover, we demonstrated that this process could easily be transposed to much larger objects, spheroids.

Indeed, in **Chapter 3** we combined magnetic alignment with magnetic assembly to achieve a multitude of variations of anisotropic microfeatures in skeletal muscle tissue. Spheroids could be used as tunable biological building blocks assembling under dipolar interactions. Regulating spheroid size and density resulted in spheroid chains with both controlled length and diameter.

Spheroid formation was notably possible thanks to our magnetic patterning technique first introduced in **Chapter 3**, where it was used to engineer in 3 hours thousands of size-controlled spheroids. However, we proved that this magnetic patterning technique was not limited to spheroids and could be expanded beyond them to produce tissues of virtually any geometry, starting with wrench-shaped tissues in **Chapter 4**, and then extending to star-, droplet-, triangle- or even cross-shaped tissues in **Chapter 5**. These tissues were fabricated within hours, could easily be modified according to our needs, and could reach the centimeter scale. Magnetic bioprinting could result in even more complex architectures through magnetic segregation of

multiple cell types. Moreover, this magnetic bioprinting showed no detrimental impact on cell viability and resulted in 3D cohesive tissues which can easily be manipulated afterwards.

Indeed, functionalizing the shape of the tissues enabled magnetic actuation, first explored with wrench-shaped tissues in **Chapter 4**, and then adapted to cross-shaped tissues in **Chapter 5**. We demonstrated that optimizing tissue shape with the right magnetic field could control specific tissue motions, enabling tissue trapping and resulting in robot-like functions through remote magnetic manipulation.

2. Engineering mature, functional muscle tissue

The development of all these magnetic-based methods was harnessed to engineer skeletal muscle tissue. While we showed in **Chapter 3** that spheroid alignment induced spheroid chain fusion, preserving tissue anisotropy and promoting muscle maturation, muscle differentiation was effectively optimized in **Chapter 4**. We showed that magnetic trapping of magnetically printed wrench-shaped tissues resulted in the fusion of myoblasts into 3D bundles of aligned multinucleated myotubes, some reaching the millimeter scale and containing more than 50 nuclei. This positive effect was observed not only on C2C12 myoblasts over the course of two weeks, but also across three distinct myoblast cell lines derived from human iPS cells, producing a more physiologically relevant model with prospects for personalized medicine. High myogenin expression confirmed proper maturation, while calcium imaging evidenced robust functionality across all cell lines by increased calcium activity and contraction upon ACh stimulation, especially within M-iPSC tissues.

Magnetic trapping also enabled tissue stretching up to 100% deformation which significantly promoted muscle differentiation. In tissues made from C2C12 cells, we observed increased alignment and fusion, leading to myotubes containing more than 80 nuclei and reaching nearly two millimeters in length. M-iPSC tissues displayed strong indicators of differentiation after only three days when stretched, with increases in myogenin positive cells and adult myosin heavy chains expression, and an overwhelming presence of alpha-actinin striations throughout the tissues. Stretching also doubled the population of quiescent Pax 7 positive satellite, which are essential for muscle regeneration. Calcium activity and contractility doubled in all cell lines after mechanical stretching, with M-iPSC tissues contracting by 20% following ACh stimulation after just three days in culture.

3. Investigating tissue biomechanics

While **Chapter 4** focused on muscle maturation, **Chapter 5** leveraged geometrical and mechanical cues to further investigate the biomechanical properties of magnetically printed tissues.

Although we did show that printed tissues naturally tended to mature toward a spherical shape, magnetic trapping enabled preservation of their initial shape even in non-physiological cross-shaped tissues. This notably demonstrated the impact of geometrical cues on muscle differentiation, as cross-shaped tissues cultured in this geometry over a week displayed higher differentiation along the branches compared to the center of the tissues.

Regarding mechanical cues, we showed that maximal deformation of printed tissues depended solely on stretching speed, whereas cyclical fatigue was influenced by tissue geometry as well as cycle amplitude and frequency. Interestingly, while stretching tissues in **Chapters 3** and **4** improved parallel alignment, we showed in **Chapter 5** that cyclical stretching induced oblique cell alignment. Moreover, magnetic segregation made it possible to highlight that the distribution of multiple cell types within a tissue directly impacts its response to mechanical deformation.

II. Limitations

Alongside these substantial results, some aspects warrant further consideration and discussion, which we will address in this section.

1. Potential impact of magnetic nanoparticles

All magnetic tissue engineering approaches rely on magnetic materials, either in close contact with cells in the scaffold, or directly internalized by cells and stored in endosomes. The three studies presented in this manuscript belong to the latter category. While magnetic nanoparticles enable complex remote manipulation, like any other foreign bodies, they can influence cellular behavior. Indeed, studies have shown cytotoxic effects of superparamagnetic iron oxide nanoparticles notably due to their surface charge[420]. Nanoparticles associated ferroptosis was also observed in cardiac cells[421], and even leveraged for cancer treatments[49].

These adverse effects can be due to the presence of positive charges on the nanoparticles. Herein, the citrate coating we used produces anionic nanoparticles with a zeta potential of -35mV. This citrate coating promotes stabilization and minimizes non-specific interactions with cell components, favoring biocompatibility. In a previous study, citrate coated magnetite nanoparticles notably did not impact *in vitro* cell cultures, and even when injected *in vivo* no toxicity or organ morphological changes were observed, aside from an accumulation of iron in the liver[418]. Another potential cause of adverse effects is the release of ferrous iron (Fe^{2+}), which can trigger the production of cytotoxic reactive oxygen species (ROS). This mechanism is actually the basis for using iron oxide nanoparticles to deliberately induce ferroptosis in therapeutic contexts. However, such an effect requires nanoparticles that contain Fe^{2+} in their structure, which is the case for magnetite (Fe_3O_4), but not for maghemite (γ-Fe_2O_3). The latter, maghemite, is the form most commonly used for biomedical applications and was used exclusively in all our studies. Nonetheless, it should also be noted that magnetite nanoparticles could still be considered as they surface oxidize over time into maghemite.

As observed in past research[421] and in **Chapter 3**, any potential cytotoxicity is time- and dose-dependent. Nonetheless, we showed that consecutive incubations at low concentrations for short periods of time made it possible to have cells internalize much more than they would otherwise, without any impact on their metabolic activity. This seemed to indicate that negative effects at high concentrations or extended periods of time were related to the incubation or internalization process, rather the internalized iron itself.

Regarding the fate of nanoparticles within the body, multiple studies, including the one in **Chapter 4**, have shown that cells can degrade the nanoparticles[424,583]. This is due to enzymatic processes, notably involving ferritin. In some cases, remagnetization was even observed, implying that cells could produce their own magnetic nanoparticles out of degraded iron[583], which further confirms the biocompatibility of magnetic nanoparticles and provides a possible new source for biogenic nanoparticle production.

While the use of foreign bodies such as iron oxide nanoparticles always has potential risks, which should be investigated, we have provided evidence that their presence did not adversely affect our engineered tissues, notably with metabolic assays, LIVE/DEAD assays at multiple stages of tissue culture and monitoring of iron degradation over time. Moreover, the successful enhancement of muscle differentiation and function in labeled tissues offers additional confirmation that magnetic nanoparticles did not impair myogenesis.

2. Scaffolds in tissue engineering

In addition to magnetic nanoparticles, another external factor that has remained a concern throughout this manuscript is the scaffold. Our initial approach in **Chapter 3** is based on a collagen I and Matrigel matrix. Although this scaffold favored colonization, it also resulted in cells losing their anisotropic organization instead of fusing into myotubes. On the other hand, tissues made in **Chapters 4** and **5** were engineered without any surrounding matrix, aggregated solely by magnetic forces. Although these scaffold-free tissues were more prone to breakage, due to external forces or their own growing contractility, they also exhibited unprecedented levels of maturation within just a few days.

This contrast raises an important question: is the presence of a matrix always beneficial for skeletal muscle tissue engineering. Almost every single skeletal muscle tissue engineering approach heavily relies on a scaffold[42–44], yet matrix accounts for less than 10% of native skeletal muscle tissue[174]. Such low levels are difficult to replicate *in vitro* with conventional matrix-based strategies[261]. High cell density, which is essential to trigger myoblasts fusion through prolonged contact between cell membranes[25], is often undermined by overabundant matrix content. However, matrix also plays a key mechanical role, contributing to half of the load bearing capabilities of skeletal muscle, even as a small fraction of the tissue [175].

Therefore, skeletal muscle tissue engineering must reach the right balance between optimal cell density for fusion, and sufficient tissue integrity. Scaffold free magnetic printed tissues can offer a flexible starting point, as matrix can be integrated at later stages when necessary. However, some of our own results have highlighted challenges with this approach. Indeed, cross shaped tissues embedded in a matrix in **Chapter 5** had their cells align perpendicularly to the overall geometry, likely due to the isotropic force transmission by the surrounding matrix. Without isotropic boundary conditions cells naturally align with the main axis of the tissue. However, matrix embedding can introduce multidirectional stresses, preventing the desired alignment to occur[388]. If the matrix is disorganized, it can also create isotropic guidance cues. This may explain the perpendicular cell migration observed in spheroid chains presented in **Chapter 3**, even though the overall anisotropy is still preserved over time.

One possible solution would be to allow proper tissue maturation and reorganization before introducing a matrix to support long term structural stability. Incorporation of matrix in magnetic printed tissues remains to be further investigated in order to enhance both maturation and cohesion of anisotropic tissues.

3. Force measurement

As mechanical forces are intimately linked to muscle function and differentiation, they are commonly monitored in skeletal muscle tissue engineering. It is therefore important to acknowledge the methodologies we followed for evaluating contractility, which slightly diverge from standard approaches.

Indeed, most force measurements in skeletal muscle tissue engineering rely on the use of pillars on which the muscle tissue can exert forces[260–264]. They can either be inferred from pillar deflection[262–264,269,270,272] or directly using a force transducer[260,261,267,268,271]. This notably makes it possible to monitor the changes in the developed force throughout tissue culture time.

In our system, magnetic needles are necessary to trap the magnetic printed tissues, making the integration of a transducer technically challenging. Instead of two deformable pillars, a single elastic pillar could have been placed in between the needles with a slight offset with the needles axis, deflecting the muscle tissue. As the tissue would contract, the pillar would bend and be brought back towards the axis between the two needles[584]. However, it could have undermined cell alignment, which is essential for muscle maturation. Moreover, mechanical stretching might have biased these measurements.

Despite these hurdles, we still aimed to evaluate stresses in the tissues we engineered. In the study of **Chapter 4** we introduced deformable beads as stress sensors, which had originally been designed to evaluate stresses in zebra fish embryos[553,560]. Their main drawback is that real-time evolution of the forces within a construct is more challenging to monitor. However, once a tissue is fixed the beads' deformations can be used to observe the spatial distribution of the stresses, along with their directions, unlike conventional methods which provide only a single, global force value of the whole tissue. These beads could therefore potentially be used in complex tissues beyond the uniaxial geometry.

Moreover, force measurement is essentially meant to evaluate the functionality and contractility of skeletal muscle tissues, which we have consistently demonstrated through multiple alternative assays in **Chapter 4**, including the increasing deformation of the elastic beads. Indeed, functionality in tissues made from M-iPSC was evident through spontaneous contractions and the presence of alpha-actinin striations, indicating sarcomeres in nearly all cells by day 3. Calcium imaging confirmed increasing calcium transients over time, essential for contraction. Besides, in all four myoblast cell types, ACh stimulation resulted in significantly enhanced calcium signals and visible contractions, with both effects doubling in pre-stretched tissues. Overall, these findings demonstrate that muscle functionality and contractility is not limited to a single force measurement.

III. Perspectives

The current limitations of our approaches are also opening new perspectives for improving the skeletal muscle constructs and the technology. This final section discusses such prospects for potential studies, with an eye toward future biomedical applications.

1. Enhancing the complexity of the muscle constructs

The skeletal muscle constructs presented in **Chapter 4** have reached high levels of maturation and functionality. Therefore, improving upon their current complexity could bridge the gap with native skeletal muscles even further.

First, other mechanical stimulations could be investigated. In **Chapter 4**, we only investigated the impact of a single 50 or 100% deformation. The automatized stretching system in **Chapter 5** was primarily used to probe the mechanical properties of the tissues but some of its dynamic protocols could also favor muscle maturation. Previous studies using automatized mechanical stimulation systems have explored how varying strain profiles can better mimic mechanical *in vivo* cues [261,265–267,272,280]. As these were usually performed on tissues with a high scaffold composition, it could be very interesting to study how cell-only tissues would react to these more complex protocols.

Electrical stimulation is another common strategy in skeletal muscle tissue engineering[260,262,267–272], as electrical current can trigger muscle contraction. It can therefore be used to either test muscle functionality or stimulate for enhanced maturation. Magnetic needles could potentially be adapted to deliver electrical stimulation, enabling the integration of dual mechanical and electrical inputs in the same platform.

Beyond expanding the repertoire of possible stimulations, one promising strategy to further enhance tissue complexity and physiological relevance is by including other cell types. We have already explored the possibilities of adding fibroblasts in magnetic muscle constructs of **Chapters 3** and **5**, but we have not yet precisely investigated how they would promote muscle maturation in our constructs, as they do *in vivo* [521,522,585]. Moreover, their intrinsic ability to secrete extracellular matrix could be leveraged to help tissues produce their own matrix, improving their cohesion. Their integration in the constructs could be optimized to mimic as closely as possible the *in vivo* matrix composition.

Motor neurons are also essential in native skeletal muscle as they trigger contraction[195]. Co-culture with motor neurons could therefore be very beneficial[262,586]. In order to investigate the potential of such co-culture, we have performed a first attempt by applying **Chapter 4**'s approach to a mixture of C2C12 myoblasts with NSC-34 motor neuron-like mouse cells[586], which were both NP3-labeled. Interestingly, NSC-34 cells that were initially randomly dispersed throughout the tissues (Fig. 6.1A-B), progressively migrated to the edge of the tissues, most likely due to surface tension sorting (Fig. 6.1C-E). Nonetheless, they still appear to branch towards inner myotubes, that display remarkable maturation. These initial observations warrant

much further investigation into the dynamics and functional outcomes of motor neuron co-culture.

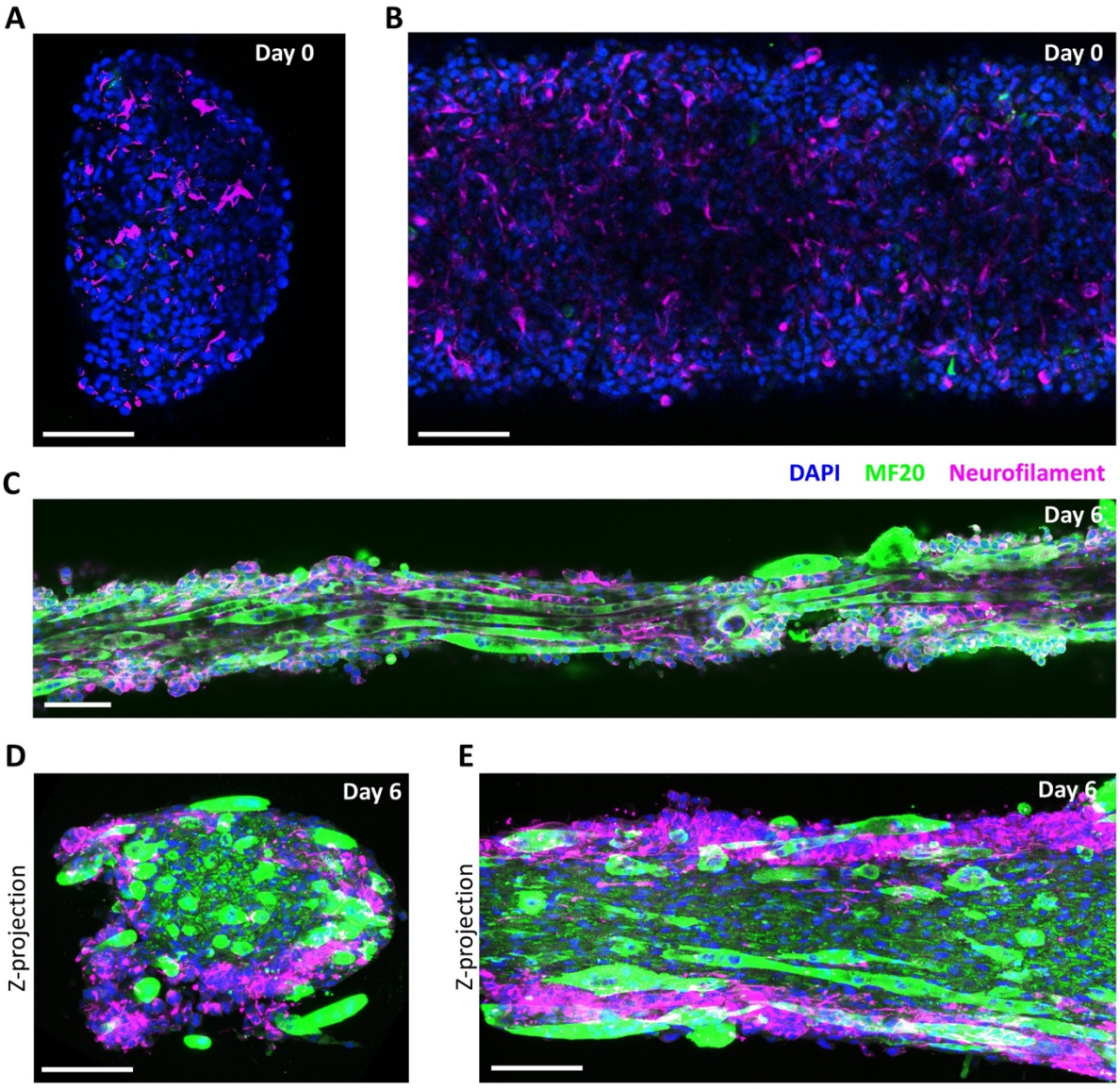

Figure 6.1. Confocal imaging of magnetically printed wrench-shaped tissues made with C2C12 myoblasts mixed with NSC-34 mouse motor neuron-like cells. *Images of z-slices of wrench-shaped tissues' central fibers on day 0 from (A) a transverse and (B) a longitudinal section, and (C) after 6 days of culture trapped between needles, from a longitudinal section. Z-projections of multiple z-slices imaged over 100 µm-thick (D) transverse and (E) longitudinal sections, each sliced from a central position of a 6-day-old, trapped tissue's central fiber. Both cell types were initially NP3-labeled. All tissues were stained for DAPI to observe nuclei, MF20 to observe differentiating muscle cells, and neurofilament to observe NSC-34 cells. (Scale bar = 100 µm, DAPI in blue, MF20 in green, neurofilament in magenta).*

Vascularization is equally critical for myogenesis[193]. Studies have attempted co-culture of myoblasts with endothelial cells[259,587,588], such as HUVECs, showing that they could improve muscle maturation and contractility[589]. Nonetheless, vascularization requires the formation of hollow channels and flow, which could be challenging to achieve with our current system. Hollow magnetic needles could offer a solution by enabling tissue immobilization while simultaneously allowing fluid perfusion.

The source of these different cell types is also crucial. We have shown that we could use human iPSC derived myoblasts in **Chapter 4**. Integrating other cell type similarly derived from human iPSC could drastically improve the functional relevance of the tissues[262], especially if these different cell types were derived from the same patient iPS cells.

So far, we have only discussed co-culture of myoblasts with only one of these other cell-types, but they all need to be present to reproduce skeletal muscle tissue. These initial experiments with motor neuron like cells do seem to indicate that multiple cell types could spontaneously reorganize. Guiding this reorganization is therefore essential and will most likely require further developing the magnetic tissue engineering techniques we have established so far.

2. Improving the technology

Recapitulating the complexity of native tissue architectures necessitates increasingly sophisticated and precise engineering strategies. Although the magnetic-based techniques presented in this manuscript are already advanced, they can still be more upgraded.

We have introduced magnetic segregation in **Chapter 5** to create core shell structures with multiple cell types, but it is far from the only type of architectures observed *in vivo*. When discussing magnetic patterning in **Chapter 2**, we have introduced studies performing sequential patterning steps. By varying magnet size, shape, and cell type, it made it possible to pattern each cell population with high spatial specificity[300,430,431]. To demonstrate the feasibility of sequential patterning using our magnetic bioprinting platform, we fabricated distinct NiFe patterns in the shapes of the clamps and the central fibers of the wrench-shaped tissues (Fig. 6.2A-B). Bioprinting first the myoblasts on the fiber patterns and then fibroblasts on the clamp patterns made it possible to create wrench-shaped tissues with specific positions for both cell types (Fig. 6.2C). A third cell type like motor neurons could also be distributed throughout the tissues (Fig. 6.2D). Although very preliminary, this proof of concept warrants further exploration in future studies to investigate how precise this step-by-step bioprinting process can be, and how many cell types can be successfully integrated.

After bioprinting, precise guidance and control of tissue morphogenesis are also essential, as demonstrated in **Chapters 4** and **5**. Magnetic actuation was notably leveraged by adapting tissue shape to trap them with a two- or four-needle system. For magnetically printing tissues with non-uniaxial architectures, systems incorporating multiple magnetic anchors – potentially

asymmetric - could be envisioned. So far, all needles were placed in the same plane, but they could very well be placed at different heights in order to create 3D architectures. Beyond magnetic clipping, the geometry of magnetic printed tissues can be engineered for alternative actuation modalities, like flower-shaped magnetic tissues meant to fold under a magnetic field [437,470]. Part of our constructs could be magnetically trapped while another could be designed to undergo some type of magnetic folding, to mimic heart valves opening and closing for instance.

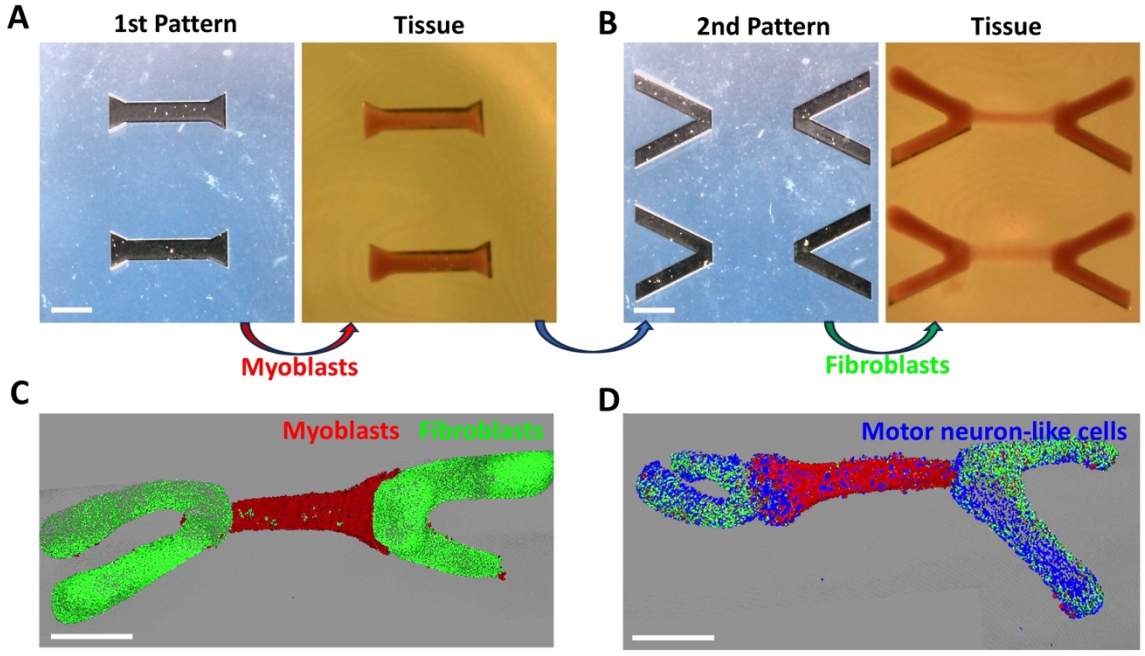

Figure 6.2. Step-by-step magnetic bioprinting. *Patterns to magnetically bioprint (A) in a first step the central fiber of wrench-shaped tissues out of myoblasts and (B) in a second step the clamps out of fibroblasts. 3D reconstruction from confocal imaging of step-by-step magnetically bioprinted wrench-shaped tissues (C) with a central fiber made of mCherry LifeAct C2C12 myoblasts and clamps made of GFP LifeAct NiH3T3 fibroblasts, (D) with the possibility to add NSC-34 motor neuron-like cells (previously labeled with far red DiD dye) throughout the tissue. All cells were NP3-labeled. (Scale bar = 1 mm, myoblasts in red, fibroblasts in green, motor neuron-like cells in blue)*

Advanced magnetic trapping and actuation techniques will also necessitate precisely tailored magnetic field configurations. We have already seen in **Chapter 5** that trapping a four branched magnetic tissue requires to carefully choose the different magnets polarizations to optimize the magnetic field lines. Adding new magnetic anchors or functionalities would therefore require the adequate magnetic field. Previous studies have used complex 3D magnet shapes to assemble spheroids via 3D levitation, but they still struggled to fully control the final geometry[53,334]. Combining these magnets with optimal magnetic needles or anchors could improve such control. Halbach arrays involving series of multiple magnets strategically

positioned and oriented could be particularly useful to engineer specific magnetic fields and gradients[459], precisely controlling the magnetic field lines and therefore the placement of the tissues. These configurations could be particularly advantageous for the magnetic alignment strategies outlined in **Chapter 3**. Since cells or spheroids align along magnetic fields, if those are bent or modified in any way, so should cellular chains be.

Beyond improving upon their magnetic aspect, the techniques presented in this manuscript could also be elevated by combining them with other tissue engineering approaches. Tissues of different shapes could be assembled together or with an electrospun scaffold. They could be magnetically bioprinted to fit into specific microfluidic compartments to apply specific shear stresses on them. Additionally, magnetically printed cellular constructs could be incorporated into bioprinted tissues during gel extrusion processes. The shape of the cell-only magnetic tissues can easily be controlled through magnetic bioprinting, while the surrounding scaffold could be extruded with a specific design.

Although this manuscript primarily emphasizes magnetic-based strategies, it is important to stress that this magnetic toolbox is intended to complement, rather than compete with existing platforms, collectively advancing the field of tissue engineering.

3. Future applications

While our primary focus was skeletal muscle tissue, all the magnetic technologies we have developed, and their potential applications could apply to virtually any type of tissue. Magnetic alignment could be applied to kidney cells or gut organoids, to replicate tubular nephrons or intestinal tissues respectively. Vascular or nervous networks could be bioprinted in any desired shape. Wrench shaped tissues could be engineered with cardiomyocytes, magnetically trapped and then cyclically stimulated. A bi-directional stretching system could even apply multidirectional stresses on cross-shaped cardiac tissues to further reproduce the cardiac micro-environment. Overall, the magnetic tissue engineering toolbox introduced in this manuscript is versatile and holds potential for engineering and studying a wide range of complex or anisotropic tissue.

Specifically for skeletal muscle, producing mature and functional tissue provided deeper insight on myogenesis. Beyond their potential for biomechanical investigations, these skeletal muscle constructs could be used as patient-specific avatars[3,4]. This could notably enable testing the impact of various drugs to evaluate their toxicity or their beneficial effects following injury [269–271]. Engineering tissues with myoblasts derived from human iPSC could also facilitate drug screening at a personalized level. Rather than testing drugs directly on patients, they could be screened on skeletal muscle constructs magnetically engineered with the patients' cells. Such personalized medicine could also be applied to pathological cases. Myoblasts could be derived from iPSC induced from patients suffering from myopathies, and we could then study how myogenesis would occur in our platform with their cells[262]. This could potentially enable

treating these myopathies *in vitro* and then replicating what has been performed on magnetically printed constructs to their associated patients.

Beyond drug screening, the potential of magnetic skeletal muscle constructs extends to potential grafts. Their magnetic properties could be leveraged to enhance precision and reduce invasiveness during operations. Indeed, cellular patches could be magnetically bioprinted in any desired geometry, to match the site where they are needed. Moreover, their potential for magnetic trapping and actuation could facilitate their placements. Instead of needles, magnetic stents could be used to guide and then anchor the tissues. As we have seen with wrench- and cross-shaped tissues, clamps can be integrated to enable magnetic actuation. Magnetic stents have previously been used to guide magnetic vectors[590] and even cells *in vivo*[591], further reinforcing the possibility of guiding magnetic grafts during implantation. Post-implantation, the magnetic properties could enable ongoing guidance, stimulation[313,318], and monitoring via MRI[65].

In addition to meeting our initial goal of revealing the promise of magnetic-based approaches, the next-generation tissue engineering toolbox presented in this manuscript has opened many avenues for exploration, underscoring its vast potential for future research.

Appendix A

Supplementary information of Chapter 4

Supplementary Figures and Tables of Appendix A

Supplementary Figure 4.1 179
Supplementary Figure 4.2 180
Supplementary Figure 4.3 181
Supplementary Figure 4.4 181
Supplementary Figure 4.5 182
Supplementary Figure 4.6 183
Supplementary Figure 4.7 184
Supplementary Figure 4.8 185
Supplementary Figure 4.9 186
Supplementary Figure 4.10 188
Supplementary Figure 4.11 188
Supplementary Figure 4.12 189
Supplementary Figure 4.13 190
Supplementary Figure 4.14 191
Supplementary Figure 4.15 192
Supplementary Figure 4.16 193
Supplementary Figure 4.17 194
Supplementary Figure 4.18 196
Supplementary Figure 4.19 196
Supplementary Figure 4.20 197
Supplementary Figure 4.21 197
Supplementary Figure 4.22 198
Supplementary Figure 4.23 200
Supplementary Figure 4.24 200
Supplementary Figure 4.25 202
Supplementary Figure 4.26 202
Supplementary Figure 4.27 203
Supplementary Figure 4.28 204
Supplementary Figure 4.30 205
Supplementary Figure 4.31 207
Supplementary Figure 4.33 207
Supplementary Figure 4.34 208

Supplementary Table 4.1 209
Supplementary Table 4.2 209

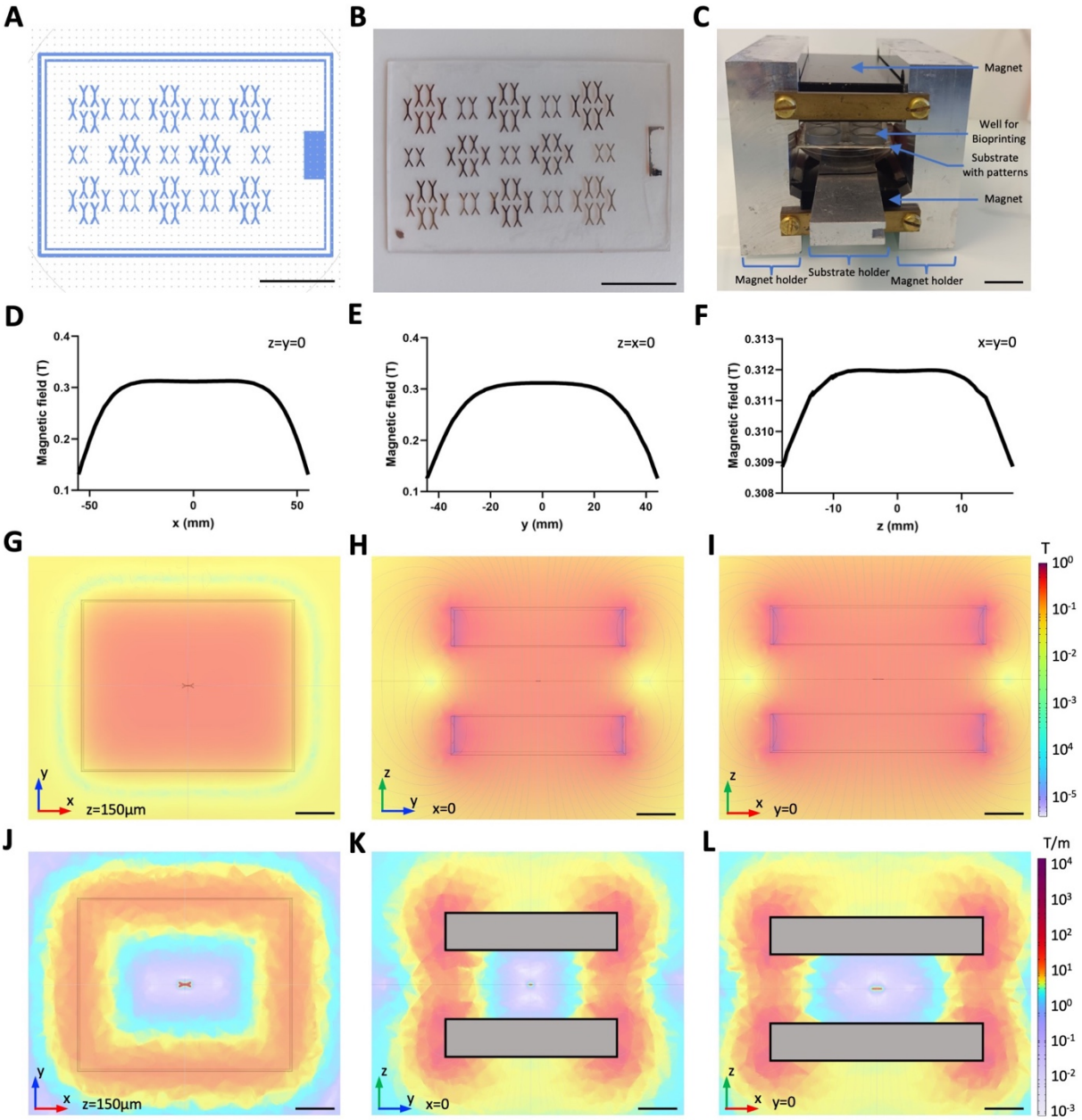

Supplementary Figure 4.1. *(A) Design of the photolithography mask on Clewin to generate (B) the substrate with the matching NiFe patterns after photolithography and NiFe electroplating. (C) Magnetic bioprinting set-up and the graphs of the simulated uniform magnetic field generated at the center the magnets without any patterns in it, plotted along the (D) x, (E) y, and (F) z axes. Heatmaps of (G, H, I) the magnetic field and (J,K,L) gradient with the field lines generated by the two strong magnets with a single NiFe pattern in the center, visualized in 3 different planes. (Scale bar = 2 cm)*

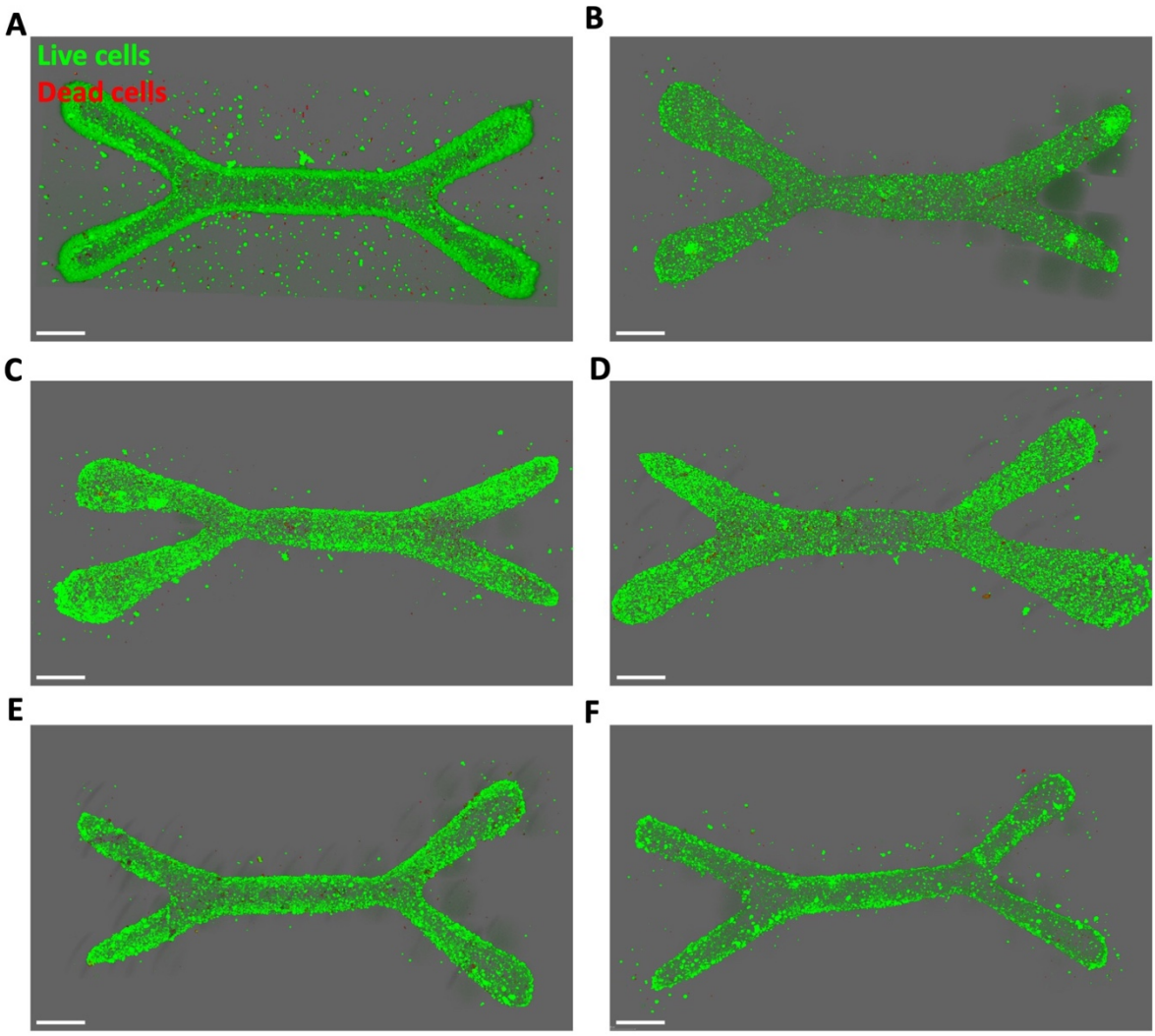

Supplementary Figure 4.2. **(**A-F) 3D reconstructions from confocal imaging of LIVE/DEAD assays performed on different tissues made from C2C12, just after they were magnetically bioprinted. (Live cells in green, dead cells in red, scale bar = 500 µm)

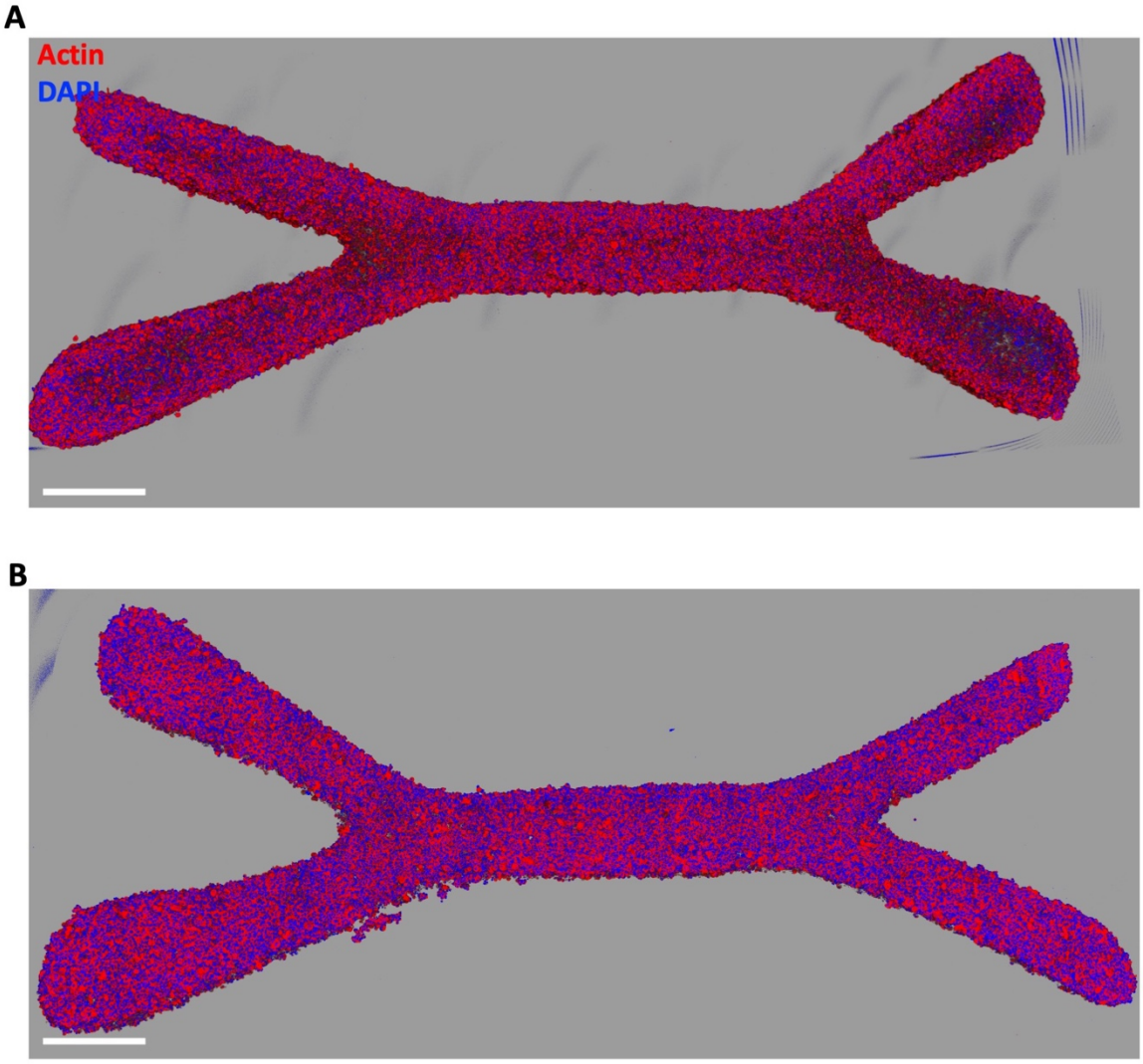

Supplementary Figure 4.3. *(A,B) 3D reconstructions from confocal imaging of different tissues made from C2C12 cells, just after they were magnetically bioprinted. (Actin in red, nuclei in blue, scale bar = 500 µm)*

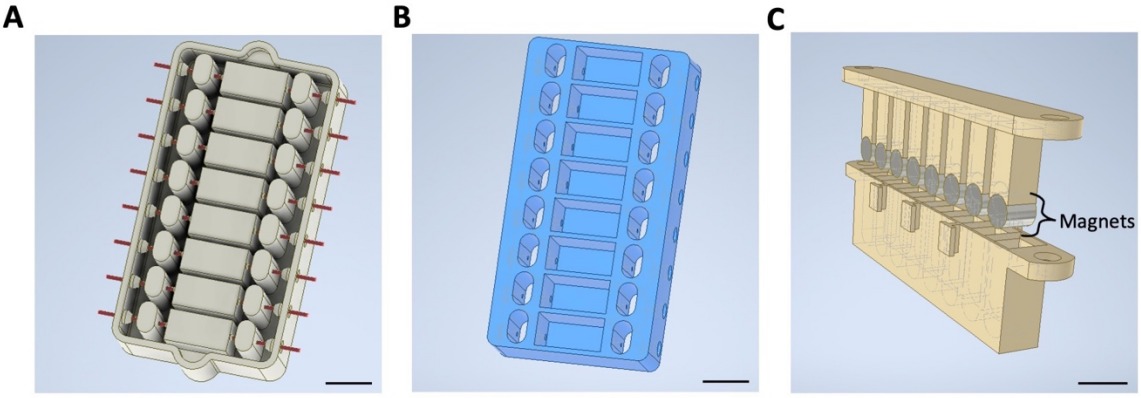

Supplementary Figure 4.4. *Designs of (A) the mould with needles inserted in it, (B) the resulting chip and (C) the opened-up system to hold the eight 6x6mm^2 cylindrical magnets together, made with Autodesk Inventor. (Scale bar = 1 cm)*

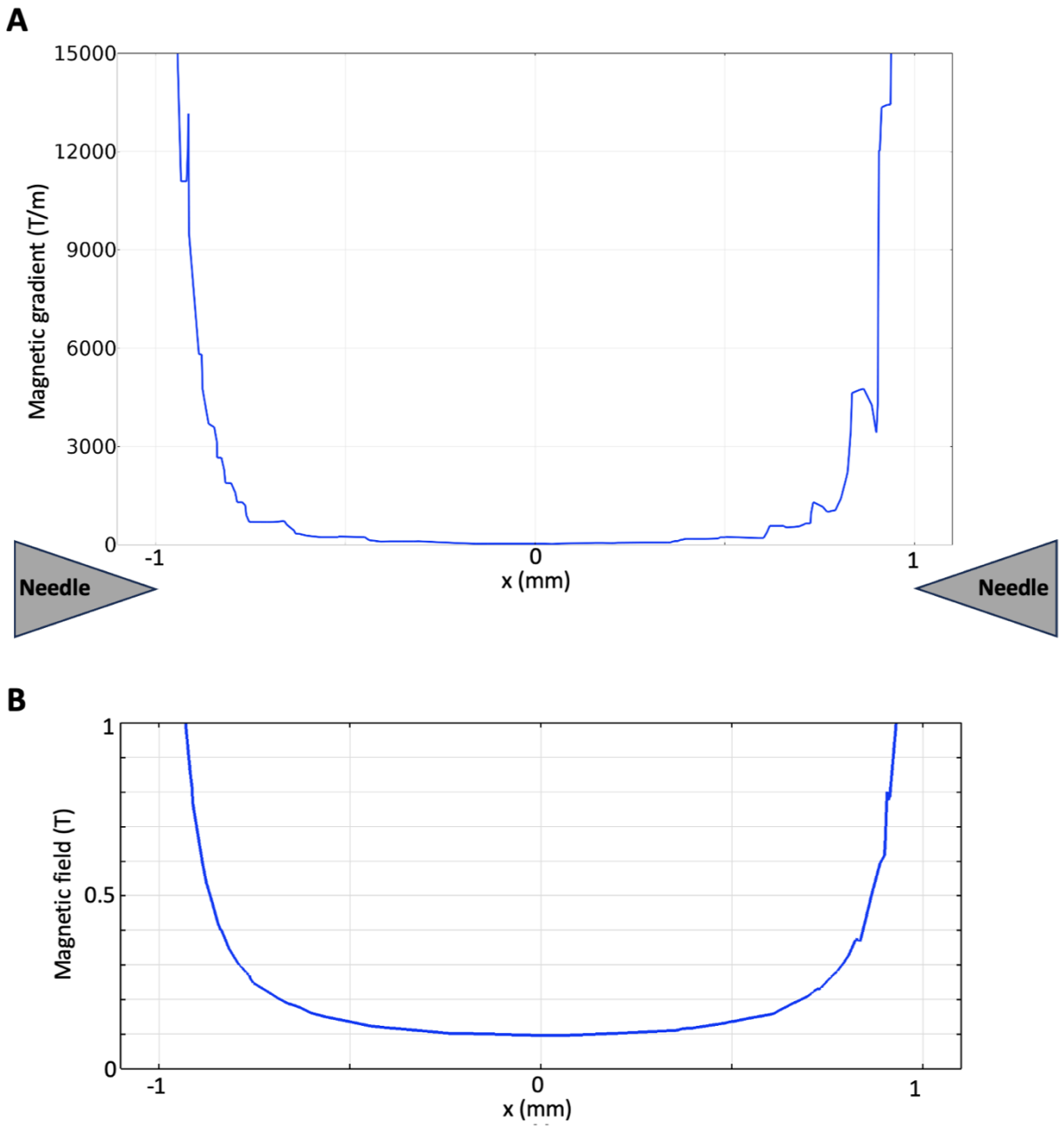

Supplementary Figure 4.5. (A-B) *Plots of (A) the magnetic gradient and (B) field between two needles in the chip along their axis, generated from Comsol simulations.*

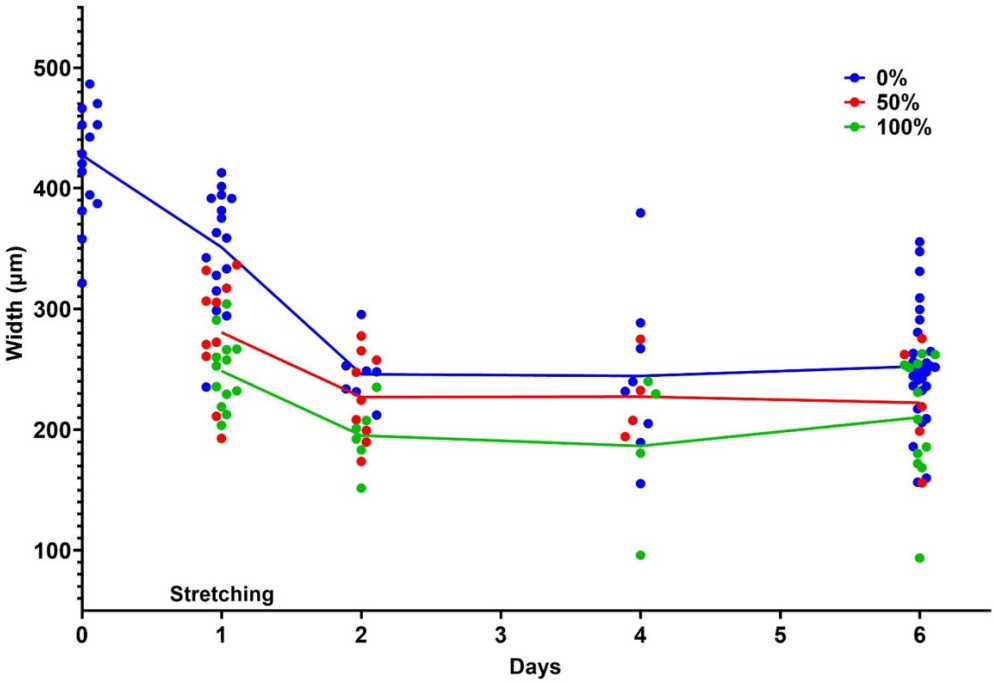

Supplementary Figure 4.6. *Evolution of the widths of tissues made of C2C12 cells from day 0, after they were bioprinted, to day 6, whether they were stretched by 0%, 50% or 100% on day 1.*

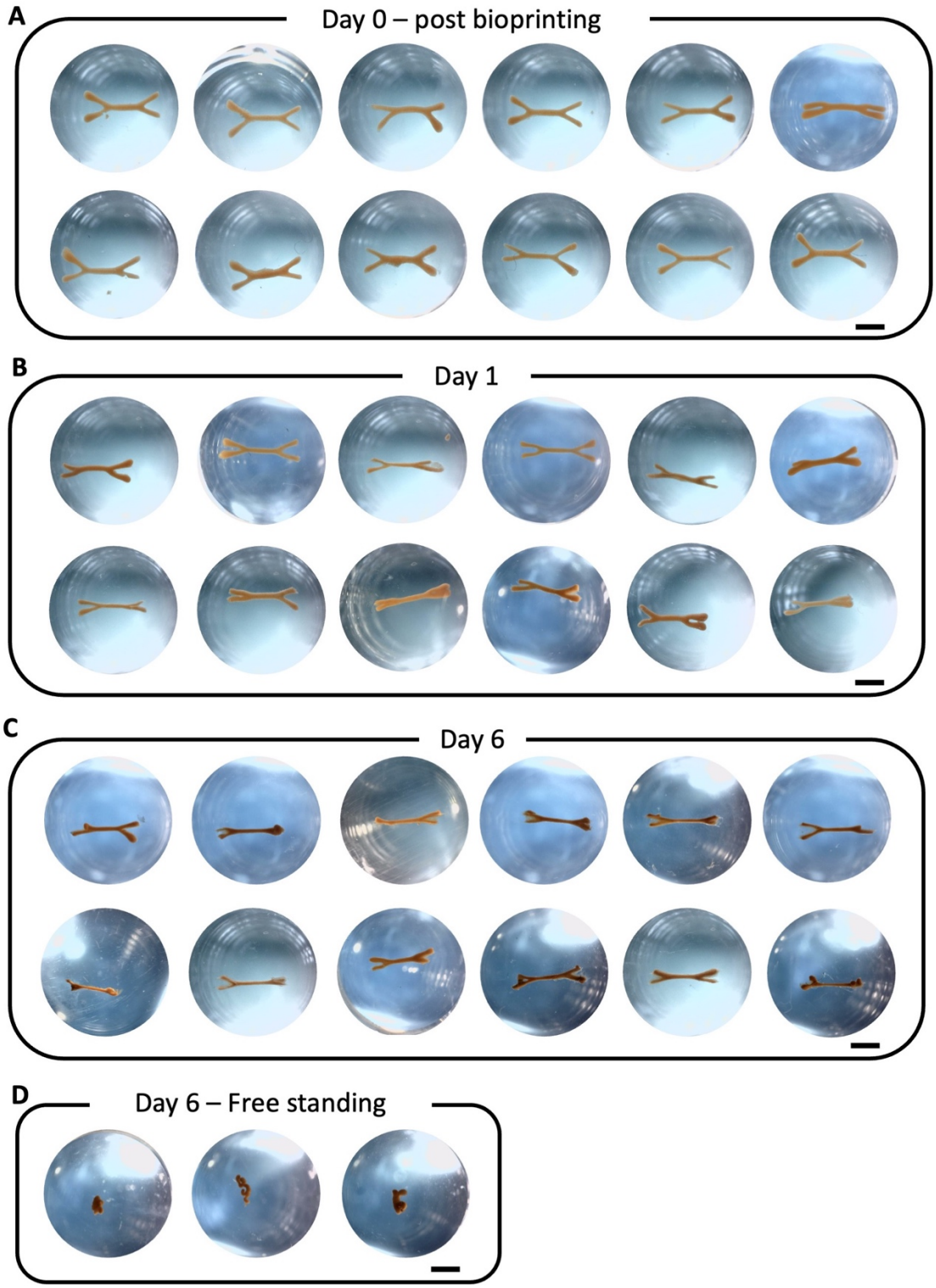

Supplementary Figure 4.7. *Different tissues made of C2C12 cells that were fixed and imaged in PBS in the wells of the 48-well plate in which they were preserved. 3D issues that were fixed (A) on day 0 just after being bioprinted, and tissues cultured trapped on the needles fixed (B) on day 1 and (C) on day 6 . (D) Tissues that were cultured free standing in a non-adherent well collected on day 6. Tissues that were trapped between needles were fixed still trapped in the chip, then removed from the needles by scrapping the clamps with tweezers and placed in PBS filled wells. They were imaged from the top using a magnifier and a dino camera. (Scale bar = 2 mm)*

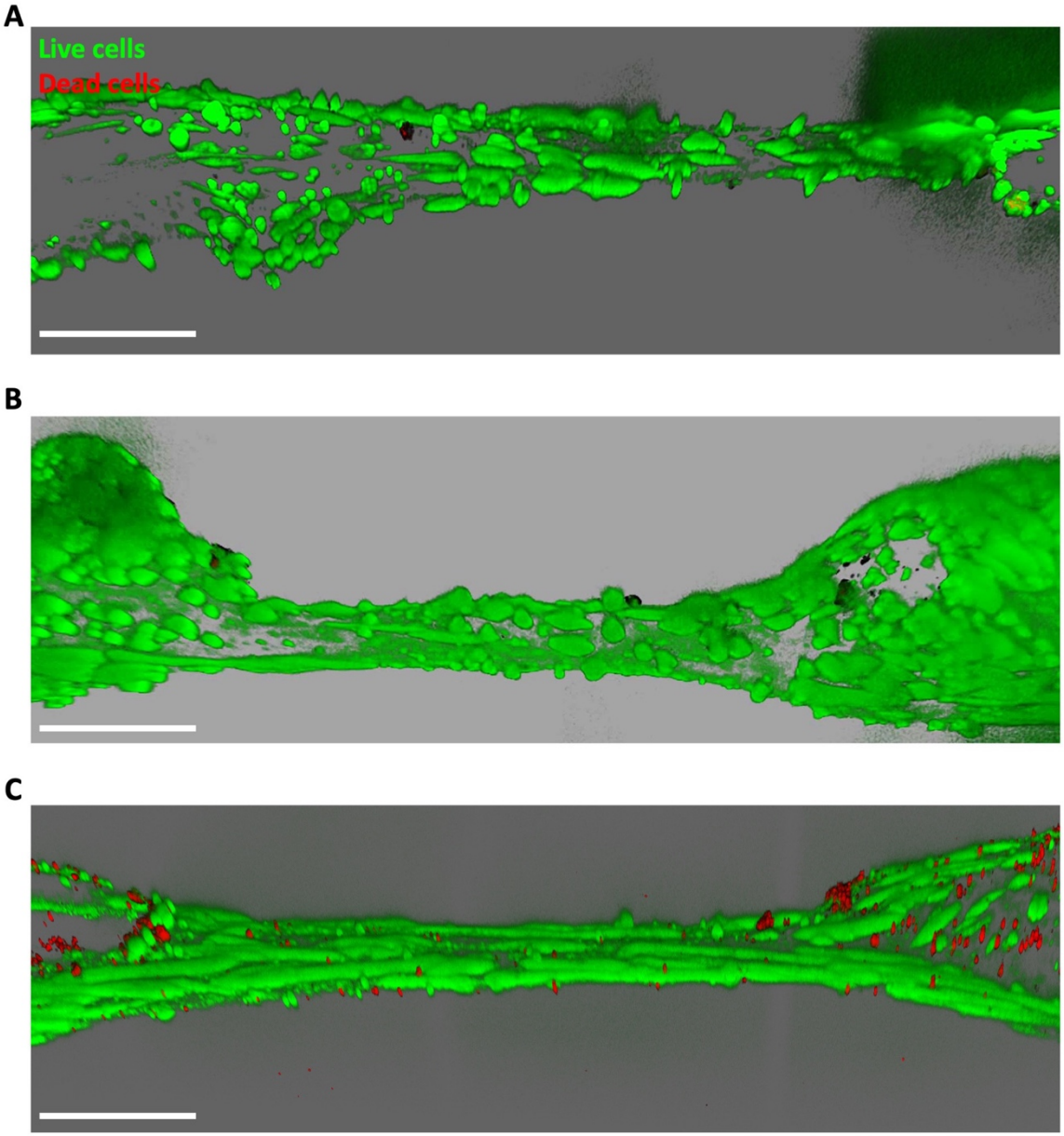

Supplementary Figure 4.8. *(A-C) 3D reconstructions from confocal imaging of LIVE/DEAD assays performed on different non-stretched 6-day-old tissues made from C2C12 cells, imaged in the chip still trapped on the needles (Live cells in green, dead cells in red, scale bar = 500 µm)*

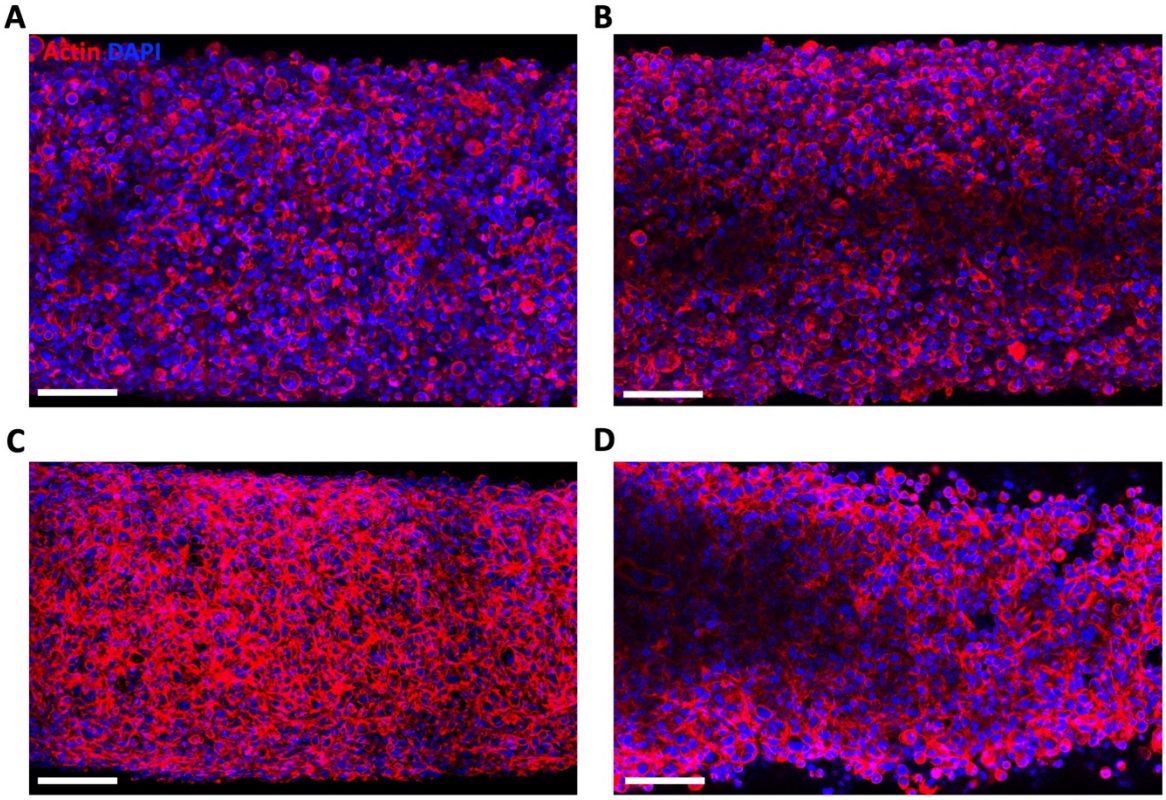

Supplementary Figure 4.9. *Confocal imaging of different tissues made of C2C12 cells on day 0, just after bioprinting (Actin in red, nuclei in blue, scale bar = 100 µm)*

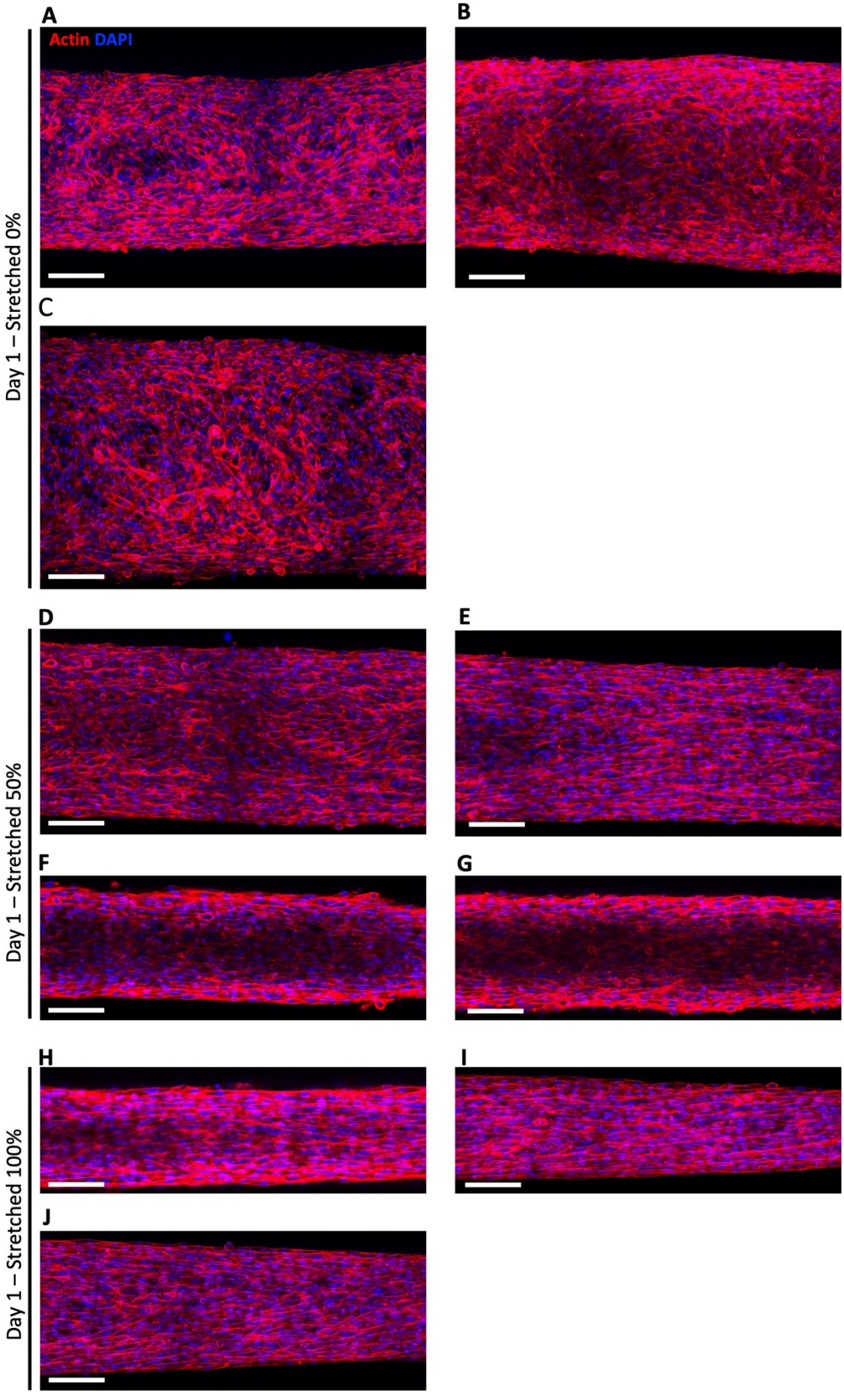
A
Actin DAPI
B
C
Day 1 – Stretched 0%
D
E
F
G
Day 1 – Stretched 50%
H
I
J
Day 1 – Stretched 100%

Supplementary Figure 4.10. *Confocal imaging of different tissues made of C2C12 cells on day 1, which were stretched by (A-C) 0%, (D-G) 50% and (H-J) 100% (Actin in red, nuclei in blue, scale bar = 100 µm)*

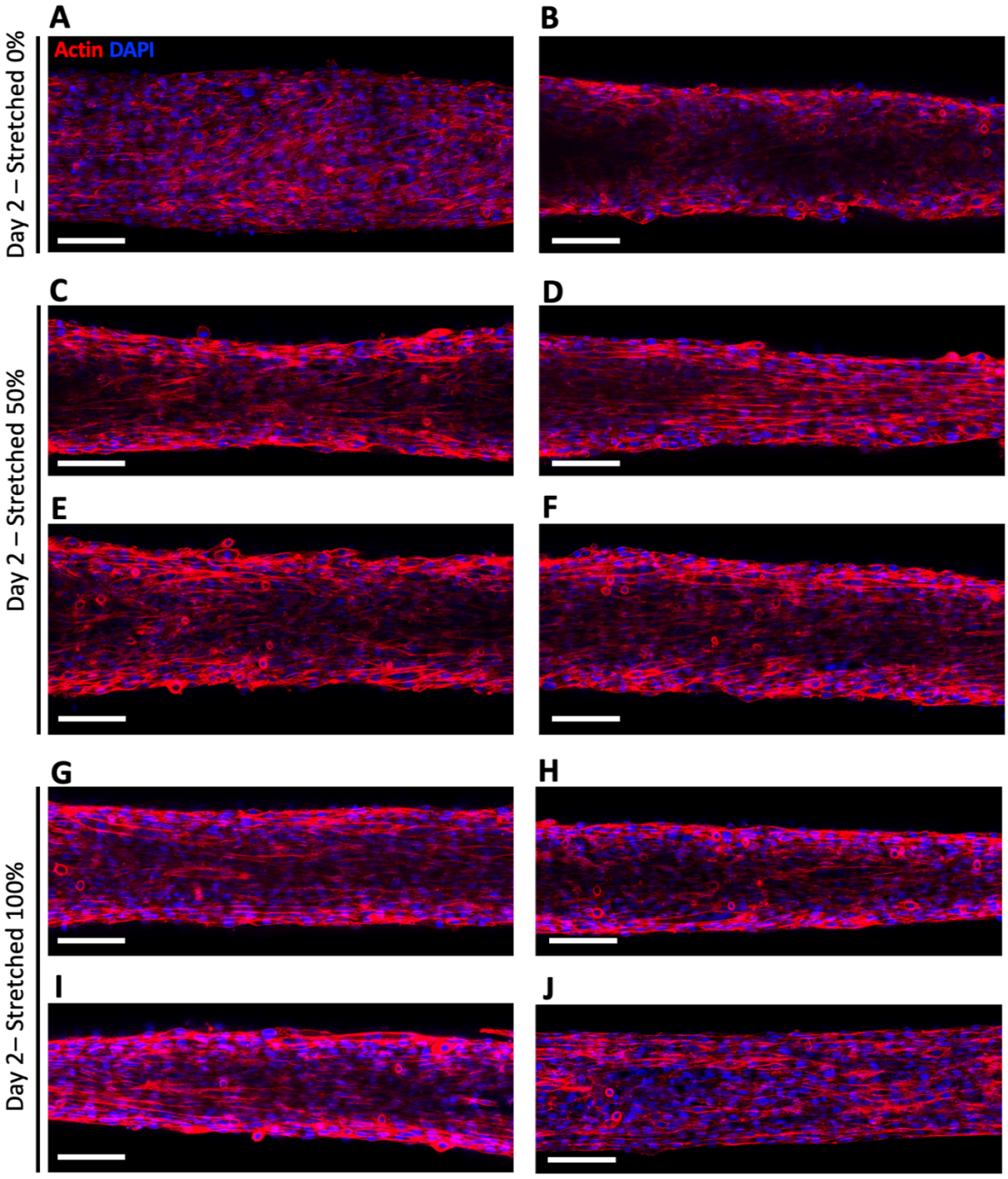

Supplementary Figure 4.11. *Confocal imaging of different tissues made of C2C12 cells on day 2, which were stretched since day 1 by (A-B) 0%, (C-F) 50% and (G-J) 100% (Actin in red, nuclei in blue, scale bar = 100 µm)*

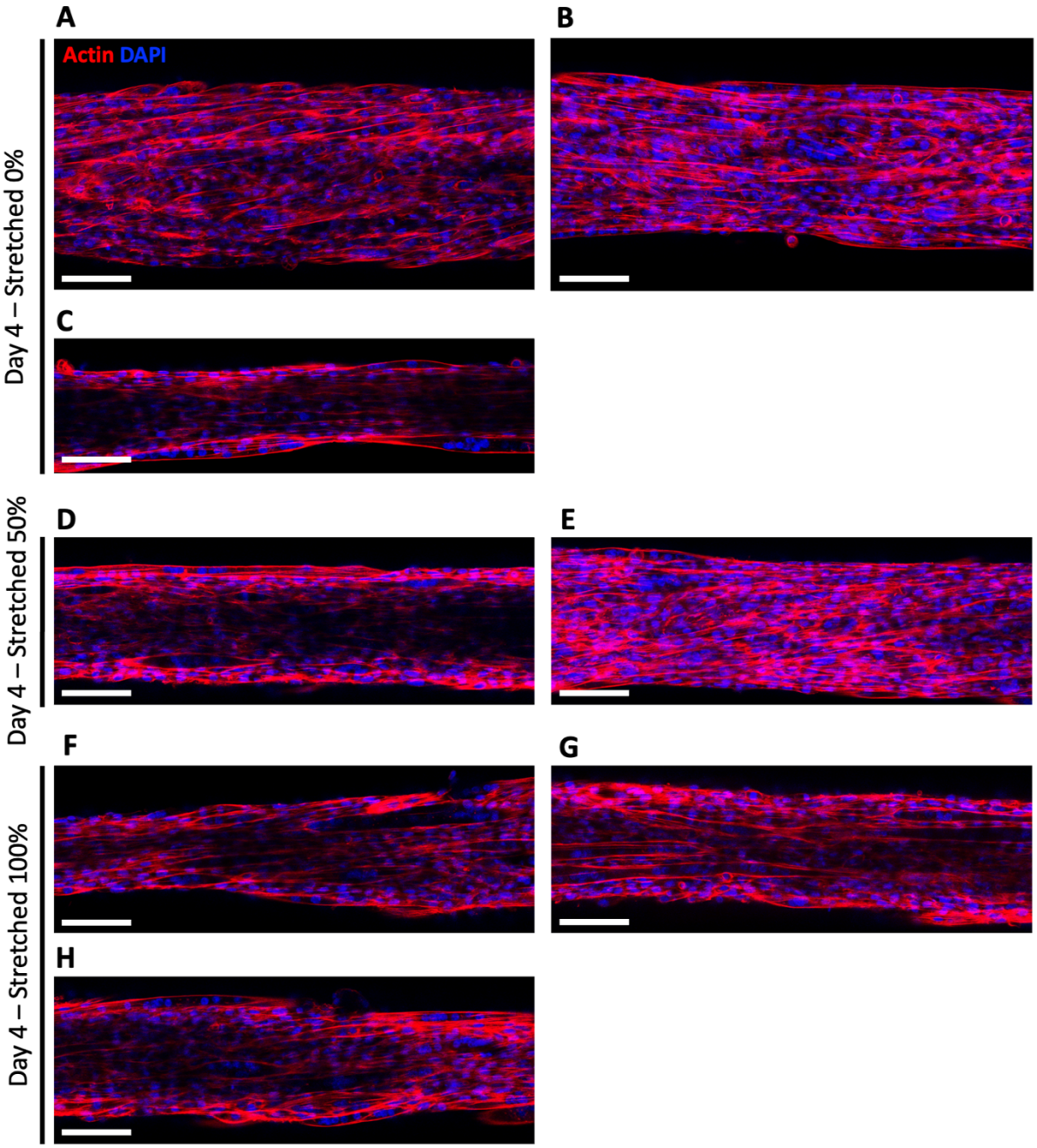

Supplementary Figure 4.12. *Confocal imaging of different tissues made of C2C12 cells on day 4, which were stretched since day 1 by (A-C) 0%, (D-E) 50% and (F-H) 100% (Actin in red, nuclei in blue, scale bar = 100 µm)*

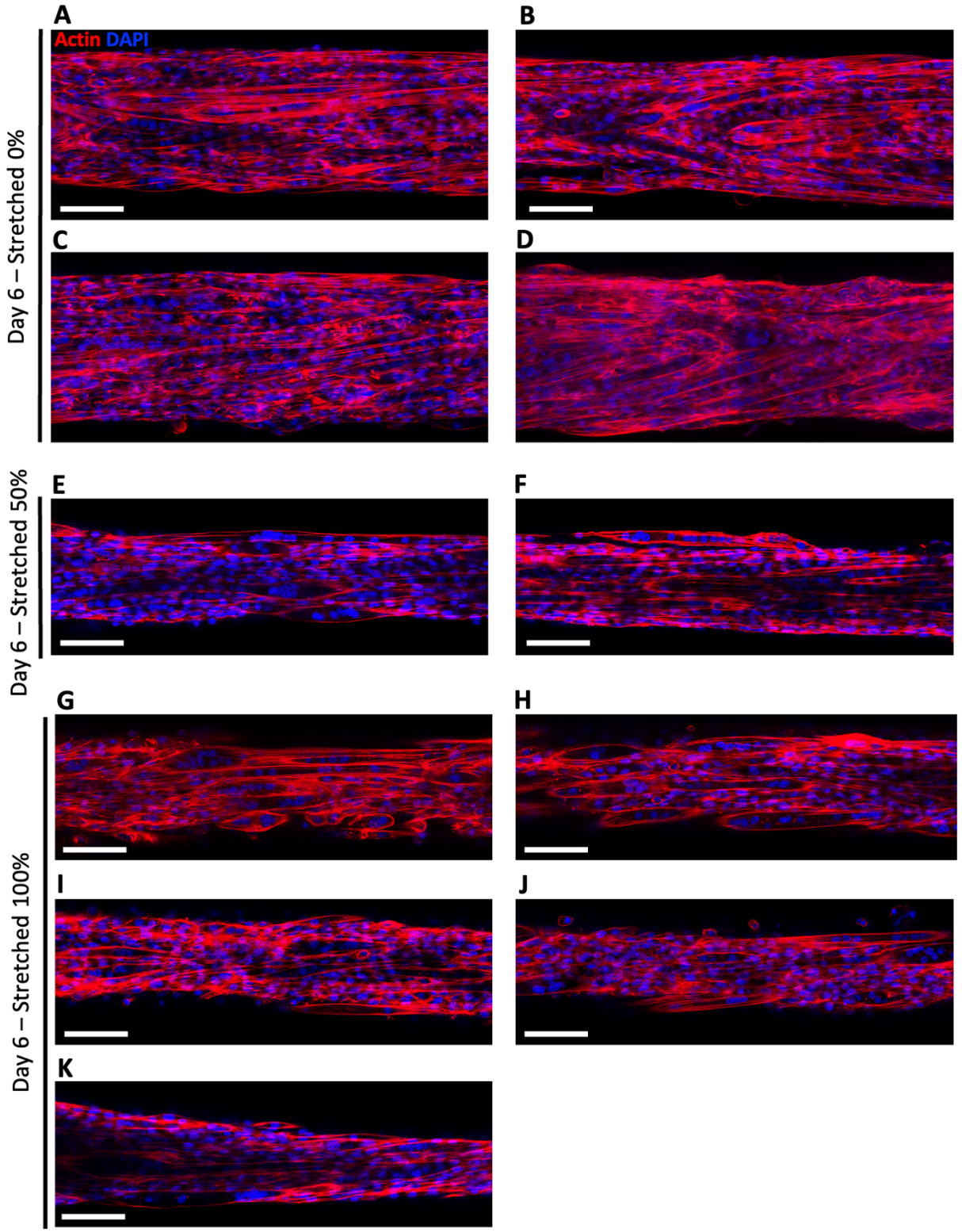

Supplementary Figure 4.13. *Confocal imaging of different tissues made of C2C12 cells on day 6, which were stretched since day 1 by (A-D) 0%, (E-F) 50% and (G-K) 100% (Actin in red, nuclei in blue, scale bar = 100 µm)*

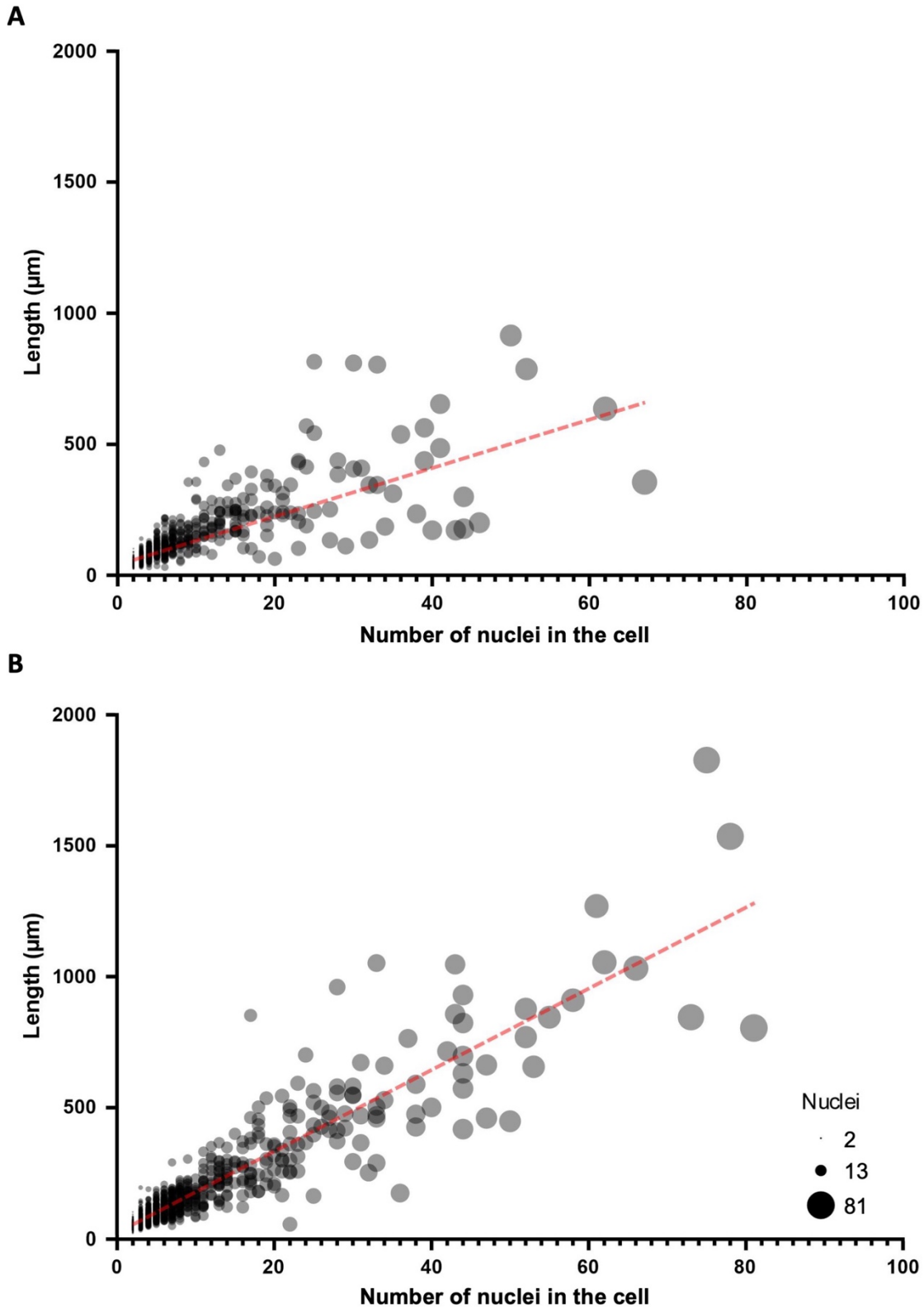

Supplementary Figure 4.14. *Scatter plots of the lengths of multinucleated cells as a function of the number of nuclei in the cells for 6-day-old tissues that were stretched by (A) 0% (n=3) and (B) 100% since day 1 (n=3). The diameter of each point is proportionate to the number of nuclei in the cell. A trendline in red was plotted from a linear regression.*

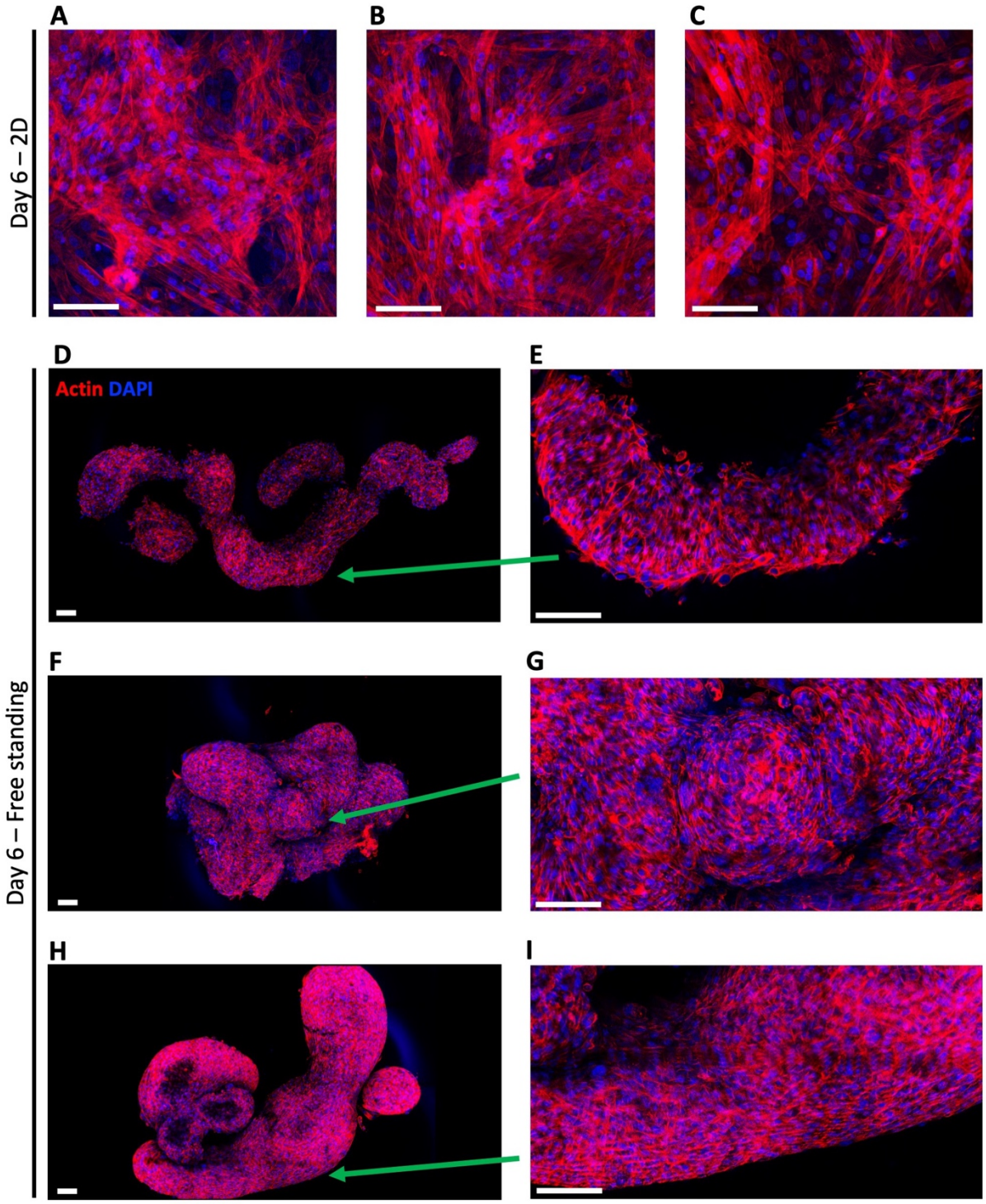

Supplementary Figure 4.15. *Confocal imaging on day 6 of (A-C) C2C12 cells cultured in 2D and of (D-I) different 3D tissues which were not trapped between needles and instead were left free standing in non-adherent wells (Actin in red, nuclei in blue, scale bar = 100 µm)*

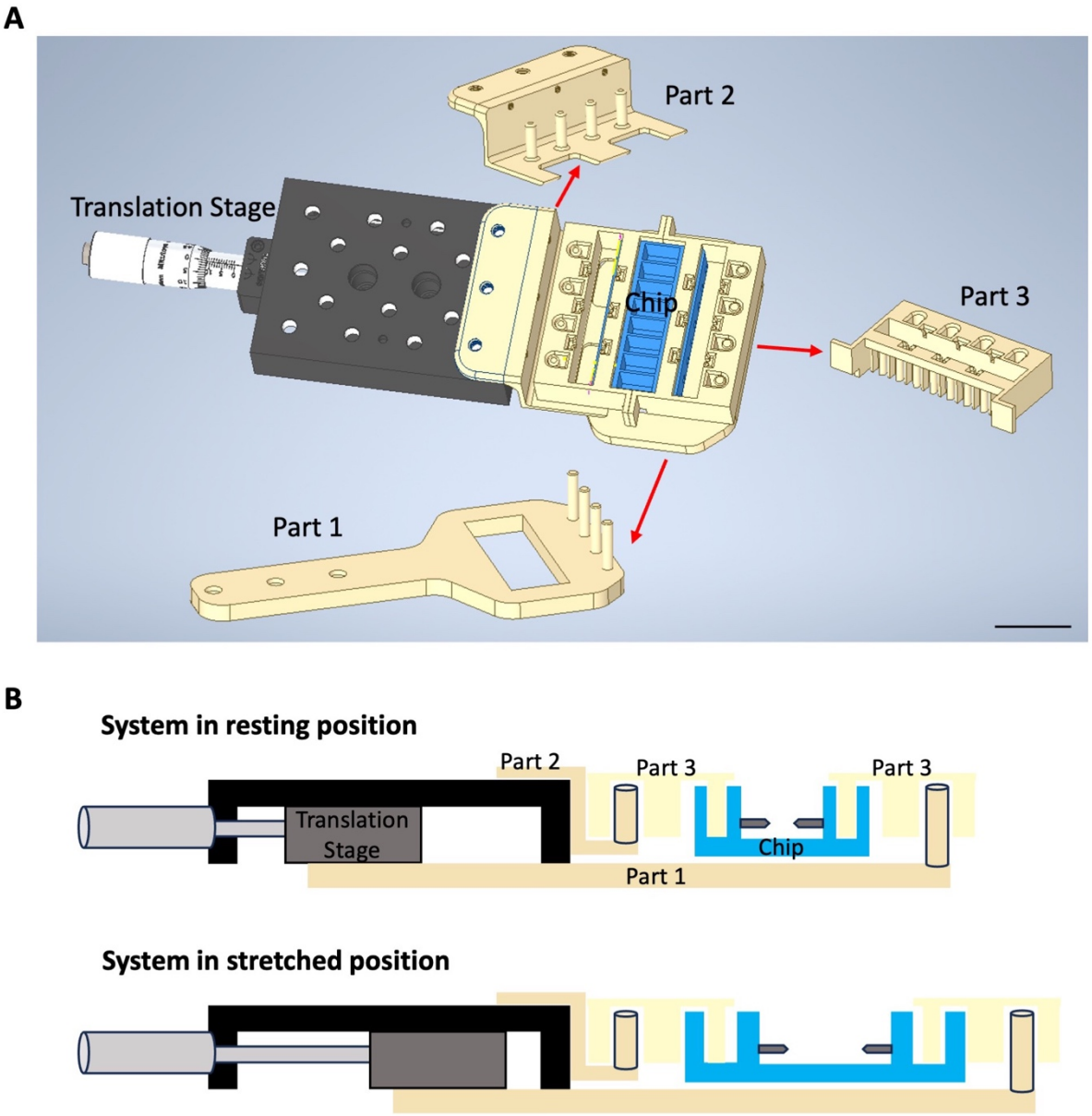

Supplementary Figure 4.16. *(A) Designs of the system stretching the chip and the individual 3D printed parts composing it, made with Autodesk Inventor (Scale bar = 3cm), and (B) simplified schematic showing how these different parts are organized from a longitudinal cut when the system is in its resting position or stretched position.*

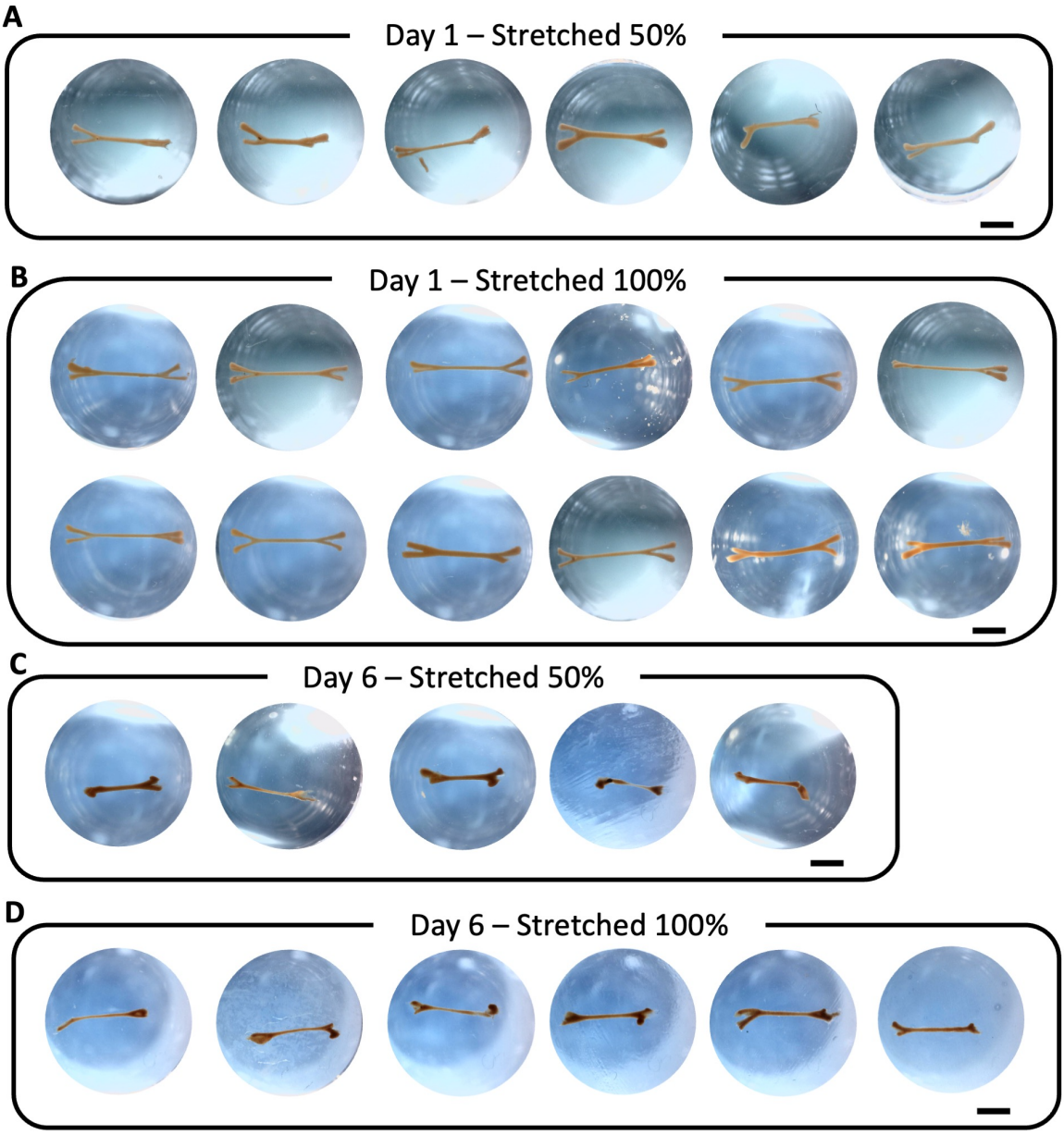

Supplementary Figure 4.17. *Different tissues made of C2C12 cells that were fixed and imaged in PBS in the wells of the 48-well plate in which they were preserved. Tissues collected on day 1 just after they were stretched by (A) 50% or (B) 100% and on day 6 which were stretched since day 1 by (C) 50% or (D) 100%. Tissues that were trapped between needles or stretched were fixed still trapped or stretched in the chip, then removed from the needles by scrapping the clamps with tweezers and placed in PBS filled wells. They were imaged from the top using a magnifier and a dino camera. (Scale bar = 2 mm)*

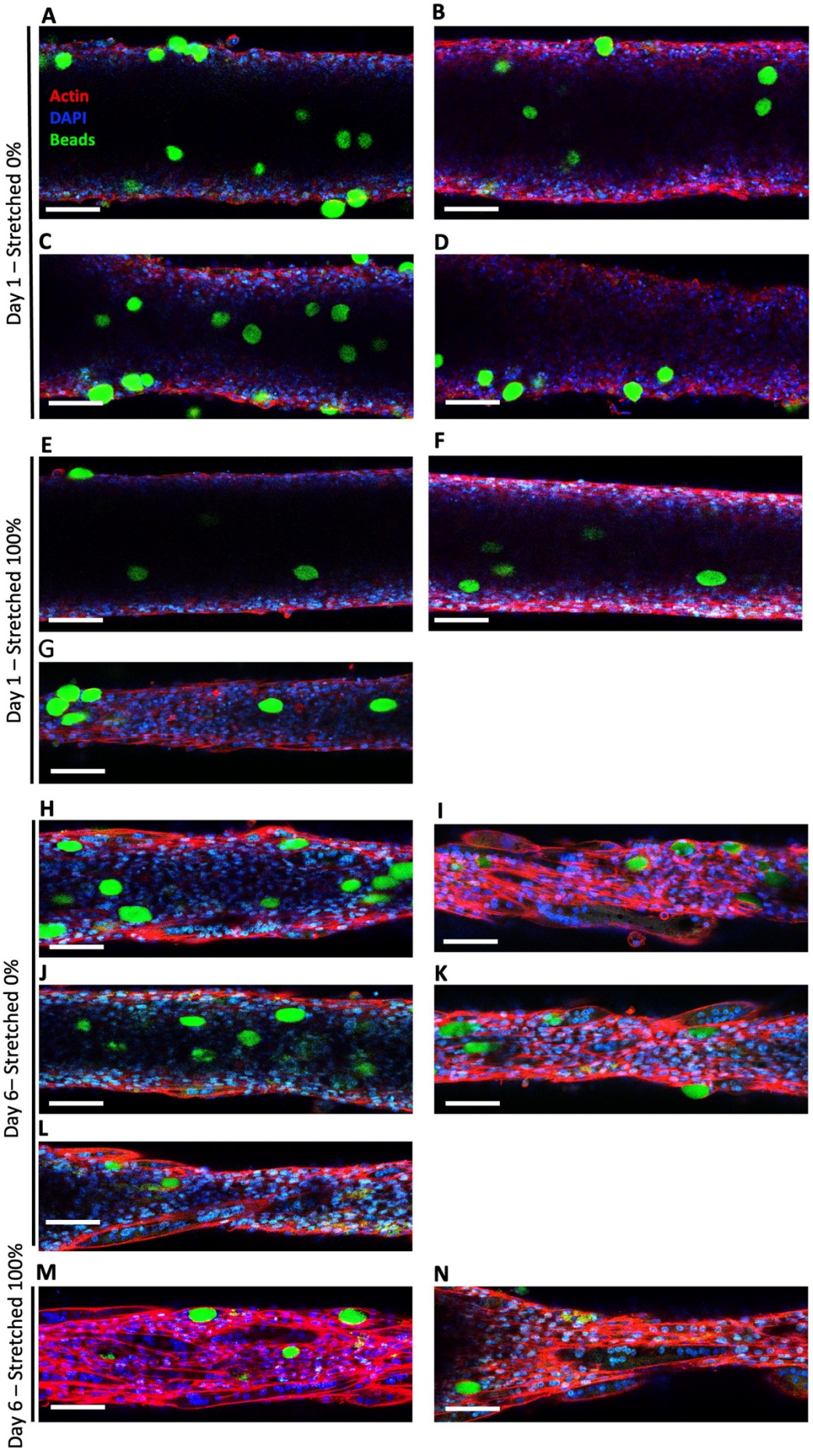
A
B
Actin
DAPI
Beads
C
D
Day 1 – Stretched 0%
E
F
G
Day 1 – Stretched 100%
H
I
J
K
L
Day 6– Stretched 0%
M
N
Day 6 – Stretched 100%

Supplementary Figure 4.18. *Confocal imaging of different tissues made of C2C12 cells, in which polyacrylamide beads were embedded, on day 1 after they were stretched by (A-D) 0% or (E-G) 100%, and on day 6 after being stretched since day 1 by (H-L) 0% or (M-N) 100%. (Actin in red, DAPI in blue, beads in green, scale bar=100 μm)*

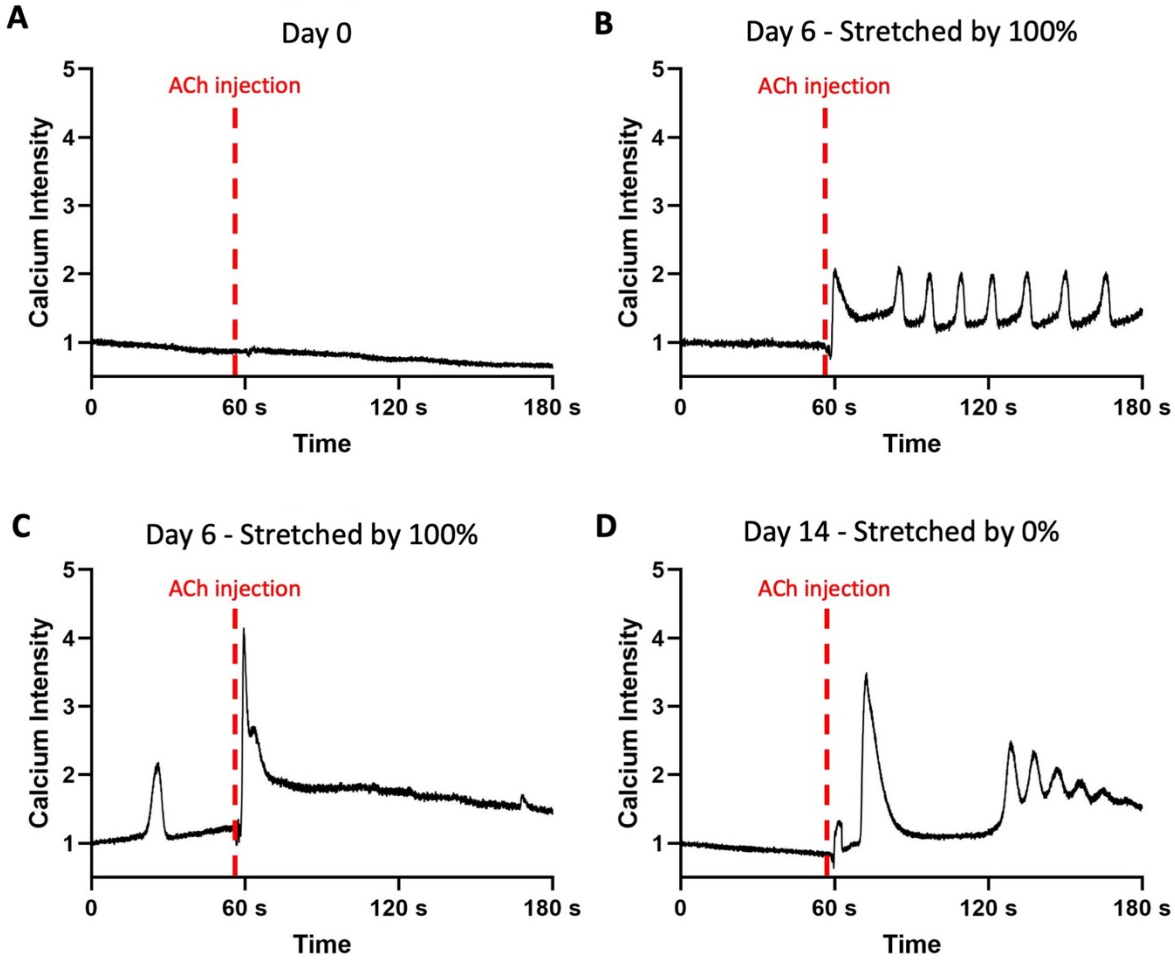

Supplementary Figure 4.19. *Kymographs of the fluctuations of the calcium signal in (A) a C2C12 cell from a tissue on day 0 just after bioprinting, (B-C) in two different C2C12 cells from tissues on day 6 stretched by 100% since day 1, and (D) a C2C12 cell from a non-stretched tissue on day 14, treated with 1 mM ACh after approximately 1min.*

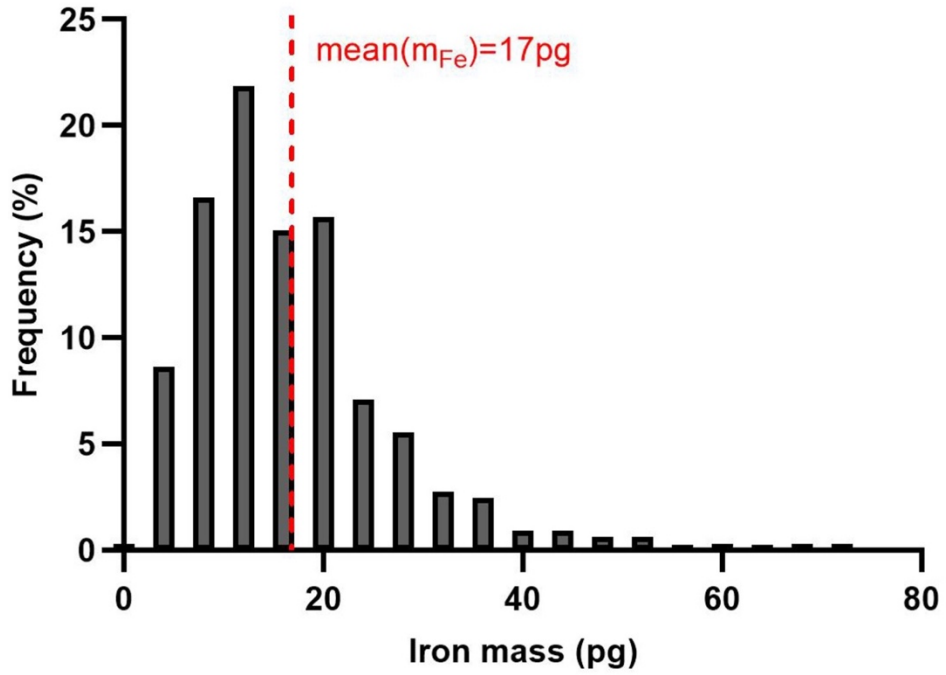

Supplementary Figure 4.20. *Histogram of the distribution of iron mass internalized per cell for M-ihPSC 1 collected just before patterning, after they were labeled with 2 mM of iron and 2 mM citrate in RPMI for 15mn once a day for the two previous days and with 0.2 mM of iron in their proliferation medium overnight between these two days*

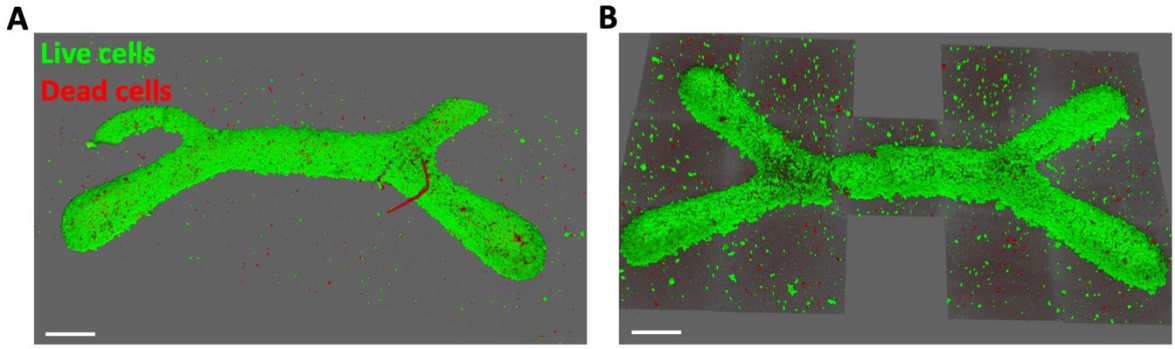

Supplementary Figure 4.21. *3D reconstructions from confocal imaging of LIVE/DEAD assays performed on different tissues made from M-hiPSC 1, just after they were magnetically bioprinted. (Live cells in green, dead cells in red, scale bar = 500 µm)*

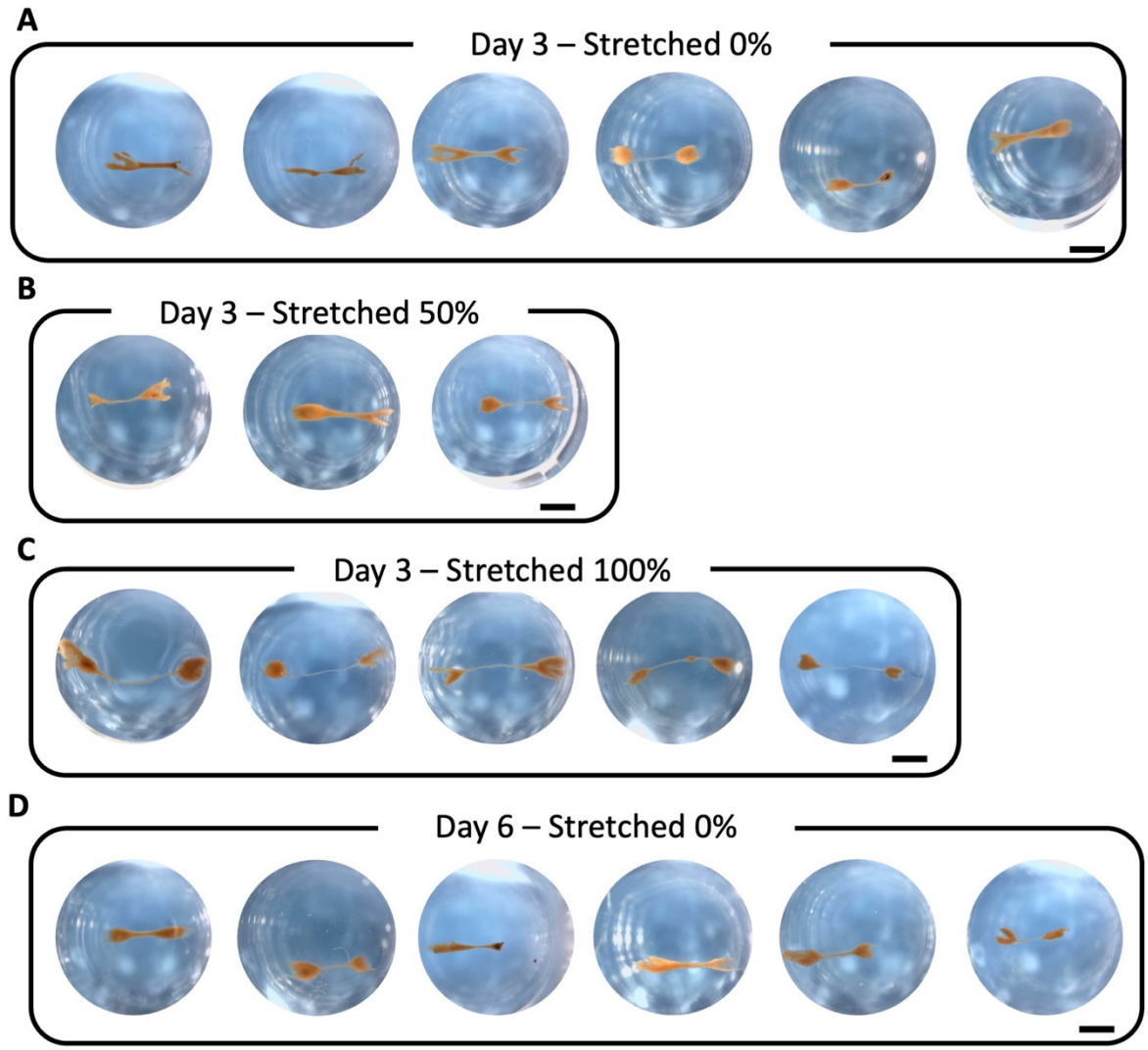

Supplementary Figure 4.22. *Different tissues made of M-hiPSC 1 that were fixed and imaged in PBS in the wells of the 48-well plate in which they were preserved. Tissues that were fixed on day 3 that were stretched since day 1 by (A) 0%, (B) 50% or (C) 100% and on (D) day 6 without stretching. Tissues that were trapped between needles or stretched were fixed still trapped or stretched in the chip, then removed from the needles by scrapping the clamps with tweezers and placed in PBS filled wells. They were imaged from the top using a magnifier and a dino camera. (Scale bar = 2 mm)*

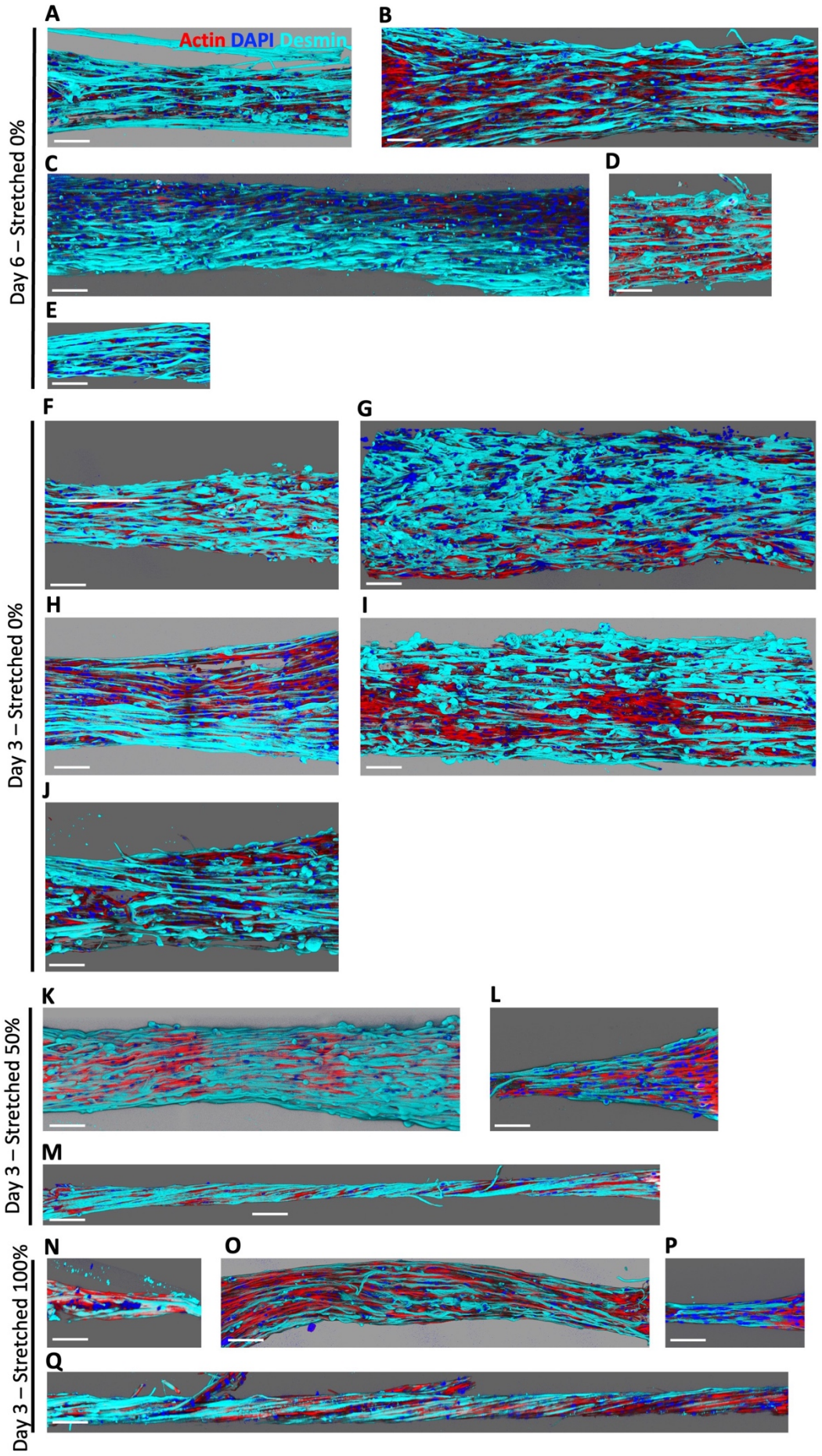
A
Actin DAPI Desmin
B
C
D
E
Day 6 – Stretched 0%
F
G
H
I
J
Day 3 – Stretched 0%
K
L
M
Day 3 – Stretched 50%
N
O
P
Q
Day 3 – Stretched 100%

Supplementary Figure 4.23. *3D reconstructions from confocal imaging of different tissues, immunostained for desmin, made from M-hiPSC 1 cultured for (A-E) 6 days with 0% stretching and 3 days with (F-J) 0%, (K-M) 50% and (N-Q) 100% stretching (actin in red, nuclei in blue, desmin in cyan, scale bar = 100 µm)*

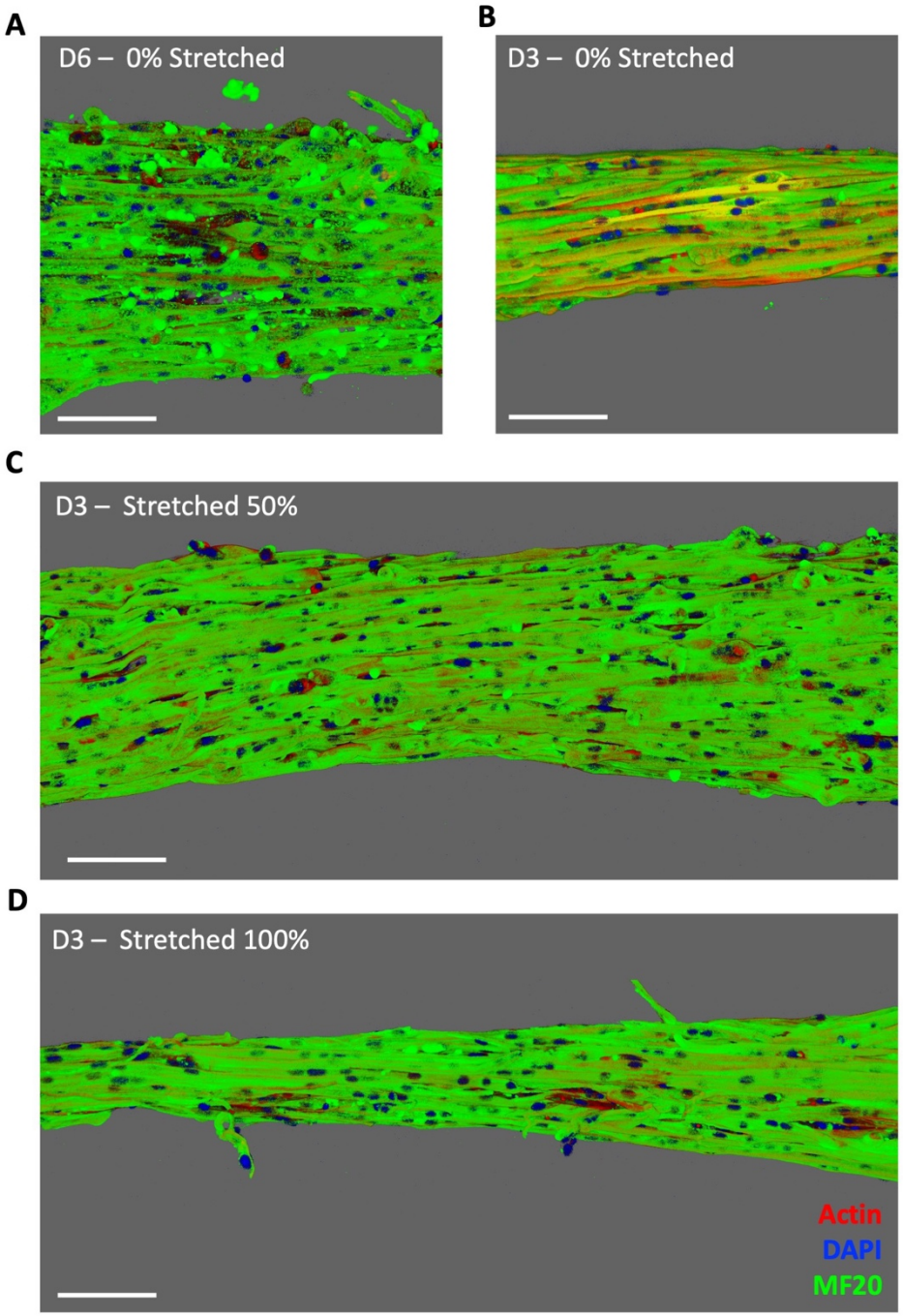

Supplementary Figure 4.24. *3D reconstructions from confocal imaging of different tissues, immunostained for MF20, made from M-hiPSC 1 cultured for (A) 6 days with 0% stretching, and 3 days with (B) 0%, (C) 50% and (D) 100% stretching. They were immunostained with MF20 antibody to see myosin heavy chains. (actin in red, nuclei in blue, MF20 in green, scale bar in 100 µm)*

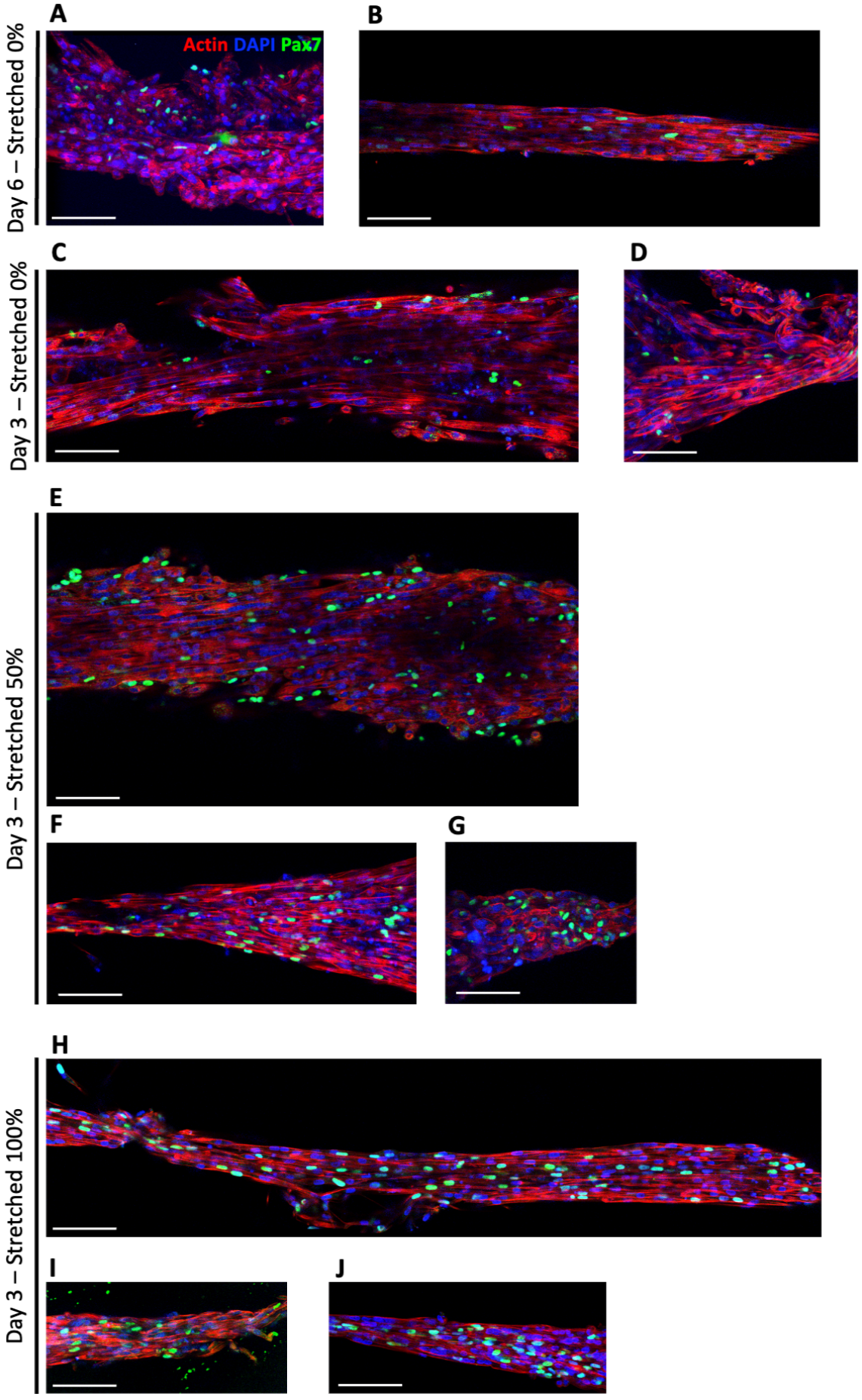
A
Actin DAPI Pax7
B
Day 6 – Stretched 0%
C
D
Day 3 – Stretched 0%
E
F
G
Day 3 – Stretched 50%
H
I
J
Day 3 – Stretched 100%

Supplementary Figure 4.25. *Confocal imaging of different tissues, immunostained for Pax 7, made from M-hiPSC 1 cultured for (A-B) 6 days with 0% stretching and 3 days with (C-D) 0%, (E-G) 50% and (H-J) 100% stretching. (actin in red, nuclei in blue, Pax7 in green, scale bar=100 µm)*

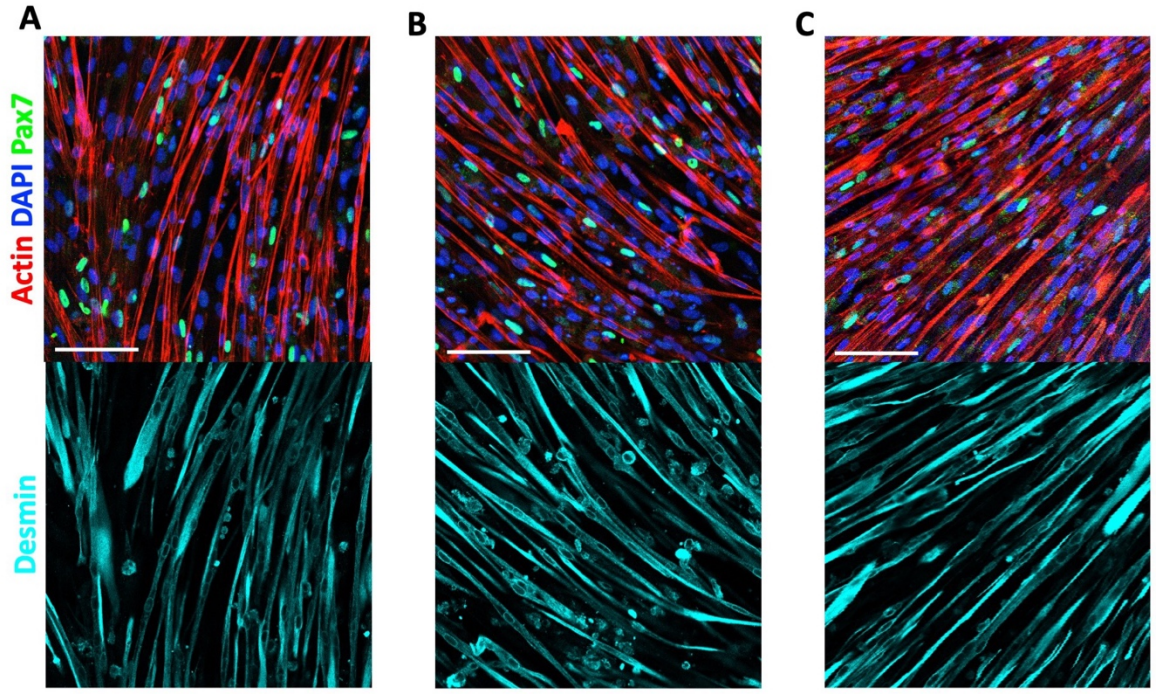

Supplementary Figure 4.26. *(A-C) Confocal imaging of three different samples of M-hiPSC 1 cultured for 6 days of differentiation in 2D, immunostained for Pax 7 and desmin (Actin in red, nuclei in blue, Pax7 in green, desmin in cyan, scale bar = 100 µm)*

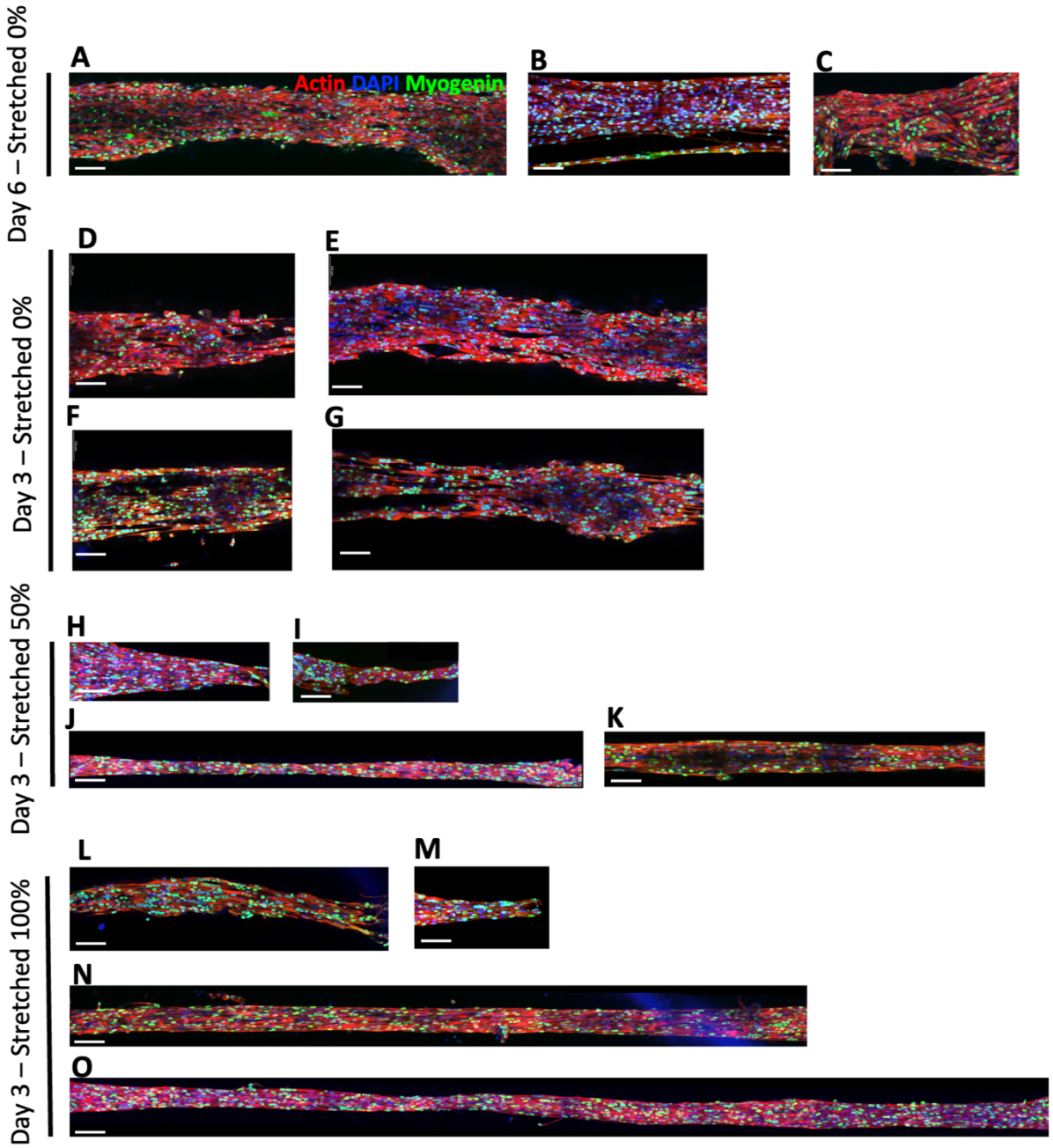

Supplementary Figure 4.27. *Confocal imaging of different tissues, immunostained for myogenin, made from M-hiPSC 1 cultured for (A-C) 6 days with 0% stretching and 3 days with (D-G) 0%, (H-K) 50% and (L-O) 100% stretching. (actin in red, nuclei in blue, myogenin in green, scale bar = 100 µm)*

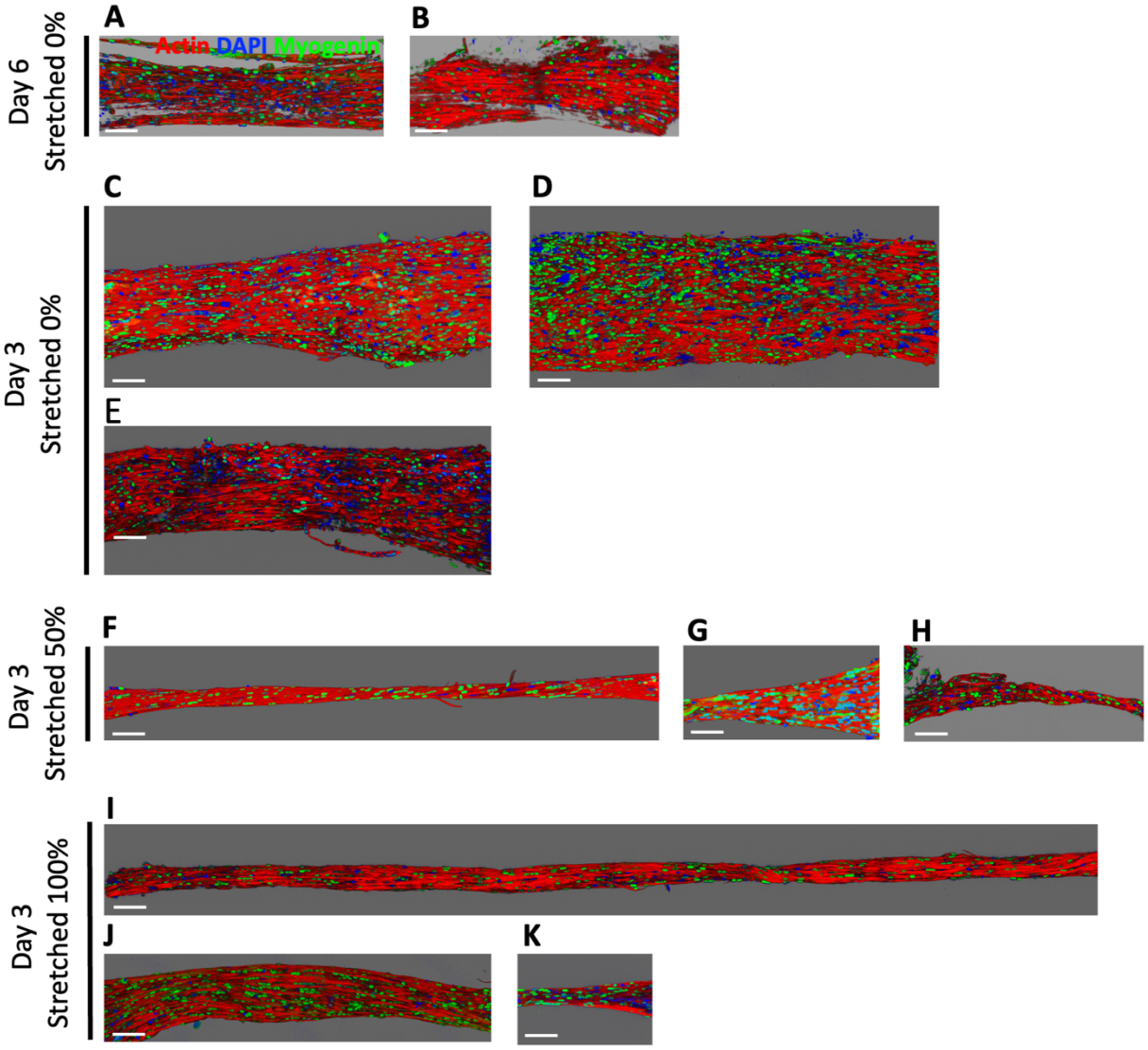

Supplementary Figure 4.28. *3D reconstructions from confocal imaging of different tissues, immunostained for myogenin, made from M-hiPSC 1 cultured for (A-B) 6 days with 0% stretching and 3 days with (C-E) 0%, (F-H) 50% and (I-K) 100% stretching. (actin in red, nuclei in blue, myogenin in green, scale bar=100 μm)*

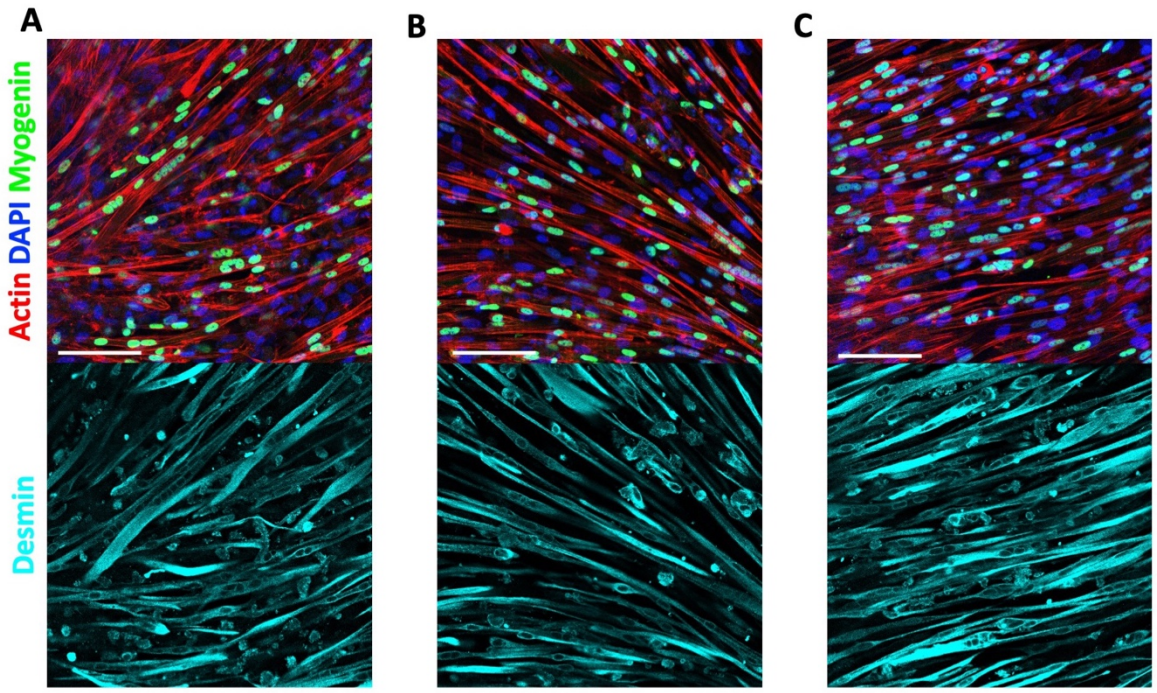

Supplementary Figure 4.29. *Confocal imaging of three different samples of M-hiPSC 1 cultured for 6 days of differentiation in 2D, immunostained for myogenin and desmin (Actin in red, nuclei in blue, myogenin in green, desmin in cyan, scale bar = 100 µm)*

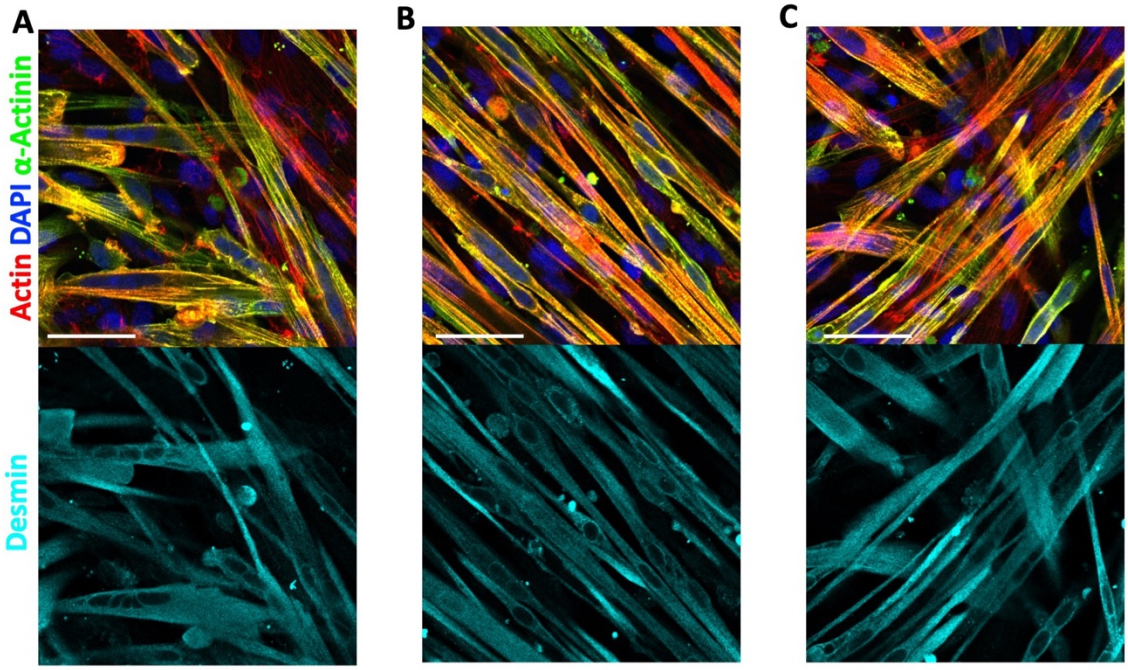

Supplementary Figure 4.30. *Confocal imaging of three different samples of M-hiPSC 1 cultured for 6 days of differentiation in 2D, immunostained for alpha-actinin and desmin (actin in red, nuclei in blue, alpha-actinin in green, desmin in cyan, scale bar = 50 µm)*

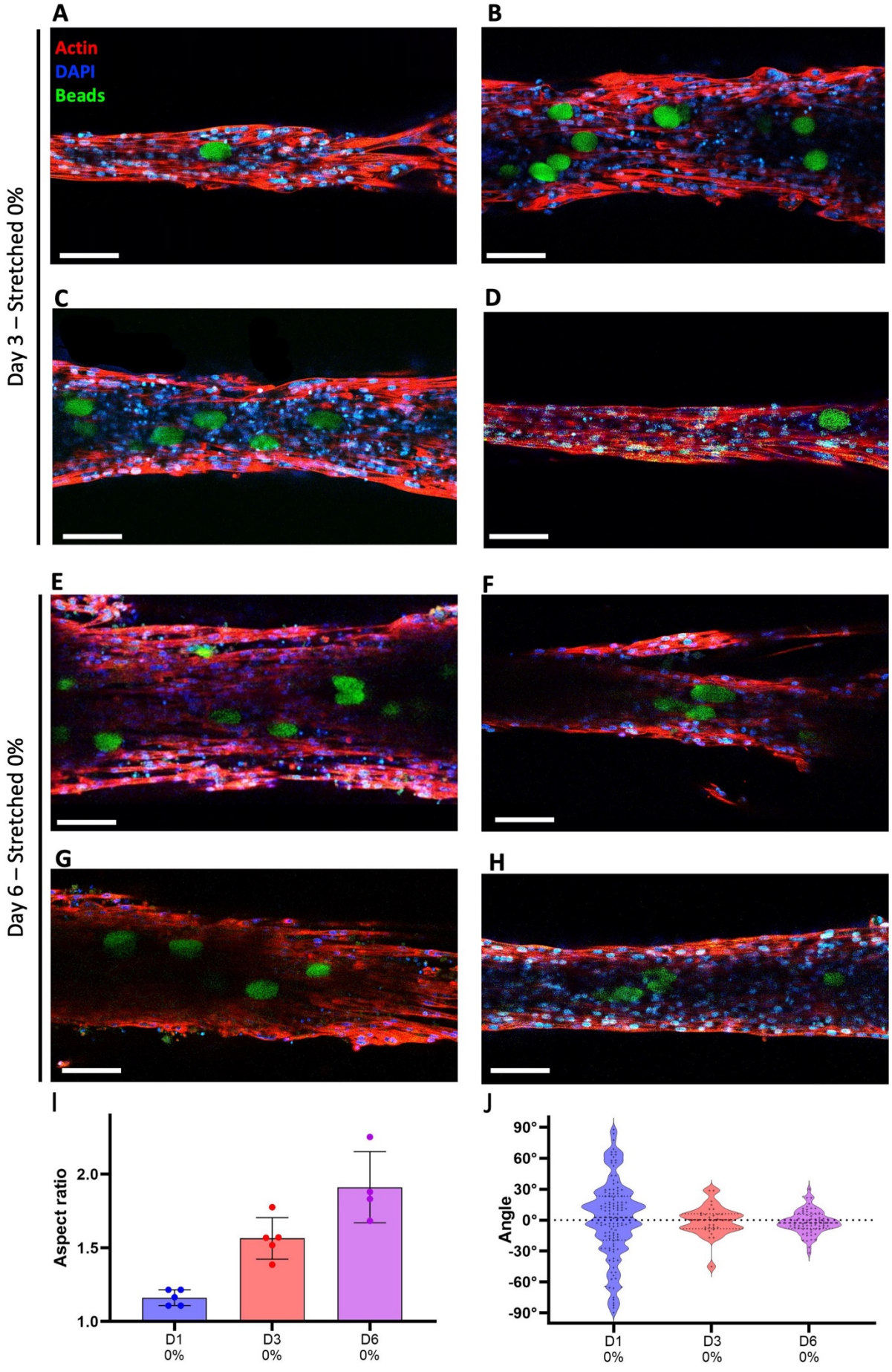
A
B
Actin
DAPI
Beads
Day 3 – Stretched 0%
C
D
E
F
Day 6 – Stretched 0%
G
H
I
Aspect ratio
2.0
1.5
1.0
D1 0%
D3 0%
D6 0%
J
Angle
90°
60°
30°
0°
-30°
-60°
-90°
D1 0%
D3 0%
D6 0%

Supplementary Figure 4.31. *Confocal imaging of different tissues made of M-hiPSC 1, in which polyacrylamide beads were embedded, which were cultured for (A-D) 3 days and (E-H) 6 days without stretching. (I) Aspect ratio and (J) orientation of the beads for tissues stretched by 0% on day 1, day 3 and day 6. Data points represent the average bead aspect ratio within one sample, and the angles of all beads across all samples. (Actin in red, nuclei in blue, beads in green, Scale bar=100 µm)*

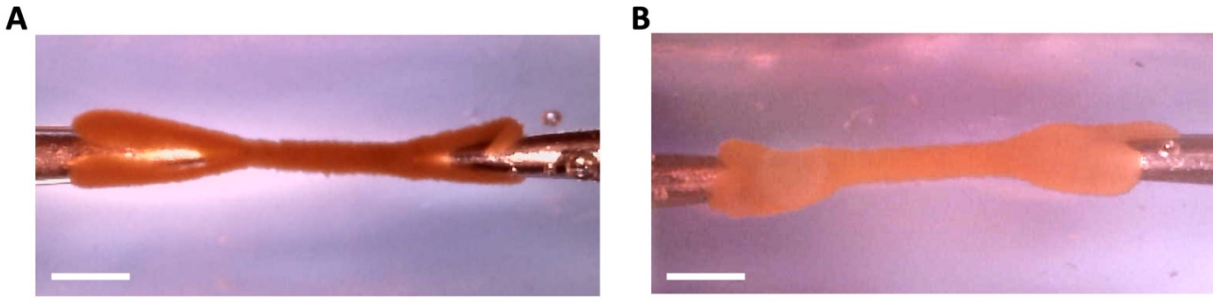

Supplementary Figure 4.32. *Tissues magnetically bioprinted from magnetically labeled M-hiPSC 2 (A) and M-hiPSC 3 (B) trapped between needles. (Scale bar = 1mm)*

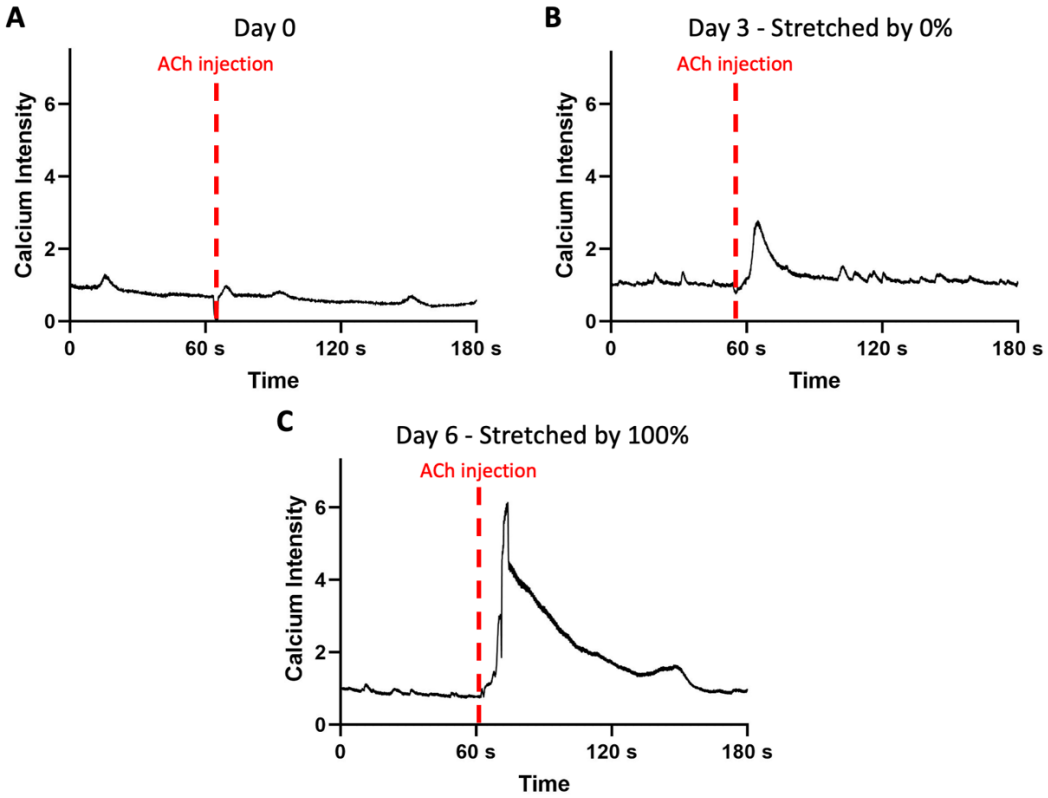

Supplementary Figure 4.33. *Kymographs of the fluctuations of the calcium signal in a M-hiPS cell from (A) a M-hiPSC 2 tissue on day 0 just after bioprinting, (B) a non-stretched M-hiPSC 3 tissue on day 3, and (C) a M-hiPSC 2 tissue on day 3 stretched by 100% since day 1, treated with 1 mM ACh after approximately 1 min.*

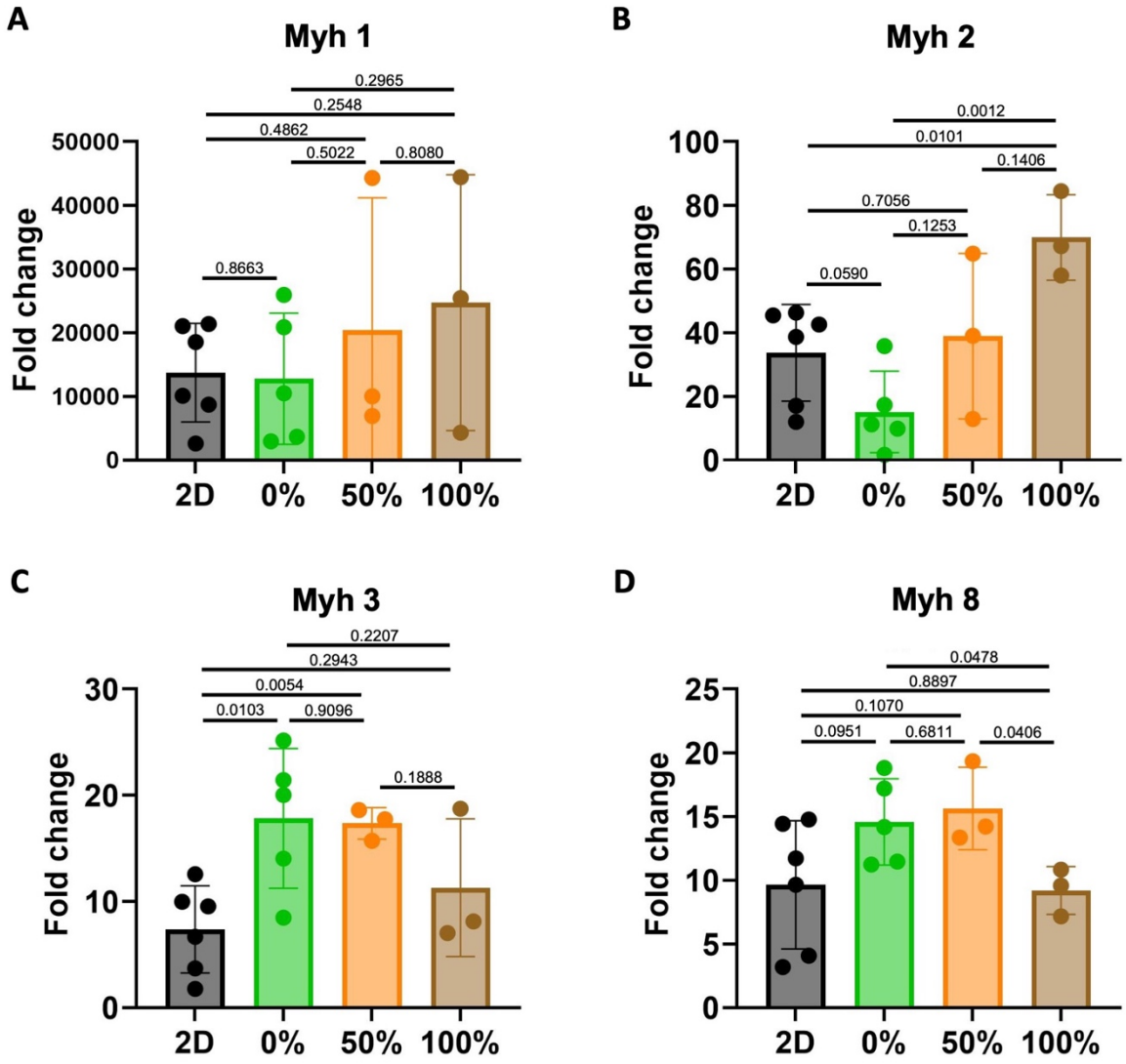

Supplementary Figure 4.34. *Fold changes of the gene expression on day 3 of (A) Myh1, (B) Myh2, (C) Myh3 and (D) Myh8 for 3D tissues stretched by 0%, 50% and 100% and 2D cultures of M-hiPSC 1, compared to the expression of cells collected on day 0.*

	M-hiPSC 1	***M-hiPSC 2***	***M-hiPSC 3***
Sex of the patient	*XX*	*XY*	*XX*
Age of the patient	*67*	*22*	*48*
Origin of the sample	*Fibroblasts*	*PBMC*	*PBMC 16525*
Cell supplier	*Phenocell*		
Reprogramming method	*Epi5 Kit - ThermoFischer #A15960*		

Supplementary Table 4.1. *Information on the origins of the three patient derived hiPS cell lines from which the three M-hiPS cell lines were derived*

F_18S	*GAGGATGAGGTGGAACGTGT*
R_18S	*TCTTCAGTCGCTCCAGGTCT*
F_Myh1	*CTCTTTGTTGGGGCAACGG*
R_Myh1	*TGAGTGCTCCTCAAGTTGGTC*
F_Myh2	*TGAAGGAGAGGGAGCTGGT*
R_Myh2	*ATGGGTACTCCTGAGGTTGGT*
F_MYH3	*AGAGGAACTTTGACAAGGTGTTG*
R_MYH3	*GGCTTCCTCGTAGGCATTTT*
F_Myh8	*TGCTGAAGCAGATAGCAGCG*
R_Myh8	*TACGAAGTGAGGGTGTGTGC*

Supplementary Table 4.2. *Primers used for qRT-PCR.*

Appendix B

Supplementary information of Chapter 5

Supplementary Figures of Appendix B

Supplementary Figure 5.1 213
Supplementary Figure 5.2 214
Supplementary Figure 5.3 215
Supplementary Figure 5.4 216
Supplementary Figure 5.5 216
Supplementary Figure. 5.6 217
Supplementary Figure 5.7 218
Supplementary Figure 5.8 219

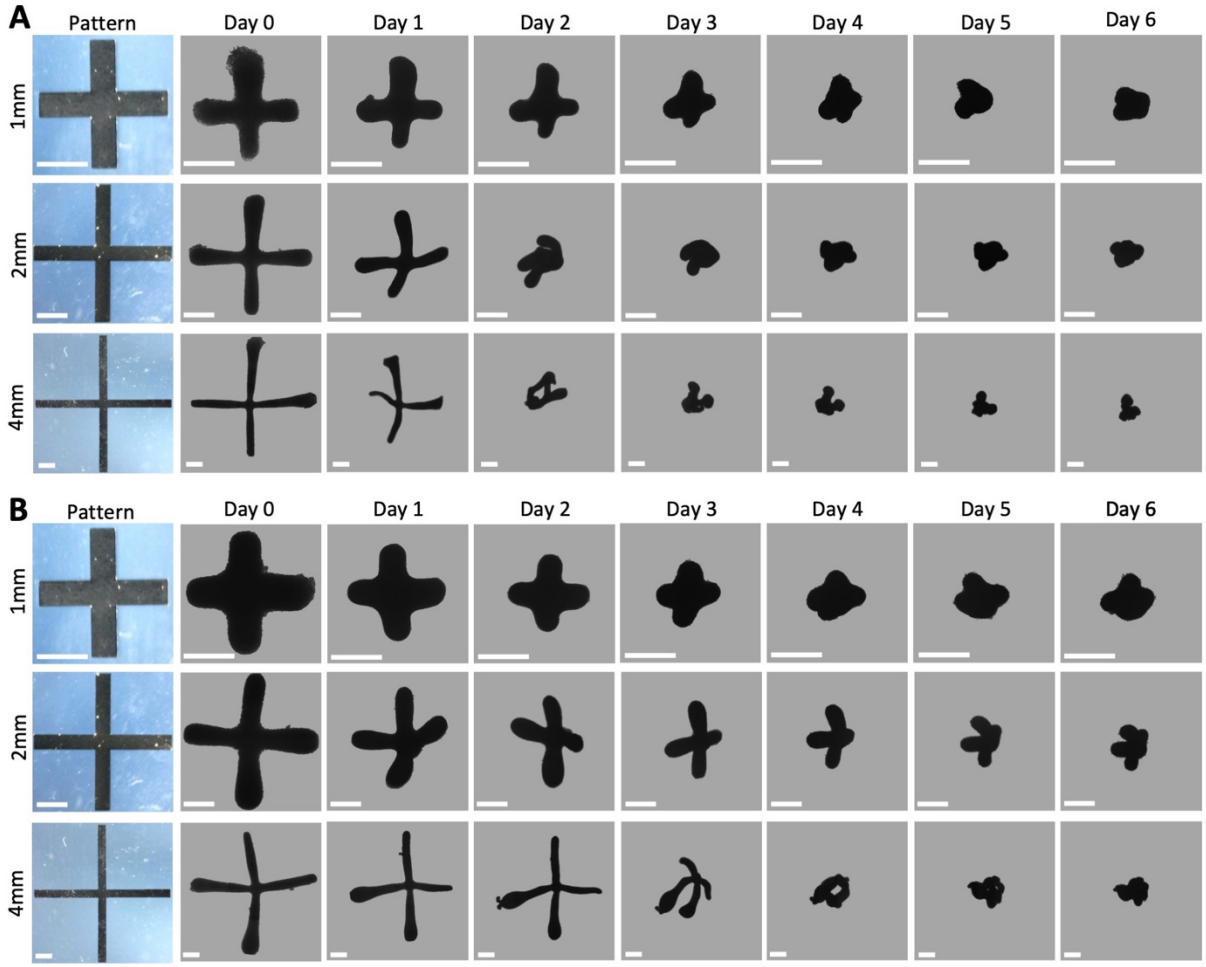

Supplementary Figure 5.1. *Additional sets of brightfield images from day 0 to day 6 of free-floating tissues made from cross patterns with 1, 2 or 4 mm long branches and with (A) 100,000 or (B) 200,000 cells per mm^2 of pattern. (Scale bar = 1 mm)*

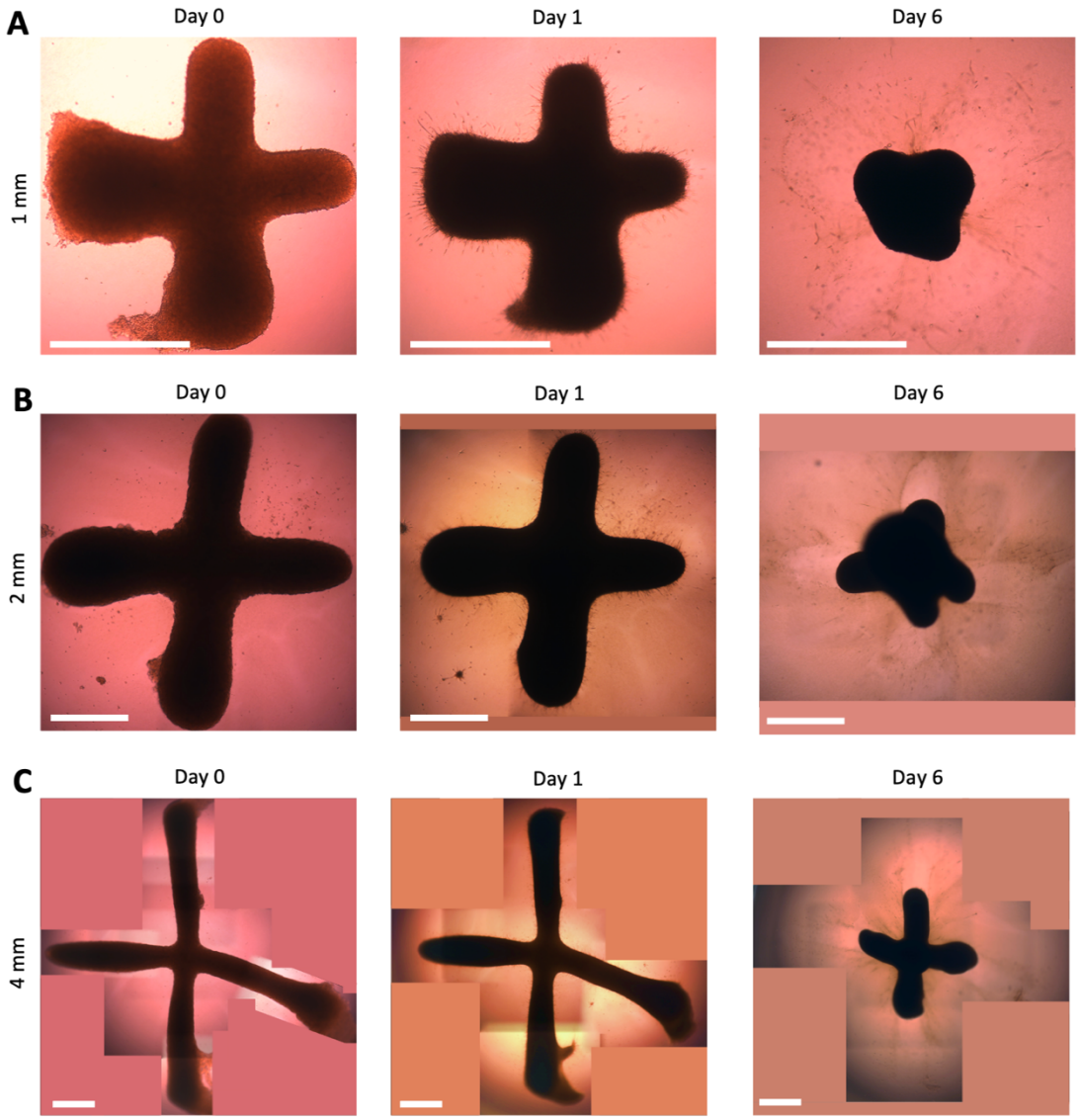

Supplementary Figure 5.2. *Additional sets of brightfield images on days 0, 1 and 6 of tissues made from cross patterns with (A) 1, (B) 2 or (C) 4 mm long branches and 200,000 cells per mm^2 of pattern, embedded in collagen. (Scale bar = 1 mm) Tissues were not segmented to show the deformation of the matrix. As tissues were reconstructed from multiple frames, blank parts were filled with a uniform background color.*

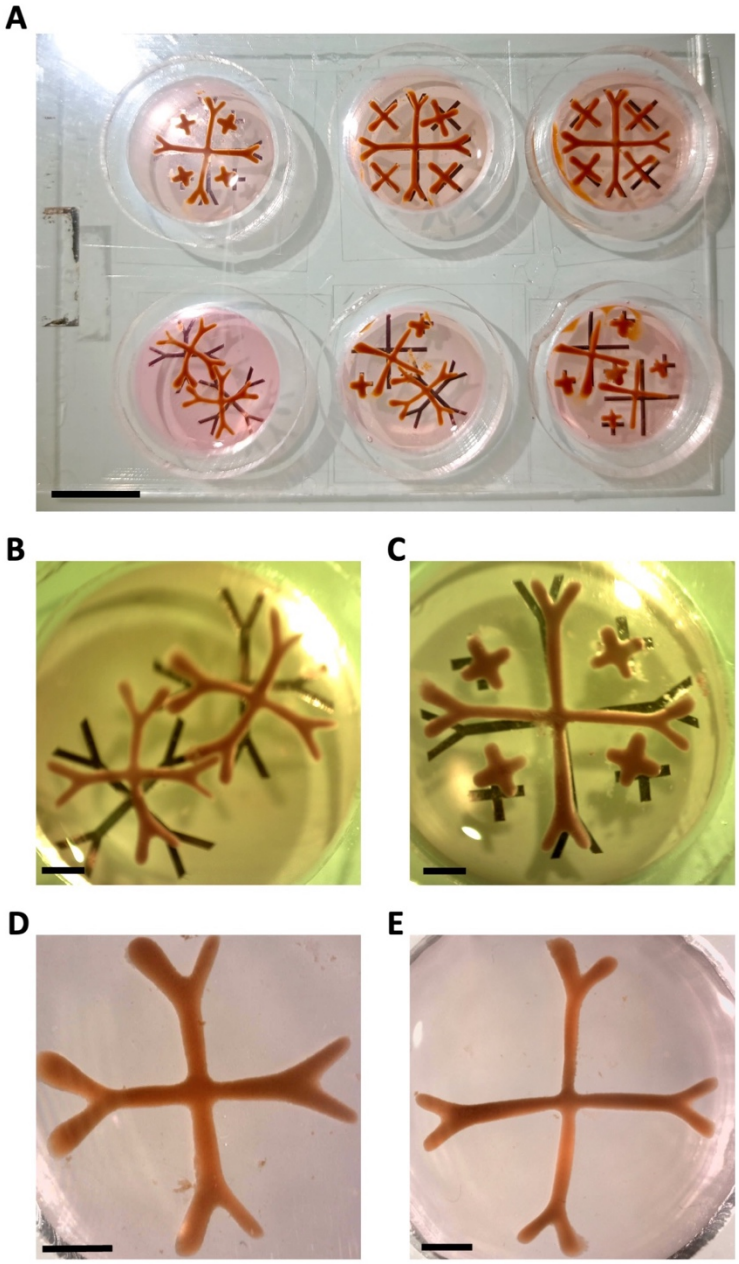

Supplementary Figure 5.3. *(A) Image of a whole glass substrate with wells on all six sets of cross shaped patterns, just after bioprinting. (scale bar = 1 cm). (B-E) Wells used to make clip-on crosses with (B) 2 mm and (C) 4 mm long branches, with a close up on a single clip-on cross, with (D) 2 mm or (E) 4 mm long branches, just after the bioprinting process. (Scale bar = 2 mm)*

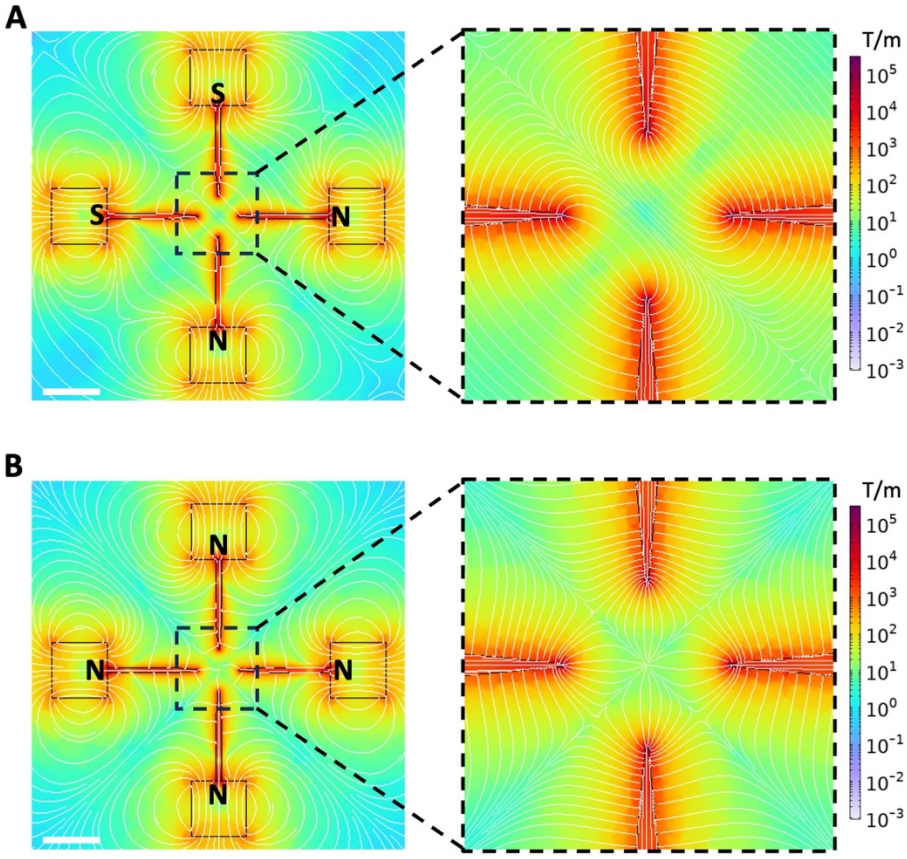

Supplementary Figure 5.4. *Simulations of the magnetic field gradient within a chip meant to trap a cross shaped tissue, either with (A) a North/North/South/South or (B) a North/North/North/North magnet configuration. Magnet polarity is indicated with N for North and S for South (Scale bar = 1 cm)*

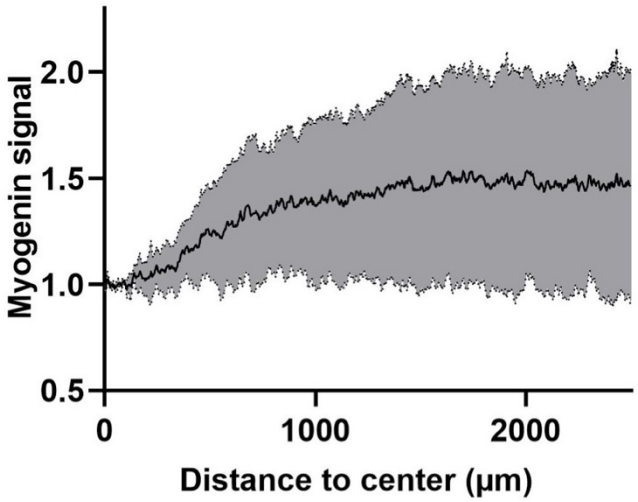

Supplementary Figure 5.5. *Spatial distribution of myogenin within a cross-shaped tissue with 4mm-long branches on day 6 plotted after normalization as a function of the distance from the center (n=3).*

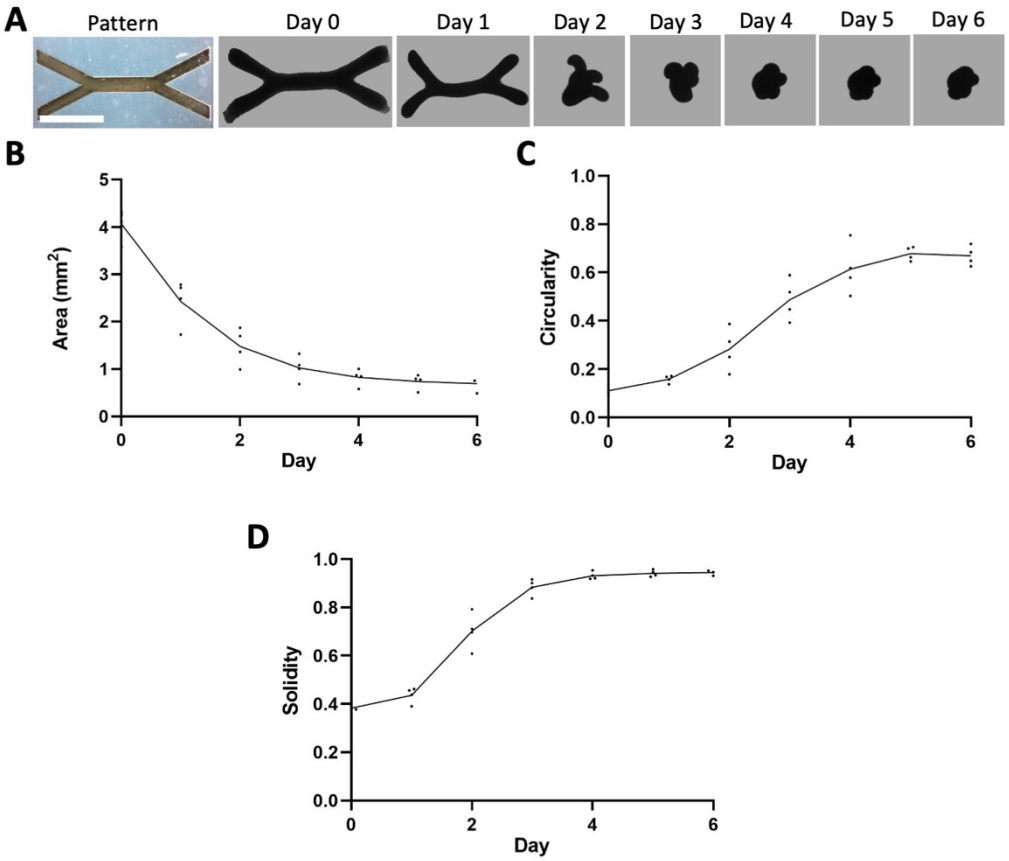

Supplementary Figure. 5.6. *(A) Additional set of brightfield images showing the evolution of a free-floating tissue printed with a wrench-shaped pattern (100,000 cells per mm² of pattern) from day 0 to day 6, and the evolution of (B) the area, (C) the circularity and (D) the solidity of wrench-shaped tissues free floating in non adherent wells. (Scale bar = 2 mm)*

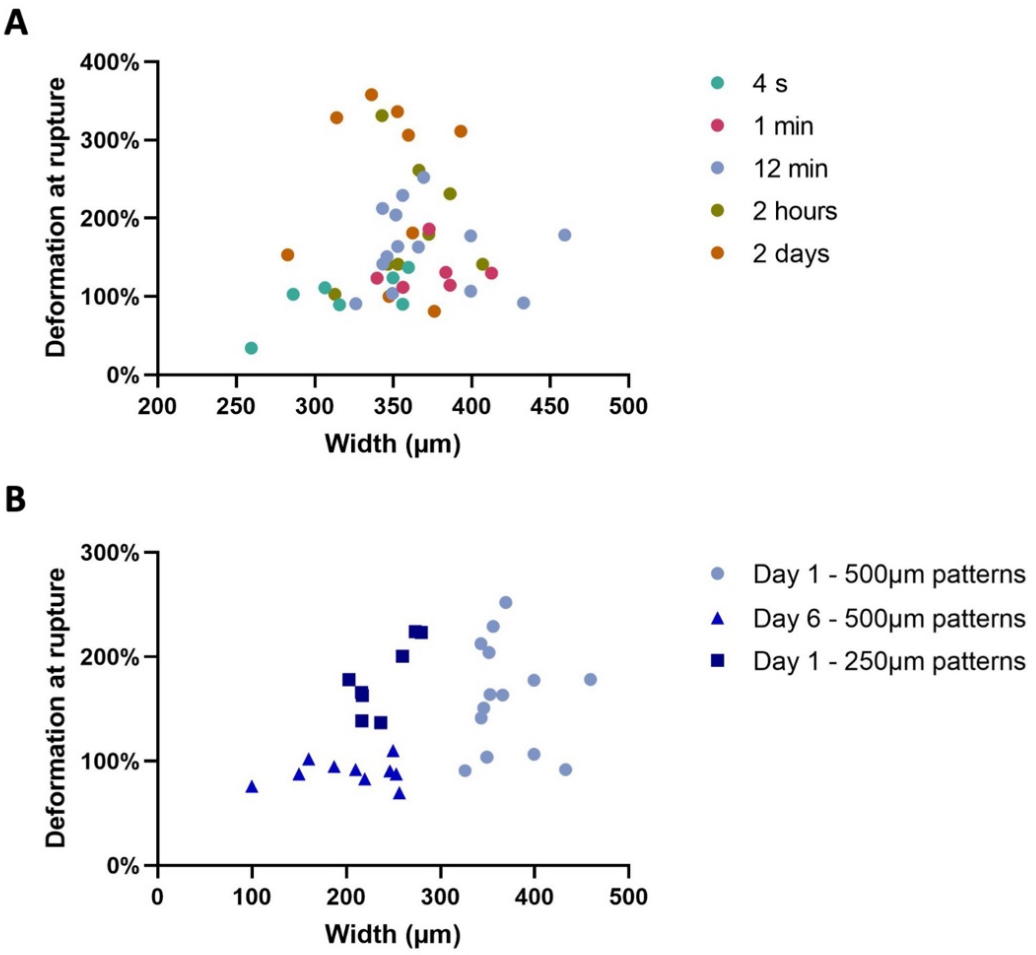

Supplementary Figure 5.7. *(A-B) Maximum deformation at rupture as a function of tissue width of (A) 1-day-old C2C12 tissues printed with 500 µm-wide patterns, stretched at rates of 100% strain over 4 s, 1 min, 12 min, 2 hours, and 2 days and of (B) tissues stretched at 100% strain over 12 min on day 1 versus day 6, printed either with 500 or 250 µm-wide patterns.*

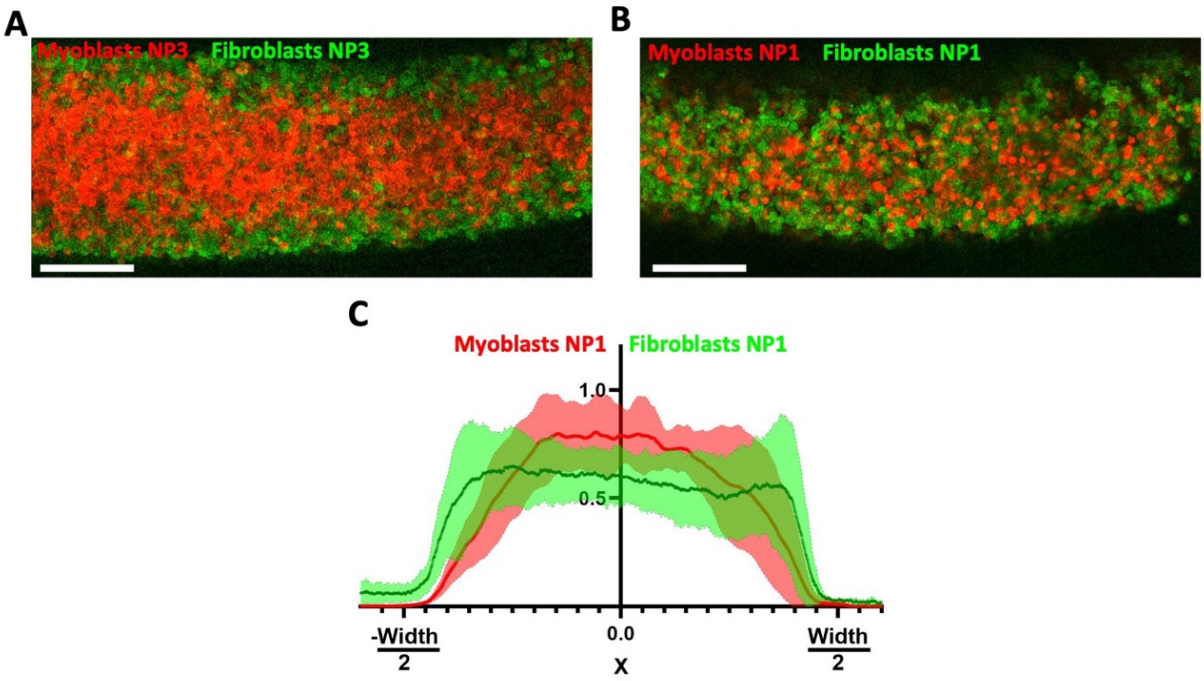

Supplementary Figure 5.8. *(A-B) Confocal Z-slices of tissues printed with (A) 50% NP3-labeled myoblasts and 50% NP3-labeled fibroblasts, and (B) 50% NP1-labeled myoblasts and 50% NP1-labeled fibroblasts. (Scale bar = 200 μm) (C) Normalized fluorescence intensity profiles of mCherry-Lifeact myoblasts and GFP-Lifeact fibroblasts along the width of the central fiber in tissues composed of 50% NP1-labeled myoblasts and 50% NP1-labeled fibroblasts.*

References

1. Global Observatory on Donation and Transplantation. INTERNATIONAL REPORT ON ORGAN DONATION AND TRANSPLANTATION ACTIVITIES 2023. *https://www.transplant-observatory.org/download/2023-global-report/* (2025).
2. Atala, A. Regenerative medicine strategies. *J Pediatr Surg* **47**, 17–28 (2012).
3. Hubrecht & Carter. The 3Rs and Humane Experimental Technique: Implementing Change. *Animals* **9**, 754 (2019).
4. Animal research is not always king: researchers should explore the alternatives. *Nature* **631**, 481–481 (2024).
5. Vacanti, C. A. History of Tissue Engineering and A Glimpse Into Its Future. *Tissue Eng* **12**, 1137–1142 (2006).
6. Vacanti, J. P. Beyond Transplantation. *Archives of Surgery* **123**, 545 (1988).
7. Langer, R. & Vacanti, J. P. Tissue Engineering. *Science (1979)* **260**, 920–926 (1993).
8. Moro, L. G. *et al.* A Brief History of Cell Culture: From Harrison to Organs-on-a-Chip. *Cells* **13**, 2068 (2024).
9. Nelson, C. M. Geometric control of tissue morphogenesis. *Biochimica et Biophysica Acta (BBA) - Molecular Cell Research* **1793**, 903–910 (2009).
10. Dicko, M. *et al.* Geometry can provide long-range mechanical guidance for embryogenesis. *PLoS Comput Biol* **13**, e1005443 (2017).
11. Lecuit, T. & Lenne, P.-F. Cell surface mechanics and the control of cell shape, tissue patterns and morphogenesis. *Nat Rev Mol Cell Biol* **8**, 633–644 (2007).
12. Weiss, P. Experiments on cell and axon orientation in vitro: The role of colloidal exudates in tissue organization. *Journal of Experimental Zoology* **100**, 353–386 (1945).
13. Jensen, C. & Teng, Y. Is It Time to Start Transitioning From 2D to 3D Cell Culture? *Front Mol Biosci* **7**, (2020).
14. Moysidou, C.-M., Barberio, C. & Owens, R. M. Advances in Engineering Human Tissue Models. *Front Bioeng Biotechnol* **8**, (2021).
15. Sutherland, R. M., Inch, W. R., McCredie, J. A. & Kruuv, J. A Multi-component Radiation Survival Curve Using an *in Vitro* Tumour Model. *Int J Radiat Biol Relat Stud Phys Chem Med* **18**, 491–495 (1970).
16. Elsdale, T. & Bard, J. COLLAGEN SUBSTRATA FOR STUDIES ON CELL BEHAVIOR. *J Cell Biol* **54**, 626–637 (1972).
17. Hughes, C. S., Postovit, L. M. & Lajoie, G. A. Matrigel: A complex protein mixture required for optimal growth of cell culture. *Proteomics* **10**, 1886–1890 (2010).
18. Xing, J., Liu, N., Xu, N., Chen, W. & Xing, D. Engineering Complex Anisotropic Scaffolds beyond Simply Uniaxial Alignment for Tissue Engineering. *Adv Funct Mater* **32**, (2022).
19. Elouneg, A. *et al.* Anisotropic mechanical characterization of human skin by in vivo multi-axial ring suction test. *J Mech Behav Biomed Mater* **141**, 105779 (2023).
20. *Cardiothoracic Critical Care*. (Elsevier, 2007). doi:10.1016/B978-0-7506-7572-7.X5001-2.
21. Helander, H. F. & Fändriks, L. Surface area of the digestive tract – revisited. *Scand J Gastroenterol* **49**, 681–689 (2014).
22. Reis & Schembra, Fr. W. Länge und Lage des Verdauungsrohres beim Lebenden. *Z Gesamte Exp Med* **43**, 94–115 (1924).
23. Janssen, I., Heymsfield, S. B., Wang, Z. & Ross, R. Skeletal muscle mass and distribution in 468 men and women aged 18–88 yr. *J Appl Physiol* **89**, 81–88 (2000).
24. Lehka, L. & Rędowicz, M. J. Mechanisms regulating myoblast fusion: A multilevel interplay. *Semin Cell Dev Biol* **104**, 81–92 (2020).
25. Ostrovidov, S. *et al.* Skeletal Muscle Tissue Engineering: Methods to Form Skeletal Myotubes and Their Applications. *Tissue Eng Part B Rev* **20**, 403–436 (2014).
26. Beldjilali-Labro, M. *et al.* Biomaterials in Tendon and Skeletal Muscle Tissue Engineering: Current Trends and Challenges. *Materials* **11**, 1116 (2018).
27. Mercuri, E., Bönnemann, C. G. & Muntoni, F. Muscular dystrophies. *The Lancet* **394**, 2025–2038 (2019).
28. Chen, J. *et al.* Deficiency of skeletal muscle Agrin contributes to the pathogenesis of age-related sarcopenia in mice. *Cell Death Dis* **15**, 201 (2024).
29. Sayed, R. K. A. *et al.* Identification of morphological markers of sarcopenia at early stage of aging in skeletal muscle of mice. *Exp Gerontol* **83**, 22–30 (2016).

30. Pollot, B. E. & Corona, B. T. Volumetric Muscle Loss. in 19–31 (2016). doi:10.1007/978-1-4939-3810-0_2.
31. Levato, R. *et al.* From Shape to Function: The Next Step in Bioprinting. *Advanced Materials* **32**, (2020).
32. Bidan, C. M. *et al.* Geometry as a Factor for Tissue Growth: Towards Shape Optimization of Tissue Engineering Scaffolds. *Adv Healthc Mater* **2**, 186–194 (2013).
33. Ingber, D. E. Is it Time for Reviewer 3 to Request Human Organ Chip Experiments Instead of Animal Validation Studies? *Advanced Science* **7**, (2020).
34. Low, L. A., Mummery, C., Berridge, B. R., Austin, C. P. & Tagle, D. A. Organs-on-chips: into the next decade. *Nat Rev Drug Discov* **20**, 345–361 (2021).
35. Mahler, G. J., Esch, M. B., Stokol, T., Hickman, J. J. & Shuler, M. L. Body-on-a-Chip Systems for Animal-free Toxicity Testing. *Alternatives to Laboratory Animals* **44**, 469–478 (2016).
36. Sontheimer-Phelps, A., Hassell, B. A. & Ingber, D. E. Modelling cancer in microfluidic human organs-on-chips. *Nat Rev Cancer* **19**, 65–81 (2019).
37. Ingber, D. E. Human organs-on-chips for disease modelling, drug development and personalized medicine. *Nat Rev Genet* **23**, 467–491 (2022).
38. Huh, D. *et al.* Reconstituting Organ-Level Lung Functions on a Chip. *Science (1979)* **328**, 1662–1668 (2010).
39. Petta, D. *et al.* Musculoskeletal tissues-on-a-chip: role of natural polymers in reproducing tissue-specific microenvironments. *Biofabrication* **14**, 042001 (2022).
40. Arrigoni, C. *et al.* Engineering complex muscle-tissue interfaces through microfabrication. *Biofabrication* **11**, 032004 (2019).
41. McKeon-Fischer, K. D., Browe, D. P., Olabisi, R. M. & Freeman, J. W. Poly(3,4-ethylenedioxythiophene) nanoparticle and poly(ε-caprolactone) electrospun scaffold characterization for skeletal muscle regeneration. *J Biomed Mater Res A* **103**, 3633–3641 (2015).
42. Fornetti, E. *et al.* A novel extrusion-based 3D bioprinting system for skeletal muscle tissue engineering. *Biofabrication* **15**, 025009 (2023).
43. Kim, J. H. *et al.* 3D Bioprinted Human Skeletal Muscle Constructs for Muscle Function Restoration. *Sci Rep* **8**, 12307 (2018).
44. Mao, Q. *et al.* Fabrication of liver microtissue with liver decellularized extracellular matrix (dECM) bioink by digital light processing (DLP) bioprinting. *Materials Science and Engineering: C* **109**, 110625 (2020).
45. Kang, H.-W. *et al.* A 3D bioprinting system to produce human-scale tissue constructs with structural integrity. *Nat Biotechnol* **34**, 312–319 (2016).
46. Demri, N. *et al.* Remote Magnetic Microengineering and Alignment of Spheroids into 3D Cellular Fibers. *Adv Funct Mater* **32**, (2022).
47. Bongaerts, M. *et al.* Parallelized Manipulation of Adherent Living Cells by Magnetic Nanoparticles-Mediated Forces. *Int J Mol Sci* **21**, 6560 (2020).
48. Moise, S., Byrne, J. M., El Haj, A. J. & Telling, N. D. The potential of magnetic hyperthermia for triggering the differentiation of cancer cells. *Nanoscale* **10**, 20519–20525 (2018).
49. Fromain, A., Perez, J. E., Van de Walle, A., Lalatonne, Y. & Wilhelm, C. Photothermia at the nanoscale induces ferroptosis via nanoparticle degradation. *Nat Commun* **14**, 4637 (2023).
50. Namiki, Y. *et al.* A novel magnetic crystal–lipid nanostructure for magnetically guided in vivo gene delivery. *Nat Nanotechnol* **4**, 598–606 (2009).
51. Dames, P. *et al.* Targeted delivery of magnetic aerosol droplets to the lung. *Nat Nanotechnol* **2**, 495–499 (2007).
52. Ito, A. *et al.* Novel Methodology for Fabrication of Tissue-Engineered Tubular Constructs Using Magnetite Nanoparticles and Magnetic Force. *Tissue Eng* **11**, 1553–1561 (2005).
53. Parfenov, V. A. *et al.* Magnetic levitational bioassembly of 3D tissue construct in space. *Sci Adv* **6**, (2020).
54. Rotherham, M. *et al.* Magnetic activation of TREK1 triggers stress signalling and regulates neuronal branching in SH-SY5Y cells. *Front Med Technol* **4**, (2022).
55. Van de Walle, A., Perez, J. E. & Wilhelm, C. Magnetic bioprinting of stem cell-based tissues. *Bioprinting* **30**, e00265 (2023).
56. Mary, G. *et al.* High-Throughput Differentiation of Embryonic Stem Cells into Cardiomyocytes with a Microfabricated Magnetic Pattern and Cyclic Stimulation. *Adv Funct Mater* **30**, (2020).

57. Du, V. *et al.* A 3D magnetic tissue stretcher for remote mechanical control of embryonic stem cell differentiation. *Nat Commun* **8**, 400 (2017).
58. Souza, G. R. *et al.* Three-dimensional tissue culture based on magnetic cell levitation. *Nat Nanotechnol* **5**, 291–6 (2010).
59. Souza, G. *et al.* Magnetically Bioprinted Human Myometrial 3D Cell Rings as A Model for Uterine Contractility. *Int J Mol Sci* **18**, 683 (2017).
60. Zwi-Dantsis, L. *et al.* Remote Magnetic Nanoparticle Manipulation Enables the Dynamic Patterning of Cardiac Tissues. *Advanced Materials* **32**, (2020).
61. Chen, C. S. 3D Biomimetic Cultures: The Next Platform for Cell Biology. *Trends Cell Biol* **26**, 798–800 (2016).
62. Frontera, W. R. & Ochala, J. Skeletal Muscle: A Brief Review of Structure and Function. *Calcif Tissue Int* **96**, 183–195 (2015).
63. Nelson, C. M. *et al.* Emergent patterns of growth controlled by multicellular form and mechanics. *Proceedings of the National Academy of Sciences* **102**, 11594–11599 (2005).
64. Lam, M. T., Sim, S., Zhu, X. & Takayama, S. The effect of continuous wavy micropatterns on silicone substrates on the alignment of skeletal muscle myoblasts and myotubes. *Biomaterials* **27**, 4340–4347 (2006).
65. Bulte, J. W. M. *et al.* Neurotransplantation of magnetically labeled oligodendrocyte progenitors: Magnetic resonance tracking of cell migration and myelination. *Proceedings of the National Academy of Sciences* **96**, 15256–15261 (1999).
66. Nahar, T. *et al.* Long-range directional growth of neurites induced by magnetic forces. *Acta Biomater* **193**, 215–230 (2025).
67. *Bancroft's Theory and Practice of Histological Techniques*. (Elsevier, 2019). doi:10.1016/C2015-0-00143-5.
68. Lowry, O. H., Gilligan, D. R. & Katersky, E. M. THE DETERMINATION OF COLLAGEN AND ELASTIN IN TISSUES, WITH RESULTS OBTAINED IN VARIOUS NORMAL TISSUES FROM DIFFERENT SPECIES. *Journal of Biological Chemistry* **139**, 795–804 (1941).
69. NEUMAN, R. E. & LOGAN, M. A. The determination of collagen and elastin in tissues. *J Biol Chem* **186**, 549–56 (1950).
70. Svensson, R. B. *et al.* Evidence of structurally continuous collagen fibrils in tendons. *Acta Biomater* **50**, 293–301 (2017).
71. Kesson, M. & Atkins, E. Soft tissues of the musculoskeletal system. in *Orthopaedic Medicine* 33–54 (Elsevier, 2005). doi:10.1016/B978-075065563-7.50008-4.
72. USHIKI, T. Collagen Fibers, Reticular Fibers and Elastic Fibers. A Comprehensive Understanding from a Morphological Viewpoint. *Arch Histol Cytol* **65**, 109–126 (2002).
73. Yang, L. *et al.* Mechanical Properties of Native and Cross-linked Type I Collagen Fibrils. *Biophys J* **94**, 2204–2211 (2008).
74. Dutov, P., Antipova, O., Varma, S., Orgel, J. P. R. O. & Schieber, J. D. Measurement of Elastic Modulus of Collagen Type I Single Fiber. *PLoS One* **11**, e0145711 (2016).
75. Wu, J. Z. & Herzog, W. Elastic anisotropy of articular cartilage is associated with the microstructures of collagen fibers and chondrocytes. *J Biomech* **35**, 931–942 (2002).
76. Schinagl, R. M., Gurskis, D., Chen, A. C. & Sah, R. L. Depth-dependent confined compression modulus of full-thickness bovine articular cartilage. *Journal of Orthopaedic Research* **15**, 499–506 (1997).
77. Rumian, A. P., Wallace, A. L. & Birch, H. L. Tendons and ligaments are anatomically distinct but overlap in molecular and morphological features—a comparative study in an ovine model. *Journal of Orthopaedic Research* **25**, 458–464 (2007).
78. Lynch, H. A., Johannessen, W., Wu, J. P., Jawa, A. & Elliott, D. M. Effect of Fiber Orientation and Strain Rate on the Nonlinear Uniaxial Tensile Material Properties of Tendon. *J Biomech Eng* **125**, 726–731 (2003).
79. Bonifasi-Lista, C., Lakez, S. P., Small, M. S. & Weiss, J. A. Viscoelastic properties of the human medial collateral ligament under longitudinal, transverse and shear loading. *Journal of Orthopaedic Research* **23**, 67–76 (2005).
80. Biewener, A. A. Tendons and Ligaments: Structure, Mechanical Behavior and Biological Function. in *Collagen* 269–284 (Springer US, Boston, MA). doi:10.1007/978-0-387-73906-9_10.

81. Barrett, B. THE LENGTH AND MODE OF TERMINATION OF INDIVIDUAL MUSCLE FIBRES IN THE HUMAN SARTORIUS AND POSTERIOR FEMORAL MUSCLES. *Cells Tissues Organs* **48**, 242–257 (1962).
82. Gollapudi, S. K., Michael, J. J. & Chandra, M. Striated Muscle Dynamics. in *Reference Module in Biomedical Sciences* (Elsevier, 2014). doi:10.1016/B978-0-12-801238-3.00251-8.
83. Minozzo, F. C., Baroni, B. M., Correa, J. A., Vaz, M. A. & Rassier, D. E. Force produced after stretch in sarcomeres and half-sarcomeres isolated from skeletal muscles. *Sci Rep* **3**, 2320 (2013).
84. Pavlov, I., Novinger, R. & Rassier, D. E. The mechanical behavior of individual sarcomeres of myofibrils isolated from rabbit psoas muscle. *American Journal of Physiology-Cell Physiology* **297**, C1211–C1219 (2009).
85. Withrow, T. J., Huston, L. J., Wojtys, E. M. & Ashton-Miller, J. A. The Relationship between Quadriceps Muscle Force, Knee Flexion, and Anterior Cruciate Ligament Strain in an in Vitro Simulated Jump Landing. *Am J Sports Med* **34**, 269–274 (2006).
86. Samuel, D. *et al.* Age-associated changes in hand grip and quadriceps muscle strength ratios in healthy adults. *Aging Clin Exp Res* **24**, 245–250 (2012).
87. Lowe, J. S. & Anderson, P. G. Contractile Cells. in *Stevens Lowes Human Histology* 71–83 (Elsevier, 2015). doi:10.1016/B978-0-7234-3502-0.00005-X.
88. Perge, J. A., Niven, J. E., Mugnaini, E., Balasubramanian, V. & Sterling, P. Why do axons differ in caliber? *J Neurosci* **32**, 626–38 (2012).
89. Debanne, D., Campanac, E., Bialowas, A., Carlier, E. & Alcaraz, G. Axon Physiology. *Physiol Rev* **91**, 555–602 (2011).
90. Stewart, J. D. Peripheral nerve fascicles: Anatomy and clinical relevance. *Muscle Nerve* **28**, 525–541 (2003).
91. Paulin, E. *et al.* A Comprehensive Review of Topography and Axon Counts in Upper-Extremity Peripheral Nerves: A Guide for Neurotization. *J Hand Surg Glob Online* **6**, 784–795 (2024).
92. Eskandari, F., Shafieian, M., Aghdam, M. M. & Laksari, K. Structural Anisotropy vs. Mechanical Anisotropy: The Contribution of Axonal Fibers to the Material Properties of Brain White Matter. *Ann Biomed Eng* **49**, 991–999 (2021).
93. Müller, B. *et al.* High-resolution tomographic imaging of microvessels. in (ed. Stock, S. R.) 70780B (2008). doi:10.1117/12.794157.
94. Papaioannou, T. G. & Stefanadis, C. Vascular wall shear stress: basic principles and methods. *Hellenic J Cardiol* **46**, 9–15 (2005).
95. Muller, W. A. & Gimbrone, M. A. Plasmalemmal proteins of cultured vascular endothelial cells exhibit apical-basal polarity: analysis by surface-selective iodination. *J Cell Biol* **103**, 2389–2402 (1986).
96. Pan, W., le Roux, C. M., Levy, S. M. & Briggs, C. A. The morphology of the human lymphatic vessels in the head and neck. *Clinical Anatomy* **23**, 654–661 (2010).
97. DIXON, J. B. *et al.* Lymph Flow, Shear Stress, and Lymphocyte Velocity in Rat Mesenteric Prenodal Lymphatics. *Microcirculation* **13**, 597–610 (2006).
98. Ramsay, D. T., Kent, J. C., Hartmann, R. A. & Hartmann, P. E. Anatomy of the lactating human breast redefined with ultrasound imaging. *J Anat* **206**, 525–534 (2005).
99. Brown, A. L. The Structure of the Nephron. *Medical Clinics of North America* **50**, 927–935 (1966).
100. Shyer, A. E. *et al.* Villification: How the Gut Gets Its Villi. *Science (1979)* **342**, 212–218 (2013).
101. Gabella, G. The force generated by a visceral smooth muscle. *J Physiol* **263**, 199–213 (1976).
102. Halpern, W., Mulvany, M. J. & Warshaw, D. M. Mechanical properties of smooth muscle cells in the walls of arterial resistance vessels. *J Physiol* **275**, 85–101 (1978).
103. Sadler, T. W. Embryology of neural tube development. *Am J Med Genet C Semin Med Genet* **135C**, 2–8 (2005).
104. Saade, M. & Martí, E. Early spinal cord development: from neural tube formation to neurogenesis. *Nat Rev Neurosci* **26**, 195–213 (2025).
105. STORER, K. P., TOH, J., STOODLEY, M. A. & JONES, N. R. The central canal of the human spinal cord: a computerised 3-D study. *J Anat* **192**, 565–572 (1998).
106. Prasad, A., Zafar, N. & Mahmud, E. Assessment of renal artery fibromuscular dysplasia: Angiography, intravascular ultrasound (with virtual histology), and pressure wire measurements. *Catheterization and Cardiovascular Interventions* **74**, 260–264 (2009).
107. Qin, Y.-X. *et al.* Prediction of trabecular bone qualitative properties using scanning quantitative ultrasound. *Acta Astronaut* **92**, 79–88 (2013).

108. Wilson, S. E. Bowman's layer in the cornea– structure and function and regeneration. *Exp Eye Res* **195**, 108033 (2020).
109. Hu, J. *et al.* Zonal Characteristics of Collagen Ultrastructure and Responses to Mechanical Loading in Articular Cartilage. *Acta Biomater* **195**, 104–116 (2025).
110. Porrelli, D. *et al.* Trabecular bone porosity and pore size distribution in osteoporotic patients – A low field nuclear magnetic resonance and microcomputed tomography investigation. *J Mech Behav Biomed Mater* **125**, 104933 (2022).
111. Whitehouse, W. J. The quantitative morphology of anisotropic trabecular bone. *J Microsc* **101**, 153–168 (1974).
112. Renders, G. A. P., Mulder, L., van Ruijven, L. J. & van Eijden, T. M. G. J. Porosity of human mandibular condylar bone. *J Anat* **210**, 239–48 (2007).
113. Kohles, S. S. & Roberts, J. B. Linear Poroelastic Cancellous Bone Anisotropy: Trabecular Solid Elastic and Fluid Transport Properties. *J Biomech Eng* **124**, 521–526 (2002).
114. Dendorfer, S., Maier, H. J., Taylor, D. & Hammer, J. Anisotropy of the fatigue behaviour of cancellous bone. *J Biomech* **41**, 636–641 (2008).
115. Linde, F., Hvid, I. & Pongsoipetch, B. Energy absorptive properties of human trabecular bone specimens during axial compression. *Journal of Orthopaedic Research* **7**, 432–439 (1989).
116. Kohles, S. S. *et al.* Direct perfusion measurements of cancellous bone anisotropic permeability. *J Biomech* **34**, 1197–1202 (2001).
117. Seong, Y., Kang, I., Song, E., Kim, H. & Jeong, S. Calcium Phosphate–Collagen Scaffold with Aligned Pore Channels for Enhanced Osteochondral Regeneration. *Adv Healthc Mater* **6**, (2017).
118. Mitzner, W., Fallica, J. & Bishai, J. Anisotropic Nature of Mouse Lung Parenchyma. *Ann Biomed Eng* **36**, 2111–2120 (2008).
119. Yablonskiy, D. A. *et al.* Quantitative *in vivo* assessment of lung microstructure at the alveolar level with hyperpolarized ^{3} He diffusion MRI. *Proceedings of the National Academy of Sciences* **99**, 3111–3116 (2002).
120. Tsunoda, S., Fukaya, H., Sugihara, T., Martin, C. J. & Hildebrandt, J. Lung volume, thickness of alveolar walls, and microscopic anisotropy of expansion. *Respir Physiol* **22**, 285–296 (1974).
121. Dua, H. S., Faraj, L. A., Said, D. G., Gray, T. & Lowe, J. Human Corneal Anatomy Redefined. *Ophthalmology* **120**, 1778–1785 (2013).
122. Loureiro, T. de O. *et al.* Corneal Epithelial Thickness Profile in Healthy Portuguese Children by High-Definition Optical Coherence Tomography. *Clin Ophthalmol* **15**, 735–743 (2021).
123. Rates, E. R. D. *et al.* Layer-by-Layer Investigation of Ultrastructures and Biomechanics of Human Cornea. *Int J Mol Sci* **23**, 7833 (2022).
124. Asbell, P. & Brocks, D. Cornea Overview. in *Encyclopedia of the Eye* 522–531 (Elsevier, 2010). doi:10.1016/B978-0-12-374203-2.00058-0.
125. Hatami-Marbini, H. & Etebu, E. An experimental and theoretical analysis of unconfined compression of corneal stroma. *J Biomech* **46**, 1752–1758 (2013).
126. Graham, H. K., Eckersley, A., Ozols, M., Mellody, K. T. & Sherratt, M. J. Human Skin: Composition, Structure and Visualisation Methods. in 1–18 (2019). doi:10.1007/978-3-030-13279-8_1.
127. Lintzeri, D. A., Karimian, N., Blume-Peytavi, U. & Kottner, J. Epidermal thickness in healthy humans: a systematic review and meta-analysis. *Journal of the European Academy of Dermatology and Venereology* **36**, 1191–1200 (2022).
128. Oltulu, P., Ince, B., Kokbudak, N., Findik, S. & Kilinc, F. Measurement of epidermis, dermis, and total skin thicknesses from six different body regions with a new ethical histometric technique. *Turkish Journal of Plastic Surgery* **26**, 56 (2018).
129. Chauhan, P., Rathawa, A., Jethwa, K. & Mehra, S. The Anatomy of the Cerebral Cortex. in *Cerebral Ischemia* 1–16 (Exon Publications, 2021). doi:10.36255/exonpublications.cerebralischemia.2021.cerebralcortex.
130. Rho, J. Y., Ashman, R. B. & Turner, C. H. Young's modulus of trabecular and cortical bone material: ultrasonic and microtensile measurements. *J Biomech* **26**, 111–9 (1993).
131. Shahar, R. *et al.* Anisotropic Poisson's ratio and compression modulus of cortical bone determined by speckle interferometry. *J Biomech* **40**, 252–264 (2007).
132. Ascenzi, A. & Benvenuti, A. Orientation of collagen fibers at the boundary between two successive osteonic lamellae and its mechanical interpretation. *J Biomech* **19**, 455–463 (1986).

133. Fujita, Y., Wagner, D. R., Biviji, A. A., Duncan, N. A. & Lotz, J. C. Anisotropic shear behavior of the annulus fibrosus: effect of harvest site and tissue prestrain. *Med Eng Phys* **22**, 349–357 (2000).
134. Huycke, T. R. *et al.* Genetic and Mechanical Regulation of Intestinal Smooth Muscle Development. *Cell* **179**, 90-105.e21 (2019).
135. STREETER, D. D., SPOTNITZ, H. M., PATEL, D. P., ROSS, J. & SONNENBLICK, E. H. Fiber Orientation in the Canine Left Ventricle during Diastole and Systole. *Circ Res* **24**, 339–347 (1969).
136. Sabatino, J. *et al.* Left Ventricular Twist Mechanics to Identify Left Ventricular Noncompaction in Childhood. *Circ Cardiovasc Imaging* **12**, (2019).
137. van Zuijlen, P. P. M. *et al.* Collagen morphology in human skin and scar tissue: no adaptations in response to mechanical loading at joints. *Burns* **29**, 423–431 (2003).
138. De Santis, S. *et al. In vitro* and *in vivo* MR evaluation of internal gradient to assess trabecular bone density. *Phys Med Biol* **55**, 5767–5785 (2010).
139. Turner, C. H., Anne, V. & Pidaparti, R. M. V. A uniform strain criterion for trabecular bone adaptation: Do continuum-level strain gradients drive adaptation? *J Biomech* **30**, 555–563 (1997).
140. Cox, T. R. & Erler, J. T. Remodeling and homeostasis of the extracellular matrix: implications for fibrotic diseases and cancer. *Dis Model Mech* **4**, 165–178 (2011).
141. LIOTTA, L., SAIDEL, G. & KLEINERMAN, J. Diffusion model of tumor vascularization and growth. *Bull Math Biol* **39**, 117–128 (1977).
142. Lewis, D. M. *et al.* Intratumoral oxygen gradients mediate sarcoma cell invasion. *Proceedings of the National Academy of Sciences* **113**, 9292–9297 (2016).
143. Valet, M., Siggia, E. D. & Brivanlou, A. H. Mechanical regulation of early vertebrate embryogenesis. *Nat Rev Mol Cell Biol* **23**, 169–184 (2022).
144. Shaffrey, C. I., Chenelle, A. G., Abel, M. F., Menezes, A. H. & Wiggins, G. C. Anatomy and Physiology of Congenital Spinal Lesions. in *Spine Surgery* 61–87 (Elsevier, 2005). doi:10.1016/B978-0-443-06616-0.50009-2.
145. Buckingham, M. & Relaix, F. PAX3 and PAX7 as upstream regulators of myogenesis. *Semin Cell Dev Biol* **44**, 115–125 (2015).
146. Tremblay, P. *et al.* A Crucial Role forPax3in the Development of the Hypaxial Musculature and the Long-Range Migration of Muscle Precursors. *Dev Biol* **203**, 49–61 (1998).
147. Bober, E., Franz, T., Arnold, H.-H., Gruss, P. & Tremblay, P. *Pax-3* is required for the development of limb muscles: a possible role for the migration of dermomyotomal muscle progenitor cells. *Development* **120**, 603–612 (1994).
148. Huang, R. & Christ, B. Origin of the epaxial and hypaxial myotome in avian embryos. *Anat Embryol (Berl)* **202**, 369–374 (2000).
149. Marcelle, C., Wolf, J. & Bronner-Fraser, M. Thein VivoExpression of the FGF Receptor FREK mRNA in Avian Myoblasts Suggests a Role in Muscle Growth and Differentiation. *Dev Biol* **172**, 100–114 (1995).
150. Cusella-De Angelis, M. G. *et al.* MyoD, myogenin independent differentiation of primordial myoblasts in mouse somites. *J Cell Biol* **116**, 1243–1255 (1992).
151. Chal, J. & Pourquié, O. Making muscle: skeletal myogenesis *in vivo* and *in vitro*. *Development* **144**, 2104–2122 (2017).
152. Fürst, D. O., Osborn, M. & Weber, K. Myogenesis in the mouse embryo: differential onset of expression of myogenic proteins and the involvement of titin in myofibril assembly. *J Cell Biol* **109**, 517–527 (1989).
153. Gros, J., Serralbo, O. & Marcelle, C. WNT11 acts as a directional cue to organize the elongation of early muscle fibres. *Nature* **457**, 589–593 (2009).
154. Lee, A. S. J. *et al.* Initiation of primary myogenesis in amniote limb muscles. *Developmental Dynamics* **242**, 1043–1055 (2013).
155. Quinn, M. E. *et al.* Myomerger induces fusion of non-fusogenic cells and is required for skeletal muscle development. *Nat Commun* **8**, 15665 (2017).
156. Sieiro-Mosti, D., De La Celle, M., Pelé, M. & Marcelle, C. A dynamic analysis of muscle fusion in the chick embryo. *Development* **141**, 3605–3611 (2014).
157. Draeger, A., Weeds, A. G. & Fitzsimons, R. B. Primary, secondary and tertiary myotubes in developing skeletal muscle: A new approach to the analysis of human myogenesis. *J Neurol Sci* **81**, 19–43 (1987).
158. Chal, J. & Pourquié, O. Making muscle: skeletal myogenesis *in vivo* and *in vitro*. *Development* **144**, 2104–2122 (2017).

159. Cossu, G. & Biressi, S. Satellite cells, myoblasts and other occasional myogenic progenitors: Possible origin, phenotypic features and role in muscle regeneration. *Semin Cell Dev Biol* **16**, 623–631 (2005).
160. DeNardi, C. *et al.* Type 2X-myosin heavy chain is coded by a muscle fiber type-specific and developmentally regulated gene. *J Cell Biol* **123**, 823–835 (1993).
161. Rowe, R. W. & Goldspink, G. Muscle fibre growth in five different muscles in both sexes of mice. *J Anat* **104**, 519–30 (1969).
162. Gros, J., Manceau, M., Thomé, V. & Marcelle, C. A common somitic origin for embryonic muscle progenitors and satellite cells. *Nature* **435**, 954–958 (2005).
163. Murach, K. A. *et al.* Fusion-Independent Satellite Cell Communication to Muscle Fibers During Load-Induced Hypertrophy. *Function* **1**, (2020).
164. Allbrook, D. B., Han, M. F. & Hellmuth, A. E. Population of muscle satellite cells in relation to age and mitotic activity. *Pathology* **3**, 233–243 (1971).
165. Wang, H., Noulet, F., Edom-Vovard, F., Le Grand, F. & Duprez, D. Bmp Signaling at the Tips of Skeletal Muscles Regulates the Number of Fetal Muscle Progenitors and Satellite Cells during Development. *Dev Cell* **18**, 643–654 (2010).
166. Wozniak, A. C. & Anderson, J. E. Nitric oxide-dependence of satellite stem cell activation and quiescence on normal skeletal muscle fibers. *Developmental Dynamics* **236**, 240–250 (2007).
167. Le Grand, F. & Rudnicki, M. A. Skeletal muscle satellite cells and adult myogenesis. *Curr Opin Cell Biol* **19**, 628–633 (2007).
168. Yang, D., Morris, S. F. & Sigurdson, L. The sartorius muscle: anatomic considerations for reconstructive surgeons. *Surgical and Radiologic Anatomy* **20**, 307–310 (1999).
169. Frontera, W. R. & Ochala, J. Skeletal Muscle: A Brief Review of Structure and Function. *Calcif Tissue Int* **96**, 183–195 (2015).
170. Klein, C. S., Marsh, G. D., Petrella, R. J. & Rice, C. L. Muscle fiber number in the biceps brachii muscle of young and old men. *Muscle Nerve* **28**, 62–68 (2003).
171. Sjöström, M., Lexell, J. & Downham, D. Y. Differences in fiber number and fiber type proportion within fascicles. A quantitative morphological study of whole vastus lateralis muscle from childhood to old age. *Anat Rec* **234**, 183–189 (1992).
172. Fujii, K. & Murota, K. Isolation of skeletal muscle collagen. *Anal Biochem* **127**, 449–452 (1982).
173. Duance, V. C., Restall, D. J., Beard, H., Bourne, F. J. & Bailey, A. J. The location of three collagen types in skeletal muscle. *FEBS Lett* **79**, 248–252 (1977).
174. Binder-Markey, B. I., Broda, N. M. & Lieber, R. L. Intramuscular Anatomy Drives Collagen Content Variation Within and Between Muscles. *Front Physiol* **11**, (2020).
175. Gillies, A. R. & Lieber, R. L. Structure and function of the skeletal muscle extracellular matrix. *Muscle Nerve* **44**, 318–331 (2011).
176. Azizi, E., Brainerd, E. L. & Roberts, T. J. Variable gearing in pennate muscles. *Proceedings of the National Academy of Sciences* **105**, 1745–1750 (2008).
177. Ward, S. R., Eng, C. M., Smallwood, L. H. & Lieber, R. L. Are current measurements of lower extremity muscle architecture accurate? *Clin Orthop Relat Res* **467**, 1074–82 (2009).
178. Rantanen, J., Rissanen, A. & Kalimo, H. Lumbar muscle fiber size and type distribution in normal subjects. *European Spine Journal* **3**, 331–335 (1994).
179. Cardasis, C. A. & Cooper, G. W. An analysis of nuclear numbers in individual muscle fibers during differentiation and growth: A satellite cell-muscle fiber growth unit. *Journal of Experimental Zoology* **191**, 347–357 (1975).
180. Cristea, A. *et al.* Effects of aging and gender on the spatial organization of nuclei in single human skeletal muscle cells. *Aging Cell* **9**, 685–697 (2010).
181. Hansson, K.-A. *et al.* Myonuclear content regulates cell size with similar scaling properties in mice and humans. *Nat Commun* **11**, 6288 (2020).
182. Bruusgaard, J. C., Liestøl, K., Ekmark, M., Kollstad, K. & Gundersen, K. Number and spatial distribution of nuclei in the muscle fibres of normal mice studied *in vivo*. *J Physiol* **551**, 467–478 (2003).
183. Goldspink, G. The proliferation of myofibrils during muscle fibre growth. *J Cell Sci* **6**, 593–603 (1970).
184. Kaisto, T. Distribution of the endoplasmic reticulum and its relationship with the sarcoplasmic reticulum in skeletal myofibers. *Exp Cell Res* **289**, 47–57 (2003).

185. Huxley, H. E. & Hanson, J. THE STRUCTURAL BASIS OF THE CONTRACTION MECHANISM IN STRIATED MUSCLE. *Ann N Y Acad Sci* **81**, 403–408 (1959).
186. HUXLEY, H. & HANSON, J. Changes in the Cross-Striations of Muscle during Contraction and Stretch and their Structural Interpretation. *Nature* **173**, 973–976 (1954).
187. HUXLEY, A. F. & NIEDERGERKE, R. Structural Changes in Muscle During Contraction: Interference Microscopy of Living Muscle Fibres. *Nature* **173**, 971–973 (1954).
188. Fredericq, L. *Génération et Structure Du Tissu Musculaire*. (Lesigne, 1875).
189. Roth, S. M. *et al.* Skeletal muscle satellite cell populations in healthy young and older men and women. *Anat Rec* **260**, 351–358 (2000).
190. Gibson, M. C. & Schultz, E. Age-related differences in absolute numbers of skeletal muscle satellite cells. *Muscle Nerve* **6**, 574–580 (1983).
191. Allouh, M. Z., Yablonka-Reuveni, Z. & Rosser, B. W. C. Pax7 Reveals a Greater Frequency and Concentration of Satellite Cells at the Ends of Growing Skeletal Muscle Fibers. *Journal of Histochemistry & Cytochemistry* **56**, 77–87 (2008).
192. Christov, C. *et al.* Muscle Satellite Cells and Endothelial Cells: Close Neighbors and Privileged Partners. *Mol Biol Cell* **18**, 1397–1409 (2007).
193. Groen, B. B. L. *et al.* Skeletal muscle capillary density and microvascular function are compromised with aging and type 2 diabetes. *J Appl Physiol* **116**, 998–1005 (2014).
194. Gatchalian, C. L., Schachner, M. & Sanes, J. R. Fibroblasts that proliferate near denervated synaptic sites in skeletal muscle synthesize the adhesive molecules tenascin(J1), N-CAM, fibronectin, and a heparan sulfate proteoglycan. *J Cell Biol* **108**, 1873–1890 (1989).
195. Davis-Dusenbery, B. N., Williams, L. A., Klim, J. R. & Eggan, K. How to make spinal motor neurons. *Development* **141**, 491–501 (2014).
196. Herzog, W. & Schappacher-Tilp, G. Molecular mechanisms of muscle contraction: A historical perspective. *J Biomech* **155**, 111659 (2023).
197. Toledo-Pereyra, L. H. *De Humani Corporis Fabrica* Surgical Revolution. *Journal of Investigative Surgery* **21**, 232–236 (2008).
198. Malmivuo, J. A., Honkonen, J. & Wendel, K. E. Did Jan Swammerdam Do the First Electric Stimulation over 100 Years before Luigi Galvani? in 13–16 (2014). doi:10.1007/978-3-319-00846-2_3.
199. William Croone's theory of muscular contraction. *Notes Rec R Soc Lond* **16**, 158–178 (1961).
200. Galvani, L. De viribus electricitatis in motu musculari. Commentarius. *De Bonoiensi Scientiarum et Artium Intituo atque Academie Commentarii* **7**, 363–418 (1791).
201. A Treatise upon the Electro-Physiological Phenomena of Animals. *Med Chir Rev* **1**, 305–321 (1845).
202. The Van Leeuwenhoek Specimens. *Notes Rec R Soc Lond* **36**, 37–59 (1981).
203. Rall, J. A. *Mechanism of Muscular Contraction*. (2014).
204. Kühne, W. *Untersuchungen Über Das Protoplasma Und Die Contractilität*. (W. Engelmann, 1864).
205. Szent-Györgyi, A. G. The early history of the biochemistry of muscle contraction. *J Gen Physiol* **123**, 631–41 (2004).
206. HUXLEY, H. E. The double array of filaments in cross-striated muscle. *J Biophys Biochem Cytol* **3**, 631–48 (1957).
207. Huxley, H. E. The Mechanism of Muscular Contraction. *Science (1979)* **164**, 1356–1366 (1969).
208. Kron, S. J. & Spudich, J. A. Fluorescent actin filaments move on myosin fixed to a glass surface. *Proceedings of the National Academy of Sciences* **83**, 6272–6276 (1986).
209. Finer, J. T., Simmons, R. M. & Spudich, J. A. Single myosin molecule mechanics: piconewton forces and nanometre steps. *Nature* **368**, 113–119 (1994).
210. Rayment, I. *et al.* Three-dimensional structure of myosin subfragment-1: a molecular motor. *Science (1979)* **261**, 50–58 (1993).
211. Lehman, W., Craig, R. & Vibert, P. Ca2+-induced tropomyosin movement in Limulus thin filaments revealed by three-dimensional reconstruction. *Nature* **368**, 65–67 (1994).
212. Harrison, R. G. The cultivation of tissues in extraneous media as a method of morpho-genetic study. *Anat Rec* **6**, 181–193 (1912).
213. Weiss, P. Cell Contact. in 391–423 (1958). doi:10.1016/S0074-7696(08)62692-3.
214. Walboomers, X. F., Ginsel, L. A. & Jansen, J. A. Early spreading events of fibroblasts on microgrooved substrates. *J Biomed Mater Res* **51**, 529–534 (2000).

215. DENBRABER, E., DERUIJTER, J., GINSEL, L., VONRECUM, A. & JANSEN, J. Quantitative analysis of fibroblast morphology on microgrooved surfaces with various groove and ridge dimensions. *Biomaterials* **17**, 2037–2044 (1996).
216. van Delft, F. C. M. J. M. *et al.* Manufacturing substrate nano-grooves for studying cell alignment and adhesion. *Microelectron Eng* **85**, 1362–1366 (2008).
217. Lücker, P. B. *et al.* A microgroove patterned multiwell cell culture plate for high-throughput studies of cell alignment. *Biotechnol Bioeng* **111**, 2537–2548 (2014).
218. Hsu, S., Chen, C., Lu, P. S., Lai, C. & Chen, C. Oriented Schwann cell growth on microgrooved surfaces. *Biotechnol Bioeng* **92**, 579–588 (2005).
219. Wang, X. *et al.* Drop-shaped microgrooves guide unidirectional cell migration for enhanced endothelialization. *Nat Commun* **16**, 1928 (2025).
220. Gao, H. *et al.* Regulation of Myogenic Differentiation by Topologically Microgrooved Surfaces for Skeletal Muscle Tissue Engineering. *ACS Omega* **6**, 20931–20940 (2021).
221. Yang, H. S. *et al.* Nanopatterned muscle cell patches for enhanced myogenesis and dystrophin expression in a mouse model of muscular dystrophy. *Biomaterials* **35**, 1478–1486 (2014).
222. Daly, A. C., Davidson, M. D. & Burdick, J. A. 3D bioprinting of high cell-density heterogeneous tissue models through spheroid fusion within self-healing hydrogels. *Nat Commun* **12**, 753 (2021).
223. Ahrens, J. H. *et al.* Programming Cellular Alignment in Engineered Cardiac Tissue via Bioprinting Anisotropic Organ Building Blocks. *Advanced Materials* **34**, (2022).
224. Nguyen, M.-L. *et al.* Studying the impact of geometrical and cellular cues on myogenesis with a skeletal muscle-on-chip. *Lab Chip* (2024) doi:10.1039/D4LC00417E.
225. You, Y. *et al.* Lung-on-a-chip composed of styrene-butadiene-styrene nano-fiber/porous PDMS composite membranes with cyclic triaxial stimulation. *Microfluid Nanofluidics* **28**, 45 (2024).
226. Williams, C. *et al.* Aligned cell sheets grown on thermo-responsive substrates with microcontact printed protein patterns. *Advanced Materials* **21**, 2161–2164 (2009).
227. Wheeler, B. C., Corey, J. M., Brewer, G. J. & Branch, D. W. Microcontact Printing for Precise Control of Nerve Cell Growth in Culture. *J Biomech Eng* **121**, 73–78 (1999).
228. Takahashi, H., Shimizu, T., Nakayama, M., Yamato, M. & Okano, T. The use of anisotropic cell sheets to control orientation during the self-organization of 3D muscle tissue. *Biomaterials* **34**, 7372–7380 (2013).
229. Okeyo, K. O., Kibe, Y. & Adachi, T. Controlling macroscale cell alignment in self-organized cell sheets by tuning the microstructure of adhesion-limiting micromesh scaffolds. *Mater Today Adv* **12**, 100194 (2021).
230. Allan, S. J., Ellis, M. J. & De Bank, P. A. Decellularized grass as a sustainable scaffold for skeletal muscle tissue engineering. *J Biomed Mater Res A* **109**, 2471–2482 (2021).
231. Gosselin, E. A. *et al.* Multi-layered silk film coculture system for human corneal epithelial and stromal stem cells. *J Tissue Eng Regen Med* **12**, 285–295 (2018).
232. Wang, S. *et al.* In vitro 3D corneal tissue model with epithelium, stroma, and innervation. *Biomaterials* **112**, 1–9 (2017).
233. Kilic, C., Girotti, A., Rodriguez-Cabello, J. C. & Hasirci, V. A collagen-based corneal stroma substitute with micro-designed architecture. *Biomater. Sci.* **2**, 318–329 (2014).
234. Takahashi, H., Nakayama, M., Shimizu, T., Yamato, M. & Okano, T. Anisotropic cell sheets for constructing three-dimensional tissue with well-organized cell orientation. *Biomaterials* **32**, 8830–8838 (2011).
235. Zhang, W. *et al.* Mechanically conditioned multilayered angle-ply collagen scaffolds promote annulus fibrosus regeneration. *Appl Mater Today* **31**, 101751 (2023).
236. Borem, R. *et al.* Angle-ply scaffold supports annulus fibrosus matrix expression and remodeling by mesenchymal stromal and annulus fibrosus cells. *J Biomed Mater Res B Appl Biomater* **110**, 1056–1068 (2022).
237. Liu, S. *et al.* Multiscale Anisotropic Scaffold Integrating 3D Printing and Electrospinning Techniques as a Heart-on-a-Chip Platform for Evaluating Drug-Induced Cardiotoxicity. *Adv Healthc Mater* **12**, (2023).
238. Eom, S. *et al.* Fabrication of an align-random distinct, heterogeneous nanofiber mat endowed with bifunctional properties for engineered 3D cardiac anisotropy. *Compos B Eng* **226**, 109336 (2021).
239. Chen, Y. *et al.* Bi-Layered Tubular Microfiber Scaffolds as Functional Templates for Engineering Human Intestinal Smooth Muscle Tissue. *Adv Funct Mater* **30**, (2020).

240. Kobayashi, M., Lei, N. Y., Wang, Q., Wu, B. M. & Dunn, J. C. Y. Orthogonally oriented scaffolds with aligned fibers for engineering intestinal smooth muscle. *Biomaterials* **61**, 75–84 (2015).
241. Williams, N. P. *et al.* Engineering anisotropic 3D tubular tissues with flexible thermoresponsive nanofabricated substrates. *Biomaterials* **240**, 119856 (2020).
242. Song, J. *et al.* Spiral-structured electrospun conductive conduits filled with aligned nanofibers for peripheral nerve regeneration. *Chemical Engineering Journal* **508**, 160899 (2025).
243. Golafshan, N., Kharaziha, M. & Alehosseini, M. A three-layered hollow tubular scaffold as an enhancement of nerve regeneration potential. *Biomedical Materials* **13**, 065005 (2018).
244. Wang, J. *et al.* Bioinspired Multichannel Nerve Guidance Conduit Based on Shape Memory Nanofibers for Potential Application in Peripheral Nerve Repair. *ACS Nano* **14**, 12579–12595 (2020).
245. Amagat, J. *et al.* Self-snapping hydrogel-based electroactive microchannels as nerve guidance conduits. *Mater Today Bio* **16**, 100437 (2022).
246. Zhang, Z. *et al.* 3D anisotropic photocatalytic architectures as bioactive nerve guidance conduits for peripheral neural regeneration. *Biomaterials* **253**, 120108 (2020).
247. Wang, X. *et al.* Biomimetic multi-channel nerve conduits with micro/nanostructures for rapid nerve repair. *Bioact Mater* **41**, 577–596 (2024).
248. Kim, J. A. *et al.* High-throughput generation of spheroids using magnetic nanoparticles for three-dimensional cell culture. *Biomaterials* **34**, 8555–8563 (2013).
249. Lu, Q. *et al.* Nerve Guidance Conduits with Hierarchical Anisotropic Architecture for Peripheral Nerve Regeneration. *Adv Healthc Mater* **10**, (2021).
250. Perez, J. E., Nagle, I. & Wilhelm, C. Magnetic molding of tumor spheroids: emerging model for cancer screening. *Biofabrication* **13**, 015018 (2021).
251. Labusca, L. *et al.* Magnetic nanoparticle loaded human adipose derived mesenchymal cells spheroids in levitated culture. *J Biomed Mater Res B Appl Biomater* **109**, 630–642 (2021).
252. Raghavan, S. *et al.* Comparative analysis of tumor spheroid generation techniques for differential *in vitro* drug toxicity. *Oncotarget* **7**, 16948–16961 (2016).
253. Liu, D., Chen, S. & Win Naing, M. A review of manufacturing capabilities of cell spheroid generation technologies and future development. *Biotechnol Bioeng* **118**, 542–554 (2021).
254. Van de Walle, A. *et al.* Real-time in situ magnetic measurement of the intracellular biodegradation of iron oxide nanoparticles in a stem cell-spheroid tissue model. *Nano Res* **13**, 467–476 (2020).
255. Whatley, B. R., Li, X., Zhang, N. & Wen, X. Magnetic-directed patterning of cell spheroids. *J Biomed Mater Res A* **102**, 1537–1547 (2014).
256. Ayan, B. *et al.* Aspiration-assisted bioprinting for precise positioning of biologics. *Sci Adv* **6**, (2020).
257. Ergene, E., Liman, G., Yilgor, P. & Demirel, G. Magnetically Actuated GelMA-Based Scaffolds as a Strategy to Generate Complex Bioprinted Tissues. *Adv Mater Technol* (2024) doi:10.1002/admt.202400119.
258. Neal, D., Sakar, M. S., Ong, L.-L. S. & Harry Asada, H. Formation of elongated fascicle-inspired 3D tissues consisting of high-density, aligned cells using sacrificial outer molding. *Lab Chip* **14**, 1907–1916 (2014).
259. Kim, H., Osaki, T., Kamm, R. D. & Asada, H. H. Multiscale engineered human skeletal muscles with perfusable vasculature and microvascular network recapitulating the fluid compartments. *Biofabrication* **15**, 015005 (2023).
260. Huang, Y.-C., Dennis, R. G., Larkin, L. & Baar, K. Rapid formation of functional muscle in vitro using fibrin gels. *J Appl Physiol* **98**, 706–713 (2005).
261. Powell, C. A., Smiley, B. L., Mills, J. & Vandenburgh, H. H. Mechanical stimulation improves tissue-engineered human skeletal muscle. *American Journal of Physiology-Cell Physiology* **283**, C1557–C1565 (2002).
262. Osaki, T., Uzel, S. G. M. & Kamm, R. D. Microphysiological 3D model of amyotrophic lateral sclerosis (ALS) from human iPS-derived muscle cells and optogenetic motor neurons. *Sci Adv* **4**, (2018).
263. Rose, N. *et al.* Bioengineering a miniaturized in vitro 3D myotube contraction monitoring chip to model muscular dystrophies. *Biomaterials* **293**, 121935 (2023).
264. Sakar, M. S. *et al.* Formation and optogenetic control of engineered 3D skeletal muscle bioactuators. *Lab Chip* **12**, 4976 (2012).

265. Matsumoto, T. *et al.* Three-Dimensional Cell and Tissue Patterning in a Strained Fibrin Gel System. *PLoS One* **2**, e1211 (2007).
266. Heher, P. *et al.* A novel bioreactor for the generation of highly aligned 3D skeletal muscle-like constructs through orientation of fibrin via application of static strain. *Acta Biomater* **24**, 251–265 (2015).
267. Aguilar-Agon, K. W., Capel, A. J., Martin, N. R. W., Player, D. J. & Lewis, M. P. Mechanical loading stimulates hypertrophy in tissue-engineered skeletal muscle: Molecular and phenotypic responses. *J Cell Physiol* **234**, 23547–23558 (2019).
268. Rao, L., Qian, Y., Khodabukus, A., Ribar, T. & Bursac, N. Engineering human pluripotent stem cells into a functional skeletal muscle tissue. *Nat Commun* **9**, 126 (2018).
269. van der Wal, E. *et al.* Highly contractile 3D tissue engineered skeletal muscles from human iPSCs reveal similarities with primary myoblast-derived tissues. *Stem Cell Reports* **18**, 1954–1971 (2023).
270. Afshar, M. E. *et al.* A 96-well culture platform enables longitudinal analyses of engineered human skeletal muscle microtissue strength. *Sci Rep* **10**, 6918 (2020).
271. Tiburcy, M. *et al.* Regeneration competent satellite cell niches in rat engineered skeletal muscle. *FASEB Bioadv* **1**, 731–746 (2019).
272. Mills, R. J. *et al.* Development of a human skeletal micro muscle platform with pacing capabilities. *Biomaterials* **198**, 217–227 (2019).
273. Yamamoto, Y. *et al.* Preparation of artificial skeletal muscle tissues by a magnetic force-based tissue engineering technique. *J Biosci Bioeng* **108**, 538–543 (2009).
274. Hu, H. *et al.* Synergic effect of magnetic nanoparticles on the electrospun aligned superparamagnetic nanofibers as a potential tissue engineering scaffold. *RSC Adv.* **3**, 879–886 (2013).
275. Luo, Z. *et al.* Vertical Extrusion Cryo(bio)printing for Anisotropic Tissue Manufacturing. *Advanced Materials* **34**, (2022).
276. Shao, L. *et al.* Omnidirectional anisotropic embedded 3D bioprinting. *Mater Today Bio* **27**, 101160 (2024).
277. Li, T. *et al.* Bioprinted anisotropic scaffolds with fast stress relaxation bioink for engineering 3D skeletal muscle and repairing volumetric muscle loss. *Acta Biomater* **156**, 21–36 (2023).
278. Hwangbo, H., Chae, S., Ryu, D. & Kim, G. In situ magnetic-field-assisted bioprinting process using magnetorheological bioink to obtain engineered muscle constructs. *Bioact Mater* **45**, 417–433 (2025).
279. Ajiteru, O. *et al.* A digital light processing 3D printed magnetic bioreactor system using silk magnetic bioink. *Biofabrication* **13**, 034102 (2021).
280. Candiani, G. *et al.* Cyclic mechanical stimulation favors myosin heavy chain accumulation in engineered skeletal muscle constructs. *J Appl Biomater Biomech* **8**, 68–75 (2010).
281. Armstrong, J. P. K. *et al.* Engineering Anisotropic Muscle Tissue using Acoustic Cell Patterning. *Adv Mater* **30**, e1802649 (2018).
282. Liang, Q. *et al.* Biomimetic Versatile Anisotropic, Electroactive Cellulose Hydrogel Scaffolds Tailored from Fern Stem Serving as Nerve Conduit and Cardiac Patch. *Advanced Science* **12**, (2025).
283. Zhang, B. *et al.* Biodegradable scaffold with built-in vasculature for organ-on-a-chip engineering and direct surgical anastomosis. *Nat Mater* **15**, 669–678 (2016).
284. Fang, Y., Zhang, T., Zhang, L., Gong, W. & Sun, W. Biomimetic design and fabrication of scaffolds integrating oriented micro-pores with branched channel networks for myocardial tissue engineering. *Biofabrication* **11**, 035004 (2019).
285. Engelmayr, G. C. *et al.* Accordion-like honeycombs for tissue engineering of cardiac anisotropy. *Nat Mater* **7**, 1003–1010 (2008).
286. Weber, M. *et al.* Multiple-Step Injection Molding for Fibrin-Based Tissue-Engineered Heart Valves. *Tissue Eng Part C Methods* **21**, 832–840 (2015).
287. Tijore, A. *et al.* Contact guidance for cardiac tissue engineering using 3D bioprinted gelatin patterned hydrogel. *Biofabrication* **10**, 025003 (2018).
288. Zhang, Y. S. *et al.* Bioprinting 3D microfibrous scaffolds for engineering endothelialized myocardium and heart-on-a-chip. *Biomaterials* **110**, 45–59 (2016).
289. Bera, A. K., Rizvi, M. S., KN, V. & Pati, F. Engineering anisotropic tissue analogues: harnessing synergistic potential of extrusion-based bioprinting and extracellular matrix-based bioink. *Biofabrication* **17**, 015003 (2025).

290. Xie, R. *et al.* Magnetically driven formation of 3D freestanding soft bioscaffolds. *Sci Adv* **10**, (2024).
291. Cui, H. *et al.* 3D printing of thick myocardial tissue constructs with anisotropic myofibers and perfusable vascular channels. *Biomaterials Advances* **153**, 213579 (2023).
292. Backman, D. E., LeSavage, B. L., Shah, S. B. & Wong, J. Y. A Robust Method to Generate Mechanically Anisotropic Vascular Smooth Muscle Cell Sheets for Vascular Tissue Engineering. *Macromol Biosci* **17**, (2017).
293. Tseng, H. *et al.* A high-throughput in vitro ring assay for vasoactivity using magnetic 3D bioprinting. *Sci Rep* **6**, 30640 (2016).
294. Lee, S., Tong, X., Han, L.-H., Behn, A. & Yang, F. Winner of the Young Investigator Award of the Society for Biomaterials (USA) for 2016, 10th World Biomaterials Congress, May 17-22, 2016, Montreal QC, Canada: Aligned microribbon-like hydrogels for guiding three-dimensional smooth muscle tissue regeneration. *J Biomed Mater Res A* **104**, 1064–71 (2016).
295. Williams, C. & Wick, T. M. Endothelial Cell–Smooth Muscle Cell Co-Culture in a Perfusion Bioreactor System. *Ann Biomed Eng* **33**, 920–928 (2005).
296. Wu, S. *et al.* Fabrication of Aligned Nanofiber Polymer Yarn Networks for Anisotropic Soft Tissue Scaffolds. *ACS Appl Mater Interfaces* **8**, 16950–16960 (2016).
297. Luo, Y. *et al.* Fabrication of 3D Biomimetic Smooth Muscle Using Magnetic Induction and Bioprinting for Tissue Regeneration. *Biomater Res* **28**, (2024).
298. Mattix, B. M. *et al.* Janus magnetic cellular spheroids for vascular tissue engineering. *Biomaterials* **35**, 949–960 (2014).
299. He, Y. J. *et al.* Cell-Laden Gradient Hydrogel Scaffolds for Neovascularization of Engineered Tissues. *Adv Healthc Mater* **10**, (2021).
300. Perea, H., Aigner, J., Hopfner, U. & Wintermantel, E. Direct Magnetic Tubular Cell Seeding: A Novel Approach for Vascular Tissue Engineering. *Cells Tissues Organs* **183**, 156–165 (2006).
301. Pinon, L. *et al.* Infection-on-Chip: an *in vitro* human vessel model to study *Neisseria meningitidis* colonization and vascular damages. Preprint at https://doi.org/10.1101/2024.02.09.579276 (2024).
302. Lansche, C. *et al.* Bioengineering a Patient-Derived Vascularized Lung Tumor-on-Chip Model to Decipher Immunomodulation by the Endothelium. *Adv Healthc Mater* e2403446 (2025) doi:10.1002/adhm.202403446.
303. Sundararaghavan, H. G., Saunders, R. L., Hammer, D. A. & Burdick, J. A. Fiber alignment directs cell motility over chemotactic gradients. *Biotechnol Bioeng* **110**, 1249–1254 (2013).
304. Ren, X. *et al.* Investigations on T cell transmigration in a human skin-on-chip (SoC) model. *Lab Chip* **21**, 1527–1539 (2021).
305. Wu, Z. *et al.* Microfluidic Printing of Tunable Hollow Microfibers for Vascular Tissue Engineering. *Adv Mater Technol* **6**, (2021).
306. Chen, L. *et al.* Micro-and-nanometer topological gradient of block copolymer fibrous scaffolds towards region-specific cell regulation. *J Colloid Interface Sci* **606**, 248–260 (2022).
307. Sundararaghavan, H. G. & Burdick, J. A. Gradients with Depth in Electrospun Fibrous Scaffolds for Directed Cell Behavior. *Biomacromolecules* **12**, 2344–2350 (2011).
308. Shao, L., Hou, R., Zhu, Y. & Yao, Y. Pre-shear bioprinting of highly oriented porous hydrogel microfibers to construct anisotropic tissues. *Biomater Sci* **9**, 6763–6771 (2021).
309. LaBelle, S. A. *et al.* Matrix anisotropy promotes angiogenesis in a density-dependent manner. *American Journal of Physiology-Heart and Circulatory Physiology* **322**, H806–H818 (2022).
310. Li, K. *et al.* Oriented/dual-gradient in structure and mechanics chitosan hydrogel bio-films based on stretching for guiding cell orientation. *Compos B Eng* **232**, 109616 (2022).
311. Shao, M., Liu, X., Zheng, T., Fu, Y. & Wang, C. Acoustofluidics enables direct ink writing of vascular scaffolds with intrinsically patterned porous microstructures. *Chemical Engineering Journal* **492**, 152258 (2024).
312. Fan, Z. *et al.* Anisotropic silk nanofiber layers as regulators of angiogenesis for optimized bone regeneration. *Mater Today Bio* **15**, 100283 (2022).
313. Han, Q. *et al.* Anisotropic topological scaffolds synergizing non-invasive wireless magnetic stimulation for accelerating long-distance peripheral nerve regeneration. *Chemical Engineering Journal* **496**, 153809 (2024).
314. Roth, J. G. *et al.* Spatially controlled construction of assembloids using bioprinting. *Nat Commun* **14**, 4346 (2023).

315. Lacko, C. S. *et al.* Magnetic particle templating of hydrogels: engineering naturally derived hydrogel scaffolds with 3D aligned microarchitecture for nerve repair. *J Neural Eng* **17**, 016057 (2020).
316. Perez, J. E., Jan, A., Villard, C. & Wilhelm, C. Surface Tension and Neuronal Sorting in Magnetically Engineered Brain-Like Tissue. *Advanced Science* **10**, (2023).
317. Ghaderinejad, P. *et al.* An injectable anisotropic alginate hydrogel containing oriented fibers for nerve tissue engineering. *Chemical Engineering Journal* **420**, 130465 (2021).
318. Yang, C.-Y. *et al.* Engineering neuroregenerative microenvironment via aligned hydrogel-assisted magnetic stimulation for complete spinal cord injury repair. *Engineered Regeneration* **5**, 139–152 (2024).
319. Xie, X. *et al.* A woven scaffold with continuous mineral gradients for tendon-to-bone tissue engineering. *Compos B Eng* **212**, 108679 (2021).
320. Fan, Z. *et al.* Simulation of Cortical and Cancellous Bone to Accelerate Tissue Regeneration. *Adv Funct Mater* **33**, (2023).
321. Nedjari, S., Awaja, F. & Altankov, G. Three Dimensional Honeycomb Patterned Fibrinogen Based Nanofibers Induce Substantial Osteogenic Response of Mesenchymal Stem Cells. *Sci Rep* **7**, 15947 (2017).
322. Yang, J. *et al.* Microfluidic bone chip to study osteogenesis of porous substrate topographies in normal and osteoporotic microenvironments. *Eur Cell Mater* **47**, 238–252 (2024).
323. Kosmidis Papadimitriou, A. *et al.* Fabrication of gradient hydrogels using a thermophoretic approach in microfluidics. *Biofabrication* **16**, 025023 (2024).
324. Reyes, R. L. *et al.* Development and assessment of modified-honeycomb-structure scaffold for bone tissue engineering. *Addit Manuf* **54**, 102740 (2022).
325. Zhang, Y. *et al.* 3D-bioprinted anisotropic bicellular living hydrogels boost osteochondral regeneration via reconstruction of cartilage–bone interface. *The Innovation* **5**, 100542 (2024).
326. Eckstein, K. N. *et al.* Controlled Mechanical Property Gradients Within a Digital Light Processing Printed Hydrogel-Composite Osteochondral Scaffold. *Ann Biomed Eng* **52**, 2162–2177 (2024).
327. Wei, X. *et al.* Hierarchically Biomimetic Scaffolds with Anisotropic Micropores and Nanotopological Patterns to Promote Bone Regeneration via Geometric Modulation. *Adv Healthc Mater* **13**, (2024).
328. Maleki, H. *et al.* Mechanically Strong Silica-Silk Fibroin Bioaerogel: A Hybrid Scaffold with Ordered Honeycomb Micromorphology and Multiscale Porosity for Bone Regeneration. *ACS Appl Mater Interfaces* **11**, 17256–17269 (2019).
329. Tseng, H. *et al.* Assembly of a Three-Dimensional Multitype Bronchiole Coculture Model Using Magnetic Levitation. *Tissue Eng Part C Methods* **19**, 665–675 (2013).
330. Baptista, D. *et al.* 3D alveolar in vitro model based on epithelialized biomimetically curved culture membranes. *Biomaterials* **266**, 120436 (2021).
331. Roy, A. *et al.* Programmable Tissue Folding Patterns in Structured Hydrogels. *Advanced Materials* **36**, (2024).
332. Zamprogno, P. *et al.* Second-generation lung-on-a-chip with an array of stretchable alveoli made with a biological membrane. *Commun Biol* **4**, 168 (2021).
333. Fayol, D. *et al.* Use of Magnetic Forces to Promote Stem Cell Aggregation During Differentiation, and Cartilage Tissue Modeling. *Advanced Materials* **25**, 2611–2616 (2013).
334. Parfenov, V. A. *et al.* Scaffold-free, label-free and nozzle-free biofabrication technology using magnetic levitational assembly. *Biofabrication* **10**, 034104 (2018).
335. Zhu, D., Tong, X., Trinh, P. & Yang, F. Mimicking Cartilage Tissue Zonal Organization by Engineering Tissue-Scale Gradient Hydrogels as 3D Cell Niche. *Tissue Eng Part A* **24**, 1–10 (2018).
336. Liu, E., Zhu, D., Gonzalez Diaz, E., Tong, X. & Yang, F. Gradient Hydrogels for Optimizing Niche Cues to Enhance Cell-Based Cartilage Regeneration. *Tissue Eng Part A* **27**, 929–939 (2021).
337. Xu, J. *et al.* Continuous magnetic-gradient hydrogel with augmented mechanical span and reverse-directional polysaccharides distribution for integrated repair of osteochondral defects. *Compos B Eng* **298**, 112361 (2025).
338. Prendergast, M. E., Heo, S.-J., Mauck, R. L. & Burdick, J. A. Suspension bath bioprinting and maturation of anisotropic meniscal constructs. *Biofabrication* **15**, 035003 (2023).
339. Barceló, X., Eichholz, K. F., Gonçalves, I. F., Garcia, O. & Kelly, D. J. Bioprinting of structurally organized meniscal tissue within anisotropic melt electrowritten scaffolds. *Acta Biomater* **158**, 216–227 (2023).

340. Rhee, S., Puetzer, J. L., Mason, B. N., Reinhart-King, C. A. & Bonassar, L. J. 3D Bioprinting of Spatially Heterogeneous Collagen Constructs for Cartilage Tissue Engineering. *ACS Biomater Sci Eng* **2**, 1800–1805 (2016).
341. Sun, Y. *et al.* 3D-bioprinting ready-to-implant anisotropic menisci recapitulate healthy meniscus phenotype and prevent secondary joint degeneration. *Theranostics* **11**, 5160–5173 (2021).
342. Gurkan, U. A. *et al.* Engineering Anisotropic Biomimetic Fibrocartilage Microenvironment by Bioprinting Mesenchymal Stem Cells in Nanoliter Gel Droplets. *Mol Pharm* **11**, 2151–2159 (2014).
343. Scalzone, A., Imparato, G., Urciuolo, F. & Netti, P. A. Bioprinting of human dermal microtissues precursors as building blocks for endogenous in vitro connective tissue manufacturing. *Biofabrication* **16**, 035009 (2024).
344. Zhao, F. *et al.* Fibroblast alignment and matrix remodeling induced by a stiffness gradient in a skin-derived extracellular matrix hydrogel. *Acta Biomater* **182**, 67–80 (2024).
345. Ma, Y. *et al.* 3D bioprinting of a gradient stiffened gelatin–alginate hydrogel with adipose-derived stem cells for full-thickness skin regeneration. *J Mater Chem B* **11**, 2989–3000 (2023).
346. Shi, B. *et al.* Three-dimensional bioprinted cell-adaptive hydrogel with anisotropic micropores for enhancing skin wound healing. *Int J Biol Macromol* **280**, 136106 (2024).
347. Lu, G. *et al.* Anisotropic Biomimetic Silk Scaffolds for Improved Cell Migration and Healing of Skin Wounds. *ACS Appl Mater Interfaces* **10**, 44314–44323 (2018).
348. Gouveia, R. M. *et al.* Controlling the 3D architecture of Self-Lifting Auto-generated Tissue Equivalents (SLATEs) for optimized corneal graft composition and stability. *Biomaterials* **121**, 205–219 (2017).
349. Farasatkia, A. & Kharaziha, M. Robust and double-layer micro-patterned bioadhesive based on silk nanofibril/GelMA-alginate for stroma tissue engineering. *Int J Biol Macromol* **183**, 1013–1025 (2021).
350. Puistola, P., Miettinen, S., Skottman, H. & Mörö, A. Novel strategy for multi-material 3D bioprinting of human stem cell based corneal stroma with heterogenous design. *Mater Today Bio* **24**, 100924 (2024).
351. Kim, H. *et al.* Shear-induced alignment of collagen fibrils using 3D cell printing for corneal stroma tissue engineering. *Biofabrication* **11**, 035017 (2019).
352. Ghosh, A., Bera, A. K., Singh, V., Basu, S. & Pati, F. Bioprinting of anisotropic functional corneal stroma using mechanically robust multi-material bioink based on decellularized cornea matrix. *Biomaterials Advances* **165**, 214007 (2024).
353. Puistola, P. *et al.* Multi-material 3D bioprinting of human stem cells to engineer complex human corneal structures with stroma and epithelium. *Bioprinting* **46**, e00391 (2025).
354. Boland, T., Xu, T., Damon, B. & Cui, X. Application of inkjet printing to tissue engineering. *Biotechnol J* **1**, 910–917 (2006).
355. Mahdavi, S. S. *et al.* Stereolithography 3D Bioprinting Method for Fabrication of Human Corneal Stroma Equivalent. *Ann Biomed Eng* **48**, 1955–1970 (2020).
356. Liverani, C. *et al.* Investigating the Mechanobiology of Cancer Cell–ECM Interaction Through Collagen-Based 3D Scaffolds. *Cell Mol Bioeng* **10**, 223–234 (2017).
357. Fu, C.-Y., Lin, C.-Y., Chu, W.-C. & Chang, H.-Y. A Simple Cell Patterning Method Using Magnetic Particle-Containing Photosensitive Poly (Ethylene Glycol) Hydrogel Blocks: A Technical Note. *Tissue Eng Part C Methods* **17**, 871–877 (2011).
358. Ahmed, A. *et al.* Microengineered 3D Collagen Gels with Independently Tunable Fiber Anisotropy and Directionality. *Adv Mater Technol* **6**, (2021).
359. Soliman, B. G. *et al.* Droplet-based microfluidics for engineering shape-controlled hydrogels with stiffness gradient. *Biofabrication* **16**, 045026 (2024).
360. Hume, R. D. *et al.* Tumour cell invasiveness and response to chemotherapeutics in adipocyte invested 3D engineered anisotropic collagen scaffolds. *Sci Rep* **8**, 12658 (2018).
361. Tomba, C., Luchnikov, V., Barberi, L., Blanch-Mercader, C. & Roux, A. Epithelial cells adapt to curvature induction via transient active osmotic swelling. *Dev Cell* **57**, 1257-1270.e5 (2022).
362. Liu, Y. & Nisisako, T. Microfluidic generation of monodispersed Janus alginate hydrogel microparticles using water-in-oil emulsion reactant. *Biomicrofluidics* **16**, 024101 (2022).
363. Lapin, B. *et al.* Construction of a Multitubular Perfusable Kidney-on-Chip for the Study of Renal Diseases. in 85–106 (2023). doi:10.1007/978-1-0716-3179-9_7.
364. Myram, S. *et al.* A Multitubular Kidney-on-Chip to Decipher Pathophysiological Mechanisms in Renal Cystic Diseases. *Front Bioeng Biotechnol* **9**, (2021).

365. Rayner, S. G. *et al.* Multiphoton-Guided Creation of Complex Organ-Specific Microvasculature. *Adv Healthc Mater* **10**, (2021).
366. Pardo, A. *et al.* Magnetically-Assisted 3D Bioprinting of Anisotropic Tissue-Mimetic Constructs. *Adv Funct Mater* **32**, (2022).
367. Tindell, R. K., Busselle, L. P. & Holloway, J. L. Magnetic fields enable precise spatial control over electrospun fiber alignment for fabricating complex gradient materials. *J Biomed Mater Res A* **111**, 778–789 (2023).
368. Bahrami, S., Solouk, A., Duprez, D. & Mirzadeh, H. Microstructure Manipulation of Polyurethane-Based Macromolecular Scaffold for Tendon/Ligament Tissue Engineering. *Macromol Mater Eng* **307**, (2022).
369. Chansoria, P. & Shirwaiker, R. 3D bioprinting of anisotropic engineered tissue constructs with ultrasonically induced cell patterning. *Addit Manuf* **32**, 101042 (2020).
370. Jin, X. *et al.* Fabrication and characterization of an acellular annulus fibrosus scaffold with aligned porous construct for tissue engineering. *J Biomater Appl* **36**, 985–995 (2022).
371. Gluais, M. *et al.* In vitro and in vivo evaluation of an electrospun-aligned microfibrous implant for Annulus fibrosus repair. *Biomaterials* **205**, 81–93 (2019).
372. Moxon, S. R. *et al.* 3D bioprinting of an intervertebral disc tissue analogue with a highly aligned annulus fibrosus via suspended layer additive manufacture. *Biofabrication* **17**, 015005 (2025).
373. Jafari, J., Han, X., Palmer, J., Tran, P. A. & O'Connor, A. J. Remote Control in Formation of 3D Multicellular Assemblies Using Magnetic Forces. *ACS Biomater Sci Eng* **5**, 2532–2542 (2019).
374. Xu, F. *et al.* Three-Dimensional Magnetic Assembly of Microscale Hydrogels. *Advanced Materials* **23**, 4254–4260 (2011).
375. Tasoglu, S. *et al.* Magnetic Levitational Assembly for Living Material Fabrication. *Adv Healthc Mater* **4**, 1469–1476 (2015).
376. Tocchio, A. *et al.* Magnetically Guided Self-Assembly and Coding of 3D Living Architectures. *Advanced Materials* **30**, (2018).
377. Yu, Y. *et al.* Bioinspired Helical Micromotors as Dynamic Cell Microcarriers. *ACS Appl Mater Interfaces* **12**, 16097–16103 (2020).
378. Xu, Z. *et al.* Hierarchically aligned heterogeneous core-sheath hydrogels. *Nat Commun* **16**, 400 (2025).
379. Kang, B. *et al.* Spatial regulation of hydrogel polymerization reaction using ultrasound-driven streaming vortex. *Ultrason Sonochem* **110**, 107053 (2024).
380. Verhulsel, M. *et al.* Developing an advanced gut on chip model enabling the study of epithelial cell/fibroblast interactions. *Lab Chip* **21**, 365–377 (2021).
381. Lapin, B. *et al.* Decoupling shear stress and pressure effects in the biomechanics of autosomal dominant polycystic kidney disease using a perfused kidney-on-chip. *Acta Biomater* (2025) doi:10.1016/j.actbio.2025.03.022.
382. Bouquerel, C. *et al.* Bridging the gap between tumor-on-chip and clinics: a systematic review of 15 years of studies. *Lab Chip* **23**, 3906–3935 (2023).
383. Low, L. A., Mummery, C., Berridge, B. R., Austin, C. P. & Tagle, D. A. Organs-on-chips: into the next decade. *Nat Rev Drug Discov* **20**, 345–361 (2021).
384. Ahmadi Bonakdar, M. & Rodrigue, D. Electrospinning: Processes, Structures, and Materials. *Macromol* **4**, 58–103 (2024).
385. Mironov, V., Boland, T., Trusk, T., Forgacs, G. & Markwald, R. R. Organ printing: computer-aided jet-based 3D tissue engineering. *Trends Biotechnol* **21**, 157–161 (2003).
386. Murphy, S. V & Atala, A. 3D bioprinting of tissues and organs. *Nat Biotechnol* **32**, 773–785 (2014).
387. Giverso, C., Loy, N., Lucci, G. & Preziosi, L. Cell orientation under stretch: A review of experimental findings and mathematical modelling. *J Theor Biol* **572**, 111564 (2023).
388. Chen, K. *et al.* Role of boundary conditions in determining cell alignment in response to stretch. *Proceedings of the National Academy of Sciences* **115**, 986–991 (2018).
389. Foolen, J., Deshpande, V. S., Kanters, F. M. W. & Baaijens, F. P. T. The influence of matrix integrity on stress-fiber remodeling in 3D. *Biomaterials* **33**, 7508–7518 (2012).
390. Minc, N., Burgess, D. & Chang, F. Influence of Cell Geometry on Division-Plane Positioning. *Cell* **144**, 414–426 (2011).
391. Davidson, L. A. *et al.* Emergent morphogenesis: Elastic mechanics of a self-deforming tissue. *J Biomech* **43**, 63–70 (2010).

392. Haupt, A. & Minc, N. How cells sense their own shape – mechanisms to probe cell geometry and their implications in cellular organization and function. *J Cell Sci* **131**, (2018).
393. Junkin, M., Leung, S. L., Whitman, S., Gregorio, C. C. & Wong, P. K. Cellular self-organization by autocatalytic alignment feedback. *J Cell Sci* **124**, 4213–4220 (2011).
394. Duclos, G., Garcia, S., Yevick, H. G. & Silberzan, P. Perfect nematic order in confined monolayers of spindle-shaped cells. *Soft Matter* **10**, 2346–2353 (2014).
395. Schakenraad, K. *et al.* Mechanical interplay between cell shape and actin cytoskeleton organization. *Soft Matter* **16**, 6328–6343 (2020).
396. Dervaux, J. & Ben Amar, M. Morphogenesis of Growing Soft Tissues. *Phys Rev Lett* **101**, 068101 (2008).
397. Black, L. D., Meyers, J. D., Weinbaum, J. S., Shvelidze, Y. A. & Tranquillo, R. T. Cell-Induced Alignment Augments Twitch Force in Fibrin Gel–Based Engineered Myocardium via Gap Junction Modification. *Tissue Eng Part A* **15**, 3099–3108 (2009).
398. O'Rourke, C., Drake, R. AL, Cameron, G. W., Jane Loughlin, A. & Phillips, J. B. Optimising contraction and alignment of cellular collagen hydrogels to achieve reliable and consistent engineered anisotropic tissue. *J Biomater Appl* **30**, 599–607 (2015).
399. Sanen, K. *et al.* Label-free mapping of microstructural organisation in self-aligning cellular collagen hydrogels using image correlation spectroscopy. *Acta Biomater* **30**, 258–264 (2016).
400. Palmquist, K. H. *et al.* Reciprocal cell-ECM dynamics generate supracellular fluidity underlying spontaneous follicle patterning. *Cell* **185**, 1960-1973.e11 (2022).
401. Toda, S., Blauch, L. R., Tang, S. K. Y., Morsut, L. & Lim, W. A. Programming self-organizing multicellular structures with synthetic cell-cell signaling. *Science (1979)* **361**, 156–162 (2018).
402. Reinhardt, J. W., Krakauer, D. A. & Gooch, K. J. Complex Matrix Remodeling and Durotaxis Can Emerge From Simple Rules for Cell-Matrix Interaction in Agent-Based Models. *J Biomech Eng* **135**, (2013).
403. Girigoswami, K., Saini, D. & Girigoswami, A. Extracellular Matrix Remodeling and Development of Cancer. *Stem Cell Rev Rep* **17**, 739–747 (2021).
404. Naylor, A., Zheng, Y., Jiao, Y. & Sun, B. Micromechanical remodeling of the extracellular matrix by invading tumors: anisotropy and heterogeneity. *Soft Matter* **19**, 9–16 (2022).
405. Kim, D.-H. *et al.* Biomechanical interplay between anisotropic re-organization of cells and the surrounding matrix underlies transition to invasive cancer spread. *Sci Rep* **8**, 14210 (2018).
406. Baba, H., Fujita, T., Mizuno, K., Tambo, M. & Toda, S. Programming Spatial Cell Sorting by Engineering Cadherin Intracellular Activity. *ACS Synth Biol* **13**, 1705–1715 (2024).
407. Méhes, E. *et al.* 3D cell segregation geometry and dynamics are governed by tissue surface tension regulation. *Commun Biol* **6**, 817 (2023).
408. Cochet-Escartin, O., Locke, T. T., Shi, W. H., Steele, R. E. & Collins, E.-M. S. Physical Mechanisms Driving Cell Sorting in Hydra. *Biophys J* **113**, 2827–2841 (2017).
409. Rundhaug, J. E. Matrix metalloproteinases and angiogenesis. *J Cell Mol Med* **9**, 267–285 (2005).
410. Massart, R. Preparation of aqueous magnetic liquids in alkaline and acidic media. *IEEE Trans Magn* **17**, 1247–1248 (1981).
411. Teja, A. S. & Koh, P.-Y. Synthesis, properties, and applications of magnetic iron oxide nanoparticles. *Progress in Crystal Growth and Characterization of Materials* **55**, 22–45 (2009).
412. Richard, S. *et al.* 3D Magnetic Alignment of Cardiac Cells in Hydrogels. *ACS Appl Bio Mater* **3**, 6802–6810 (2020).
413. Saraswathy, A. *et al.* Citrate coated iron oxide nanoparticles with enhanced relaxivity for in vivo magnetic resonance imaging of liver fibrosis. *Colloids Surf B Biointerfaces* **117**, 216–224 (2014).
414. Dulińska-Litewka, J. *et al.* Superparamagnetic Iron Oxide Nanoparticles—Current and Prospective Medical Applications. *Materials* **12**, 617 (2019).
415. Gavilán, H. *et al.* Formation Mechanism of Maghemite Nanoflowers Synthesized by a Polyol-Mediated Process. *ACS Omega* **2**, 7172–7184 (2017).
416. Ho, V. H. B. *et al.* Simple Magnetic Cell Patterning Using Streptavidin Paramagnetic Particles. *Exp Biol Med* **234**, 332–341 (2009).
417. Van de Walle, A., Kolosnjaj-Tabi, J., Lalatonne, Y. & Wilhelm, C. Ever-Evolving Identity of Magnetic Nanoparticles within Human Cells: The Interplay of Endosomal Confinement, Degradation, Storage, and Neocrystallization. *Acc Chem Res* **53**, 2212–2224 (2020).
418. Rocha, J. M. V. *et al.* In vitro and in vivo acute toxicity of a novel citrate-coated magnetite nanoparticle. *PLoS One* **17**, e0277396 (2022).

419. Wilhelm, C. & Gazeau, F. Universal cell labelling with anionic magnetic nanoparticles. *Biomaterials* **29**, 3161–3174 (2008).
420. Theumer, A. *et al.* Superparamagnetic iron oxide nanoparticles exert different cytotoxic effects on cells grown in monolayer cell culture versus as multicellular spheroids. *J Magn Magn Mater* **380**, 27–33 (2015).
421. Lu, Q. *et al.* SS-31 modification alleviates ferroptosis induced by superparamagnetic iron oxide nanoparticles in hypoxia/reoxygenation cardiomyocytes. *Heliyon* **10**, e38584 (2024).
422. Fayol, D., Luciani, N., Lartigue, L., Gazeau, F. & Wilhelm, C. Managing Magnetic Nanoparticle Aggregation and Cellular Uptake: a Precondition for Efficient Stem-Cell Differentiation and MRI Tracking. *Adv Healthc Mater* **2**, 313–325 (2013).
423. Wu, M. *et al.* Strategies to Reduce the Intracellular Effects of Iron Oxide Nanoparticle Degradation. *Nanomedicine* **12**, 555–570 (2017).
424. Curcio, A. *et al.* Elucidating the Dynamics of Biodegradation and Biosynthesis of Magnetic Nanoparticles in Human Stem Cells. *Small* (2024) doi:10.1002/smll.202407034.
425. Neuwelt, A. *et al.* Iron-Based Superparamagnetic Nanoparticle Contrast Agents for MRI of Infection and Inflammation. *American Journal of Roentgenology* **204**, W302–W313 (2015).
426. Yin, P. T., Shah, B. P. & Lee, K. Combined Magnetic Nanoparticle-based MicroRNA and Hyperthermia Therapy to Enhance Apoptosis in Brain Cancer Cells. *Small* **10**, 4106–4112 (2014).
427. Hu, Y. *et al.* Magnetic nanochain-induced anisotropic nerve assembly for spinal cord injury repair. *Chemical Engineering Journal* **501**, 157681 (2024).
428. Castro, A. L. *et al.* Engineering Anisotropic Cell Models: Development of Collagen Hydrogel Scaffolds with Magneto-Responsive PEG Microgels for Tissue Engineering Applications. *Adv Mater Technol* **9**, 2301391 (2024).
429. Rose, J. C. *et al.* Nerve Cells Decide to Orient inside an Injectable Hydrogel with Minimal Structural Guidance. *Nano Lett* **17**, 3782–3791 (2017).
430. Zhang, W. *et al.* Magnetically Controlled Growth-Factor-Immobilized Multilayer Cell Sheets for Complex Tissue Regeneration. *Advanced Materials* **29**, (2017).
431. Silva, A. S., Santos, L. F., Mendes, M. C. & Mano, J. F. Multi-layer pre-vascularized magnetic cell sheets for bone regeneration. *Biomaterials* **231**, 119664 (2020).
432. Ino, K., Ito, A. & Honda, H. Cell patterning using magnetite nanoparticles and magnetic force. *Biotechnol Bioeng* **97**, 1309–1317 (2007).
433. Zhang, H. *et al.* Magnetically Induced Anisotropic Microstructures on Polyethylene Glycol Hydrogel Facilitate BMSC Alignment and Osteogenic Differentiation. *Gels* **10**, (2024).
434. Rossi, A. *et al.* Contactless magnetically responsive injectable hydrogel for aligned tissue regeneration. *Mater Today Bio* **27**, 101110 (2024).
435. Margolis, G., Polyak, B. & Cohen, S. Magnetic Induction of Multiscale Anisotropy in Macroporous Alginate Scaffolds. *Nano Lett* **18**, 7314–7322 (2018).
436. Liu, J. *et al.* Manipulation of cellular orientation and migration by internalized magnetic particles. *Mater Chem Front* **1**, 933–936 (2017).
437. Tognato, R. *et al.* A Stimuli-Responsive Nanocomposite for 3D Anisotropic Cell-Guidance and Magnetic Soft Robotics. *Adv Funct Mater* **29**, (2019).
438. Rios, B. *et al.* Mechanically programming anisotropy in engineered muscle with actuating extracellular matrices. *Device* **1**, 100097 (2023).
439. Akiyama, H., Ito, A., Kawabe, Y. & Kamihira, M. Fabrication of complex three-dimensional tissue architectures using a magnetic force-based cell patterning technique. *Biomed Microdevices* **11**, 713–721 (2009).
440. Cao, Z., Clark, A. T., Vite, A. & Corbin, E. A. A Dynamic Gradient Stiffness Material Platform to Manipulate Cardiac Fibroblasts' Spatio-Temporal Behavior. *Adv Funct Mater* **34**, (2024).
441. Akiyama, H., Ito, A., Sato, M., Kawabe, Y. & Kamihira, M. Construction of Cardiac Tissue Rings Using a Magnetic Tissue Fabrication Technique. *Int J Mol Sci* **11**, 2910–2920 (2010).
442. Mattix, B. *et al.* Biological magnetic cellular spheroids as building blocks for tissue engineering. *Acta Biomater* **10**, 623–629 (2014).
443. Goranov, V. *et al.* 3D Patterning of cells in Magnetic Scaffolds for Tissue Engineering. *Sci Rep* **10**, 2289 (2020).
444. Sapir, Y., Cohen, S., Friedman, G. & Polyak, B. The promotion of in vitro vessel-like organization of endothelial cells in magnetically responsive alginate scaffolds. *Biomaterials* **33**, 4100–4109 (2012).

445. Di Corato, R. *et al.* High-Resolution Cellular MRI: Gadolinium and Iron Oxide Nanoparticles for in-Depth Dual-Cell Imaging of Engineered Tissue Constructs. *ACS Nano* **7**, 7500–7512 (2013).
446. Fayol, D. *et al.* Design of Biomimetic Vascular Grafts with Magnetic Endothelial Patterning. *Cell Transplant* **22**, 2105–2118 (2013).
447. Abdel Fattah, A. R. *et al.* In Situ 3D Label-Free Contactless Bioprinting of Cells through Diamagnetophoresis. *ACS Biomater Sci Eng* **2**, 2133–2138 (2016).
448. Frasca, G., Gazeau, F. & Wilhelm, C. Formation of a Three-Dimensional Multicellular Assembly Using Magnetic Patterning. *Langmuir* **25**, 2348–2354 (2009).
449. Huang, L. *et al.* Superparamagnetic Iron Oxide Nanoparticle-Mediated Forces Enhance the Migration of Schwann Cells Across the Astrocyte-Schwann Cell Boundary In vitro. *Front Cell Neurosci* **11**, (2017).
450. Yun, H.-M. *et al.* Magnetic nanocomposite scaffolds combined with static magnetic field in the stimulation of osteoblastic differentiation and bone formation. *Biomaterials* **85**, 88–98 (2016).
451. Zhuang, J., Lin, S., Dong, L., Cheng, K. & Weng, W. Magnetically actuated mechanical stimuli on Fe3O4/mineralized collagen coatings to enhance osteogenic differentiation of the MC3T3-E1 cells. *Acta Biomater* **71**, 49–60 (2018).
452. Xia, Y. *et al.* Novel magnetic calcium phosphate-stem cell construct with magnetic field enhances osteogenic differentiation and bone tissue engineering. *Materials Science and Engineering: C* **98**, 30–41 (2019).
453. Chakraborty, J. *et al.* Development of 4D-bioprinted shape-morphing magnetic constructs for cartilage regeneration using a silk fibroin-gelatin bioink. *Cell Rep Phys Sci* **5**, 101819 (2024).
454. Czichy, C. *et al.* CyMAD bioreactor: A cyclic magnetic actuation device for magnetically mediated mechanical stimulation of 3D bioprinted hydrogel scaffolds. *J Mech Behav Biomed Mater* **131**, 105253 (2022).
455. Fuhrer, R. *et al.* Pressureless Mechanical Induction of Stem Cell Differentiation Is Dose and Frequency Dependent. *PLoS One* **8**, e81362 (2013).
456. Grogan, S. P. *et al.* In situ tissue engineering using magnetically guided three-dimensional cell patterning. *Tissue Eng Part C Methods* **18**, 496–506 (2012).
457. Goodrich, R., Tai, Y., Ye, Z., Yin, Y. & Nam, J. A Magneto-Responsive Hydrogel System for the Dynamic Mechano-Modulation of Stem Cell Niche. *Adv Funct Mater* **33**, (2023).
458. Kuhnt, T. *et al.* 4D Printed Shape Morphing Biocompatible Materials Based on Anisotropic Ferromagnetic Nanoparticles. *Adv Funct Mater* **32**, (2022).
459. Blümler, P. *et al.* Contactless Nanoparticle-Based Guiding of Cells by Controllable Magnetic Fields. *Nanotechnol Sci Appl* **14**, 91–100 (2021).
460. Yanai, A. *et al.* Focused Magnetic Stem Cell Targeting to the Retina Using Superparamagnetic Iron Oxide Nanoparticles. *Cell Transplant* **21**, 1137–1148 (2012).
461. Bratt-Leal, A. M., Kepple, K. L., Carpenedo, R. L., Cooke, M. T. & McDevitt, T. C. Magnetic manipulation and spatial patterning of multi-cellular stem cell aggregates. *Integrative Biology* **3**, 1224–1232 (2011).
462. Wilhelm, C., Cebers, A., Bacri, J.-C. & Gazeau, F. Deformation of intracellular endosomes under a magnetic field. *European Biophysics Journal* **32**, 655–660 (2003).
463. Wilhelm, C., Gazeau, F. & Bacri, J.-C. Rotational magnetic endosome microrheology: Viscoelastic architecture inside living cells. *Phys Rev E* **67**, 061908 (2003).
464. Akiyama, H., Ito, A., Kawabe, Y. & Kamihira, M. Cell-patterning using poly (ethylene glycol)-modified magnetite nanoparticles. *J Biomed Mater Res A* **92A**, 1123–1130 (2010).
465. Dumas, S., Richerd, M., Serra, M. & Descroix, S. Magnetic Microtweezers: A Tool for High-Throughput Bioseparation in Sub-Nanoliter Droplets. *Adv Mater Technol* **8**, (2023).
466. Ouyang, L. *et al.* Expanding and optimizing 3D bioprinting capabilities using complementary network bioinks. *Sci Adv* **6**, (2020).
467. Simińska-Stanny, J. *et al.* 4D printing of patterned multimaterial magnetic hydrogel actuators. *Addit Manuf* **49**, 102506 (2022).
468. Hu, K. *et al.* A Novel Magnetic Hydrogel with Aligned Magnetic Colloidal Assemblies Showing Controllable Enhancement of Magnetothermal Effect in the Presence of Alternating Magnetic Field. *Advanced Materials* **27**, 2507–2514 (2015).
469. Lum, G. Z. *et al.* Shape-programmable magnetic soft matter. *Proceedings of the National Academy of Sciences* **113**, (2016).

470. Tang, J., Yin, Q., Qiao, Y. & Wang, T. Shape Morphing of Hydrogels in Alternating Magnetic Field. *ACS Appl Mater Interfaces* **11**, 21194–21200 (2019).
471. Wilhelm, F. G. J.-C. B. C. Magnetophoresis and ferromagnetic resonance of magnetically labeled cells. *European Biophysics Journal* **31**, 118–125 (2002).
472. Zhang, B., Korolj, A., Lai, B. F. L. & Radisic, M. Advances in organ-on-a-chip engineering. *Nat Rev Mater* **3**, 257–278 (2018).
473. Paggi, C. A., Teixeira, L. M., Le Gac, S. & Karperien, M. Joint-on-chip platforms: entering a new era of in vitro models for arthritis. *Nat Rev Rheumatol* **18**, 217–231 (2022).
474. Matthiesen, I., Voulgaris, D., Nikolakopoulou, P., Winkler, T. E. & Herland, A. Continuous Monitoring Reveals Protective Effects of *N* -Acetylcysteine Amide on an Isogenic Microphysiological Model of the Neurovascular Unit. *Small* **17**, (2021).
475. Ong, L. J. Y. *et al.* Self-aligning Tetris-Like (TILE) modular microfluidic platform for mimicking multi-organ interactions. *Lab Chip* **19**, 2178–2191 (2019).
476. KLÉBER, A. G. & RUDY, Y. Basic Mechanisms of Cardiac Impulse Propagation and Associated Arrhythmias. *Physiol Rev* **84**, 431–488 (2004).
477. Lieber, R. *Skeletal Muscle Structure, Function, and Plasticity*. (2022).
478. Ghovvati, M., Kharaziha, M., Ardehali, R. & Annabi, N. Recent Advances in Designing Electroconductive Biomaterials for Cardiac Tissue Engineering. *Adv Healthc Mater* **11**, (2022).
479. Soucy, J. R. *et al.* Glial cells influence cardiac permittivity as evidenced through *in vitro* and *in silico* models. *Biofabrication* **12**, 015014 (2019).
480. Koeck, K. S., Salehi, S., Humenik, M. & Scheibel, T. Processing of Continuous Non-Crosslinked Collagen Fibers for Microtissue Formation at the Muscle-Tendon Interface. *Adv Funct Mater* **32**, (2022).
481. Ebrahimi, M. *et al.* Enhanced skeletal muscle formation on microfluidic spun gelatin methacryloyl (GelMA) fibres using surface patterning and agrin treatment. *J Tissue Eng Regen Med* **12**, 2151–2163 (2018).
482. Takeda, N. *et al.* In situ cross-linked electrospun fiber scaffold of collagen for fabricating cell-dense muscle tissue. *Journal of Artificial Organs* **19**, 141–148 (2016).
483. Kim, H. N. *et al.* Nanotopography-guided tissue engineering and regenerative medicine. *Adv Drug Deliv Rev* **65**, 536–558 (2013).
484. He, X. *et al.* Uniaxially Aligned Electrospun All-Cellulose Nanocomposite Nanofibers Reinforced with Cellulose Nanocrystals: Scaffold for Tissue Engineering. *Biomacromolecules* **15**, 618–627 (2014).
485. Hadipour, A., Bayati, V., Rashno, M. & Orazizadeh, M. Aligned Poly(ε-caprolactone) Nanofibers Superimposed on Decellularized Human Amniotic Membrane Promoted Myogenic Differentiation of Adipose Derived Stem Cells. *Cell J* **23**, 603–611 (2021).
486. Jain, A. *et al.* Recapitulating pathophysiology of skeletal muscle diseases in vitro using primary mouse myoblasts on a nanofibrous platform. *Nanomedicine* **32**, 102341 (2021).
487. Fujie, T. *et al.* Engineered Nanomembranes for Directing Cellular Organization Toward Flexible Biodevices. *Nano Lett* **13**, 3185–3192 (2013).
488. Vajanthri, K. Y., Sidu, R. K., Poddar, S., Singh, A. K. & Mahto, S. K. Combined substrate micropatterning and FFT analysis reveals myotube size control and alignment by contact guidance. *Cytoskeleton* **76**, 269–285 (2019).
489. Bian, W., Liau, B., Badie, N. & Bursac, N. Mesoscopic hydrogel molding to control the 3D geometry of bioartificial muscle tissues. *Nat Protoc* **4**, 1522–1534 (2009).
490. Juhas, M., Engelmayr, G. C., Fontanella, A. N., Palmer, G. M. & Bursac, N. Biomimetic engineered muscle with capacity for vascular integration and functional maturation in vivo. *Proceedings of the National Academy of Sciences* **111**, 5508–5513 (2014).
491. Hofemeier, A. D. *et al.* Global and local tension measurements in biomimetic skeletal muscle tissues reveals early mechanical homeostasis. *Elife* **10**, (2021).
492. Xu, B., Zhang, M., Perlingeiro, R. C. R. & Shen, W. Skeletal Muscle Constructs Engineered from Human Embryonic Stem Cell Derived Myogenic Progenitors Exhibit Enhanced Contractile Forces When Differentiated in a Medium Containing EGM-2 Supplements. *Adv Biosyst* **3**, (2019).
493. Yoshioka, K. *et al.* Miniaturized skeletal muscle tissue fabrication for measuring contractile activity. *J Biosci Bioeng* **131**, 434–441 (2021).

494. Cabana, S., Curcio, A., Michel, A., Wilhelm, C. & Abou-Hassan, A. Iron Oxide Mediated Photothermal Therapy in the Second Biological Window: A Comparative Study between Magnetite/Maghemite Nanospheres and Nanoflowers. *Nanomaterials* **10**, 1548 (2020).
495. Yan, H. *et al.* "All-in-One" Nanoparticles for Trimodality Imaging-Guided Intracellular Photo-magnetic Hyperthermia Therapy under Intravenous Administration. *Adv Funct Mater* **28**, (2018).
496. Rubia-Rodríguez, I. *et al.* Whither Magnetic Hyperthermia? A Tentative Roadmap. *Materials* **14**, 706 (2021).
497. Huang, H. & Lovell, J. F. Advanced Functional Nanomaterials for Theranostics. *Adv Funct Mater* **27**, (2017).
498. Friedrich, R. P., Cicha, I. & Alexiou, C. Iron Oxide Nanoparticles in Regenerative Medicine and Tissue Engineering. *Nanomaterials* **11**, 2337 (2021).
499. Van de Walle, A. *et al.* Magnetic nanoparticles in regenerative medicine: what of their fate and impact in stem cells? *Mater Today Nano* **11**, 100084 (2020).
500. Kito, T. *et al.* iPS cell sheets created by a novel magnetite tissue engineering method for reparative angiogenesis. *Sci Rep* **3**, 1418 (2013).
501. Gonçalves, A. I., Rodrigues, M. T. & Gomes, M. E. Tissue-engineered magnetic cell sheet patches for advanced strategies in tendon regeneration. *Acta Biomater* **63**, 110–122 (2017).
502. Koudan, E. V. *et al.* Magnetic Patterning of Tissue Spheroids Using Polymer Microcapsules Containing Iron Oxide Nanoparticles. *ACS Biomater Sci Eng* **7**, 5206–5214 (2021).
503. Arifuzzaman, M., Ito, A., Ikeda, K., Kawabe, Y. & Kamihira, M. Fabricating Muscle–Neuron Constructs with Improved Contractile Force Generation. *Tissue Eng Part A* **25**, 563–574 (2019).
504. Yang, G. *et al.* Rapid construction and enhanced vascularization of microtissue using a magnetic control method. *Biofabrication* **13**, 035040 (2021).
505. Almeida, A. F. *et al.* Magnetic triggers in biomedical applications – prospects for contact free cell sensing and guidance. *J Mater Chem B* **9**, 1259–1271 (2021).
506. Kim, Y. *et al.* Remote active control of nanoengineered materials for dynamic nanobiomedical engineering. *VIEW* **1**, (2020).
507. Ishihara, K., Nakayama, K., Akieda, S., Matsuda, S. & Iwamoto, Y. Simultaneous regeneration of full-thickness cartilage and subchondral bone defects in vivo using a three-dimensional scaffold-free autologous construct derived from high-density bone marrow-derived mesenchymal stem cells. *J Orthop Surg Res* **9**, 98 (2014).
508. Norotte, C., Marga, F. S., Niklason, L. E. & Forgacs, G. Scaffold-free vascular tissue engineering using bioprinting. *Biomaterials* **30**, 5910–5917 (2009).
509. Lee, J.-S. *et al.* Angiogenic factors secreted from human ASC spheroids entrapped in an alginate-based hierarchical structure via combined 3D printing/electrospinning system. *Biofabrication* **12**, 045028 (2020).
510. Zhang, K. *et al.* Cellular Nanofiber Structure with Secretory Activity-Promoting Characteristics for Multicellular Spheroid Formation and Hair Follicle Regeneration. *ACS Appl Mater Interfaces* **12**, 7931–7941 (2020).
511. Carr, L. *et al.* A nanosecond pulsed electric field (nsPEF) can affect membrane permeabilization and cellular viability in a 3D spheroids tumor model. *Bioelectrochemistry* **141**, 107839 (2021).
512. Li, Q. *et al.* Universal Peptide Hydrogel for Scalable Physiological Formation and Bioprinting of 3D Spheroids from Human Induced Pluripotent Stem Cells. *Adv Funct Mater* **31**, (2021).
513. Zhang, X. *et al.* 3D Bioprinting of Biomimetic Bilayered Scaffold Consisting of Decellularized Extracellular Matrix and Silk Fibroin for Osteochondral Repair. *Int J Bioprint* **7**, 401 (2021).
514. Chae, S., Hong, J., Hwangbo, H. & Kim, G. The utility of biomedical scaffolds laden with spheroids in various tissue engineering applications. *Theranostics* **11**, 6818–6832 (2021).
515. Sun, W. *et al.* The bioprinting roadmap. *Biofabrication* **12**, 022002 (2020).
516. Hull, S. M. *et al.* 3D Bioprinting using UNIversal Orthogonal Network (UNION) Bioinks. *Adv Funct Mater* **31**, (2021).
517. Plan Sangnier, A. *et al.* Impact of magnetic nanoparticle surface coating on their long-term intracellular biodegradation in stem cells. *Nanoscale* **11**, 16488–16498 (2019).
518. Lévy, M., Wilhelm, C., Devaud, M., Levitz, P. & Gazeau, F. How cellular processing of superparamagnetic nanoparticles affects their magnetic behavior and NMR relaxivity. *Contrast Media Mol Imaging* **7**, 373–383 (2012).

519. Fayol, D., Luciani, N., Lartigue, L., Gazeau, F. & Wilhelm, C. Managing Magnetic Nanoparticle Aggregation and Cellular Uptake: a Precondition for Efficient Stem-Cell Differentiation and MRI Tracking. *Adv Healthc Mater* **2**, 313–325 (2013).
520. Chal, J. & Pourquié, O. Making muscle: skeletal myogenesis *in vivo* and *in vitro*. *Development* **144**, 2104–2122 (2017).
521. Chapman, M. A., Meza, R. & Lieber, R. L. Skeletal muscle fibroblasts in health and disease. *Differentiation* **92**, 108–115 (2016).
522. Mathew, S. J. *et al.* Connective tissue fibroblasts and Tcf4 regulate myogenesis. *Development* **138**, 371–384 (2011).
523. Kim, J. A. *et al.* High-throughput generation of spheroids using magnetic nanoparticles for three-dimensional cell culture. *Biomaterials* **34**, 8555–8563 (2013).
524. Whatley, B. R., Li, X., Zhang, N. & Wen, X. Magnetic-directed patterning of cell spheroids. *J Biomed Mater Res A* **102**, 1537–1547 (2014).
525. Tseng, P., Judy, J. W. & Di Carlo, D. Magnetic nanoparticle–mediated massively parallel mechanical modulation of single-cell behavior. *Nat Methods* **9**, 1113–1119 (2012).
526. Kosheleva, N. V. *et al.* Cell spheroid fusion: beyond liquid drops model. *Sci Rep* **10**, 12614 (2020).
527. Beaune, G., Sinkkonen, L., Gonzalez-Rodriguez, D., Timonen, J. V. I. & Brochard-Wyart, F. Fusion Dynamics of Hybrid Cell–Microparticle Aggregates: A Jelly Pearl Model. *Langmuir* **38**, 5296–5306 (2022).
528. Tsai, A.-C., Liu, Y., Yuan, X. & Ma, T. Compaction, Fusion, and Functional Activation of Three-Dimensional Human Mesenchymal Stem Cell Aggregate. *Tissue Eng Part A* **21**, 1705–1719 (2015).
529. Cui, H. *et al.* Assembly of Multi-Spheroid Cellular Architectures by Programmable Droplet Merging. *Advanced Materials* **33**, (2021).
530. Gérémie, L. *et al.* Evolution of a confluent gut epithelium under on-chip cyclic stretching. *Phys Rev Res* **4**, 023032 (2022).
531. Roman, W. & Gomes, E. R. Nuclear positioning in skeletal muscle. *Semin Cell Dev Biol* **82**, 51–56 (2018).
532. Zhao, J. *et al.* Boost Tendon/Ligament Repair With Biomimetic and Smart Cellular Constructs. *Front Bioeng Biotechnol* **9**, (2021).
533. Vilarta, R. & De Campos Vidal, B. Anisotropic and Biomechanical Properties of Tendons Modified by Exercise and Denervation: Aggregation and Macromolecular Order in Collagen Bundles. *Matrix* **9**, 55–61 (1989).
534. Martina, M.-S. *et al.* The in vitro kinetics of the interactions between PEG-ylated magnetic-fluid-loaded liposomes and macrophages. *Biomaterials* **28**, 4143–4153 (2007).
535. Perez, J. E. *et al.* Transient cell stiffening triggered by magnetic nanoparticle exposure. *J Nanobiotechnology* **19**, 117 (2021).
536. Chuah, Y. J., Kuddannaya, S., Lee, M. H. A., Zhang, Y. & Kang, Y. The effects of poly(dimethylsiloxane) surface silanization on the mesenchymal stem cell fate. *Biomater Sci* **3**, 383–390 (2015).
537. Demri, N. *et al.* Magnetic printing and actuation of stretchable muscle tissue. Preprint at https://doi.org/10.1101/2025.02.19.638972 (2025).
538. Paggi, C. A., Hendriks, J., Karperien, M. & Le Gac, S. Emulating the chondrocyte microenvironment using multi-directional mechanical stimulation in a cartilage-on-chip. *Lab Chip* **22**, 1815–1828 (2022).
539. Sharma, S., Venzac, B., Burgers, T., Schlatt, S. & Le Gac, S. Testis-on-chip platform to study ex vivo primate spermatogenesis and endocrine dynamics. *Organs-on-a-Chip* **4**, 100023 (2022).
540. Moysidou, C. *et al.* 3D Bioelectronic Model of the Human Intestine. *Adv Biol* **5**, (2021).
541. Jouybar, M., Sleeboom, J. J. F., Vaezzadeh, E., Sahlgren, C. M. & den Toonder, J. M. J. An in vitro model of cancer invasion with heterogeneous ECM created with droplet microfluidics. *Front Bioeng Biotechnol* **11**, (2023).
542. Nie, J. *et al.* A Cell Pre-Wrapping Seeding Technique for Hydrogel-Based Tubular Organ-On-A-Chip. *Advanced Science* (2024) doi:10.1002/advs.202400970.
543. Moussus, M. *et al.* Intracellular stresses in patterned cell assemblies. *Soft Matter* **10**, 2414–2423 (2013).
544. Ingber, D. E. Mechanical control of tissue growth: Function follows form. *Proceedings of the National Academy of Sciences* **102**, 11571–11572 (2005).

545. Bugnicourt, G., Brocard, J., Nicolas, A. & Villard, C. Nanoscale Surface Topography Reshapes Neuronal Growth in Culture. *Langmuir* **30**, 4441–4449 (2014).
546. Garibyan, M. *et al.* Engineering programmable material-to-cell pathways via synthetic notch receptors to spatially control differentiation in multicellular constructs. *Nat Commun* **15**, 5891 (2024).
547. Eyckmans, J. & Chen, C. S. 3D culture models of tissues under tension. *J Cell Sci* (2016) doi:10.1242/jcs.198630.
548. Rouwkema, J., Koopman, B. F. J. M., Blitterswijk, C. A. Van, Dhert, W. J. A. & Malda, J. Supply of Nutrients to Cells in Engineered Tissues. *Biotechnol Genet Eng Rev* **26**, 163–178 (2009).
549. Li, E. W., McKee-Muir, O. C. & Gilbert, P. M. Cellular Biomechanics in Skeletal Muscle Regeneration. in 125–176 (2018). doi:10.1016/bs.ctdb.2017.08.007.
550. Fernandes, A. R., Martins, J. P., Gomes, E. R., Mendes, C. S. & Teodoro, R. O. Drosophila motor neuron boutons remodel through membrane blebbing coupled with muscle contraction. *Nat Commun* **14**, 3352 (2023).
551. Sunadome, K. *et al.* Directionality of developing skeletal muscles is set by mechanical forces. *Nat Commun* **14**, 3060 (2023).
552. Kim, S., Uroz, M., Bays, J. L. & Chen, C. S. Harnessing Mechanobiology for Tissue Engineering. *Dev Cell* **56**, 180–191 (2021).
553. Träber, N. *et al.* Polyacrylamide Bead Sensors for in vivo Quantification of Cell-Scale Stress in Zebrafish Development. *Sci Rep* **9**, 17031 (2019).
554. Sequeira, V., Nijenkamp, L. L. A. M., Regan, J. A. & van der Velden, J. The physiological role of cardiac cytoskeleton and its alterations in heart failure. *Biochimica et Biophysica Acta (BBA) - Biomembranes* **1838**, 700–722 (2014).
555. Hicks, M. R. *et al.* Regenerating human skeletal muscle forms an emerging niche in vivo to support PAX7 cells. *Nat Cell Biol* **25**, 1758–1773 (2023).
556. Ganassi, M., Badodi, S., Wanders, K., Zammit, P. S. & Hughes, S. M. Myogenin is an essential regulator of adult myofibre growth and muscle stem cell homeostasis. *Elife* **9**, (2020).
557. Sjöblom, B., Salmazo, A. & Djinović-Carugo, K. α-Actinin structure and regulation. *Cellular and Molecular Life Sciences* **65**, 2688–2701 (2008).
558. El Haj, A. J. *et al.* An *in vitro* model of mesenchymal stem cell targeting using magnetic particle labelling. *J Tissue Eng Regen Med* **9**, 724–733 (2015).
559. Lee, J. S. *et al.* Magnetically Coated Bioabsorbable Stents for Renormalization of Arterial Vessel Walls after Stent Implantation. *Nano Lett* **18**, 272–281 (2018).
560. Girardo, S. *et al.* Standardized microgel beads as elastic cell mechanical probes. *J Mater Chem B* **6**, 6245–6261 (2018).
561. Duque, J. *et al.* Rupture strength of living cell monolayers. *Nat Mater* **23**, 1563–1574 (2024).
562. Harris, A. R. *et al.* Characterizing the mechanics of cultured cell monolayers. *Proceedings of the National Academy of Sciences* **109**, 16449–16454 (2012).
563. Guven, S. *et al.* Multiscale assembly for tissue engineering and regenerative medicine. *Trends Biotechnol* **33**, 269–279 (2015).
564. Mobaraki, M., Ghaffari, M., Yazdanpanah, A., Luo, Y. & Mills, D. K. Bioinks and bioprinting: A focused review. *Bioprinting* **18**, e00080 (2020).
565. Agrawal, A. *et al.* Smooth Muscle Cell Alignment and Phenotype Control by Melt Spun Polycaprolactone Fibers for Seeding of Tissue Engineered Blood Vessels. *Int J Biomater* **2015**, 1–8 (2015).
566. Meng, F. *et al.* Mechanical stretching boosts expansion and regeneration of intestinal organoids through fueling stem cell self-renewal. *Cell Regeneration* **11**, 39 (2022).
567. Gauvin, R. *et al.* Dynamic mechanical stimulations induce anisotropy and improve the tensile properties of engineered tissues produced without exogenous scaffolding. *Acta Biomater* **7**, 3294–3301 (2011).
568. Jungbauer, S., Gao, H., Spatz, J. P. & Kemkemer, R. Two Characteristic Regimes in Frequency-Dependent Dynamic Reorientation of Fibroblasts on Cyclically Stretched Substrates. *Biophys J* **95**, 3470–3478 (2008).
569. Throm Quinlan, A. M., Sierad, L. N., Capulli, A. K., Firstenberg, L. E. & Billiar, K. L. Combining Dynamic Stretch and Tunable Stiffness to Probe Cell Mechanobiology In Vitro. *PLoS One* **6**, e23272 (2011).

570. Arif, Z. U., Khalid, M. Y., Ahmed, W. & Arshad, H. A review on four-dimensional (4D) bioprinting in pursuit of advanced tissue engineering applications. *Bioprinting* **27**, e00203 (2022).
571. Hannezo, E., Prost, J. & Joanny, J.-F. Mechanical Instabilities of Biological Tubes. *Phys Rev Lett* **109**, 018101 (2012).
572. Wyczalkowski, M. A., Chen, Z., Filas, B. A., Varner, V. D. & Taber, L. A. Computational models for mechanics of morphogenesis. *Birth Defects Res C Embryo Today* **96**, 132–152 (2012).
573. Palmquist, K. H. *et al.* Reciprocal cell-ECM dynamics generate supracellular fluidity underlying spontaneous follicle patterning. *Cell* **185**, 1960-1973.e11 (2022).
574. Taymour, R., Kilian, D., Ahlfeld, T., Gelinsky, M. & Lode, A. 3D bioprinting of hepatocytes: core–shell structured co-cultures with fibroblasts for enhanced functionality. *Sci Rep* **11**, 5130 (2021).
575. Bonfanti, A., Duque, J., Kabla, A. & Charras, G. Fracture in living tissues. *Trends Cell Biol* **32**, 537–551 (2022).
576. Gonzalez-Rodriguez, D. *et al.* Detachment and fracture of cellular aggregates. *Soft Matter* **9**, 2282 (2013).
577. Colbert, M.-J., Brochard-Wyart, F., Fradin, C. & Dalnoki-Veress, K. Squeezing and Detachment of Living Cells. *Biophys J* **99**, 3555–3562 (2010).
578. Merkel, R., Nassoy, P., Leung, A., Ritchie, K. & Evans, E. Energy landscapes of receptor–ligand bonds explored with dynamic force spectroscopy. *Nature* **397**, 50–53 (1999).
579. Papafilippou, E., Baldauf, L., Charras, G., Kabla, A. & Bonfanti, A. Interplay of damage and repair in the control of epithelial tissue integrity in response to cyclic loading. (2024).
580. Sumi, A. *et al.* Adherens Junction Length during Tissue Contraction Is Controlled by the Mechanosensitive Activity of Actomyosin and Junctional Recycling. *Dev Cell* **47**, 453-463.e3 (2018).
581. Liu, Y. & Dai, F. A review of experimental and theoretical research on the deformation and failure behavior of rocks subjected to cyclic loading. *Journal of Rock Mechanics and Geotechnical Engineering* **13**, 1203–1230 (2021).
582. Gadallah, R., Murakawa, H., Ikushima, K., Shibahara, M. & Tsutsumi, S. Numerical investigation on the effect of thickness and stress level on fatigue crack growth in notched specimens. *Theoretical and Applied Fracture Mechanics* **116**, 103138 (2021).
583. Van de Walle, A. *et al.* Biosynthesis of magnetic nanoparticles from nano-degradation products revealed in human stem cells. *Proceedings of the National Academy of Sciences* **116**, 4044–4053 (2019).
584. Kim, H., Kim, M.-C. & Asada, H. H. Extracellular matrix remodelling induced by alternating electrical and mechanical stimulations increases the contraction of engineered skeletal muscle tissues. *Sci Rep* **9**, 2732 (2019).
585. Roman, W., Martins, J. P. & Gomes, E. R. Local Arrangement of Fibronectin by Myofibroblasts Governs Peripheral Nuclear Positioning in Muscle Cells. *Dev Cell* **46**, 102-111.e6 (2018).
586. Kim, J. & Kim, G. Formation of various cell-aggregated structures in the core of hydrogel filament using a microfluidic device and its application as an in vitro neuromuscular junction model. *Chemical Engineering Journal* **472**, 144979 (2023).
587. Gilbert-Honick, J. & Grayson, W. Vascularized and Innervated Skeletal Muscle Tissue Engineering. *Adv Healthc Mater* **9**, (2020).
588. Wan, L., Flegle, J., Ozdoganlar, B. & LeDuc, P. Toward Vasculature in Skeletal Muscle-on-a-Chip through Thermo-Responsive Sacrificial Templates. *Micromachines (Basel)* **11**, 907 (2020).
589. Osaki, T., Sivathanu, V. & Kamm, R. D. Crosstalk between developing vasculature and optogenetically engineered skeletal muscle improves muscle contraction and angiogenesis. *Biomaterials* **156**, 65–76 (2018).
590. Mangual, J. O., Li, S., Ploehn, H. J., Ebner, A. D. & Ritter, J. A. Biodegradable nanocomposite magnetite stent for implant-assisted magnetic drug targeting. *J Magn Magn Mater* **322**, 3094–3100 (2010).
591. Uthamaraj, S., Tefft, B. J., Hlinomaz, O., Sandhu, G. S. & Dragomir-Daescu, D. Ferromagnetic Bare Metal Stent for Endothelial Cell Capture and Retention. *J Vis Exp* (2015) doi:10.3791/53100.

Summary

Tissue engineering aims to recreate physiologically relevant, functional biological tissues for biomedical applications. Among the most challenging targets are anisotropic tissues, such as skeletal muscle, where oriented architectures are essential to both structure and function. By leveraging the properties of magnetic nanoparticles internalized by cells, remote magnetic forces can be applied to guide anisotropic tissue morphogenesis.

After reviewing the biology of anisotropic tissues and the current engineering strategies, this PhD thesis introduces three original magnetic anisotropic tissue engineering approaches, specifically applied to skeletal muscle. These studies were made possible thanks to an initial optimization of magnetic nanoparticle internalization by myoblasts. The first magnetic platform was designed for generating small spheroids from these magnetically labeled cells at high throughput, aligning them in a collagen matrix, and ultimately revealing a transition from a linear arrangement of spheroids to a continuous fiber. To further enhance control over tissue shape and function, a novel magnetic bioprinting technique was established. This system enabled the engineering of wrench-shaped tissues that can be clipped onto two magnetic attractors, to preserve their initial shape and allow up to 100% stretching. Magnetic trapping and mechanical stimulation accelerated the differentiation of functional muscle tissues in just a few days, particularly when they were engineered with myoblasts derived from human induced pluripotent stem cells. The versatility of magnetic bioprinting was then explored by creating tissues of arbitrary shapes - triangles, droplets, squares, and crosses. The cross-shaped tissues, in particular, allowed for a clear demonstration of the relationship between tissue geometry, mechanical constraints, and differentiation. Additionally, this work investigated the resistance to rupture of magnetically printed tissues while also establishing the feasibility of co-culturing fibroblasts, using magnetism to precisely control the spatial segregation of different cell types.

Overall, this PhD thesis highlights the potential of magnetic forces for engineering structured, functional tissues, particularly skeletal muscle, and paves the way for biomedical applications in disease modeling, mechanobiology, and remotely guided tissue grafting.

Keywords: Tissue engineering – Magnetic nanoparticles – Magnetic bioprinting – Skeletal muscle – Biomechanics – Microfabrication